

MAGNETIC RESONANCE IMAGING  
OF THE INNER EAR

Jan Walter Casselman

Jan Walter Casselman

MAGNETIC RESONANCE IMAGING OF THE INNER EAR

Jan Walther Casselman

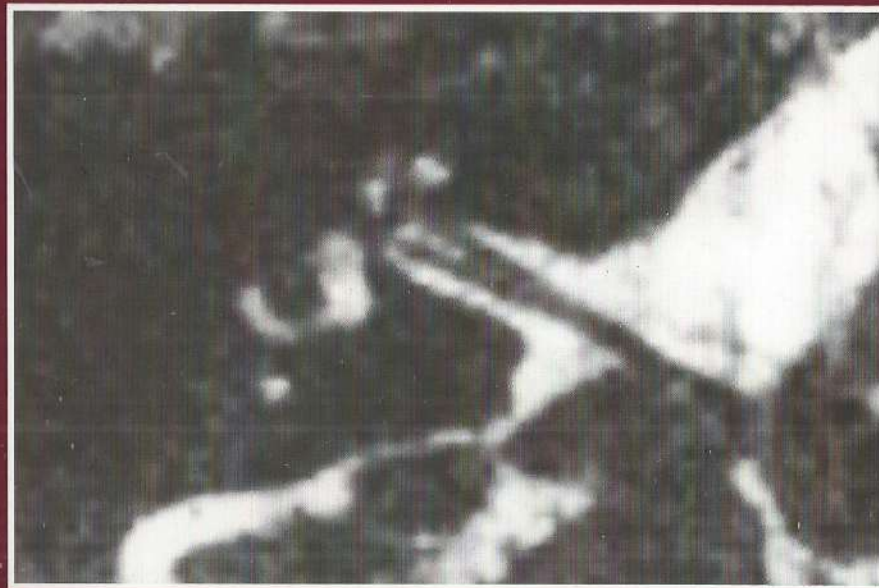
MAGNETIC RESONANCE IMAGING OF THE INNER EAR

UNIVERSITEIT GENT

*Faculteit Geneeskunde*

# MAGNETIC RESONANCE IMAGING OF THE INNER EAR

Jan Walther Casselman



*Promoters: Prof. Dr. P. Van Cauwenberge*

*Prof. Dr. M. Kunnen*

*Co-Promoter: Prof. F.W.J. Albers*

*Thesis submitted for partial fulfilment of the requirements for  
the degree of "Geaggregeerde voor het Hoger Onderwijs"*

Department of Radiology and Medical Imaging

A.Z. St.-Jan Brugge

Brugge

1994

MAGNETIC RESONANCE IMAGING  
OF THE INNER EAR

UNIVERSITEIT GENT

*Faculteit Geneeskunde*

**MAGNETIC RESONANCE IMAGING  
OF THE INNER EAR**

**Jan Walther Casselman**

*Promoters: Prof. Dr. P. Van Cauwenberge*

*Prof. Dr. M. Kunnen*

*Co-Promoter: Prof. F.W.J. Albers*

*Thesis submitted for partial fulfilment of the requirements for  
the degree of "Geaggregeerde voor het Hoger Onderwijs"*

Department of Radiology and Medical Imaging

A.Z. St.-Jan Brugge

Brugge

1994

*This work is dedicated to Lut, Wouter,  
An-Katrien and Liesbeth.*

## ACKNOWLEDGEMENTS

This is the ideal opportunity to thank those people who were indispensable in the achievement of this thesis.

First of all I want to thank my promoters Prof. Dr. P. VAN CAUWENBERGE and Prof. Dr. M. KUNNEN, and my co-promoter Prof. Dr. F. ALBERS, for giving me the opportunity to carry out this work. Prof. Dr. P. Van Cauwenberge saw the clinical possibilities of my work and has been encouraging me to continue. Prof. Dr. M. Kunnen also believed in the use of new radiological techniques to study the inner ear and supported my work. My co-promoter Prof. Dr. F. Albers has been enthusiastic about my new MR technique since the beginning and our co-operation has resulted in several interesting clinical applications and studies.

Further I want also to thank Prof. Dr. A. BAERT who gave me the opportunity to do my radiological studies, and I am also thankful for the education in neuroradiology that I received from Prof. Dr. G. WILMS.

I certainly do not want to forget to thank a very good friend, Prof. Dr. A.A. MANCUSO. His contagious enthusiasm is unique and since I had the opportunity to work with him at the University of Florida, Gainesville, I have never lost my enthusiasm for Head and Neck radiology. I still remember our long discussions on any imaginable head and neck subject, and I'm also grateful for the initiation in magnetic resonance he gave me. Teaching at such a high level, with such an intensity and in a very amicable way was a new experience for me and I'll never forget it.

I also realize that it would have been impossible to develop and test new MR sequences for the inner ear if I did not have the support of my colleagues in Bruges. I appreciated very much the support of Dr. G. PATTYN, who was often as excited by the results as I was and made it practically possible for me to undertake this thesis.

Thanks also to Mr. Willy DAENEKINDT, Benny ROELENS and Peter DALLET, our three MR-technicians who performed the large amount of MR-studies I needed for this thesis in a very dedicated and patient-friendly way.

The help of Mrs. G. VANDEMAELE (MR-applications, Siemens, Brussels) and Mr. M. DEIMLING (Medical Engineering Group Siemens, Erlangen) was also indispensable for the development of the sequences I needed for this thesis.

I also want to express my gratitude to many Otorhinolaryngology colleagues and especially to Dr. R. KUHWEIDE, Dr. W. AMPE, Dr. G. D'HONT, Dr. B. ARS and Prof.

Dr. E. OFFECIERS who taught me the clinical aspects of inner ear pathology and pushed me in the right direction with the new imaging possibilities.

Finally I want to thank my parents, who offered me the chance to study and supported me for years. And last but not least I'm very grateful for the understanding of my wife, Lut. She helped me with the 'patient' material and with the manuscript and without her co-operation it would have been impossible to write this thesis.

I am also grateful for the financial support I received from the following companies: SOLVAY-DUPHAR, SIEMENS Belgium, CODALI-GUERBET, SCHERING DIAGNOSTICS and AGFA-GEVAERT. Their contribution allowed me to edit this thesis in a professional way.

# CONTENTS

<b>ACKNOWLEDGEMENTS</b>	5
<b>I. GENERAL INTRODUCTION</b>	11
1. Conventional Radiography of the Inner Ear	11
2. Computed Tomography of the Inner Ear	11
3. Magnetic Resonance of the Inner Ear	12
4. References	13
<b>II. AIMS OF THE STUDIES</b>	17
<b>III. MATERIAL AND METHODS</b>	19
<b>1. Anatomy of the Inner Ear</b>	19
1.1. Cerebellopontine angle	19
1.2. Internal Auditory Canal	20
1.3. The Inner Ear - Bony Labyrinth	21
1.3.1. Vestibule	22
1.3.2. Semicircular canals	23
1.3.3. Cochlea	23
1.4. The Inner Ear - Membranous Labyrinth	23
1.4.1. Cochlear duct	24
1.4.2. The round window membrane	24
1.4.3. Sensory organs of the vestibular labyrinth	25
1.4.4. Endolymphatic duct and sac	26
1.4.5. Vascular system	26
1.4.6. Spiral ganglion - Scarpa's ganglion	27
1.5. The Inner Ear - Perilymphatic & Endolymphatic Spaces	27
1.6. References	28
<b>2. Magnetic Resonance Techniques</b>	30
2.1. Basic Principles	30
2.1.1. Properties of atomic nuclei	30
2.1.2. Nuclei in a magnetic field	30
2.1.3. Macroscopic magnetization	31
2.1.4. Radiofrequent pulses and magnetic resonance	32
2.2. Spin-Echo Imaging	33
2.2.1. T1-relaxation (spin-lattice)	33
2.2.2. T2-relaxation (spin-spin)	34

2.2.3. T2* relaxation and spin-echo	34	2.5.1. Pathology causing contrast enhancement inside the membranous labyrinth	94
2.2.4. T1 contrast	35	2.5.2. Temporal bone tumors involving the bony and membranous labyrinth	97
2.2.5. T2 contrast	36	2.5.3. Congenital malformations of the membranous labyrinth	103
2.3. Gradients - Slice Selection - Spatial Encoding Methods	37	2.5.4. Pathology causing obliteration of the labyrinthine fluid spaces	103
2.3.1. Gradients-slice selection	37	2.5.5. Conclusion	108
2.3.2. Spacial encoding methods	39	2.6. Acknowledgments	108
2.3.3. Phase encoding	40	2.7. References	109
2.3.4. Frequency encoding	41	2.8. Addendum: Possible Causes of Labyrinth Enhancement - Updated Overview	110
2.3.5. Phase and frequency encoding	41	2.8.1. Enhancement in the membranous labyrinth	110
2.4. Imaging Cycle - 2D Multislice Imaging - 3D Volume Imaging	42	2.8.2. Enhancement in the bony labyrinth	115
2.4.1. Imaging cycle	42	2.8.3. Conclusion	118
2.4.2. Multislice imaging	43	2.8.4. References	119
2.4.3. Three dimensional (3D) volume imaging	44	<b>3. MR of the Inner Ear in Patients with Cogan Syndrome</b>	121
2.5. Gradient-Echo Imaging, 3DFT-CISS Sequence	45	3.1. Abstract	121
2.5.1. Gradient-echo imaging with small flip angles	45	3.2. Introduction	122
2.5.2. 3DFT-CISS (Constructive interference in steady state) sequence	47	3.3. Subjects and Methods	122
2.6. References	51	3.4. Results	124
<b>3. Patients-Sequences</b>	52	3.5. Discussion	125
3.1. Patients	52	3.6. Conclusion	134
3.2. Sequences	53	3.7. References	134
<b>IV. GENERAL RESULTS</b>	55	<b>4. Magnetic Resonance Examination of the Inner Ear and Cerebellopontine Angle in Patients with Vertigo and/or Abnormal Findings at Vestibular Testing</b>	137
<b>V. STUDIES - RESULTS</b>	57	4.1. Abstract	137
1. Constructive Interference in Steady State-3DFT MR Imaging of the Inner Ear and Cerebellopontine Angle	59	4.2. Introduction	138
1.1. Abstract	59	4.3. Subjects and Methods	138
1.2. Introduction	59	4.3.1. Patients	138
1.3. Subject and Methods	60	4.3.2. Techniques	143
1.4. Results	69	4.3.3. Treatment of the data	143
1.4.1. Normal inner ears	69	4.4. Results	144
1.4.2. Pathologic inner ears	70	4.4.1. Posterior fossa	144
1.5. Discussion	70	4.4.2. IAC	144
1.6. Acknowledgements	81	4.4.3. Membranous labyrinth	144
1.7. References	81	4.5. Discussion and Comments	144
1.8. Addendum I	82	4.5.1. Posterior fossa pathology	145
1.9. Addendum II	85	4.5.2. Internal auditory canal pathology	149
2. Pathology of the Membranous Labyrinth: Comparison of T1- and T2-weighted and Gadolinium-Enhanced Spin-Echo and 3DFT-CISS Imaging	89	4.5.3. Membranous labyrinth pathology	152
2.1. Abstract	89	4.5.4. Meniere's disease	162
2.2. Introduction	90	4.6. Conclusions	164
2.3. Subjects and Methods	90	4.7. References	167
2.4. Results	91	<b>5. The Value of Gradient-Echo (3DFT-CISS) MR Imaging in the Detection of Congenital Inner Ear Malformations</b>	171
2.5. Discussion	93	5.1. Introduction	171

2.2.3. T2* relaxation and spin-echo	34	2.5.1. Pathology causing contrast enhancement inside the membranous labyrinth	94
2.2.4. T1 contrast	35	2.5.2. Temporal bone tumors involving the bony and membranous labyrinth	97
2.2.5. T2 contrast	36	2.5.3. Congenital malformations of the membranous labyrinth	103
2.3. Gradients - Slice Selection - Spatial Encoding Methods	37	2.5.4. Pathology causing obliteration of the labyrinthine fluid spaces	103
2.3.1. Gradients-slice selection	37	2.5.5. Conclusion	108
2.3.2. Spacial encoding methods	39	2.6. Acknowledgments	108
2.3.3. Phase encoding	40	2.7. References	109
2.3.4. Frequency encoding	41	2.8. Addendum: Possible Causes of Labyrinth Enhancement - Updated Overview	110
2.3.5. Phase and frequency encoding	41	2.8.1. Enhancement in the membranous labyrinth	110
2.4. Imaging Cycle - 2D Multislice Imaging - 3D Volume Imaging	42	2.8.2. Enhancement in the bony labyrinth	115
2.4.1. Imaging cycle	42	2.8.3. Conclusion	118
2.4.2. Multislice imaging	43	2.8.4. References	119
2.4.3. Three dimensional (3D) volume imaging	44	<b>3. MR of the Inner Ear in Patients with Cogan Syndrome</b>	121
2.5. Gradient-Echo Imaging, 3DFT-CISS Sequence	45	3.1. Abstract	121
2.5.1. Gradient-echo imaging with small flip angles	45	3.2. Introduction	122
2.5.2. 3DFT-CISS (Constructive interference in steady state) sequence	47	3.3. Subjects and Methods	122
2.6. References	51	3.4. Results	124
<b>3. Patients-Sequences</b>	52	3.5. Discussion	125
3.1. Patients	52	3.6. Conclusion	134
3.2. Sequences	53	3.7. References	134
<b>IV. GENERAL RESULTS</b>	55	<b>4. Magnetic Resonance Examination of the Inner Ear and Cerebellopontine Angle in Patients with Vertigo and/or Abnormal Findings at Vestibular Testing</b>	137
<b>V. STUDIES - RESULTS</b>	57	4.1. Abstract	137
<b>1. Constructive Interference in Steady State-3DFT MR Imaging of the Inner Ear and Cerebellopontine Angle</b>	59	4.2. Introduction	138
1.1. Abstract	59	4.3. Subjects and Methods	138
1.2. Introduction	59	4.3.1. Patients	138
1.3. Subject and Methods	60	4.3.2. Techniques	143
1.4. Results	69	4.3.3. Treatment of the data	143
1.4.1. Normal inner ears	69	4.4. Results	144
1.4.2. Pathologic inner ears	70	4.4.1. Posterior fossa	144
1.5. Discussion	70	4.4.2. IAC	144
1.6. Acknowledgements	81	4.4.3. Membranous labyrinth	144
1.7. References	81	4.5. Discussion and Comments	144
1.8. Addendum I	82	4.5.1. Posterior fossa pathology	145
1.9. Addendum II	85	4.5.2. Internal auditory canal pathology	149
<b>2. Pathology of the Membranous Labyrinth: Comparison of T1- and T2-weighted and Gadolinium-Enhanced Spin-Echo and 3DFT-CISS Imaging</b>	89	4.5.3. Membranous labyrinth pathology	152
2.1. Abstract	89	4.5.4. Meniere's disease	162
2.2. Introduction	90	4.6. Conclusions	164
2.3. Subjects and Methods	90	4.7. References	167
2.4. Results	91	<b>5. The Value of Gradient-Echo (3DFT-CISS) MR Imaging in the Detection of Congenital Inner Ear Malformations</b>	171
2.5. Discussion	93	5.1. Introduction	171

5.2. Materials and Methods	172
5.3. Results	174
5.4. Discussion	174
5.4.1. Large vestibular aqueduct syndrome (LVAS)	175
5.4.2. Lateral semicircular canal - vestibule dysplasia (LCVD)	180
5.4.3. Other Pathologies	183
5.5. Conclusion	183
5.6. References	188
<b>6. Three-Dimensional Magnetic Resonance Imaging of the Inner Ear in Idiopathic Sudden Sensorineural Hearing Loss</b>	191
6.1. Abstract	191
6.2. Introduction	191
6.3. Subjects and Methods	192
6.4. Results	192
6.5. Discussion	194
6.6. References	196
<b>7. 3DFT-Magnetic Resonance Imaging of the Inner Ear in Meniere's Disease</b>	199
7.1. Abstract	199
7.2. Introduction	199
7.3. Subjects and Methods	200
7.4. Results	201
7.5. Discussion	206
7.6. References	206
<b>VI. CONCLUSIONS AND SUMMARY</b>	209
1. Anatomy	209
2. MR Sequences Used to Study the Inner Ear	209
3. The Value of the Different MR Sequences in the Study of Inner Ear Pathologies	210
4. Value of MR and Especially the 3DFT-CISS Technique in the Study of Patients Presenting with Specific Signs and Symptoms	212
5. Conclusion	213
<b>VII. SAMENVATTING EN CONCLUSIE</b>	215
1. Anatomie	215
2. MR Sekwenties Gebruikt bij de Studie van het Binnenoor	215
3. De Waarde van de Verschillende MR Sekwenties bij de Studie van Binnenoorletsels	217
4. De Waarde van MR en in het Bijzonder van de 3DFT-CISS Techniek bij het Onderzoek van Patiënten met Welbepaalde Klinische Tekens en Symptomen	219
5. Conclusie	220

# I. GENERAL INTRODUCTION

## 1. Conventional Radiography of the Inner Ear

For many years radiologists only had conventional radiography to study the inner ear and internal auditory canal (IAC). The problem was that the orbital walls and other bony structures of the jaws, mid-face and skull base were often hiding the inner ear. This superimposition was overcome by using adequate radiological projections. The most successful projections were the Schuller, Chaussee III, Guillen, Towne, Stenvers, Hirtz and Skull anterior-posterior (with petrous pyramids inside orbits) projections (1-4). Every projection had its advantages showing some of the inner ear structures better than the other projections, but a combination of different projections was often necessary to have an overview of the total inner ear.

In the late 1950s, tomography began in France and quickly became the method of choice to evaluate the middle and inner ear. Superimposition was now avoided with tomography and the bone structures of the inner ear and IAC could for the first time be seen in more detail. Hypocycloid or spiral movement, known as polytomography, provided better images than linear tomography. Again different polytomographic projections were used to visualize different parts of the inner or middle ear (2-4) but today polytomography of the temporal bone is avoided due to the irradiation and is replaced by Computed Tomography (CT). Both conventional tomography and polytomography allowed only evaluation of the bony inner ear and bony walls of the IAC. The membranous labyrinth, the nerves in the IAC and cerebellopontine angle (CPA) remained invisible. However, these techniques made it possible to recognize inner ear fractures, congenital inner ear malformations, labyrinthitis ossificans, invasion of the inner ear by cholesteatoma or other tumours, otospongiosis and large tumours (acoustic schwannomas) in the porus or IAC etc. (5-9).

Opaque cerebellopontine cisternography was needed to detect smaller lesions in the CPA and IAC. The use of positive contrast medium in the diagnosis of acoustic neuroma was introduced by Scanlan (10).

## 2. Computed Tomography of the Inner Ear

In the late seventies and early eighties CT became the most accurate technique to study the inner ear. The first anatomic studies showed that the bony labyrinth could now be seen in detail (11-12) and also revealed better visualization of the structures of the IAC and CPA due to better contrast resolution between bone, cerebrospinal fluid (CSF) and brain tissue. Reports on better detectability of acoustic schwannomas in the CPA and even in the IAC were published very early on (13-15). The nerves and vascular loop in the CPA, and

especially the nerves inside the IAC, remained difficult to see, and pneumocisternomeatography was necessary to recognize these structures and was even needed to detect small schwannomas inside the auditory canal (16-18).

Several generations of CT-scanners followed one another and the latest scanners are able to detect very small anatomic structures. They can also show most of the inflammatory, traumatic and tumoural lesions affecting the bony labyrinth.

However, small acoustic schwannomas in the CPA and IAC and pathology of the membranous labyrinth remain very difficult to detect. In the membranous labyrinth only air (posttraumatic) and calcifications (labyrinthitis ossificans) are easy to recognize (19-20). Labyrinthitis or tumours inside the membranous labyrinth remain invisible on CT. Neuritis of the facial or cochleovestibular nerve are also invisible on CT, but small schwannomas along the course of the second and third part of the facial nerve and in the geniculate ganglion are visible thanks to the changes of the bony walls of the facial nerve canal caused by the schwannomas (21).

### 3. Magnetic Resonance of the Inner Ear

In the eighties magnetic resonance emerged as an excellent diagnostic method to look for pathology in the CPA and IAC. The advantages of the MR technique were its higher "contrast resolution" and the absence of artefacts produced by the surrounding bone. The routine T1- and T2-weighted spin-echo images allowed detection of acoustic schwannomas in the CPA and IAC (22-23).

The intravenous administration of contrast material, Gadolinium (Gd)-DTPA or Gd-DOTA, made MR even more sensitive in the detection of small schwannomas in the CPA and IAC (24). Together with the use of thinner MR slices, gadolinium also led to the detection of enhancement of the nerves in the IAC and of the geniculate ganglion and second and third part of the facial nerve in case of neuritis (25). The combination of thin MR slices and Gd also drew attention to the membranous labyrinth, where sporadically enhancement could be seen. The first report on intralabyrinthine enhancement was published in 1990 (26).

The possibilities of MR in the study of the inner ear were already astonishing but further research and experience were needed. The T1-weighted images were still 3 mm thick and relatively poor in contrast resolution, therefore they were not able to exclude very small lesions in the IAC (volume-averaging artefacts) and obliteration of the intralabyrinthine fluid spaces could not be seen. The intralabyrinthine fluid was visible as high signal on T2-weighted images but these images were too thick (4 mm and more) so that the membranous labyrinth was only visible on 1 or 2 images. Moreover the meaning of enhancement in the IAC or membranous labyrinth was unclear. Differentiation between tumour enhancement or neuritis in the IAC was not always possible on these images and differentiation between an intralabyrinthine tumour that enhanced and leakage of Gd inside the intralabyrinthine fluid in case of infection or vascular disease was not possible.

Therefore at several sites, radiologists started to look for other MR-sequences providing thinner slices and better contrast between fluid, nerves and bone in order to be able to study the membranous labyrinth.

In 1991 I started to use an abandoned sequence, Constructive Interference in Steady State (CISS) three-dimensional Fourier transformation (3DFT) sequence, originally designed to study the medulla and the surrounding CSF. My first aim was to test whether detailed evaluation of the membranous labyrinth (thin slices, high spatial resolution) was possible and if I could recognize the nerves in the IAC. Reliable visualization of the three branches of the cochleovestibular nerve and of the facial nerve are required before one can make a diagnosis of nerve aplasia or hypotrophy. The detectability of the vascular loop in the CPA and IAC is another important requirement. A good sequence should be able to show both the nerves and the vascular loop in order to evaluate conflicts between both structures.

The possible causes of enhancement in the membranous labyrinth and IAC on T1-weighted images of the temporal bone were also studied. Gadolinium-enhanced images were the most sensitive images available so far and correlation with the findings on the 3DFT-CISS images would be possible if we better understood the causes of the intralabyrinthine enhancement.

Once the capabilities of the Gd-enhanced T1-weighted images in patients presenting with sensorineural hearing loss and/or vertigo and the 3DFT-CISS images in the study of the normal inner ear were known, we compared the value of these sequences with one another and with unenhanced T1-weighted and T2-weighted images in patients with acoustic schwannomas and in patients with pathology of the membranous labyrinth. The key questions were if the 3DFT-CISS sequence would be able to detect new intralabyrinthine pathology (e.g. fibrous obliterations of the intralabyrinthine fluid spaces) and if the combined use of this sequence with the Gd-enhanced T1-weighted sequence would result in a better differential diagnosis (e.g. neuritis or labyrinthitis versus tumour).

In a next step the sequences were tested in patients presenting with particular clinical signs or in patients with a known syndrome or disease. First the MR sequences were tested in patients with Cogan's syndrome because it was known from pathologic studies that fibrous obliteration occurred in these patients. In particular, the potential ability of the 3DFT-CISS sequence to show obliteration of the intralabyrinthine fluid spaces was tested in these patients.

Further the value of both the Gd-enhanced T1-weighted sequence and the 3DFT-CISS sequence were tested in a study of patients presenting with vertigo and/or abnormal findings at vestibular testing. Here once again we wanted to know if the 3DFT-CISS could detect pathology invisible with the other MR sequences.

Finally the value of the 3DFT-CISS sequences in the detection of congenital inner ear malformations, in patients with Meniere's disease and in patients with idiopathic sudden sensorineural hearing loss, was evaluated.

The findings of the above mentioned studies should finally enable us to find a combination of MR sequences that best detects all possible pathologies and makes better differential diagnoses possible.

### 4. References

1. Claus E, Lemahieu SF, Ernould D. The most used otoradiological projections. *J Belge Radiol* 1980; 63:183-203.

2. Ruenes R, De la Cruz A. X-ray and imaging techniques and anatomy. In: Ruenes R, De la Cruz A, ed. *Otologic radiology with clinical correlations*. 1st ed. New York: Macmillan Publishing Company, 1986; 1-29.
3. Théron J, Laval-Jeantet M, Juster M. Radioanatomie du temporal. In: Vignaud J, ed. *Traité de radiodiagnostic*, Tome 17, 1 temporal. 1st ed. Paris: Masson & Cie, 1974; 50-74.
4. Dulac GL. Notions générales sur les incidences radiographiques et tomographiques du rocher. *J Belge Radiol* 1971; 54:191-197.
5. Jensen J. Malformations of the inner ear in deaf children: A tomographic and clinical study. *Acta Radiol* 1969; Suppl 286:1-97.
6. Frey KW. Die tomographie der labyrinthmissbildungen. *Fortschr Röntgenstr* 1965; 102:1-10.
7. Røvsing H, Jensen J. Tomographic visualization of labyrinthine fistula. *Radiology* 1968; 90:261-267.
8. Valvassori GE. Radiologic diagnosis of cochlear otosclerosis. *Laryngoscope* 1965; 75: 1563-1570.
9. Keleman G, Linthicum FH. Labyrinthine otosclerose. *Acta Otolaryngol (Stockh)* 1969; Suppl 253:1-68.
10. Scanlan RL. Positive contrast medium in diagnosis of acoustic neuroma. *Arch Otolaryng* 1964; 80:698-706.
11. De Smedt E, Potvliege R, Pimontel-Appel B, Claus E, Vignaud J. High resolution CT-scan of the temporal bone, a preliminary report. *J Belge Radiol* 1980; 63:205-212.
12. Shaffer KA, Haughton VM, Wilson CR. High resolution computed tomography of the temporal bone. *Radiology* 1980; 134:409-414.
13. Davis KR, Parker SW, New PFJ, Roberson GH, Taveras JM, Ojemann RJ, Weis AD. Computed tomography of acoustic neuroma. *Radiology* 1977; 124:81-86.
14. Gyldensted C, Lester J, Thomsen J. Computer tomography in the diagnosis of cerebellopontine angle tumors. *Neuroradiol* 1976; 11:191-197.
15. Valavanis A, Schubiger O, Wellauer J. Computed tomography of acoustic neuromas with emphasis on small tumor detectability. *Neuroradiol* 1978; 16:598-600.
16. Vignaud J, Le Roux B. L'oreille. In: Vignaud J, ed. *Tomodensitométrie cranio-encéphalique*. 1st ed. Paris: Vigot, 1987; 369-420.
17. Wilms G, Casselman J. Cisternografie met lucht-computertomografie voor het opsporen van kleine acusticus neurinoma's. *Tijdschr voor Geneeskunde* 1987; 43:619-622.
18. Johnson DW. Air-cisternography of the cerebellopontine angle using high resolution computed tomography. *Radiology* 1984; 151:401-403.
19. Veillon F, Charneau D, Stierle JL, Bourjat P, Budor P. Pathologie inflammatoire de l'oreille moyenne. In: Veillon F, ed. *Imagerie de l'oreille*. 1st ed. Paris: Médecine-Sciences Flammarion, 1991; 75-191.
20. Veillon F, Baur P, Dosch JC, Braun M, Pharaboz C. Traumatismes de l'os temporal. In: Veillon F, ed. *Imagerie de l'oreille*. 1st ed. Paris: Médecine-Sciences Flammarion, 1991; 243-281.
21. Lo WWM. Tumors of the temporal bone and the cerebellopontine angle. In: Som PM, Bergeron RT, eds. *Head and neck imaging*. 2nd ed. St.-Louis: Mosby Year Book 1991; 1046-1108.

22. Kingsley DPE, Brooks GB, Leung AWL, Johnson MA. Acoustic neuromas: evaluation by magnetic resonance imaging. *Am J Neuroradiol* 1985; 6:1-5.
23. New PFJ, Bachow TB, Wismer GL, Rosen BR, Brady TJ. MR imaging of the acoustic nerves and small acoustic neuromas at 0.6 T: a prospective study. *Am J Neuroradiol* 1985; 6:165-170.
24. Curati WL, Graif M, Kingsley DPE, Niendorf HP, Young IR. Acoustic neuromas: Gd-DTPA enhancement in MR imaging. *Radiology* 1986; 158:447-451.
25. Daniels DL, Czervionke LF, Pojunas et al. Facial nerve enhancement in MR imaging. *Am J Neuroradiol* 1987; 8:605-607.
26. Brogan M, Chakeres DW. Gd-DTPA-enhanced MR imaging of cochlear schwannoma. *Am J Neuroradiol* 1990; 11:407-408.

## II. AIMS OF THE STUDY

1. To assess the value of the three-dimensional Fourier transformation MR technique "CISS" (Constructive interference in steady state) in the detailed anatomic study of the inner ear and to evaluate whether this technique can provide additional information in the study of pathologic inner ears.
2. To compare the value of unenhanced T1-weighted images, T2-weighted images, gadolinium-enhanced T1-weighted images, and three-dimensional Fourier transformation-constructive interference in steady state (3DFT-CISS) images in depicting lesions of the membranous labyrinth. To list all possible causes of intralabyrinthine contrast enhancement (Gadolinium).
3. To determine whether the bony and soft-tissue obliterations of the intralabyrinthine fluid spaces reported in pathologic studies of patients with Cogan's syndrome can be detected with MR or CT.
4. To assess the value of the different MR techniques (unenhanced T1-weighted images, T2-weighted images, gadolinium-enhanced T1-weighted images, and 3DFT-CISS images), used in the MR study of the inner ear, in patients with vertigo and/or abnormal findings at vestibular testing.
5. To determine the sensitivity of unenhanced T1-weighted images, gadolinium-enhanced T1-weighted images and 3DFT-CISS images in the detection of congenital inner ear malformations.
6. To evaluate whether CT and especially MR (unenhanced T1-weighted images, gadolinium-enhanced T1-weighted images and 3DFT-CISS images) are able to detect inner ear pathology in patients with Idiopathic Sudden Sensorineural Hearing Loss (ISSHL) and whether the radiological findings can help in the understanding of the pathogenesis of ISSHL.
7. To assess the value of 3DFT-CISS MR of the inner ear in patients with Meniere's disease.

### III. MATERIAL AND METHODS

#### 1. Anatomy of the Inner Ear

In this chapter the normal anatomy of the cerebellopontine angle (CPA), internal auditory canal (IAC) and inner ear is described. Special attention is paid to the structures which are today visible on selective inner ear MR-images and that will be encountered in the studies.

##### 1.1. CEREBELLOPONTINE ANGLE

The angle between the cerebellum (posteriorly) and the pons (anteriorly) is called the CPA. The postero-medial border of the petrous bone constitutes the antero-lateral border of the CPA. The CPA is filled with cerebrospinal fluid and the facial and vestibulocochlear nerve are situated in the centre of this space. The trigeminal nerve, the superior petrosal vein, the choroid plexus in the lateral recess of the fourth ventricle and the posterior inferior- and anterior inferior cerebellar arteries are also located in the CPA. The CPA is further continuous with the prepontine cistern above and the cerebellomedullary cistern below.

The facial nerve has two roots, a larger motor root (or facial nerve, properly) and a very small root, the intermediate nerve (or nerve of Wrisberg), carrying sensory and parasympathetic fibres. Both facial nerve roots run obliquely through the CPA towards the IAC. The facial nerve arises in the pons and emerges from the medullopontine sulcus, 2-3 mm more anteriorly and medially than the vestibulocochlear nerve. The vestibulocochlear nerve is situated slightly inferior and posterior to the facial nerve and follows the facial nerve towards the IAC. Both the floccule and the lateral choroid plexus of the fourth ventricle extend into the CPA just under the level of the vestibulocochlear nerve and just above the level of the glossopharyngeal nerve (1).

The anterior inferior cerebellar artery, emerging from the middle part of the basilar artery, runs through the CPA. It makes a loop with a lateral convexity near the internal acoustic pore. This loop can enter the IAC where a "nerve-vessel" conflict may occur. From this lateral convexity originates the labyrinthine artery and also frequently the subarcuate artery. The labyrinthine artery supplies the membranous labyrinth (see below). The anterior inferior cerebellar artery, after forming its loop, runs further posteriorly over the superior surface of the floccule and then divides into a medial and lateral branch, both supplying the cerebellum (2).

Veins, draining blood from the antero-lateral part of the cerebellum, pons and medulla oblongata into the superior petrosal sinus, are present in the high and anterior part of the

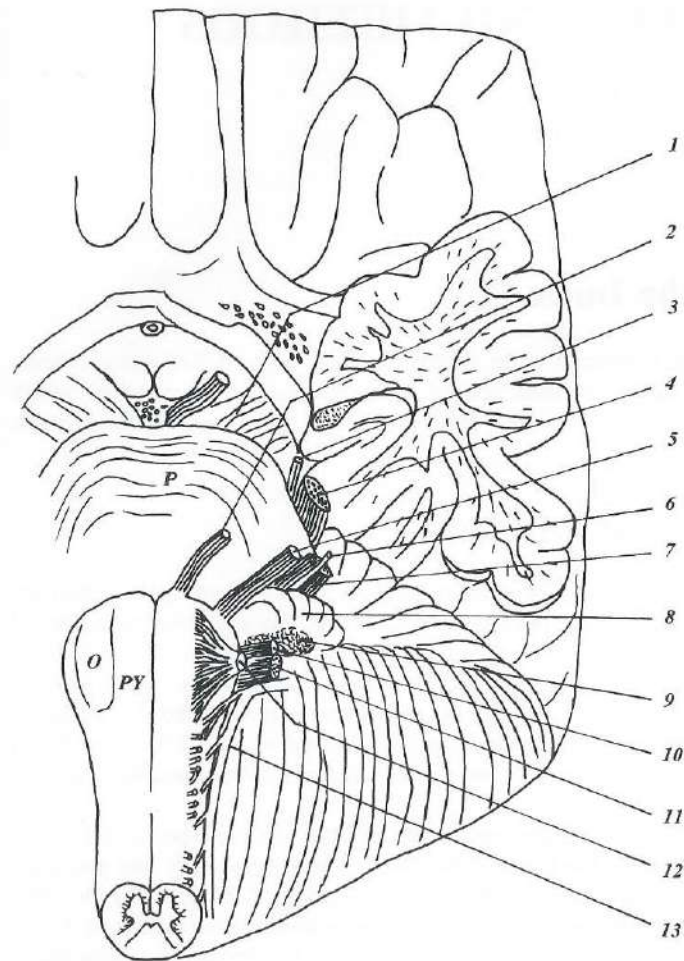


**Fig. 1.** Anatomy of the cerebellopontine angle. Cerebral peduncle (1), Abducent nerve - nerve VI (2), Trochlear nerve - nerve IV (3), Trigeminal nerve - nerve V (4), Facial nerve - nerve VII (5), Intermedius nerve (6), Vestibulocochlear nerve - nerve VIII (7), Floccule (8), Choroid plexus of the fourth ventricle (9), Glossopharyngeal nerve - nerve IX (10), Vagus nerve - nerve X (11), Hypoglossal nerve - nerve XII (12) and Accessory nerve - nerve XI (13). O = inferior olive, P = pons or bridge, PY = pyramid.

CPA. The largest of these veins, the superior petrosal vein of Dandy, is located near the root-entry zone of the trigeminal nerve. The inferior cerebellar veins and the labyrinthine veins (coming out of the IAC) drain into the inferior petrosal sinus.

Finally all nerves in the CPA are surrounded by an arachnoid membrane.

## 1.2. INTERNAL AUDITORY CANAL

The vestibule is separated from the lateral wall of the IAC by the lamina cribrosa which is pierced by multiple neural structures. The lateral aspect of the IAC is called the "fundus". The facial nerve, the cochlear, inferior vestibular and superior vestibular branch of the vestibulocochlear nerve, the labyrinthine artery and vein and sometimes also the loop of the anterior inferior cerebellar artery are the structures that are located in the IAC. The facial

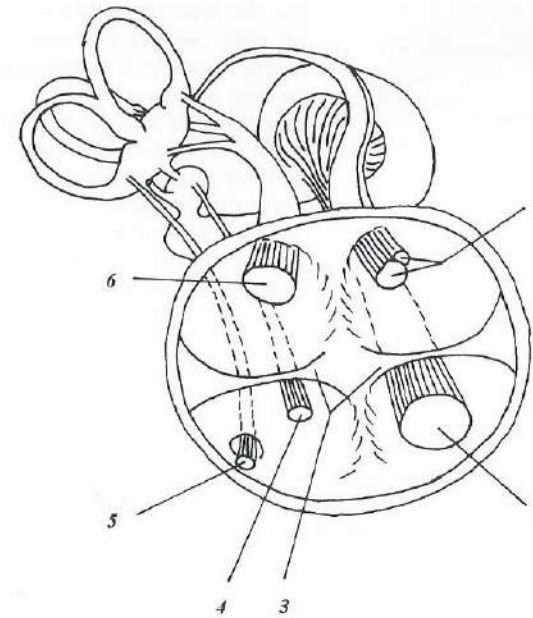


**Fig. 2.** Anatomy of the fundus of the internal auditory canal. The typical distribution of the nerves in the fundus is shown. Facial nerve and intermediate nerve anterosuperiorly (1), cochlear nerve anteroinferiorly (2), falciform or transverse crest (3), inferior vestibular nerve (4) and singular nerve (posterior ampullary nerve) (5) posteroinferiorly, superior vestibular nerve posterosuperiorly (6). (Modified from Proctor B, Nager GT)

nerve and the superior vestibular branch of the vestibulocochlear nerve have a parallel course in the superior part of the IAC. The vestibulocochlear nerve is bifurcating (in its cochlear and inferior vestibular branch) in the inferior part of the IAC.

The fundus of the IAC is divided into two compartments by a 2-3 mm, short calcified horizontal plate, the falciform or transverse crest (3) (Fig. 2). The facial nerve lies anterosuperiorly and leaves the IAC through the labyrinthine segment of the Fallopian canal. The bony wall lying posteriorly to the labyrinthine portion of the Fallopian canal and separating it from the superior vestibular branch is called Bill's bar, in honour of William House, who pioneered surgery of the IAC. The superior vestibular branch supplies the utricle and the superior and lateral semicircular canals. The cochlear and inferior vestibular branch are located under the falciform crest. The cochlear branch of the vestibulocochlear nerve lies in the antero-inferior compartment of the fundus and enters the cochlear foramen (area cochleae) to supply the cochlea. Posterior to the cochlear branch, the inferior vestibular branch of the vestibulocochlear nerve supplies the saccule. Fibres from the inferior vestibular branch traverse the singular foramen located in the bottom of the IAC. This is the posterior ampullary nerve or singular nerve which innervates the posterior semicircular canal (Fig. 2).

## 1.3. THE INNER EAR - BONY LABYRINTH

The inner ear consists of the bony labyrinth, membranous labyrinth and perilymphatic and endolymphatic spaces. The membranous labyrinth is enclosed within the bony labyrinth and is separated from it by the perilymphatic space.

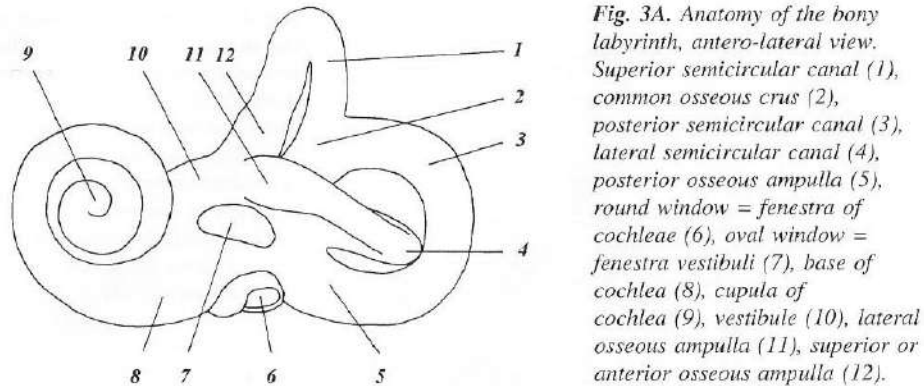
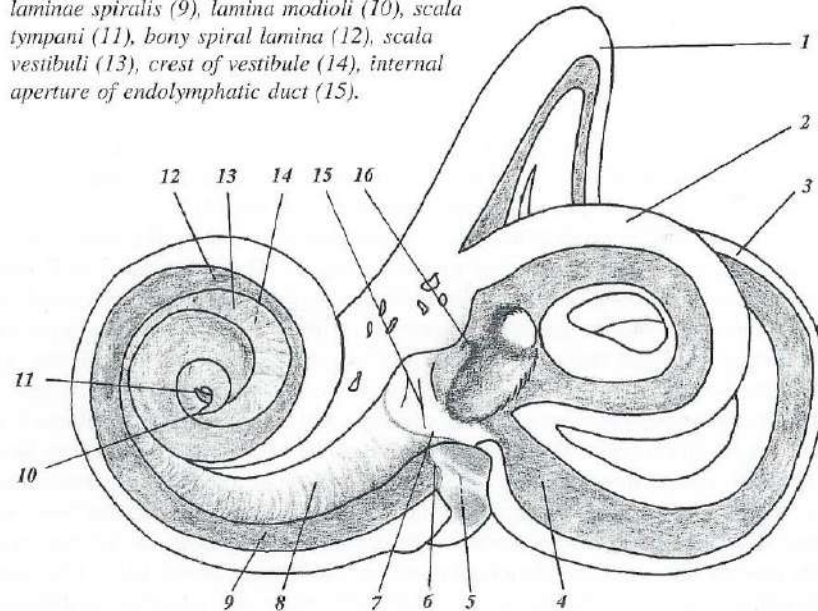


**Fig. 3A.** Anatomy of the bony labyrinth, antero-lateral view. Superior semicircular canal (1), common osseous crus (2), posterior semicircular canal (3), lateral semicircular canal (4), posterior osseous ampulla (5), round window = fenestra of cochleae (6), oval window = fenestra vestibuli (7), base of cochlea (8), cupula of cochlea (9), vestibule (10), lateral osseous ampulla (11), superior or anterior osseous ampulla (12).

**Fig. 3B.** Bony labyrinth, cochlea, vestibulum and semicircular canals have been filed open. Superior semicircular canal (1), lateral semicircular canal (2), posterior semicircular canal (3), posterior osseous ampulla (4), fossula of round window (5), crest of cochlear window (6), cochlear recess (of vestibule) (7), bony spiral lamina (8) hamulus laminae spiralis (9), lamina modioli (10), scala tympani (11), bony spiral lamina (12), scala vestibuli (13), crest of vestibule (14), internal aperture of endolymphatic duct (15).



### 1.3.1. Vestibule

The bony labyrinth consists of the vestibule, semicircular canals and the cochlea. The vestibule is the central portion of the bony labyrinth. It is a cavity with an ovoid shape and a diameter of approximately 4mm. This cavity is continuous with the cochlea anteriorly and with the semicircular canals posteriorly. The vestibule has several openings. The larg-

est opening is the oval window at the footplate of the stapes. There is also an opening towards the vestibular aqueduct, and finally multiple very small openings for the entrance of the vestibular nerve branches are situated on the floor and the medial wall of the vestibule (near the fundus of the IAC) (4) (Fig. 3A, B).

### 1.3.2. Semicircular canals

The three semicircular canals have an enlarged anterior end, the ampulla. The non-enlarged posterior ends of the superior and posterior semicircular canals join and form the bony common crus. All three semicircular canals are continuous with the vestibule. The lateral canal forms a ridge on the medial wall of the middle ear cavity and the superior border of the superior canal forms a ridge on the antero-lateral surface of the petrous bone, the arcuate eminence. Both the superior and posterior semicircular canal have a vertical orientation. The superior canal is directed anterolaterally at an angle of about 45° to the midsagittal plane, the posterior canal is directed posterolaterally at a corresponding angle. The anterior limb of the lateral semicircular canal lies in a higher plane than the posterior limb, resulting in a 30° angulation of the canal with the horizon (4).

### 1.3.3. Cochlea

The cochlea is a conical structure. Its base lies on the fundus of the IAC and its apex has an antero-lateral orientation and is directed slightly downward. The base has a diameter of approximately 9 mm and is perforated by numerous apertures for the passage of the cochlear nerve (5). These apertures are actually located in the broad base of the modioli. The modioli is the conical central axis of the cochlea. It is about 5 mm high and ends at the apex of the cochlea, the cupula. A 30 mm long bony canal winds spirally around this central axis and takes about  $2^{1/2}$  to  $2^{3/4}$  turns around the modioli. The first turn bulges towards the middle ear cavity and this protruding cochlear surface is known as the promontorium. A thin osseous spiral lamina projects from the modioli into the bony canal and only partially divides it (Fig. 3B). The remaining gap between the osseous spiral lamina and the outer wall of the bony cochlea is closed by the basilar membrane (see membranous labyrinth). The resulting bony canals above and under the membrane communicate at the apex of the modioli via a small opening, the helicotrema. The cochlea has two openings. One opening, the round window, which is covered by the secondary tympanic membrane, is situated in the first turn of the cochlear canal. The other opening is the aperture of the cochlear canaliculus or cochlear aqueduct. This aperture leads to a small canal with an opening on the inferior surface of the petrous bone just above the jugular foramen.

## 1.4. THE INNER EAR - MEMBRANOUS LABYRINTH

The inner ear consists of the utricle, saccule, semicircular ducts, endolymphatic duct, cochlear duct, and a series of intercommunicating channels, (6, 7).

### 1.4.1. Cochlear duct

The cochlear duct is filled with endolymph and is a spiral blind pouch inside the cochlea (Fig 4). The cochlear duct begins in the cochlear recess (Fig. 3B) and follows the cochlea through its basilar, middle and apical turns (7, 8). The cochlear duct has a triangular shape, is attached to the outer wall of the cochlea and divides the perilymphatic space inside the cochlea into two portions, the scala vestibuli and the scala tympani. The outer wall of the duct is formed by the thick spiral ligament and the endosteum of the bony canal, the roof by Reissner's membrane and the floor corresponds to the basilar membrane and the outer part of the osseous spiral lamina (Fig. 5). The organ of Corti is situated inside this duct and is the site of placement of the supporting and sensory hair cells that mediate hearing.

### 1.4.2. The round window membrane

The round window is closed by a membrane with a transverse diameter of 3mm and a vertical diameter of 1.5mm. The function of the round window membrane is very important, because this membrane allows perilymph movement every time the stapedial footplate

**Fig. 4.** Endolymphatic and perilymphatic spaces inside the cochlea. Vibrations of the sound waves are transmitted from the tympanic membrane over the malleus (1), incus (2), stapes (3) and the footplate of the stapes at the oval window (4) to the perilymph inside the scala vestibuli (5). The vibrations then pass the helicotrema (7) and reach the scala tympani (8) and cause the round window membrane (9) to move in the opposite direction to the oval window (4). The cochlear duct (6), containing the endolymph, is a blind pouch, surrounded by the perilymphatic spaces. Cochlear aqueduct (10), tympanic membrane (11), Eustachian tube (12). (After D.A. Charetia).

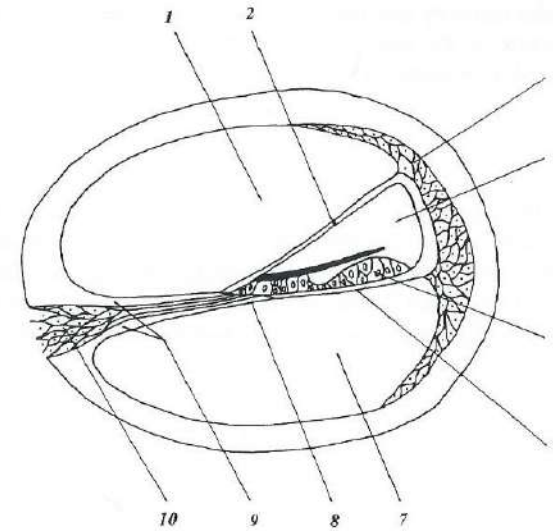
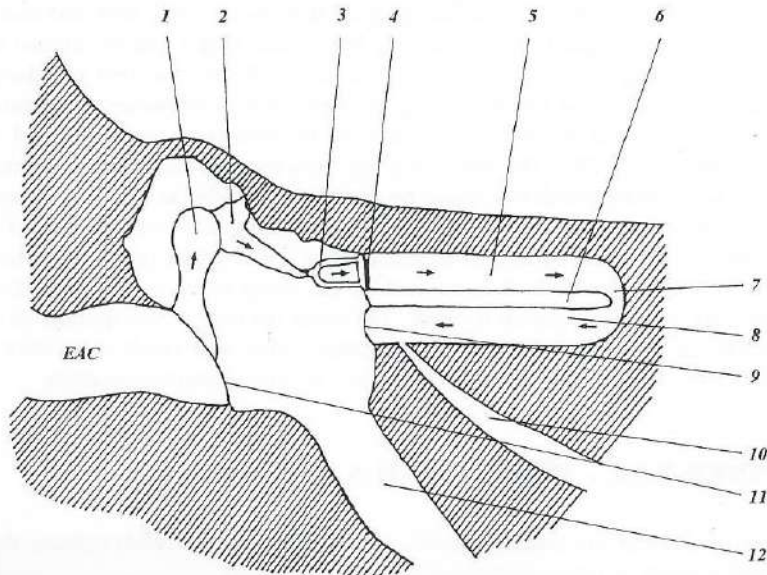


**Fig. 5.** Scala vestibuli (1), Reissner's membrane (2), spiral ligament (3), cochlear duct or scala media (4), organ of Corti (5), basilar membrane (6), scala tympani (7), bony spiral lamina (8), modiolus (9) and spiral ganglion (10).

displaces the perilymph adjacent to the oval window diaphragm. Consequently the movements of the diaphragms of the oval and round window are 180 degrees out of phase with one another.

### 1.4.3. Sensory organs of the vestibular labyrinth

The cristae inside the ampullae of the semicircular ducts and the maculae of the utricle and saccule are the sensory organs of the vestibular labyrinth (see also Fig. 7).

The semicircular ducts are very small and their diameter is only one quarter of the diameter of the bony semicircular canals. Each duct has an ampulla at its anterior end. The medial end of the superior and the upper end of the posterior duct form the common crus. This explains why the semicircular ducts open by five orifices in the utricle (Fig. 7). A crista is present in the base of each ampulla. This is a crestlike septum made up of connective tissue, with a sensory epithelium (sensory hair cells carrying cilia) on top and covered by a gelatinous cupula, into which the cilia project. These ampullary crests are the organs of kinetic balance because they are stimulated by movement of the endolymph. These movements are caused by angular acceleration of the head and result in a deviation of the cupulae covering the cilia.

The utricle is located in the vestibule. The utricular duct emerges from the anteromedial part of the utricle and by joining the saccular duct forms the endolymphatic duct. As already mentioned the five orifices of the three semicircular ducts also open in the utricle. The saccule is situated in a recess near the opening of the scala vestibuli of the cochlea. The saccular duct connects the saccule with the endolymphatic duct and the ductus reuniens connects the saccule with the basal end of the cochlear duct (Fig. 7). The macula of the saccule is situated along the anterior wall of the saccule but it is predominantly the macula of the utricle which is the organ of static balance. The macula is composed of a layer of

otoliths covering the sensory epithelium (sensory hair cells carrying cilia). Under the influence of gravity the otoliths exert traction on the cilia of the hair cells corresponding to a particular head position or a linear head acceleration (5).

#### 1.4.4. Endolymphatic duct and sac

The endolymphatic duct arises at the confluence of the saccular and utricular ducts (6) and is located inside the vestibular aqueduct. The duct becomes wider at the site where the vestibular aqueduct reaches the posterior fossa and ends in a larger endolymphatic sac. This sac is located between the periosteum of the petrous bone and the dura mater (Fig. 4). The extraosseous endolymphatic sac volume represents more than two-thirds of the total endolymphatic sac volume (9).

#### 1.4.5. Vascular system

The membranous labyrinth is supplied by the labyrinthine artery (internal auditory artery). This artery originates on an arterial loop, consistently found near the internal acoustic pore. This loop is more often (80% of the cases) the main trunk or a branch of the anterior inferior cerebellar artery (see above), less frequently the accessory anterior cerebellar artery (17%) and rarely the posterior inferior cerebellar artery (3%) (10). The labyrinthine artery supplies the dura and nerves inside the IAC, the adjacent bone and medial aspect of the inner ear. The artery then divides into the common cochlear artery and vestibular branches. These vestibular branches supply the maculae, the ampullary crests, the semicircular ducts and the basal one-third of the cochlear duct. The common cochlear artery supplies the spiral ganglion and the upper two-thirds of the cochlear duct (Fig. 6).

The vestibular veins drain the blood from the semicircular ducts, saccule and utricle into the vein of the vestibular aqueduct, the labyrinthine vein, and also into the vein of the

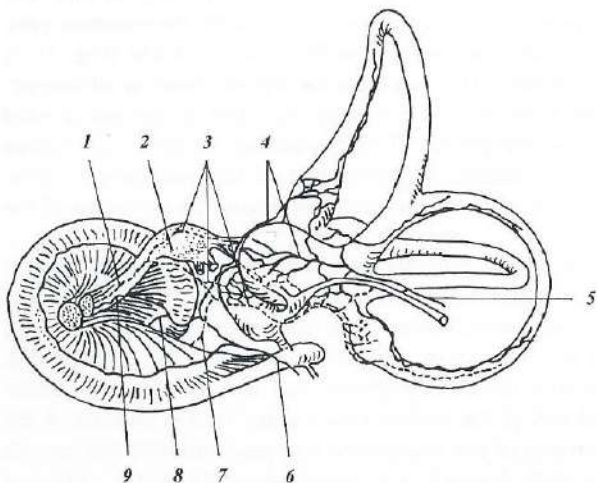


**Fig. 6.** Arteries supplying and veins draining the membranous labyrinth. Labyrinthine artery (1), Scarpa's ganglion (2), vestibular branches of the labyrinthine artery (3), vestibular veins (4), vein of the vestibular aqueduct (5), vein of the cochlear aqueduct (6), cochlear branch of the labyrinthine artery (7), posterior and anterior spiral veins (often forming a common modiolar vein at the base of the cochlea) (8), labyrinthine vein (9).

cochlear aqueduct. The vein of the cochlear aqueduct is located in a canal near the cochlear aqueduct (not inside the aqueduct) and empties into the inferior petrosal sinus. The labyrinthine vein follows the labyrinthine artery inside the IAC and then drains into the inferior petrosal sinus or directly into the internal jugular vein. The main veins of the cochlea are the posterior and anterior spiral veins. They form the common modiolar vein at the base of the cochlea and this vein drains partially into the labyrinthine vein and partially into the vein of the cochlear aqueduct (Fig. 6).

#### 1.4.6. Spiral ganglion - Scarpa's ganglion

Impulses received by the organ of Corti are transmitted by peripheral cochlear fibres to the cell bodies of the spiral ganglion, and then to the central nervous system by the cochlear branch of the vestibulocochlear nerve. The spiral ganglion is situated in the spiral canal of the modiolus of the cochlea (11) (Fig.5).

Impulses generated in the sensory cells of the cristae and maculae are transmitted by peripheral vestibular fibres to the cell bodies of the vestibular ganglion (Scarpa's ganglion), and then to the central nervous system by the vestibular branches of the vestibulocochlear nerve. Scarpa's ganglion is situated in the trunk of the nerve at the lateral end of the internal auditory canal (11) (Fig. 6).

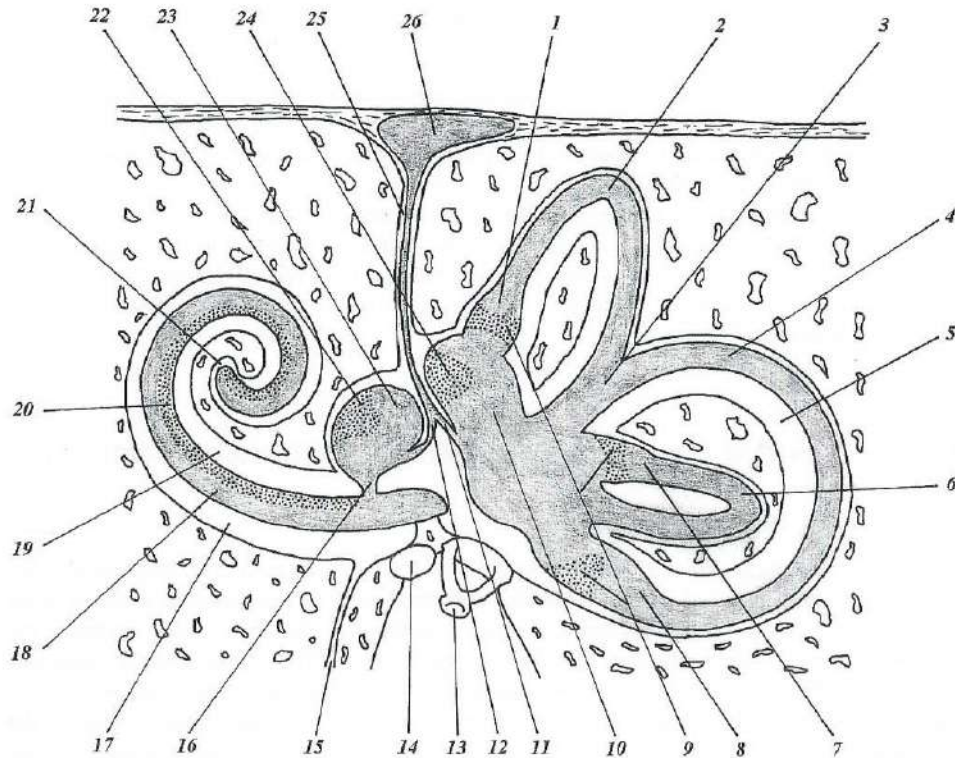
## 1.5. THE INNER EAR - PERILYMPHATIC & ENDOLYMPHATIC SPACES

The perilymphatic space around the semicircular ducts is at both ends continuous with the perilymphatic space of the vestibule and this space is in turn continuous with the scala vestibuli. As already described above a small opening at the apex of the cochlea, the helicotrema, allows the perilymph to pass from the scala vestibuli to the scala tympani and vice versa. The perilymph in the scala tympani finally reaches the round window (Fig. 7) and also reaches the cochlear aqueduct where a potential communication between the subarachnoid space and the perilymphatic space is possible. However this aqueduct is most often completely filled with arachnoid and fibrous tissue. The perilymphatic space also surrounds the endolymphatic duct. However the duct, the vein and connective tissue nearly completely fill the vestibular aqueduct so that hardly any fluid surrounds the endolymphatic duct. The endolymphatic sac is covered by dura so that no communication exists between the perilymphatic space and the cerebrospinal fluid in the posterior fossa.

The cochlear duct, the ductus reuniens, the saccule, the saccular duct, the utricular duct, the utricle, the semicircular ducts and the endolymphatic duct and sac are all filled with endolymph.

All these endolymphatic spaces are linked with one another and form one large endolymphatic space, although valves exist in the ductuli between the vestibular and cochlear compartments of the endolymphatic space.

**Fig. 7.** The membranous labyrinth and the endolymphatic spaces (grey) and the perilymphatic spaces (white). Superior (or anterior) membranaceous ampulla (1), superior semicircular duct (2), common membranous crus (3), posterior membranaceous ampulla (4), posterior semicircular canal (5), lateral semicircular duct (6), lateral membranaceous ampulla (7), posterior membranaceous ampulla (8), crista ampullaris superior-lateralis-posterior (9), utricle (10), utricular duct (11), saccular duct (12), stapes with footplate in oval window-fenestrae vestibuli (13), round window -fenestrae of cochlea (14), canaliculus of cochlea (15), ductus reuniens or Hensen's duct (16), scala tympani (17), cochlear duct (18), scala vestibuli (19), organ of Corti (20), cupula of cochlea (21), macula sacculi (22), saccule (23), macula utriculi (24), endolymphatic duct (25), endolymphatic sac (26).



## 1.6. REFERENCES

1. Veillon F, Nataf E, Dietemann JL, Pharaboz C, Cosnard G, Sarrat P. Tumeurs des régions adjacentes à l'os temporal: rappel concernant l'anatomie normale et la radio-anatomie de l'angle ponto-cérébelleux. In: Veillon F, ed. *Imagerie de l'oreille*. 1st ed. Paris: Médecine-Sciences Flammarion, 1991; 283-288.
2. Moret J, Lasjaunias P, Delvert JP. Blood supply of the ear and cerebellopontine angle. In: *The ear diagnostic imaging CT scanner, tomography and magnetic resonance*. Paris, Masson, 1986:67-68.
3. Swartz JD. The inner ear. In: Swartz JD, ed. *Imaging of the temporal bone: a text/atlas*. 1st ed. New York: Thieme Medical Publishers, 1986; 117-160.
4. Veillon F. Anatomie de l'os temporal normal. In: Veillon F, ed. *Imagerie de l'oreille*. 1st ed. Paris: Médecine-Science Flammarion, 1991; 1-19.
5. Bergeron RT, Lo WWM, Swartz JD, Hasso AN, Liu DPC, Broadwell RE. The temporal bone - Introduction to the temporal bone. In: Som PM, Bergeron RT, 2nd ed. St-Louis: Mosby Year Book 1991; 925-944.
6. Donaldson JA, Miller JM. Anatomy of the ear. In: Paparella MM, Shumrick DA, eds. *Otolaryngology*, Vol. 2. The ear. Philadelphia: W.B. Saunders, 1980; 22-64.
7. Anson BJ, Donaldson JA. *Surgical anatomy of the temporal bone and ear*. Philadelphia: W.B. Saunders, 1973.
8. Anson BJ, Harper DG, Winch TR. The vestibular system: Anatomic considerations. *Arch Otolaryngol* 1967; 85:53-70.
9. Bast TH, Anson BJ. The temporal bone and the ear. Springfield, IL: Charles C Thomas, 1949:30-100.
10. Mazzoni A. Internal auditory artery supply to the petrous bone. *Ann Otol Rhinol Laryngol* 1972; 81:13-21.
11. Mafee MF, Charletta D, Kumar A, Belmont H. Large vestibular aqueduct and congenital sensorineural hearing loss. *Am J Neuroradiol* 1992; 13:805-819.

## 2. Magnetic Resonance Techniques

In this chapter the basic principles of magnetic resonance are reviewed. These principles help us to understand how a two-dimensional spin-echo image is created. These spin-echo images, unenhanced and Gd-enhanced T1-weighted spin-echo images (in some cases even T2-weighted spin-echo images), are routinely used in the study of the inner ear. The difference between 2DFT and 3DFT imaging and spin-echo and gradient-echo sequences will also be discussed and enables us to understand how the 3DFT-CISS sequence, so often necessary in the study of the inner ear, is constructed.

### 2.1. BASIC PRINCIPLES

#### 2.1.1. Properties of atomic nuclei

The nuclei of atoms consist of neutrons and protons. Certain nuclei possess angular momentum or spin. When a nucleus has an odd number of protons or neutrons, then the resulting electric charge is spinning and produces a magnetic moment (1). This magnetic moment expresses the strength and direction of the magnetic field surrounding the nucleus. The fields produced by these magnetic dipoles are analogous to those of a microscopic bar magnet.

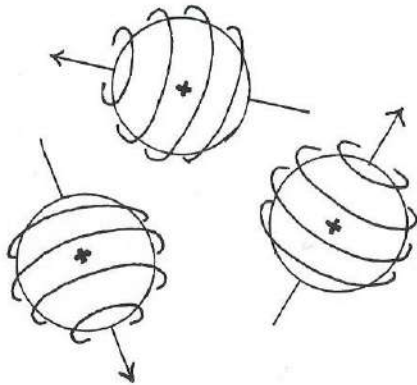


*Fig. 1. Spinning hydrogen nuclei are essentially positively charged protons. Before they are placed in a magnetic field, the magnetic vectors of the positively charged protons are randomly oriented.*

#### 2.1.2. Nuclei in a magnetic field

When the nuclei are exposed to an external magnetic field, then the randomly oriented magnetic dipoles line up with the magnetic field. Protons have a spin quantum  $I = 1/2$  and therefore can align in the parallel ( $m = +1/2$ ) or antiparallel ( $m = -1/2$ ) correlating with a low- and high-energy state respectively (2).

The precessional rate depends on the field strength ( $B_0$ ) and the nuclear species studied. The Larmor equation shows the relationship between the field strength ( $B_0$ ) and the precessional frequency ( $F$ ):  $F = \omega/2\pi = \gamma B_0/2\pi$ .

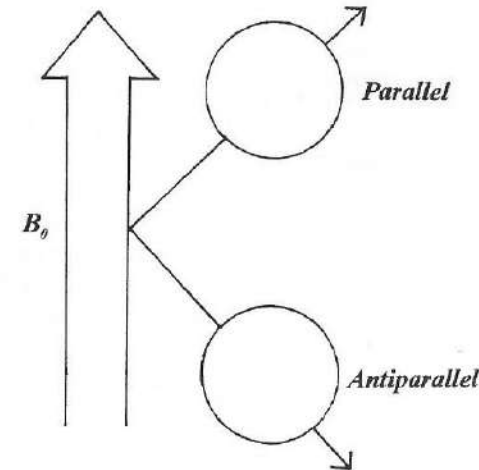


*Fig. 2. Low- (parallel) and high-energy (antiparallel) magnetic moment vectors when placed in a magnetic field  $B_0$ . The proton spins precess at a slight angle due to the interaction between the field  $B_0$  and the magnetic moments.*

( $\gamma$  = the magnetogyric ratio and is related to the strength of the magnetic moment of the nucleus studied,  $\omega$  = angular frequency in radians per second, the frequency  $F = 42.58$  MHz for a field strength of 1 Tesla.)

Using the Larmor equation,  $\gamma$  for protons ( $= \gamma H$ ) can be calculated at 1 Tesla:

$$42.58 \cdot 10^6 \text{ Hz} = \gamma H \times 1 \text{ Tesla} / 2\pi \text{ or } \gamma H = 42.58 \cdot 10^6 \text{ Hz} \times 6.28 / 1 \text{ Tesla} = 2.674 \cdot 10^8$$

#### 2.1.3. Macroscopic magnetization

When a patient is placed into a magnet, some of the individual magnetic moments will align parallel with  $B_0$ , and some will align antiparallel. The parallel orientation corresponds to the low-energy status and therefore more magnetic moments will align parallel. However the fractional excess population in the lower (parallel) energy status is only estimated at between one and six spins per 100,000. This seems very low, but  $10^{23}$  hydrogen nuclei are present per  $\text{cm}^3$  water, resulting in  $10^{18}$  more magnetic moments in the low-energy status per  $\text{cm}^3$  water, which is a lot. The net magnetization of all parallel and antiparallel magnetic

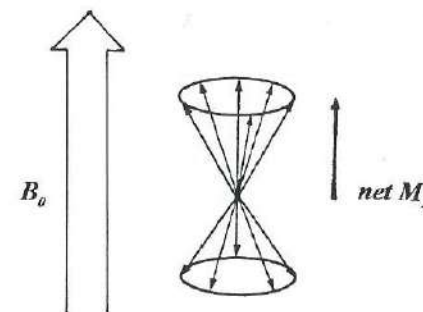


*Fig. 3. The individual magnetic moments result in a macroscopic magnetization  $M_z$  parallel to the axis of the external field  $B_0$ . Because of the random phases, the transverse components of magnetization of individual spins cancels out.*

moments is a parallel magnetization vector  $M_Z$  (3). The magnitude of this vector is proportional to the number of protons in the tissue imaged and the strength of the magnetic field  $B_0$ , and inversely proportional to the tissue temperature (1).

### 2.1.4. Radiofrequency pulses and magnetic resonance

Resonance is the induction of transition between the lower- and higher-energy states of the proton spins. Irradiation of tissue in a magnetic field with RF (radiofrequency) energy at the Larmor frequency will cause transition between the two energy levels (4). During RF pulsation at resonance condition, the spins are no longer influenced by the static field  $B_0$ .

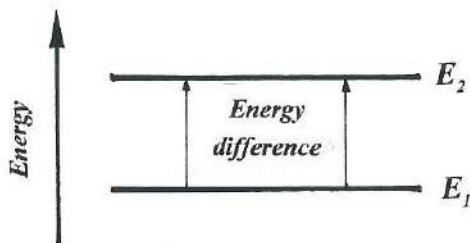


Fig. 4. RF pulses applied at the Larmor frequency will shift spins from the low-energy (parallel) to the high-energy (antiparallel) alignment.

The existing magnetization  $M_Z$  is at this moment submitted to the RF field  $B_1$  and the net magnetization vector  $M_Z$  will begin to precess about  $B_1$  at a frequency  $\omega_1 = \gamma B_1$  and will move from the longitudinal (Z) alignment to the transverse plane (XY). At a given duration (amplitude) of  $B_1$  the  $M_Z$  vector will be rotated by  $90^\circ$  into the transverse plane, i.e. (XY). This happens exactly at time  $T = \pi/2\omega_1$ , and after an exact  $90^\circ$  pulse both energy levels will be equally populated resulting in a longitudinal magnetization  $M_Z = 0$ . All magnetization is turned into the transverse plane  $M_{XY}$ .

No longer influenced by RF excitation,  $M_{XY}$  will begin to precess around the  $B_0$  axis. This will induce an alternating current in a coil which is located in the transverse plane and which is tuned to resonate at the Larmor frequency. The sinusoidal signal generated in this receiver coil shows a free-induction decay (FID) signal pattern.

After each RF-pulse excitation the induced transverse magnetization will start to decrease ("decay") due to T1 and T2 relaxation processes.

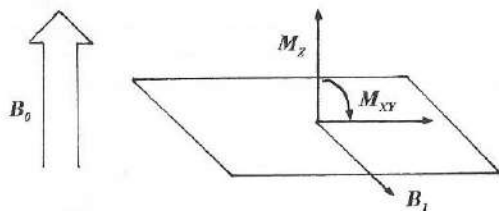


Fig. 5. A second magnetic field  $B_1$  perpendicular to  $B_0$  is created by an RF pulse. The longitudinal magnetization  $M_Z$  can thus be rotated  $90^\circ$  into the transverse plane.

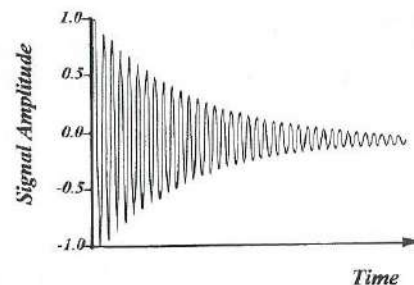


Fig. 6. The sinusoidal signal generated in the receiver coil decays exponentially in time.

## 2.2. SPIN-ECHO IMAGING

### 2.2.1. T1-relaxation (spin-lattice)

The superimposed RF field is removed after the  $90^\circ$  RF pulse and a realignment of the proton magnetic moments to the longitudinal +Z axis occurs. More proton spins will return to the low-energy (parallel) level than to the high-energy (antiparallel) level and this explains the growing amplitude of the longitudinal magnetization component  $M_Z$ . During the return the proton spins have to get rid of their absorbed energy and in fact they have to give their energy to the environment (lattice) or neighbouring magnetic nuclei.

When components of the intrinsic magnetic fields of the high-energy RF-stimulated spins and low-energy surrounding proton spins both oscillate at the Larmor frequency, then a lot of transitions can occur and the relaxation (loss of energy) will be fast (2).

The molecular mobility of a tissue's constituent molecules will also determine the rate of spin-lattice energy transfer. Triglycerides (larger molecules) have a slow molecular tumbling rate due to their larger momentum of inertia and due to friction with adjacent molecules. This results in efficient spin-lattice energy transfer and short T1 and T2 relaxation times. Small water molecules have a fast molecular tumbling rate and therefore have little chance to give off their energy to neighbouring molecules and the relaxation time will be long.

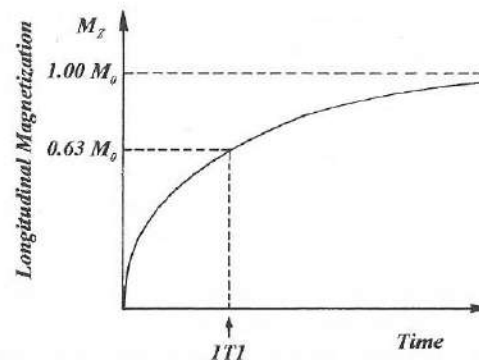


Fig. 7. One T1 is the time needed to achieve 63% of the original longitudinal magnetization  $M_0$ .

It's clear that the exact rate at which longitudinal remagnetization occurs depends on the molecular environment of the protons. One T1 period is defined as the length of time following the pulse that is required to restore 63% of the original longitudinal magnetization (Fig. 7).

### 2.2.2. T2-relaxation (spin-spin)

Intermolecular dipolar interactions among the proton spins themselves are responsible for the loss of the transverse magnetization or T2 or "spin-spin" relaxation. Proton spins produce very small local magnetic environments affecting the adjacent spins so that the nuclei precess at slightly different rates in the "XY" plane. This spread of resonance frequencies results in loss of phase coherence of the individual nuclear magnetic moments and subsequent loss of transverse magnetization  $M_{XY}$  (5).

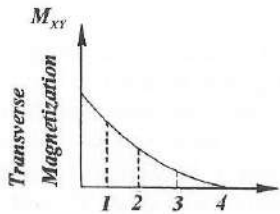
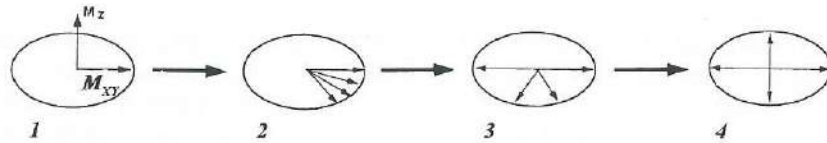


Fig. 8. After the  $90^\circ$  RF pulse intermolecular dipolar interactions cause progressive dephasing of the precessing transverse magnetization. A range of precessional frequencies occurs due to the magnetic field inhomogeneities, causing the various components which comprise the transverse magnetization to spread out (dephasing). The loss of transverse magnetization immediately results in signal loss.

### 2.2.3. T2\* relaxation and spin-echo

After a  $90^\circ$  RF pulse the signal should decay with a time constant T2 or transverse relaxation time. But in reality the transverse magnetization decays faster, with a time constant T2\*. This is caused by spatial inhomogeneity of the magnetic field. Spins at different locations, experience slightly different magnetic fields, causing slightly different precession frequencies. This once again results in loss of their phase coherence and the transverse magnetization shrinks.

To avoid this fast decay a "spin-echo" is used instead of the FID.

A  $180^\circ$  RF pulse applied some time "t" after the  $90^\circ$  pulse, can re-establish the phase coherence at time "2t". The time interval 2t is also known as the echo delay time TE ( $t = TE/2$ ).

The  $90^\circ$  RF pulse results in coherent (in phase) magnetization at  $t = 0$ . At time TE/2 or t the dephased transverse magnetization is turned into mirror image positions by a  $180^\circ$  RF pulse. At time 2t or TE the fast precessing spins catch up with the slow ones, resulting in

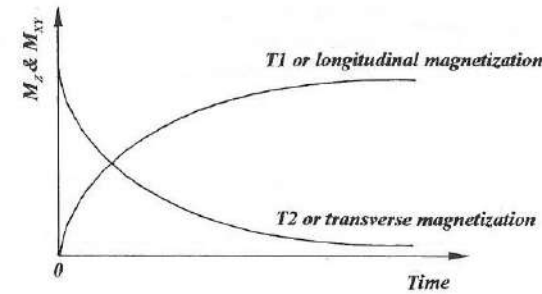
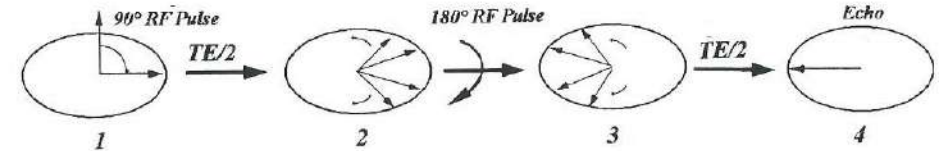


Fig. 9. After a  $90^\circ$  RF pulse the magnetization lies in the transverse plane and at this moment ( $t=0$ ) only the transverse magnetization can be measured (T2 magnetization), the  $M_z = 0$ . Later, T2 and T2\* relaxation causes progressive exponential loss of transverse (T2) magnetization ( $M_{XY}$ ) whereas longitudinal magnetization increases exponentially due to T1 relaxation.

Fig. 10. Immediately after the  $90^\circ$  RF pulse (1) the  $B_0$  inhomogeneity is starting to cause phase loss of the transverse magnetization components (2). A  $180^\circ$  RF pulse rotates the components into mirror image positions on the opposite side of the transverse plane (3). Precession continues and fast precessing spins catch up with the slower spins resulting in a rephasing (4) and a strong MR signal.



coherent magnetization at time 2t. This can be compared with a race track. At time t the runners have run different distances according to their speed. At this point the runners are asked to run in the opposite direction with the same speed as before. It's obvious that at time 2t all runners line up together at the starting post. This process is illustrated in Fig. 10.

The coherent (in phase) transverse magnetization results in a strong MR-signal called "spin-echo".

### 2.2.4. T1 contrast

After the  $90^\circ$  RF pulse, realignment of the magnetization with the static magnetic field  $B_0$  occurs and can be detected with a receiver coil. The entire process has to be repeated for each phase-encoding step (each time with a different amplitude of the phase encoding gradient, see below), or for example 256-times for an image with a resolution of 256 points in the phase-encoding direction. However the time between two RF-pulses (repetition time -TR) must be long enough so that sufficient recovery of longitudinal magnetization can take place.

On the other hand, when the TR interval is too long, all tissues will recover almost their entire longitudinal magnetization and the inherent T1 differences of tissues will be lost (Fig. 11).

Short TR intervals will result in varying longitudinal magnetization for tissues with different T1 relaxation times. A tissue with a short T1 will show more transverse magnetization following the  $90^\circ$  RF excitation because of the greater recovery of longitudinal

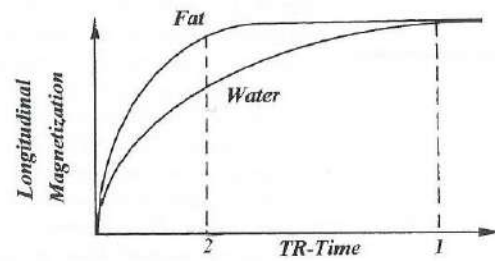


**Fig. 11.** When the TR interval is too long, all tissues will recover almost their entire longitudinal magnetization and the inherent T1 differences will be lost (1). The recovery of the longitudinal magnetization will differ for tissues with different spin-lattice relaxation times when short TR intervals are used (2). The shorter the T1 relaxation, the larger the longitudinal magnetization recovery will be and the larger the transverse magnetization (high signal) will be, which will be detected after the 90° pulse.

magnetization. Consequently, tissues with short T1 values will exhibit more signal and are hyperintense when compared with tissues with longer T1 values (Fig. 11).

A short TE is also used when T1 weighting is required in order to minimize the contribution of the T2 relaxation to the image (see below).

### 2.2.5. T2 contrast

As mentioned before the spin-echo pulse technique (90° RF pulse followed by a 180° RF pulse) is used because the FID decays as function of T2\* and results in too fast a loss of phase coherence of the spins in the axial plane "XY". The resulting signal-to-noise ratio of a FID is insufficient for acceptable image quality.

When a 180° RF pulse is delivered after a delay TE/2 (following the 90° RF pulse), then phase coherence is re-established at time TE after the initial 90° RF pulse and results in a maximum amplitude at that time.

When a spin-echo pulse technique is used the signal is based on intrinsic random fluctuating fields in the tissue and is a true measure of spin-spin or T2 relaxation.

The longer the TE (time to echo), the smaller the amplitude of the spin-echo signal because of the cumulative effect of the dephasing due to T2 relaxation. A second or third

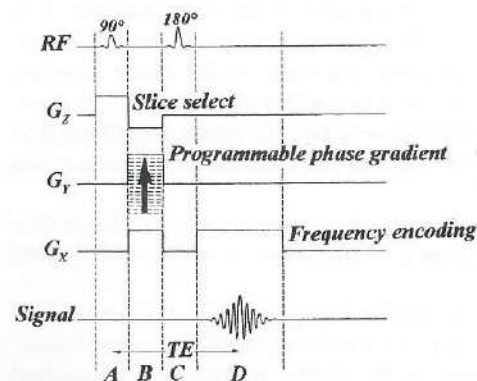


**Fig. 12.** Spin-echo sequence, relationship between RF-pulses, TE and resulting amplitude of the signal.

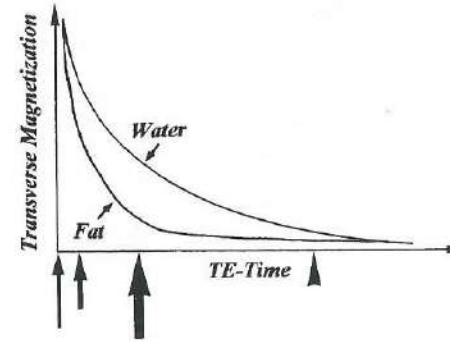


**Fig. 13.** T2 decay in fat and water, two tissues with different T2 values. Both tissues start with the same transverse magnetization when a long TR is used (long black arrow). When a very short (small black arrow) or very long (black arrowhead) TE is chosen, little T2 contrast between the two tissues is seen. However, an intermediate TE results in optimal T2 contrast differences (large black arrow).

spin-echo can be generated by using additional 180° RF pulses at appropriate TE intervals. The echo will then have again a highest amplitude at times 2TE and 3TE (4). The amplitudes of these multiple echoes again decay as a function of T2 rather than T2\*. Therefore exponential loss of signal intensity is seen as TE increases. Thus image contrast is gained at the expense of a weaker signal.

Routinely a long TR and intermediate TE is used when T2-weighted images are generated. A long TR results in complete recovery of longitudinal magnetization in all tissues (see Fig. 11), thereby minimizing the effect of underlying T1 differences between the tissues.

At an intermediate TE the signal from tissues with a long T2 will decay more slowly than the signal of tissues with a short T2, and therefore the signal of the tissues with a long TE will be higher (hyperintense) (Fig. 13).

## 2.3. GRADIENTS - SLICE SELECTION - SPATIAL ENCODING METHODS

### 2.3.1. Gradients-slice selection

The term "gradient" means that the strength of a magnetic field is altered in a selected direction. The homogeneous magnetic field  $B_0$  of the superconducting magnet is changed slightly in a linear way by the use of gradient coils. Three gradient coils enable us to apply a slightly linear changing magnetic field in the X, Y and Z direction. For example, when a current is passing through the Z gradient coil, the main magnetic field  $B_0$  changes, for instance from 1,5 tesla in the middle of the magnet (isocentre) to 1,51 tesla at the front end and 1,49 tesla at the back end of the magnet.

In such a varying magnetic field along the Z direction (long axis of the body), the protons in every X-Y plane of the subject will resonate at a different frequency (see Larmor equation: for each nuclear species, the resonance frequency is linked to the field strength). If the patient is irradiated with a 90° RF pulse consisting of a narrow range of frequencies, then only nuclei in a narrow part (section) of the body will be excited (6).

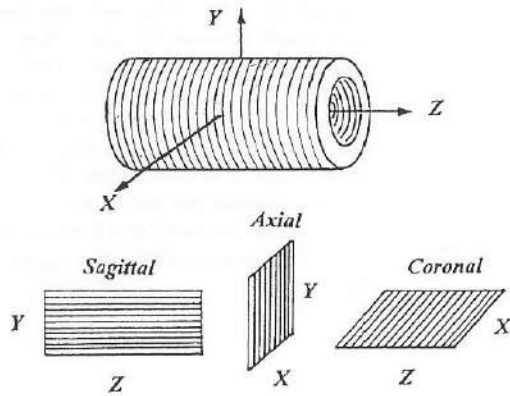


**Fig. 14.** The generally accepted magnet axes directions are shown. The main magnetic magnet. The gradient coils, installed inside the magnet, can create  $B_0$  gradients along these X, Y and Z directions in order to select a slice (see also Fig. 15), to frequency encode and to phase encode protons (see below).

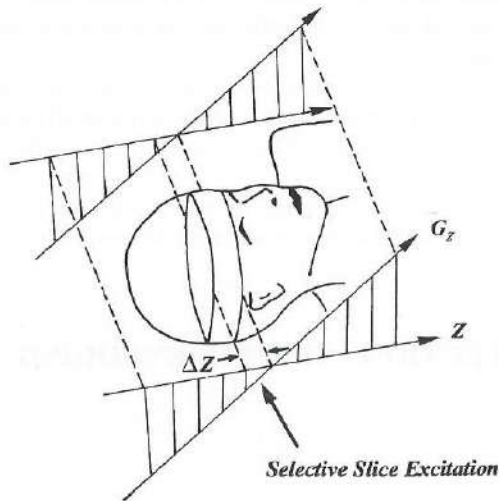


**Fig. 15.** The Z gradient ( $G_z$ ) creates a magnetic field that changes along the long axis of the body (Z-axis) and the resonant frequency for different sites in the body will change accordingly. A narrow band of RF irradiation excites nuclei in a narrow range, for example  $\Delta Z$ .

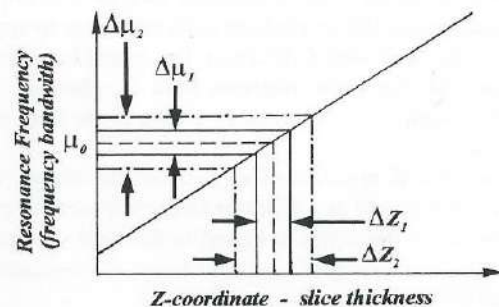


**Fig. 16A.** Slice thickness using different RF frequency bandwidths. At a given gradient strength (mounting field strength, black line), a narrow frequency bandwidth  $\Delta\mu_1$  will excite protons in only a narrow region (section) of the body ( $\Delta Z_1$ ). A wider RF bandwidth ( $\Delta\mu_2$ ) selects a thicker slice ( $\Delta Z_2$ ).

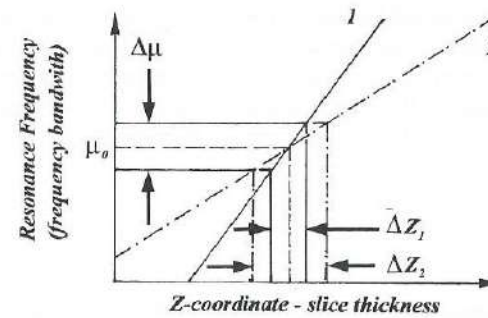


**Fig. 16B.** Slice thickness using different gradient strengths. At a given frequency bandwidth  $\Delta\mu$ , a thick slice  $\Delta Z_2$  is selected when a weak magnetic gradient (2) is used. A stronger (steeper) magnetic gradient (1) selects a thinner slice  $\Delta Z_1$ .

The thickness of that section will be proportional to the frequency range used. If the patient is irradiated with a  $90^\circ$  RF pulse consisting of a narrow range of frequencies, then only nuclei in a narrow part (section) of the body will be excited (Fig. 16 A)(3). In practice the range of frequencies used is dependent on the amplitude or the strength of the slice selection gradient used and not by changing the frequency band (Fig. 16 B).

If the gradient is along the X or Y axis, then sections in the sagittal and coronal planes can be obtained.

### 2.3.2. Spatial encoding methods

An MR image represents the characteristics of tissue contained in a specific slice through the patient's body. The image is constructed of an array of pixels where the brightness (intensity) of each pixel is related to the characteristics of tissue in a corresponding voxel (volume element).

During MR imaging three different functions are used to create a specific slice within the patient's body and also to create individual voxels within the slice.

These three functions are selective excitation (= slice selection, see above), phase encoding and frequency encoding. These functions are created by temporary gradients in the magnetic field and these magnetic field gradients are produced by energizing three sets of coils (gradient coils) that are located within the bore of the magnet (see above).

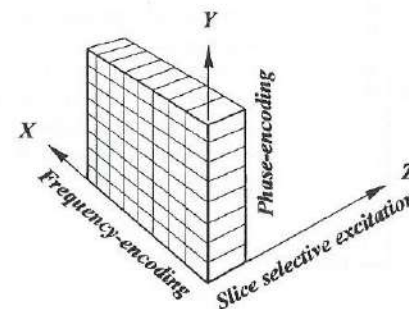


**Fig. 17.** Before an image can be built, spatial encoding in three spatial dimensions must take place. The slice selection or selective excitation is used to select the part of the body that will be examined and also determines the slice thickness. Frequency and phase encoding methods are used to recognize the different pixels (and their corresponding signal) in the XY plane.

How the slice and thickness of slice are selected has already been mentioned above. But the RF signals from all voxels within a slice are emitted simultaneously and picked up by the receiver coil as one composite signal. Therefore the signals from each individual voxel must be encoded so that they can be separated afterwards during the image reconstruction process. A phase and frequency encoding method are used to create the two "in-plane" or "XY" dimensions of the MR image.

### 2.3.3. Phase encoding

The voxels are separated in one direction of the image by using phase encoding. A gradient ( $G_Y$ ) is applied in the Y-direction. When the gradient is on, the strength of the magnetic field increases in one direction so that the voxels at one end are in a stronger field than those at the other end. The effect is that the magnetization vectors of the voxels in the

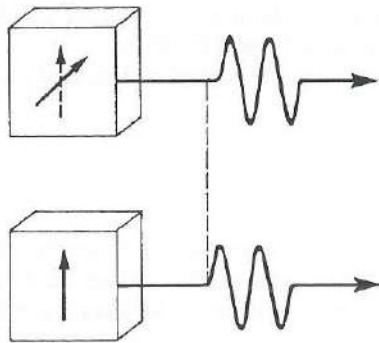


*Fig. 18. Due to a momentary gradient, the magnetic vector in the voxel at the bottom of the image, is located in a weaker magnetic field than the vector at the top of the image. The result is that the transverse magnetization vector in the stronger magnetic field rotates faster than the vector in the weaker magnetic field. Consequently the two voxels produce signals that are "out of phase".*

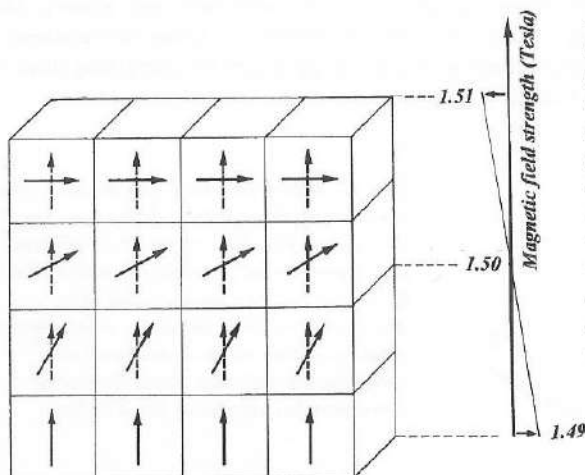


*Fig. 19. Vertically oriented magnetic field gradient, creating a higher magnetic field at the top of the matrix. The higher magnetic field strength results in a faster rotation of the magnetization vectors and hence in a larger phase shift in all voxels within the top row. All voxels within one row have the same phase shift but the phase shift varies linearly from top to bottom in every column.*

stronger field will start to rotate faster than those located in the weaker field and the magnetization vectors get out of phase (7). Consequently by applying phase encoding gradients we add a supplementary dephasing to the T2 dephasing which is locally encoded.

Once the  $G_Y$  gradient is turned off, all voxels are again located in the same strength magnetic field and the magnetization vectors of all voxels rotate again at the same speed. However, the phase shift induced by the  $G_Y$  gradient will remain.

It has to be mentioned that the operator can select the specific direction that will be phase encoded just as he can also select the slice selection direction (Z-axial, Y-coronal, X-sagittal).

The phase encoding gradient is turned on for a short period every imaging cycle (see below). The gradient strength is changed slightly from one cycle to another. When the image matrix is 256 in the phase encoding direction, then the imaging cycle must be repeated 256 times with each time a slightly changed gradient ( $G_Y$ ) strength.

### 2.3.4. Frequency encoding

Frequency encoding is used to resolve the tissue voxels in the other direction. Now a magnetic field gradient ( $G_X$ ) is created while the RF signal is produced within the voxels. The transverse magnetization vectors inside the voxels rotate faster in a stronger magnetic field (top of the image) than in a weaker magnetic field and the resulting RF signals have different frequencies (6).

In the presence of a gradient the magnetization vectors in each column of a matrix of voxels rotate at a different rate and produce signals with different frequencies (Fig. 21).

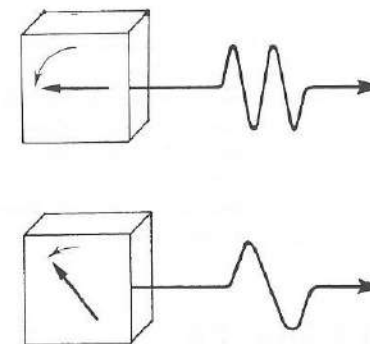


*Fig. 20. Voxels are located in magnetic fields of different strengths when a gradient magnetic field ( $G_X$ ) is created. The magnetic vector of the voxel located in the stronger magnetic field (at the top of the image) rotates faster and produces a signal with a higher frequency.*

### 2.3.5. Phase and frequency encoding

Each voxel has an individual "signal phase - signal frequency" combination when both encoding methods are used (Fig. 22). This means that every voxel (pixel) of the image-matrix can be recognized during the imaging reconstruction process (Fourier transformation).

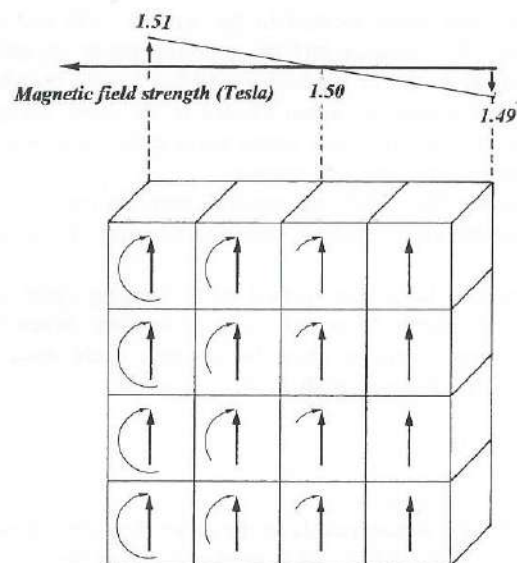


**Fig. 21.** A matrix of voxels under the influence of a horizontal frequency encoding gradient. The curved lines represent the precessional frequency. In every row this frequency varies linearly with the gradient magnetic field. However the rotation frequency is the same for all magnetization vectors located in one column.

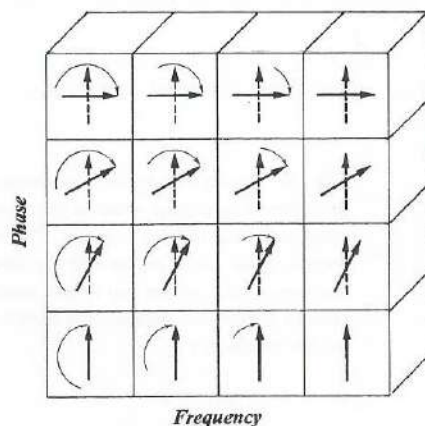


**Fig. 22.** Phase and frequency encoded matrix of voxels. The phase encoding gradient was applied for a short period of time, the frequency encoding gradient is turned on during the formation of the echo (see below). The echo signals, coming from each voxel with, for every voxel, an individual phase-frequency combination, is sampled during this period of echo formation. Columns are distinguished by their linear variation in precessional frequency, rows are distinguished by their linear variation in phase angle.

## 2.4. IMAGING CYCLE - 2D MULTISLICE IMAGING - 3D VOLUME IMAGING

### 2.4.1. Imaging cycle

During each imaging cycle of duration TR, the following events take place (8) (see Fig. 23).

**Period A:** A  $90^\circ$  RF pulse (converting longitudinal into transverse magnetization, = excitation pulse) is applied in the presence of a slice-selection gradient ( $G_z$ ). The

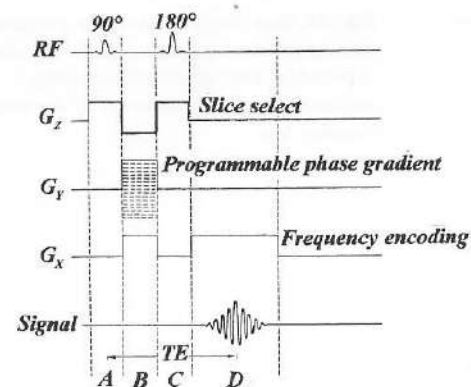


**Fig. 23.** Two-dimensional Fourier transformation (2DFT) imaging sequence. Diagram showing the sequence in which RF pulses, gradients and signal sampling are applied during different periods (A-D) of the imaging cycle.

presence of this slice-selection gradient limits the action of the pulse to the tissue within the selected slice.

**Period B:**  $\Rightarrow$  The phase-encoding gradient  $G_y$  is applied; with each cycle the gradient strength changes slightly.

$\Rightarrow$  Spins which dephase as a result of the slice-selection gradient are rephased by a compensatory negative gradient  $G_z$ .

$\Rightarrow$  A gradient  $G_x$  is also applied to compensate in advance for the phase changes that will be induced by this same  $G_x$  gradient during the sampling period.

**Period C:** A  $180^\circ$  RF pulse is applied, generating a spin-echo during the sampling period (D). Once again the  $G_z$  gradient is turned on simultaneously so that the specific action will be limited to the tissue contained within the selected slice.

**Period D:** (Sampling period) The frequency-encoding gradient is turned on, causing the spins to be frequency encoded along the X-axis. The same gradient strength  $G_x$  is maintained during the multiple imaging cycles. In the same period the signal (echo) is sampled.

During each imaging cycle one composite signal is produced, containing information coming from each voxel in the studied slice. Although all individual signal components are phase and frequency encoded, it is impossible to discern the individual voxel components, of one composite signal. Therefore several composite signals (views) are needed. This is achieved by repeating the imaging cycle at least as many times as there are voxel (pixel) rows to be created.

### 2.4.2. Multislice imaging

$TR \times N_y \times NEX$  (repetition time  $\times$  number of phase encoding steps  $\times$  number of excitations) is the time needed for one imaging cycle. This means that a routine T1-weighted sequence with a TR of 0.9 seconds, 256 phase encodings steps (resolution) and 1 excitation lasts  $0.9 \text{ sec} \times 256 \times 1 = 230 \text{ seconds} = 3.84 \text{ minutes}$ . In practice at least 10 contiguous slices are needed, which would result in a total examination time of more than 38 minutes; this is unacceptable.

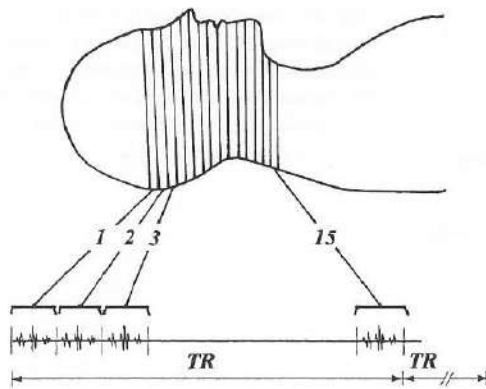


Fig. 24. In a single TR interval excitation and signal measurement of different slices is possible. This results in multislice acquisition without extension of the total imaging time.

The TR is responsible for this long examination time but cannot be changed without affecting the image contrast. But the actual data acquisition time represents only a fraction of the pulse repetition time (TR). Therefore the time following sampling can be used to excite sequentially other slices at a given (same) value of the phase-encoding gradient (6). Using this technique it is often possible to excite more than 10 slices within one TR interval of 900 msec, resulting in the above mentioned 3.84 minutes for a multiple slice examination.

### 2.4.3. Three dimensional (3D) volume imaging

With this imaging method an entire volume of tissue is excited by each RF pulse instead of a single slice (Fig. 25).

Therefore the RF signals must be encoded during the acquisition phase with spatial information in the slice-selection direction so that protons from different voxels along the

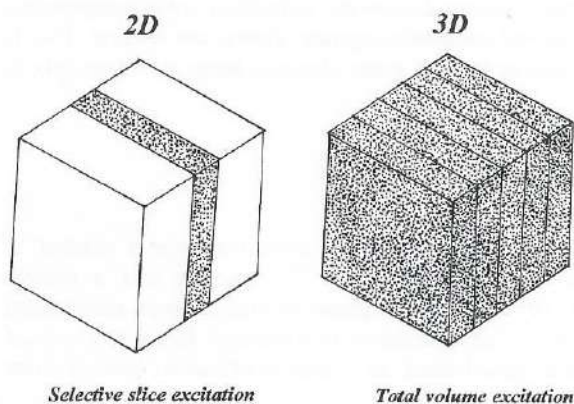


Fig. 25. In 2DFT imaging a slice of tissue is selected by using a slice selection gradient ( $G_z$ ). No gradient is present during the application of the excitation pulse in 3D volume imaging and therefore an entire anatomic region is excited.

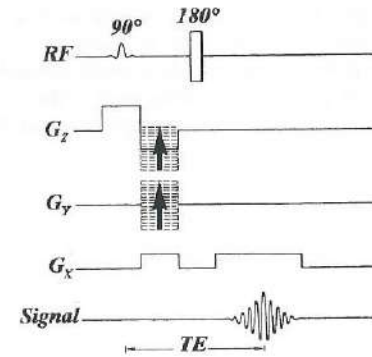


Fig. 26. Pulse timing diagram of a 3DFT-sequence. The sequence starts with a  $90^\circ$  RF pulse which may be chosen to be selective so as to excite a volume or slab of tissue encompassing the desired slices. This is followed by phase encoding in both the Z and Y direction. Finally during the sampling period the frequency-encoding gradient  $G_x$  is applied.

Z-co-ordinate can be differentiated. This is achieved by applying a supplementary slice selection table phase-encoding gradient ( $G_z$ ).

Just as in 2D-acquisition, a  $G_y$  gradient must be applied to differentiate protons with a different location along the Y-axis. The two phase-encoding gradients,  $G_y$  and  $G_z$ , are usually applied simultaneously. Data collection occurs during the application of the readout gradient  $G_x$ . However one excitation is needed for each increment of the  $G_y$  or  $G_z$  gradient and the increment of  $G_y$  must be independent of the increment of  $G_z$ .

For example, if 32 slices are to be formed (Z-direction), the total number of imaging cycles will be increased by a factor of 32. The imaging time can be calculated as follows:  $TR \times N_z \times N_y \times NEX$ . If we take again the same example with a  $TR = 0.9$  sec, XY resolution of  $256 \times 256$  ( $N_y = 256$ ) and 1 excitation and we want to divide the volume of tissue into 32 slices, then the examination time will be  $0.9 \text{ sec} \times 32 \times 256 \times 1 = 7373$  seconds = 122 minutes. Such examination times are once again unacceptable, and the only solution is to reduce the TR; therefore short TRs are used when 3D-volume imaging is used. For example, a  $TR = 50$  msec would result in an examination time of 8.7 minutes.

## 2.5. GRADIENT-ECHO IMAGING, 3DFT-CISS SEQUENCE

### 2.5.1. Gradient-echo imaging with small flip angles

As long as the longitudinal magnetization has recovered (almost) completely from the effect of the RF pulse (long TR), a  $90^\circ$  pulse provides the highest signal. With shortening of the TR-values the signal becomes weaker and eventually the spin system becomes "saturated". Then better signal to noise ratios per unit time can be achieved when pulse flip angles less than  $90^\circ$  are used (9) (the RF pulse is shorter). The RF pulse causes only a small excursion of the magnetization and a steady state is achieved in which most of the magnetization remains longitudinal at all times (Fig. 27).

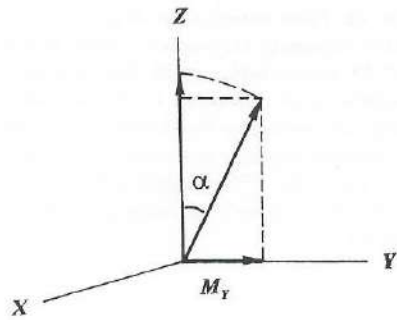


Fig. 27. The flip angle is reduced to a value ( $\alpha$ ) less than  $90^\circ$  in order to minimize saturation. As a result a steady state is built up whereby most of the magnetization remains longitudinal at all times.

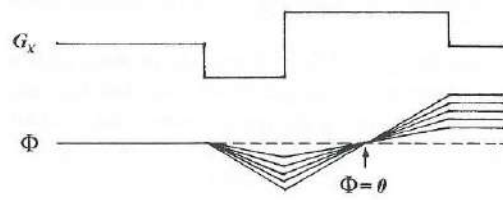


Fig. 28. Scheme explaining the gradient rephasing and gradient-induced echo formation. The spins get out of phase during the period when the readout gradient is negative ( $-G_x$ ). However rephasing occurs during the period when the readout gradient becomes positive ( $+G_x$ ). All spins are back in phase at the centre of the positive readout gradient ( $\Phi = 0$ ). During this period the signal is sampled.

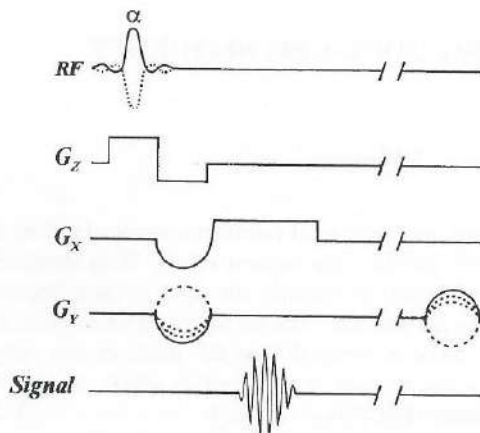


Fig. 29. Gradient-echo sequence: The  $180^\circ$  RF pulse is replaced by a gradient refocusing (sign inversion of the readout gradient) and a rephasing gradient applied at the end of the sequence to compensate for the view-to-view phase change induced by the phase-encoding gradient. The  $90^\circ$  RF pulse is replaced by an  $\alpha$ -RF pulse ( $\alpha < 90^\circ$ ).

Small flip angle imaging allows reduction of the pulse repetition time (TR) and results in very short scan times. Once small flip angle pulses are used,  $180^\circ$  RF pulses following the excitation RF pulses can no longer be used as they would invert the longitudinal magnetization (along the Z-axis). As TR further shortens, this would result in "zero" longitudinal magnetization.

Therefore, when small flip angle excitation RF pulses are used, echoes are generated by gradient reversal (of the readout gradient) instead of a  $180^\circ$  RF pulse. During the rephasing period all spins fall back in phase and at that moment the echo is sampled (Fig. 28).

This "gradient" refocusing takes less time than the  $180^\circ$  RF pulse refocusing. Therefore gradient-echo imaging with small flip angles can be acquired very quickly, as both small flip angle pulses and "gradient" refocusing result in shorter imaging times.

The contrast of gradient-echo images is adjusted predominantly by varying the flip angle, as the TR must be kept short (imaging time!).

All gradient-echo sequences (FLASH = Fast Low Angle Shot, FISP = Fast Imaging with Steady-State Precession, GRASS = Gradient-Recalled Acquisition in the Steady State...) have repetitive RF excitations and constant TR intervals. A steady state (continuous longitudinal magnetization, no saturation) is established after a certain number of excitation pulses. Transverse magnetization may or may not be included in the steady state. This is the key point that distinguishes the different variants of gradient-echo imaging (FLASH, FISP, refocused FLASH/FISP/spoiled GRASS).

The transverse magnetization dephases and does not contribute to the signal when the TR is much longer than the T2 relaxation time of the examined tissues ( $TR \gg T2$ ). For high flip angles one obtains normal T1 contrast ( $= 80-90^\circ$ ); for low  $\alpha$ , proton density contrast ( $\alpha < 15^\circ$ ) and T2 contrast ( $15 < \alpha < 25^\circ$ ) are obtained. However, when the TR is much shorter than the T2 relaxation time ( $TR \ll T2$ ), the residual transverse magnetization contributes to the image and a real T2 weighting is obtained for high flip angles. (10).

### 2.5.2. 3DFT-CISS (Constructive Interference in Steady State) sequence

The 3DFT-CISS sequence is used to study the cerebellopontine angle, internal auditory canal and inner ear.

It is a typical 3D-volume imaging technique. It is also a gradient-echo sequence with a reduced flip angle of  $50^\circ$ . The name of the sequence also states that during this sequence a steady state is established.

However, this 3DFT-CISS sequence differs somewhat from other 3DFT sequences like FISP (Fast Imaging with Steady Precession) or FLASH (Fast Low Angle Shot) sequences.

The major advantage of the 3DFT-CISS sequence over the other 3DFT sequences is that not only the fluid inside the membranous labyrinth and the internal auditory canal, but also the fast flowing fluid around the brain stem, always have a high signal and remain white. Other steady state 3DFT sequences (like FISP) can also give strong T2-weighting but are very sensitive to flow. The exact reasons for the signal loss of the moving cerebrospinal fluid are discussed in detail in Chapter IV.1 and IV.3.

In the 3DFT-CISS technique (consisting of two true-FISP sequences) flow compensation is applied to each gradient ( $G_z$ ,  $G_y$ ,  $G_x$ ) over each TR cycle. In this case, spins moving at a constant velocity will have the same phase after the application of the gradient

pulses as they had before. Therefore the cerebrospinal fluid around the brain stem remains white on 3DFT-CISS images, but other technical problems occur when this sequence is used. One of these problems is that this sequence produces images that show destructive interference bands of low signal intensity. The cause of these low signal intensity bands and the solution (using two true-FISP sequences, one with alternating (+-) and one with non-alternating (++) RF pulses) to this problem are described in Chapter IV.1 and IV.3., subjects and methods (see also Fig. 31)

However, one correction has been added to the 3DFT-CISS technique described in these chapters. The mathematical postprocessing operation that produces a new set of images with a homogeneous intensity distribution over the whole image, by taking the information provided by the two different true-FISP sequences, has changed. The Maximum Intensity Projection (MIP) postprocessing has been replaced by the "addition of raw-data" postprocessing. Both postprocessing techniques are used to take selectively the high signals out of the corresponding true-FISP images (taken at the same spot in the inner ear) in order to get rid of the dark bands and to create a homogeneous image with good contrast between fluid and surrounding bone and soft tissues.

The MIP software selects only the pixels with the highest signal intensity out of one of the two corresponding images, whereas the "addition" software adds the high signals of both corresponding images resulting in higher signal intensity of the fluid and better contrast (see Figs. 30, 31).

**Fig. 30.** Difference between the "MIP" and the "addition of raw-data" postprocessing techniques. The MIP technique selects for each image pixel the highest signal intensity out of the true-FISP image with alternating (+-) or out of the true-FISP image with non-alternating (++) RF pulses. The addition technique takes the highest signal intensity out of both images (raw-data of the images) and adds them, resulting in a new image with higher signal intensity of fluid than that achieved with the MIP technique.

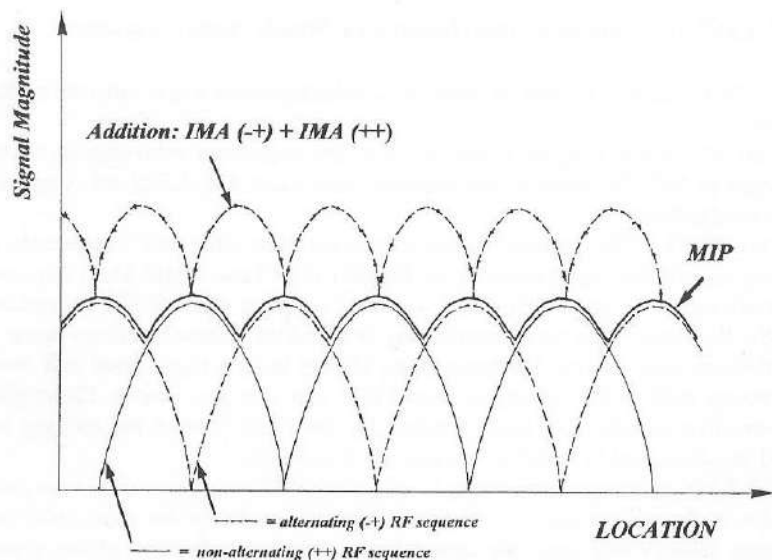


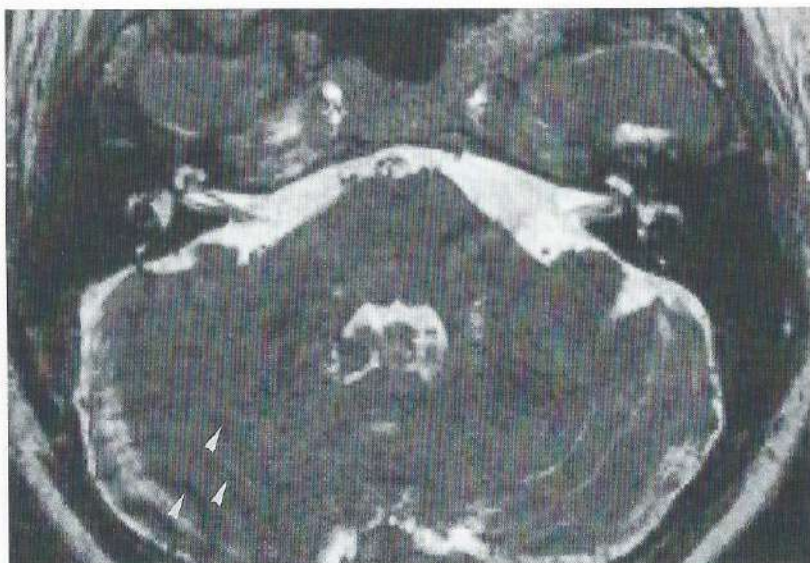
**Fig. 31.** Axial true-FISP image with alternating (-+) (A) and non-alternating (++) (B) RF pulses and the resulting CISS image using the "raw-data addition" postprocessing. The images are made through the centre of the membranous labyrinth.



A



B



C

A. A destructive interference band of low signal intensity is passing through the left cerebellopontine angle and through the fourth ventricle (white arrows) on this true-FISP image with alternating RF pulses (-+). Notice also the black lines produced by metal in the region of the occipital bone or soft tissues on the right (arrowheads).

B. The destructive interference band is shifted posteriorly (white arrows) on the true-FISP image with non-alternating RF pulses (++), and both the left cerebellopontine angle and fourth ventricle are now visible. The black artifact lines on the right side have also changed in position (arrowheads).

C. Final CISS image, made by adding the information provided by the two true-FISP images (A+B). In this case the newer "raw-data addition" software was used. On this image the large destructive interference band is no longer visible and even the artefacts, produced by metal, on the right have almost completely disappeared (arrowheads). Further details on the causes of these destructive interference bands and how two true-FISP sequences (one with alternating and one with non-alternating RF pulses) can be used to overcome these low signal intensity lines are given in Chapter IV.1 and IV.3., subjects and methods.

## 2.6. REFERENCES

1. Brant-Zawadzki M. Magnetic resonance imaging principles: the bare necessities. In: Brant-Zawadzki M, Norman D, ed. Magnetic resonance imaging of the central nervous system. 1st ed. New York: Raven Press 1987; 1-12.
2. Wehrli FW. Principles of magnetic resonance. In: Stark DD, Bradley WG, ed. Magnetic resonance imaging. 1st ed. St. Louis: The C.V. Mosby Company 1988; 3-23.
3. Villafana T. Fundamental physics of magnetic resonance imaging. Radiol Clin North Am 1988; 26:701-715.
4. Kucharczyk J, Chew WM. Basic principles. In: Higgins CB, Hricak H, Helms CA, ed. Magnetic resonance imaging of the body. 2nd ed. New York: Raven Press 1992; 127-135.
5. Osborn AG, Hendrick RE. Introduction to MR imaging: Part I. Basic physics and instrumentation. In: Stark DD, Bradley WG, ed. Diagnostic categorical course in MR imaging, syllabus. 1st ed. Oak Brook: Radiological Society of North America 1988; 7-13.
6. Sprawls P. Spatial characteristics of the MR image. In: Stark DD, Bradley WG, ed. Magnetic resonance imaging. 1st ed. St. Louis: The C.V. Mosby Company 1988; 24-35.
7. Moseley ME. Imaging techniques, pulse sequences from spin-echo to diffusion. In: Higgins CB, Hricak H, Helms CA, ed. Magnetic resonance imaging of the body 2nd ed. New York: Raven Press 1992; 157-174.
8. Hendrick RE, Osborn AG. Introduction to MR imaging: Part II. Pulse sequences and image contrast. In: Stark DD, Bradley WG, ed. Diagnostic categorical course in MR imaging, syllabus. 1st ed. Oak Brook: Radiological Society of North America 1988; 15-25.
9. Nataf E, Halimi Ph. Généralités sur l'IRM. In: Veillon F, ed. Imagerie de l'oreille. 1st ed. Paris: Médecine-sciences Flammarion, 1991; 39-59.
10. Chien D, Edelman RR. Ultrafast imaging using gradient echoes. Magnetic Resonance Quarterly 1991; 7:31-56.

### 3. Patients - Sequences

#### 3.1. PATIENTS

Over a period of 34 months (from February 1991 to December 1993) 650 patients (289 men, 361 women, with ages ranging from 7 to 87 years with an average of 49.5 years) underwent an MR examination of the inner ear.

Most of the 650 patients underwent an MR examination because they had sensorineural hearing loss (SNHL) or vertigo and/or abnormal findings at vestibular testing. Some were also referred because they had a combination of SNHL and vertigo or simply because the clinician wanted to rule out an acoustic schwannoma.

However, as the diagnostic possibilities of gadolinium-enhanced T1-weighted images and 3DFT-CISS images became known, other smaller groups of patients were referred in order to check the diagnostic capabilities of these images in more specific inner ear disease. The most important indications that were encountered are listed in Table I.

*Table I: Most frequent indications*

- Sensorineural hearing loss (majority of the patients - exclusion of acoustic schwannoma)
- Vertigo (167 patients, however often in combination with other signs and especially SNHL)
- Peripheral facial palsy
- Meniere's disease (study of 20 patients)
- Sudden deafness (study of 5 patients)
- Tinnitus
- Cogan's syndrome (study of 6 patients)
- Large temporal bone tumours involving the bony and membranous labyrinth
- Congenital malformations

The patient selection was certainly influenced by the referral pattern in our hospital. First of all, clinicians aware of the possibilities of the 3DFT-CISS sequence sent patients in whom they expected membranous labyrinth pathology (Cogan's syndrome) or rare pathology (cases they followed for a long time without being able to demonstrate the pathology in a radiological way). Furthermore a lot of the patients, referred from other hospitals had already undergone a routine brain and temporal bone CT, and routine pathology was already excluded (for example large acoustic schwannomas). Therefore in these selected patients, with a negative CT but with persisting clinical signs, an MR study was justified and the patients were referred. It's obvious that in these patients more subtle inner ear pathology (more frequently in the membranous labyrinth) or very small lesions in the internal auditory canal or cerebellopontine angle (invisible on CT) are expected.

Only a limited number of patients were involved in the first studies (see V.1, V.2). Only the later studies (V.4 and V.5) included all 650 patients. Studies V.3, V.6 and V.7 were focused on a limited number of patients with a particular pathology.

#### 3.2. SEQUENCES

All patients were studied on a one tesla active shielded superconductive system (Magnetom SP 42, Siemens, Erlangen, Germany). All patients were studied with a new 3DFT-CISS sequence. I was looking for a sequence which could show the structures of the inner ear and IAC in more detail and tested this abandoned 3DFT-CISS sequence, originally designed to study the medulla and the surrounding CSF. The first results were mediocre but new tests with this sequence, after I changed some of the parameters of this sequence, were very promising and I started to use this sequence in all patients. Later, in co-operation with Dr. M. Deimling (Medical Engineering Group Siemens A.G., Erlangen, Germany), this sequence was further ameliorated and even some basic elements of the sequence were changed, see III.2.5.2. and V.1.8.-1.9. (ADDENDUM I - II). A standard circular polarized head coil was used allowing simultaneous imaging of both inner ears. Sequences a)  $\Rightarrow$  d) were used in all patients; sequences e)  $\Rightarrow$  f) were more selectively used.

- a) axial 3 mm thick contiguous nonenhanced T1-weighted spin-echo images
- b) axial 3 mm thick contiguous gadolinium-enhanced T1-weighted spin-echo images
- c) coronal 3 mm thick contiguous gadolinium-enhanced T1-weighted spin-echo images
- d) axial 1 mm (end 1993 even 0.7 mm) thick 3DFT-CISS images
- e) axial 4mm thick T2-weighted spin-echo images (in patients older than 45 years and in younger patients in whom demyelinating disease was suspected, or if there was an increased risk of vascular disease)
- f) axial 1mm thick 3DFT- Fast Imaging with Steady Precession (FISP) images (vascular "time of flight" sequence). This sequence was used (only in a few patients) when a vascular anomaly or lesion was suspected in the cerebellopontine angle or near the internal acoustic pore. On these images only the flowing blood has a high signal (white); the other tissues have a lower signal intensity (grey or black).

The most frequently used parameters of these sequences are shown in Table II. The parameters of the T1 and T2-weighted sequences changed during the 34 months of the study and the parameters in italics are those that were used at the end of the study (December 1993).

The introduction of the "rectangular field of view = RECFOV" software enabled us to use fewer phase encoding steps or a smaller matrix (for instance a  $192 \times 256$  instead of a  $256 \times 256$  matrix can be used without loss of spatial resolution when a RECFOV of 3/4 is used). For example only 7.5 cm of a field of view of 10 cm (in the phase encoding direction) is measured when a RECFOV of 3/4 is used. The resolution of 75 mm/192 or 100 mm/256 is the same, 0.39 mm, but the acquisition is shortened by a quarter when the RECFOV technique is used. This resulted in shorter T1 (now routinely 5 min 49 sec) examination times although other parameters (TR, acquisitions, flip angle) were also often slightly changed and contributed to the time gain (T2 = 9 min 27 sec).

In all patients, 0.1 mmol/kg of Gd-tetra-azacyclododecane tetraacetic acid (Gd-DOTA, Dotarem, Guerbet Laboratories, Aulnay-sous-Bois, France) or Gd-diethylenetriamine pentaacetic acid (Gd-DTPA, Magnevist, Schering AG, Berlin, FRG) was injected after the nonenhanced T1-weighted images and 3DFT-CISS images were acquired. The intravenous

gadolinium administration should only take place after the 3DFT-CISS images are acquired as gadolinium can produce or aggravate artefacts on these images.

*Table II: Sequence parameters.*

	T1 spin-echo	3DFT-CISS (1mm)	3DFT-CISS (0.7 mm)	T2 spin-echo	3DFT-FISP (vascular)
Repetition time (TR)	500 msec 450 msec	20 msec	15 msec	2500 msec 2200 msec	43 msec
Echo time (TE)	15 msec 14 msec	8 msec	21 msec	15/90 msec 13/80 msec	10 msec
slice thickness	3 mm	1 mm	0.7 mm	4-5 mm	1 mm
gap	0	0	0	0.5-0.8 mm	0
field of view	230 210	176	170	230	230
matrix	256 × 256 192 × 256*	256 × 256	256 × 256	256 × 256	256 × 256
number of acquisitions	3	1	1	1	1
acquisition time	6 min 27 sec 5 min 49 sec	2 × 2 min 46 sec	2 × 4 min 3 sec	10 min 42 sec 9 min 27 sec	5 min 55 sec
flip angle	90° 75°	50°	65°	90° 65°	40°
slab	-	32 mm	22.4 mm	-	32
partitions	-	32	32	-	32

\*In combination with a rectangular field of view of 3/4, resulting in an effective 256 × 256 matrix.

## IV. GENERAL RESULTS

MR of the inner ear, including the 3DFT-CISS sequence, was able to demonstrate pathology in 113 or 17.4% of the 650 patients studied. The lesions that were found in these 113 patients are listed in Table I.

*Table I: Inner ear pathology found with MR in 650 patients.*

Pathology	Number of patients	Percentage
Schwannomas <sup>(1)</sup>	37	5.7%
Obliteration of the intralabyrinthine fluid spaces <sup>(2)</sup>	18	2.7%
Congenital malformations <sup>(3)</sup>	16	2.5%
Facial nerve neuritis	13	2.0%
CPA or temporal bone tumours (schwannomas excluded) <sup>(4)</sup>	9	1.4%
Labyrinthitis	5	0.8%
Vascular anomaly or pathology in the CPA or posterior fossa <sup>(5)</sup>	5	0.8%
Cogan's syndrome	5	0.8%
Facial nerve schwannoma	3	0.5%
Varia (otosclerosis - sequel of nerve resection)	2	0.3%
TOTAL	113	17.4%

- (1) Nine of the 37 schwannomas had a completely intracanalicular location and two were located inside the cochlea, one inside the vestibule.
- (2) In 18 patients obliterations of the intralabyrinthine fluid spaces were recognized. These obliterations were most often caused by soft tissue obliterations (normal CT findings).
- (3) Congenital malformations of the inner ear were found in 15 patients and in none of these patients a congenital malformation was suspected clinically (congenital inner ear malformations are normally studied with CT).
- (4) Less frequent tumours of the cerebellopontine angle and temporal bone that were found were: meningiomas (3), metastases (2), cholesterol granuloma (1), fibrous dysplasia (1), glomus jugulare tumour (1) and a presumed chondrosarcoma (1).
- (5) Three tortuous basilar-vertebral arteries, one tortuous posterior inferior cerebellar artery and one ectatic superior petrous vein were detected, and contact with the facial and/or vestibulocochlear nerve could be seen in these patients.

Cerebellar and brain stem infarction and/or atrophy were frequently found. However, the relationship between the symptoms and MR findings cannot be proven in these cases and therefore cerebellar and brain stem infarction and/or atrophy are not listed in the Table above (see also V. 4.).

## V. STUDIES - RESULTS

### 1. Constructive Interference in Steady State-3DFT MR Imaging of the Inner Ear and Cerebellopontine Angle

*Jan W. Casselman, Rudolf Kuhweide, Michael Deimling, Willy Ampe, Ides Dehaene, and Ludo Meeus*

*Published in: Am J Neuroradiol 1993; 14:47-57.*

# 1. Constructive Interference in Steady State-3DFT MR Imaging of the Inner Ear and Cerebellopontine Angle

Jan W. Casselman<sup>(1)</sup>, Rudolf Kuhweide<sup>(2)</sup>, Michael Deimling<sup>(4)</sup>,  
Willy Ampe<sup>(2)</sup>, Ides Dehaene<sup>(3)</sup>, and Ludo Meeus<sup>(1)</sup>

From the departments of Radiology<sup>(1)</sup>, Otorhinolaryngology<sup>(2)</sup>,  
and Neurology<sup>(3)</sup>, A.Z. St.-Jan Brugge, Brugge, Belgium,  
and Medical Engineering Group Siemens A.G.<sup>(4)</sup>, Erlangen, Germany.

*Published in: Am J Neuroradiol 1993; 14:47-57.*

## 1.1. ABSTRACT

**Purpose:** To assess the value of a three-dimensional Fourier transformation MR technique "CISS" (constructive interference in steady state) in imaging the inner ear.

**Subjects:** We studied 50 normal inner ears (40 axial, 10 coronal) and 10 pathologic inner ears in 60 patients.

**Results:** The cochlea, semicircular canals, and vestibulum were visualized in detail. Cranial nerve VII and the cochlear, superior vestibular, and inferior vestibular branch of cranial nerve VIII were identified in 90%, 94%, 80%, and 88% of the cases, respectively. A vascular loop was recognized inside the internal auditory canal in 6%, and in the porus in 30%, of the cases. The high signal of the cerebrospinal fluid and labyrinthine fluids (perilymph and endolymph) on the CISS images made excellent delineation of tumours in the cerebellopontine angle and internal canal possible and allowed detection of tumoural labyrinth involvement. The thin sections, high resolution of the images, and capability of producing multiplanar and three-dimensional reconstructions often offered additional information.

**Conclusions:** The CISS sequence allows detailed study of the normal and pathologic inner ear and promises to be highly valuable in the demonstration of the vascular loop.

**Index terms:** Temporal bone, anatomy; Temporal bone, magnetic resonance; Ear, magnetic resonance; Magnetic resonance, technique.

## 1.2. INTRODUCTION

Computed tomography (CT) has long been the method of choice in the investigation of the labyrinth and internal auditory canal (IAC). With the advent of magnetic resonance (MR) it became clear that MR was superior in the demonstration of soft-tissue structures of

the inner ear (1-3); however, two-dimensional Fourier-transformation (2DFT) spin-echo MR techniques provided sections that were 3 mm thick, insufficient for detailed imaging of the inner ear (2, 4), while 3DFT gradient-echo MR studies (1-mm contiguous sections) often lacked good cerebrospinal fluid (CSF)-nerve contrast within the IAC or were very time consuming (1, 2). We present a 3DFT sequence—"constructive interference in steady state" (CISS)—that allows fast and detailed imaging of the inner ear structures and provides excellent CSF-nerve contrast within the IAC and cerebellopontine angle (CPA).

### 1.3. SUBJECTS AND METHODS

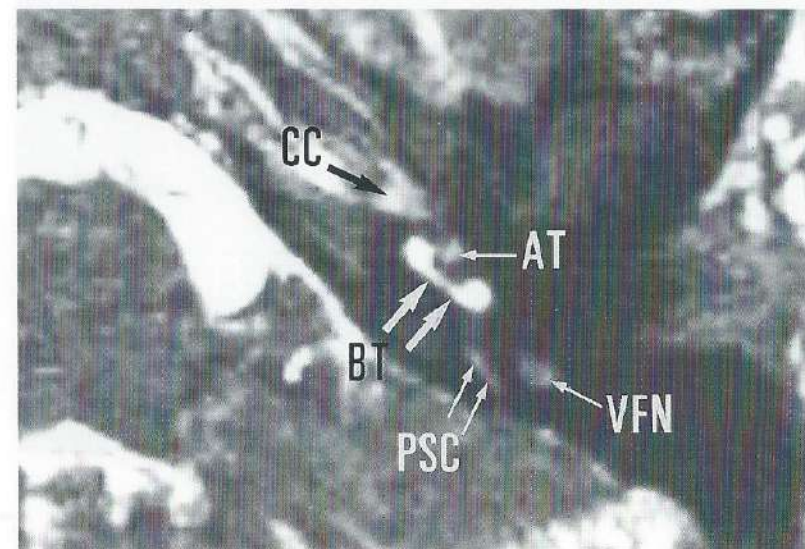
Sixty inner ears were studied using the CISS sequence. In 50 cases (average age of subjects 47 years; 23 men, 27 women), MR was performed for exclusion of acoustic schwannomas (neuromas). An additional CISS sequence was used to study the anatomy of the inner ear only when the routine nonenhanced and gadolinium-enhanced T1-weighted spin-echo images showed no abnormalities. Forty of the 50 CISS studies were done in the axial plane, 10 in the coronal plane. Ten pathologic inner ears (average age of subjects, 47

**Table 1:** Reliability of CISS images to show inner ear structures

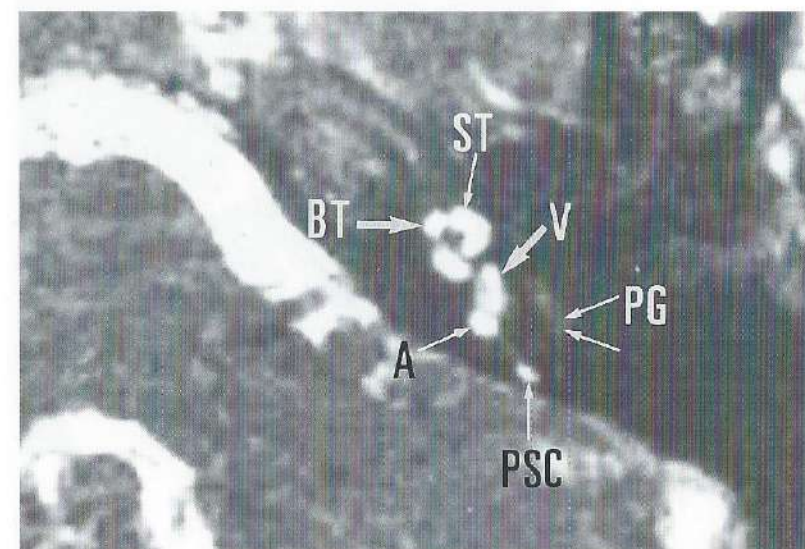
	40 Inner Ears Axial Plane No./%	10 Inner Ears Coronal Plane No./%
Cochlea	40/100	10/100
Vestibulum	40/100	10/100
LSC-PSC-SSC	40/100	10/100
Internal Carotid Artery	40/100	10/100
Cranial nerve VII	36/90	9/90
Cochlear branch of nerve VIII	38/95	9/90
Superior vestibular branch of nerve VIII	33/82.5	7/70
Inferior vestibular branch of nerve VIII	36/90	8/80
Anterior segment of facial nerve	39/97.5	7/70
Geniculate ganglion	36/90	5/50
Horizontal segment of facial nerve	34/85	8/80
Posterior genu of facial nerve	23/57.5	8/80
Vertical segment of facial nerve	25/62.5	7/70
Canal of subarcuate artery	26/65	2/20
Vestibular aqueduct	29/72.5	0/

Note: LSC = lateral semicircular canal, PSC = posterior semicircular canal, SSC = superior semicircular canal.

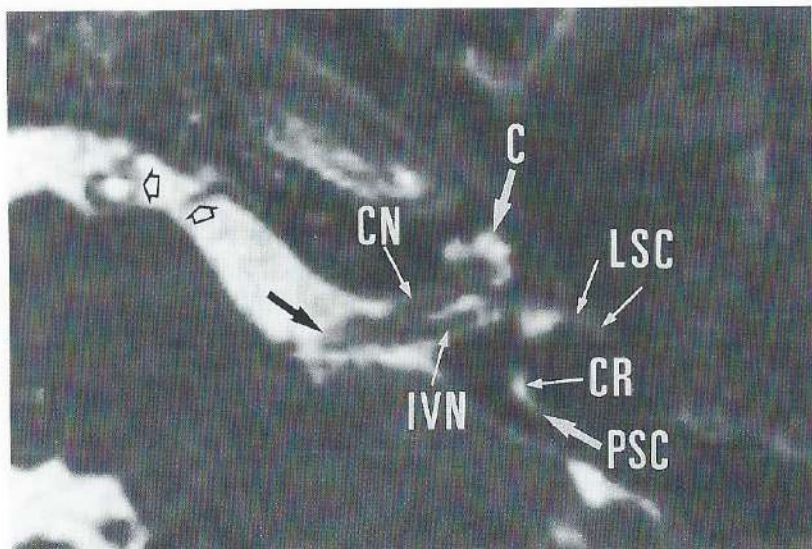
**Fig. 1.** Axial (A-E) and coronal (F-G) 1-mm CISS images through a normal left inner ear.



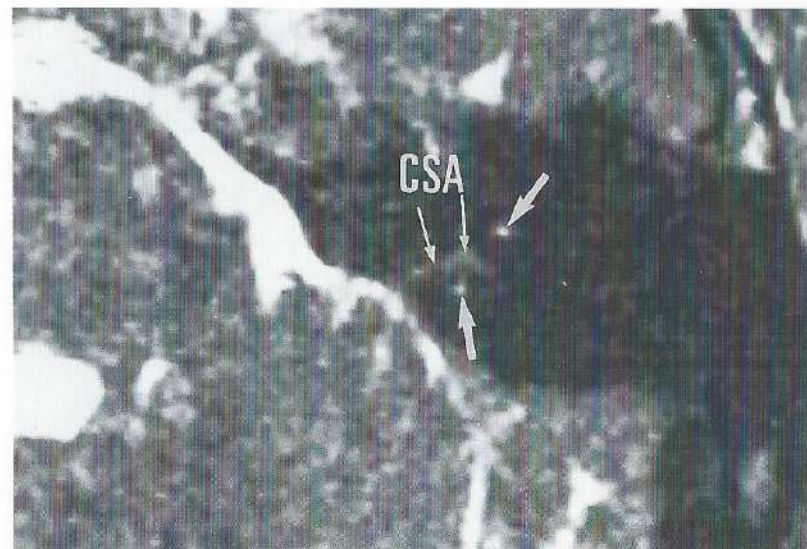
A



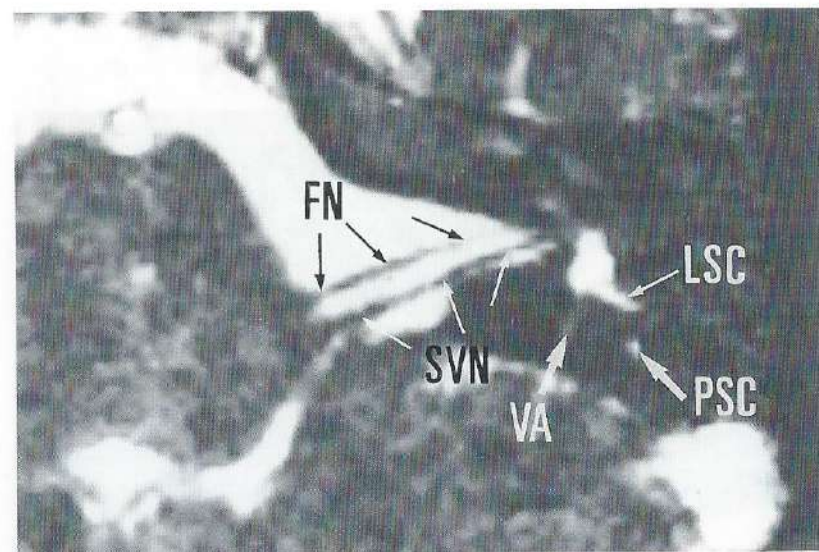
B



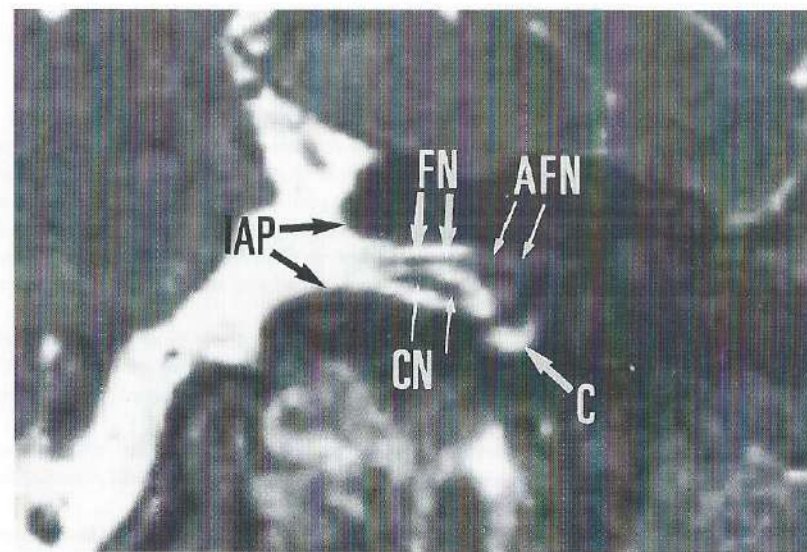
C



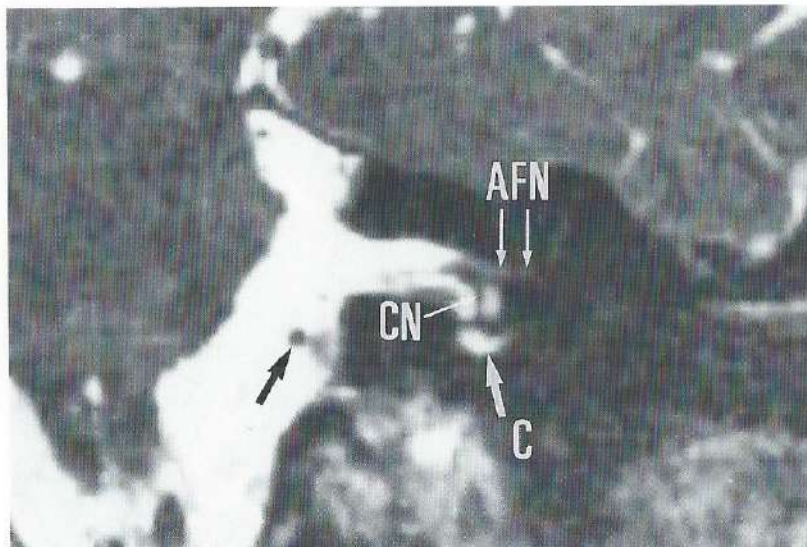
E



D



F



### G

**A.** Level of basal turn of the cochlea. The high signal inside the posterior semicircular canal (PSC), basal turn (BT), and apical turn (AT) of the cochlea are seen. The vertical segment of the facial nerve is also identified (VFN). The carotid artery in the carotid canal is also recognized (CC).

**B.** Level of the utriculosaccular structures. High-signal peri- and endolymph is seen in the basal (BT) and second turn (ST) of the cochlea, in the utriculosaccular structures (V), and in the posterior semicircular canal (PSC) and its ampulla (A). The posterior genu of the facial nerve (PG) has an intermediate signal. The modiolus can be seen as a low-signal structure inside the cochlea.

**C.** Level of the inferior part of the IAC. Good CSF-nerve contrast makes visualization of the V-shaped bifurcation of the nerve inside the IAC possible and the cochlear branch (CN) and inferior vestibular branch (IVN) of cranial nerve VIII can be seen. At this level, a part of the posterior semicircular canal (PSC) is visible and a part of the crus commune of the superior and posterior semicircular canals (CR) is identified. The CSF in the CPA remains high in intensity when the CISS sequence is used in combination with the head coil, making visualization of nerves (large black arrow) and vessels (open black arrows) in the CSF spaces possible. LSC, lateral semicircular canal; C, cochlea.

**D.** Level of the superior part of the IAC. The typical parallel course of the facial nerve (FN) and superior vestibular branch of cranial nerve VIII (SVN) can be followed throughout the CPA and IAC. The posterior limb of the lateral semicircular canal (LSC), the posterior semicircular canal (PSC) and the vestibular aqueduct (VA) can also be recognized.

**E.** Level of the canal of the subarcuate artery. The visualization of the canal of the subarcuate artery (CSA) depends on the size of the canal. The canal can be seen between the anterior and posterior limb of the superior semicircular canal (large white arrows).

**F.** Coronal CISS image through the anterior part of the IAC. The cochlear branch of cranial nerve VIII (CN) and the facial nerve (FN) can be identified in the coronal plane. The anterior segment of the facial nerve in the bony canal (AFN) can also be seen. The bony walls of the internal acoustic pore (IAP) are well seen and a part of the cochlea is visible (C).

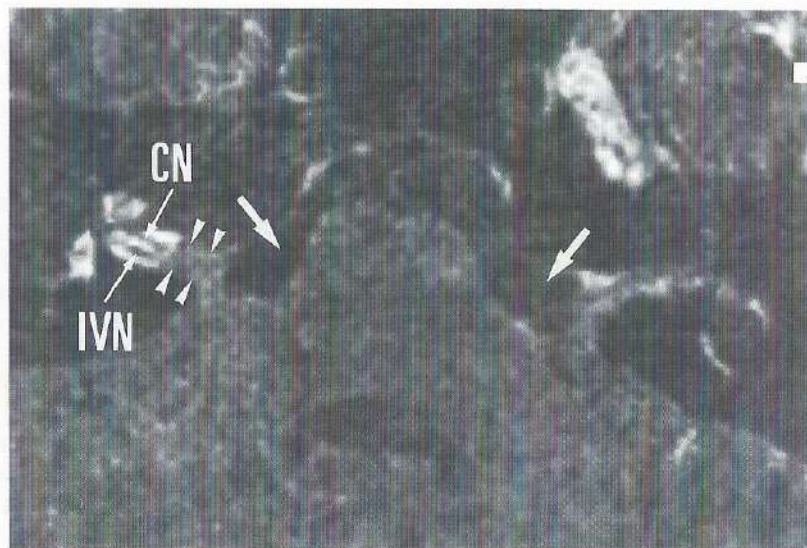
**G.** Coronal CISS image 1mm anterior to F. The cochlear branch of cranial nerve VIII (CN) is seen entering the cochlea (C). The anterior segment of the facial nerve (AFN) and the vascular loop in the CPA (large black arrow) can also be recognized.

years; one man, nine women) were also examined with the CISS sequence scheme after the diagnosis had been made with CT and/or MR. Three acoustic schwannomas, one facial nerve schwannoma, one CPA meningioma, one cholesterol granuloma, one glomus jugulare tumour, one case of metastasis in the IAC, one case of fibrous dysplasia, and one case of congenital narrowing (or osteoma formation) of the internal acoustic pore (meatus) (IAP) were studied. In the 50 normal inner ears, visualization of small anatomical structures was checked on the CISS images (Table I) (Figs. 1A-1G); in particular, visualization of the facial nerve and the cochlear, inferior vestibular, and superior vestibular branch of cranial nerve VIII was verified, as was the presence of a vascular structure (artery) in the CPA, near or in the IAP or in the IAC (Table II).

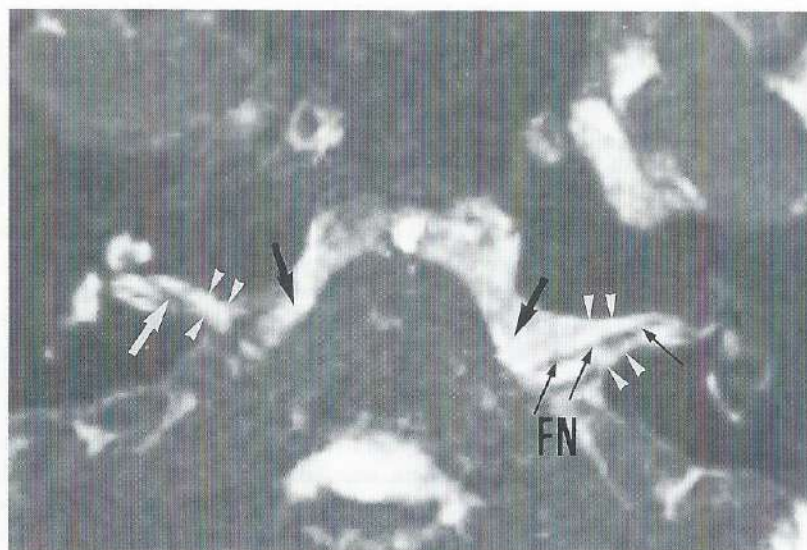
All studies were performed on a 1-T active shielded system (Magnetom SP 42, Siemens, Erlangen, Germany). The use of a standard circular polarized head coil allowed simultaneous imaging of both inner ears. A CISS sequence scheme was used in all cases (5). Fast imaging with steady precession (FISP) and PSIF (mirror sequence of FISP) (contrast-enhanced fast acquisition steady state (CE-FAST)) sequences basically rely on the steady state of both longitudinal and transversal magnetization (6, 7). This steady state is established by excitation of the spin system with radiofrequency pulses at a short repetition time (TR)  $\ll$  T<sub>2</sub>. The development to this state is achieved using a short prescan time of about 1 second before starting the data acquisition itself. As is well known from flow imaging, moving spins will accumulate additional phase shifts when moving along field gradients. If the motion is not constant in time, transverse magnetization will experience random phase shifts and the magnetization may cancel completely (thus completely avoiding a steady state of the transverse magnetization). Therefore, moving cerebrospinal fluid (CSF) does not produce any signal when standard FISP or PSIF sequences are used. (Fig. 2A). Even for very slow flow, the CSF signal may disappear because these flow-induced phase shifts will accumulate over many TR intervals, thus creating a large amount of phase shifts in the magnetization.

Flow compensation techniques have to be used to make sure that spins, independent of their actual velocity, are being refocused. The flow compensation must be applied to each gradient over each TR cycle, unlike standard flow compensation sequences (eg, motion refocusing angiography sequences), in which the flow compensation is applied to the echo. A steady state flow-compensated 3D-FISP sequence is shown in Figure 3. All three gradients are balanced, indicating that the average value of each gradient is zero. In this case, spins moving at a constant velocity will have the same phase after the application of the gradient pulses as they had before (8). Running a sequence as shown in Figure 3 will produce an image that shows bands of low signal intensity. The occurrence of these bands is not the indication of any system imperfection but is related to basic physical effects. These dark bands are caused by very small magnetic field inhomogeneities and local field distortions due to susceptibility changes that are normally produced by the patient. These inhomogeneities will cause corresponding frequency offsets. If the frequency at a given location is such that the phase angle accumulation over one TR period corresponds to  $\pi$ , or odd integers thereof, the magnetization cancels, and a dark point appears in the image. At another location, the frequency offset might be larger, eg,  $2\pi$  or a multiple thereof, and the magnetization will interfere constructively, resulting in a high signal intensity at this particular point.

Fig. 2. Axial FISP (A) and CISS (B) images of the same patient through both CPAs and inner ears (same matrix).



A



B

A. 1-mm FISP section, 28/10/1 (TR/TE/excitations), angle =  $90^\circ$  and acquisition time = 15 minutes 20 seconds. This 1-mm section shows the cochlear branch (CN) and inferior vestibular branch (IVN) of cranial nerve VIII on the right side but the V-shaped bifurcation is not seen because of signal loss in the medial part of the IAC (white arrowheads). More important CSF flow produces nearly total signal loss in the CPAs (large white arrows). The use of a surface coil can result in more detailed images of the inner ear but will also lead to even more important signal loss in the CPA and near the porus.

B. On this 1-mm CISS image the V-shaped bifurcation of the cochlear and inferior vestibular branch is easily recognized (large white arrow) on the right; there is no signal loss of the CSF in the medial part of the IAC (white arrowheads) or CPA (large black arrows). This makes identification of the facial nerve (FN) throughout the CPA and IAC possible on the left side (small black arrows) (compare with A). Also the inner ear structures are better seen and have a higher signal on this CISS image than on the FISP image.

The solution to this inherent problem is to acquire two data sets successively with a "true FISP" (6) sequence of alternating (+-) and nonalternating (++) radiofrequency pulses. The position of the dark bands is shifted in the second data set to the position of high intensity of the first data set. Because of the successive character of data collection, patient movements occurring between the two acquisitions will degrade image quality significantly. An interleaved sequence would destroy the steady state and, therefore, reduce the high CSF-brain contrast. A simple mathematical postprocessing operation (maximum intensity projection (9)) takes the information of each pair of images of the two 3-D data sets created in this way to produce an image with a homogeneous intensity distribution over the whole image and a very good contrast between CSF and nerves (Figs. 1A-1G and 2B). Each data set covers a volume of 32 mm for application in the inner ear. This slab is divided into 32 partitions, resulting in an effective section thickness of 1 mm. The measure-

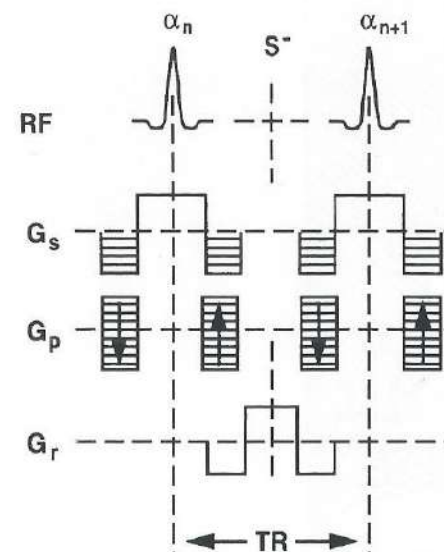
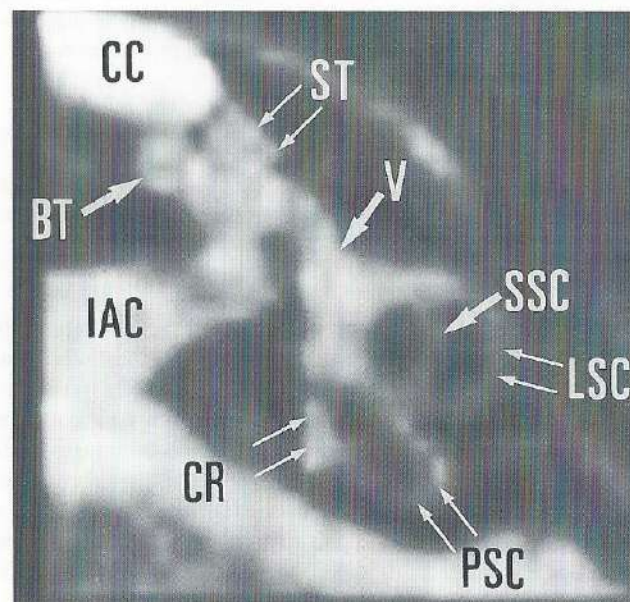
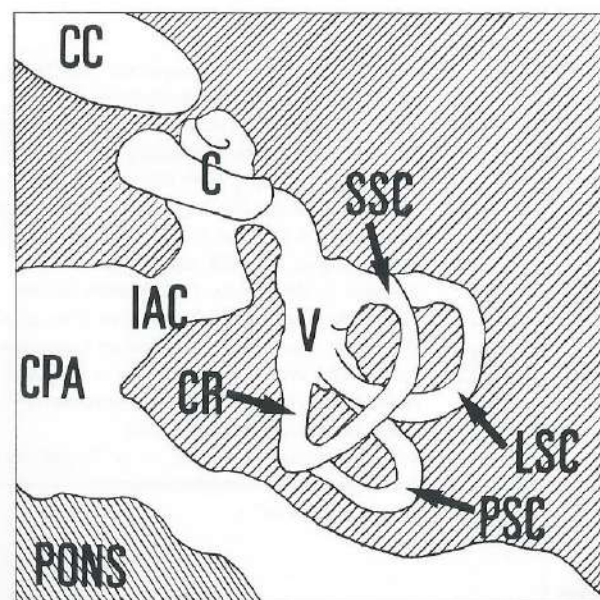


Fig. 3. True FISP 3-D sequence. The three gradients are balanced indicating that the average value of each gradient in the section selection ( $G_s$ ), phase encoding ( $G_p$ ), and frequency encoding ( $G_r$ ) direction is zero. The signal is not flow-refocused at the echo time ( $\Phi(s) = 0$ ,  $\Phi(v) \neq 0$ ) but steady-state refocusing at each TR interval is achieved ( $\Phi(s) = 0$ ,  $\Phi(v) = 0$ ). This is sufficient to retain the high signal for slow motion. High flow (eg, vessels) are depicted as hypointense zones. This true FISP sequence is repeated twice when the CISS sequence scheme is used, once with nonalternating radiofrequency ( $\alpha_n = \alpha_{n+1} = \alpha^{++}$ ) and once with alternating radiofrequency ( $\alpha_n = \alpha_{n+1} = \alpha^+$ ).

Fig. 4. 3-D reconstruction of the left cochlea and labyrinth reconstructed from an axial 3DFT-CISS data set, craniocaudad view (A) and corresponding drawing (B).



Simultaneous visualization of the total membranous labyrinth including basal (BT) and second/apical (ST) turn of the cochlea, utriculosaccular structures (V), superior (SSC), lateral (LSC), and posterior (PSC) semicircular canals, common crus (CR) of posterior and superior semicircular canals is possible only on 3-D reconstructions. IAC, internal auditory canal; CC, carotid artery in carotid canal; CPA cerebellopontine angle.



ment parameters are: TR = 20 msec, TE = 8 msec, matrix size = 256 × 256, field of view = 176 mm and flip angle = 50°. The result is a total acquisition time of 2 times 2.46 minutes and an inplane resolution of each of the 3-D partitions of 0.69 × 0.69 mm. Shim optimisation on the patient is not required. A targeted maximum intensity projection on the CISS data set allows also 3-D reconstructed imaging of the inner ear (1) (Fig. 4). The use of a field of view of 176 mm also allows examination of both inner ears when the head coil is used (Fig. 2B). No special hardware requirements will hamper the implementation of this technique. The image quality will benefit from higher field strength. The software is presently available on Siemens 1.0- and 1.5-T systems.

## 1.4. RESULTS

### 1.4.1. Normal Inner Ears

In the axial plane, the facial nerve was identified in the IAC in 90% of the cases (Figs. 1D, 1F, and 1G); the cochlear branch of cranial nerve VIII in 95% (Figs. 1C, 1F, and 1G) of the cases; and the inferior and superior vestibular branch of nerve VIII in 90% and 82.5% of the cases, respectively, (Figs. 1C-1D). In the majority of cases, the anterior segment, geniculate ganglion, and horizontal segment of the facial nerve were visible on the axial images, whereas the posterior genu and the vertical segment were less often visible (Table I) (Figs. 1A, 1B, 1F, and 1G). The vestibular aqueduct was identified in 72.5% and the canal of the subarcuate artery in 65% of the cases (Fig. 1E). The basal, second, and apical turn of the cochlea, the vestibulum, all three semicircular canals, and the internal carotid artery were always recognized on the axial and coronal CISS images (Fig. 1).

In the coronal plane, the four nerves were detected in a similar way as in the axial plane (Table I). The geniculate ganglion of the facial nerve was less often visualized, and the posterior genu and vertical segment were more often seen than in the axial plane. It was far more difficult to identify the canal of the subarcuate artery on the coronal images and in the 10 coronal studies no vestibular aqueduct was found.

Table II: Position of arterial structures (vascular loop) in relation to the CPA, IPA, and IAC

	Axial Plane 40 Inner Ears No./%	Coronal Plane 10 Inner Ears No./%	Total 50 Inner Ears No./%
Vessel in CPA	26/65	6/60	32/64
Vessel near or in IPA	12/30	3/30	15/30
Vessel in IAC	2/5	1/10	3/6

Note: CPA = cerebellopontine angle, IPA = internal acoustic pore or porus, IAC = internal auditory canal.

In 64% of the 50 normal inner ears (coronal and axial plane), a vascular structure was found in the CPA; in 30% of the cases the vessel was present in the IAP; and in 6% of the cases a loop was seen in the IAC (Fig. 5).

#### 1.4.2. Pathologic Inner Ears

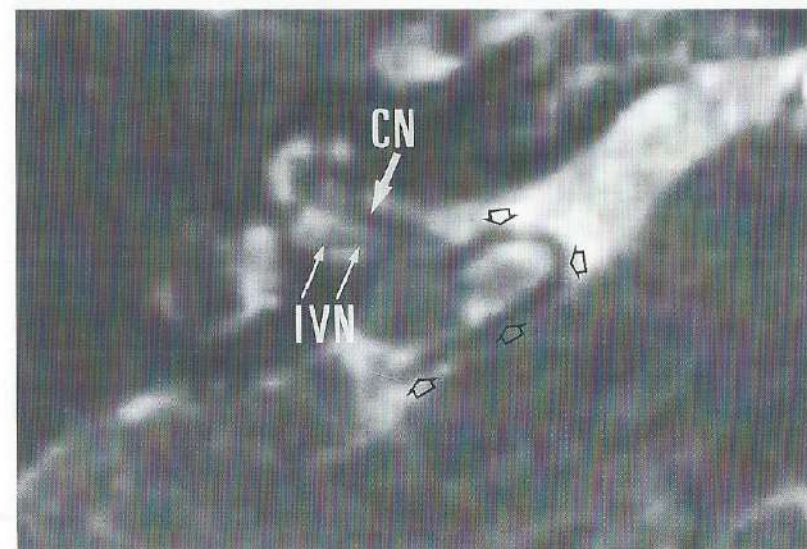
All clinical data on the 10 patients that were examined with the CISS sequences are listed in Table III, including diagnosis, findings during clinical examination, and findings on the CISS images. The major benefits of the CISS sequence scheme—good nerve-CSF contrast in IAC and CPA, good visualization of bony walls due to CSF-bone contrast on thin sections, high in-plane resolution, high intensity of the labyrinthine fluids, ability to make 3-D and multiplanar reconstructions—all contributed to better visualization of the pathology in these cases. Only in one case was the CISS sequence scheme of no benefit at all (case 4).

### 1.5. DISCUSSION

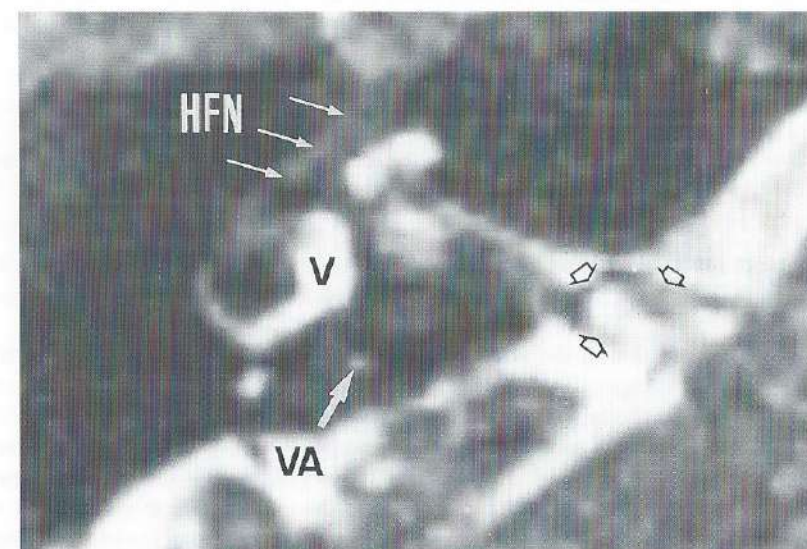
3DFT sequences of the inner ear will only be used when they provide supplementary information and when they are short, so that they can be added to a routine study of the inner ear. Spatial resolution and contrast between different structures are also important (1, 4). Our study shows that the CISS sequence scheme enables us to obtain high-resolution images with good contrast between CSF and nerves (Figs. 1 and 2). Consequently, the reliability of this sequence to show the four nerves within the IAC separately is high. The most difficult nerve to visualize was the superior vestibular branch of cranial nerve VIII, which was often difficult to separate from the inferior vestibular branch. One of the reasons these nerves cannot always be separated is because we used the head coil and studied both inner ears simultaneously, so that images perfectly parallel to the IAC could not always be achieved. Another reason is that in very narrow IACs the nerves are closer together and less CSF is present, so that the spatial resolution can become critical (10) and the high CSF-nerve contrast is lost. In these circumstances, one has to rely on the typical anatomical pattern of the nerves to distinguish them from one another.

On axial images, the inferior vestibular branch and the cochlear branch of cranial nerve VIII can be seen as a V-shaped bifurcating nerve in the distal half of the IAC (Figs. 1C, 2B, and 5A). The superior vestibular branch of cranial nerve VIII and cranial nerve VII can be seen as parallel structures throughout the total length of the IAC (10, 11) (Fig. 1D). It is important to use the head coil. Surface coil imaging provides good images of the labyrinth but there is a rapid loss of signal in the deeper regions, resulting in loss of contrast between CSF and nerves, especially in the CPA and proximal IAC. But the high signal of the CSF in the CPA is also lost due to CSF flow, as is the case when FISP sequences are used (Fig. 2A). The very high signal of the intralabyrinthine fluid on CISS images is reflected in the 100% reliability in visualizing the structures of the labyrinth. The weakness of the CISS sequence scheme is the lack of contrast between soft tissues and even between soft tissues and bone. This weakness explains the inconstant identification of the facial nerve, especially in the vertical segment and posterior genu, where only bone and no endolymph is

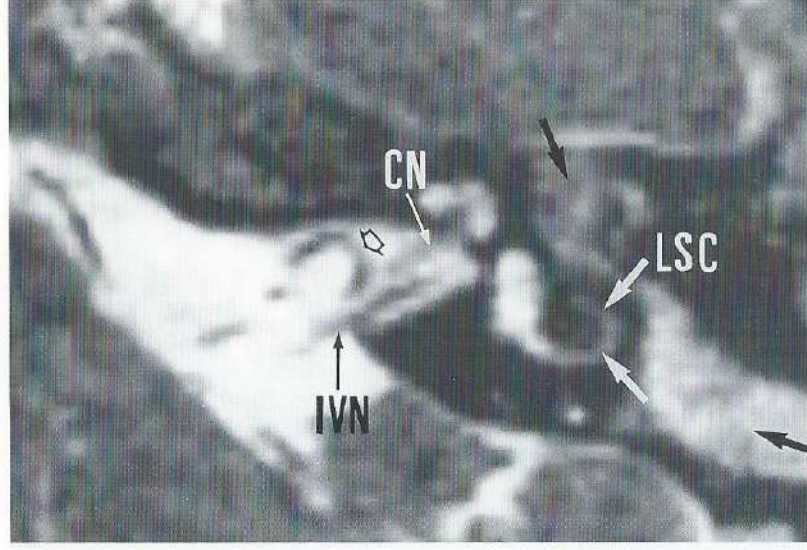
Fig. 5. CISS images of different localizations of the vascular loop.



A



B



C

A. Axial CISS image of the vascular loop in the right CPA. The vascular loop (open black arrows) can be identified and its relation to the cochlear nerve (CN) and inferior vestibular branch (IVN) of cranial nerve VIII can be assessed due to the high contrast between high-signal CSF and nerves and vessels.

B. Axial CISS image of a vascular loop in the right internal acoustic pore. The convexity of the vascular loop (open black arrows) can be seen inside the IAP. The vestibulum (V), horizontal segment of the facial nerve (HFN), and the vestibular aqueduct (VA) (oblique cut through the aqueduct) are also identified.

C. Axial CISS image of a vascular loop in the left IAC. The vascular loop (open black arrow) can be seen deep inside the wide IAC and its relation to the cochlear (CN) and inferior vestibular (IVN) nerve can be evaluated. The total lateral semicircular canal (LSC) is only visible when the imaging plane is tilted 30° upward anteriorly. Notice also the high-signal collections in the middle ear cavity and antrum (large black arrows).

present adjacent to the nerve. For the same reason, the canal of the subarcuate artery is less frequently seen. This canal can also be very thin so that the spatial resolution can pose a problem.

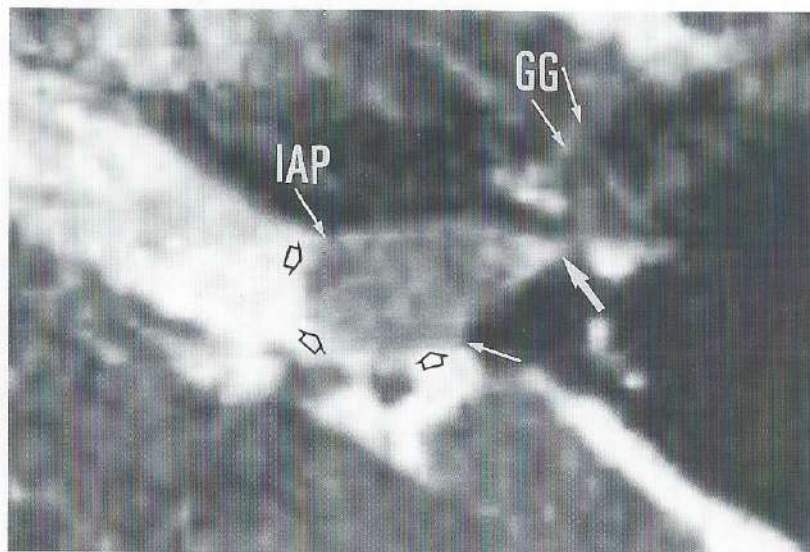
The better identification of the vestibular aqueduct on axial images (Figs. 1D, 5B, and 5C) than on coronal images is explained by the parasagittal orientation of the aqueduct. The vascular supply of the labyrinth is derived from the anterior inferior cerebellar artery in 80% of cases, from the accessory anterior cerebellar artery in 17%, and from the posterior inferior cerebellar artery in 3% of the cases (12). CISS images often show an artery in the CPA cistern (64% of cases), in or near the porus (30% of cases), and in the IAC (6% of cases) (Figs. 5A-5C). On these images not only are the vessels seen, but the relation of the vessels to the cranial nerves VII and VIII are also appreciated. Therefore, 3DFT MR could well replace angiography and air CT cisternography in the diagnosis of

Table III: Clinical findings and findings on CISS images in 10 patients with inner ear pathology

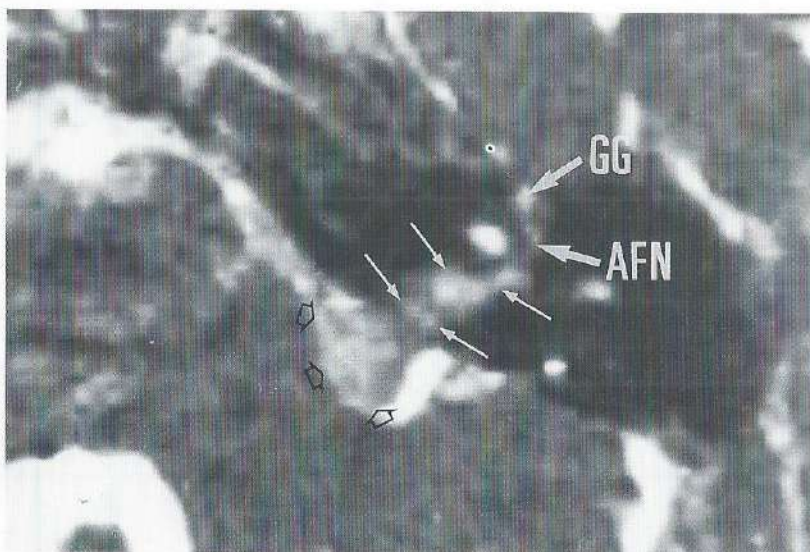
Case	Age/Sex	Diagnosis/Affected Side	Clinical Findings	Findings on CISS Images	Contribution of CISS
1	62/F	Acoustic schwannoma/L	SNHL, abnormal ABR	12 x 18 mm lesion centered on porus with widening of the porus	Evaluation relation tumor-IAC walls, evaluation of extension in CPA
2	62/F	Acoustic schwannoma/L	Disequilibrium	Mass in IAC, extension in CPA	Delineation tumor versus IAC walls and CPA, CSF, and structures
3	78/F	Acoustic schwannoma/L	SNHL, abnormal ABR	10 x 4 mm mass inside IAC, normal porus	Evaluation of relation tumor-IAC walls, normal porus
4	35/M	Facial nerve schwannoma/L	Facial nerve palsy	Enlargement of geniculate ganglion	
5	71/F	CPA meningioma/L	Vertebrobasilar ischaemic disease symptoms	Lesion in CPA, extension to geniculate ganglion	Visualization of connection between lesion in CPA and in geniculate ganglion, shows nerves perpendicular to the mass
6	30/F	Cholesterol granuloma/L	SNHL in the low frequency range	Lesion in bony labyrinth, fistulization to PSC	Visualization of fistula
7	41/F	Recurrent glomus jugulare tumour/L	Mixed hearing loss	Glomus tumor with involvement of bone around PSC, PSC remains intact	Confirmation of intact membranous labyrinth
8	60/F	Breast carcinoma metastasis/L	Facial pain, facial nerve palsy	Tumor in CPA, IAC, and geniculate ganglion	Delineation of tumor versus CSF in CPA
9	15/F	Fibrous dysplasia/R	Disequilibrium, conductive hearing loss, temporal-occipital-parietal skull deformities	Bone alterations, IAC-V semicircular canal involvement	Shows involvement of membranous labyrinth (3-D reconstructions)
10	22/F	Presumed congenital stenosis or osteomas IAP/L+R	SNHL, abnormal ABR	Narrow IAPs	Evaluation bony IAP, 3-D data allowed multiplanar reconstruction

Note: L = left, R = right, ABR = auditory evoked brain-stem responses, CPA = cerebellopontine angle, CSF = cerebrospinal fluid, IAC = internal auditory canal, IAP = internal acoustic pore (meatus), PSC = posterior semicircular canal, SNHL = sensorineural hearing loss, V = vestibulum.

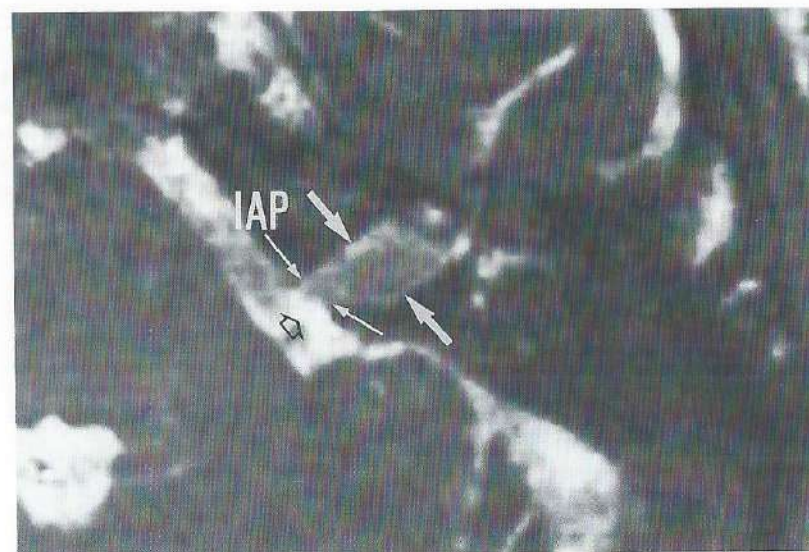
Fig. 6. CISS imaging of acoustic schwannomas, axial images through the IAC.



A



B



C

A. Acoustic schwannoma centered on the left IAP (case 1). Extension of the schwannoma in the CPA (open black arrows) and widening of the internal acoustic pore (IAP) (small white arrows) can be evaluated due to the high tumor-CSF-bone contrast and high resolution. Even CSF entrapped near the fundus of the IAP can be seen (large white arrow). Notice also the geniculate ganglion (GG).

B. Acoustic schwannoma filling up the total left IAC (small white arrows) with extension in CPA and lying against the brain stem (open black arrows) (case 2). GG, geniculate ganglion; AFN, anterior segment of the facial nerve.

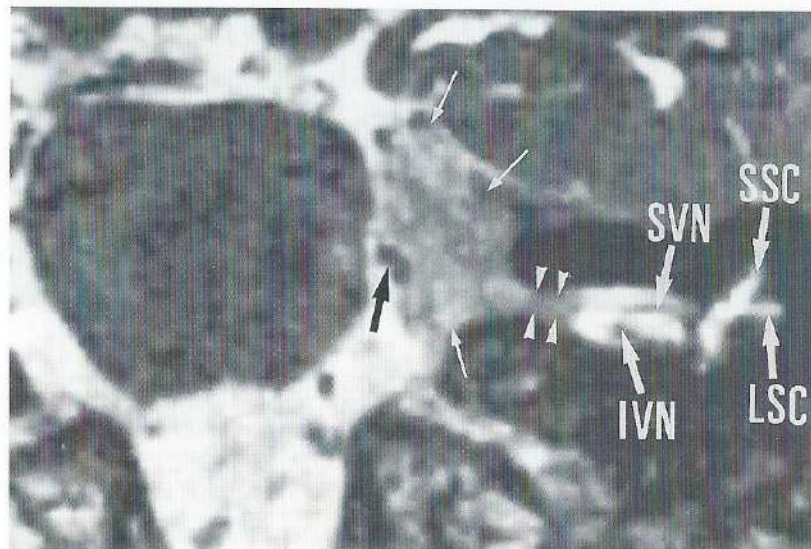
C. Acoustic schwannoma completely inside the left IAC (case 3). The schwannoma surrounded by a thin layer of CSF (large white arrows) produces only widening of the middle part of the IAC. The internal acoustic pore (IAP) and CSF in the CPA near the porus (open black arrow) can be seen.

cross-compression of the vestibular nerve by the arterial loop in patients with intractable vertigo or motion intolerance. Mazzoni reported a vascular loop inside the IAC in 40% and near the porus in 37% of cases (13). Other authors mention that the convexity of the loop is seen in the porus or enters the IAC in 40%-67% of the cases (14), correlating better with our findings on the CISS images.

In case of pathology of the inner ear, CISS images often provided additional information (Table III). Gadolinium-enhanced T1-weighted images remain necessary; the diagnosis of labyrinthitis, neuritis, tumoral invasion of nerves (case 8), and meningeal involvement (case 5) cannot be made or are more difficult to make without the use of gadolinium (15, 16). On the other hand, in case of acoustic schwannoma, CISS images allow exact measurement of the tumor size without the use of gadolinium (cases 1-3). The relation of the schwannoma to the CPA and porus is best seen on CISS images because of the high signal of the CSF in the CPA cistern and the easily recognized bony porus borders and bony IAC

**Fig. 7.** Seventy-one-year-old woman with meningioma in the left CPA (case 5), coronal CISS image.

A large meningioma (small white arrows) is seen in the CPA with extension in the IAC (white arrowheads). The porus is not enlarged and the tumour is attached to the tentorium. The superior (SVN) and inferior (IVN) vestibular branch of cranial nerve VIII can be seen coming out of the mass in a perpendicular way, making the diagnosis of acoustic schwannoma unlikely. The vascular loop is displaced medially (black arrow). SSC, superior semicircular canal; LSC, lateral semicircular canal.



walls (Fig. 6). The bony structures are more difficult to evaluate when only routine spin-echo images are used; often CT was required to make bone evaluation possible. Extension of other tumors in the CPA cistern (cases 5-8) can also be seen on CISS images.

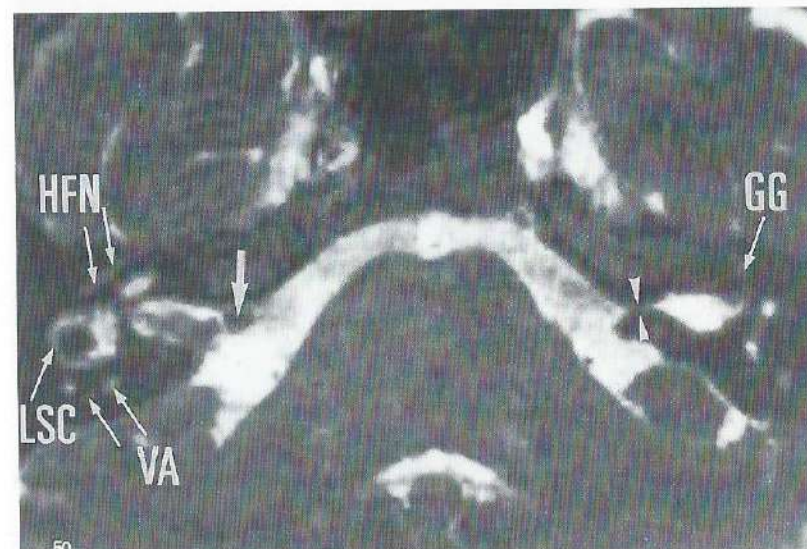
3DFT-CISS images can also play a role in the differential diagnosis between acoustic schwannoma and other tumours. When cranial nerves VII and VIII can be seen coming out of a tumour in a perpendicular way, then an acoustic schwannoma is unlikely (case 5) (Fig. 7). The thin adjacent sections make it possible to see thin structures or lesions. The small fistula between the cholesterol granuloma and the posterior semicircular canal (case 6) and the connection between the CPA meningioma and the small meningioma extension in the gasserian ganglion (case 5) were recognized only on the CISS images. Thin adjacent sections are also suited to make reconstructions in other planes, which can often add important information (case 10) (Fig. 8). The high signal of the intralabyrinthine fluids on the CISS images makes it possible to detect or exclude involvement of the membranous labyrinth (cases 7-9) (Fig. 9).

Another advantage of the high signal of the endolymph-perilymph and the high contrast with the surrounding bony labyrinth on CISS images is that these images can be used to make 3-D membranous labyrinth reconstructions (1) (Fig. 10). Narrowing or obliteration of the endolymph spaces can be detected (case 9) (Figs. 9 and 10). Finally, the weak contrast

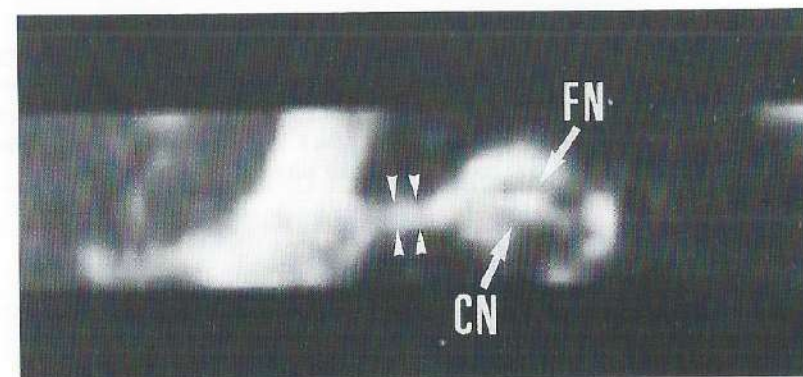
**Fig. 8.** Twenty-two-year-old woman with presumed congenital stenosis of the porus or osteomas of the porus on both sides (case 10). Axial CISS image (A) and coronal reconstruction (B).

A. The extreme narrowing of the left porus (white arrowheads) is easily recognized due to the high CSF-bone contrast. A calcification (presumed osteoma) is narrowing the right porus (large white arrow). The horizontal segment of the facial nerve (HFN), the total lateral semicircular canal (LSC), and the vestibular aqueduct (VA) are recognized on the right side. GG, geniculate ganglion.

B. The coronal reconstruction through the left IAC confirms the narrowing of the porus (white arrowheads) and the spatial and contrast resolution of the reconstruction is good enough to recognize the facial nerve (FN) and the cochlear branch of the vestibular nerve (CN).



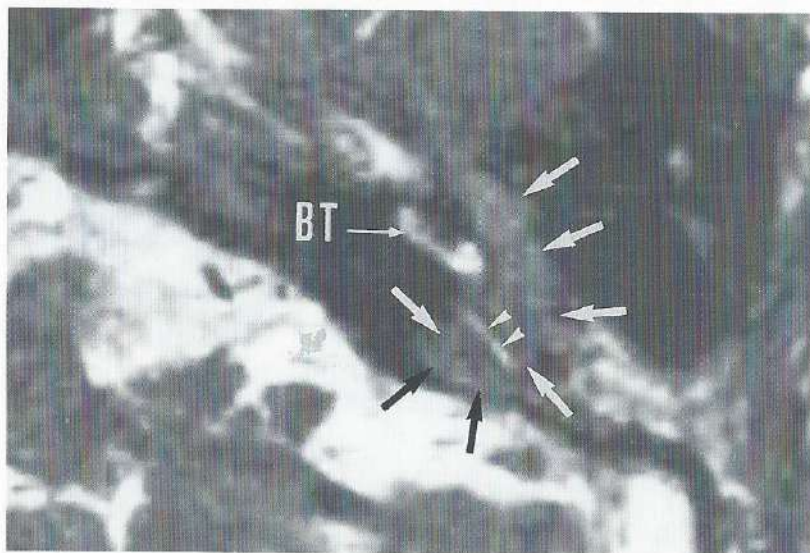
A



B

**Fig. 9.** Recurrent glomus jugulare tumour in 41-year-old woman (case 7). Axial CISS image through the left inner ear.

The tumour is seen in the middle ear cavity and in the inner ear with destruction of bone around the posterior semicircular canal (large arrows). This CISS image indicates that the membranous labyrinth is still intact and shows the high signal of the endolymph inside the posterior semicircular canal (white arrowheads). CT remains, of course, the first study to evaluate bone destruction, but CISS images can detect more reliably obliteration of the endo- and perilymph spaces (also uncalcified obliteration) and, at the same time, allow good evaluation of bone destruction. BT, basal turn of cochlea.

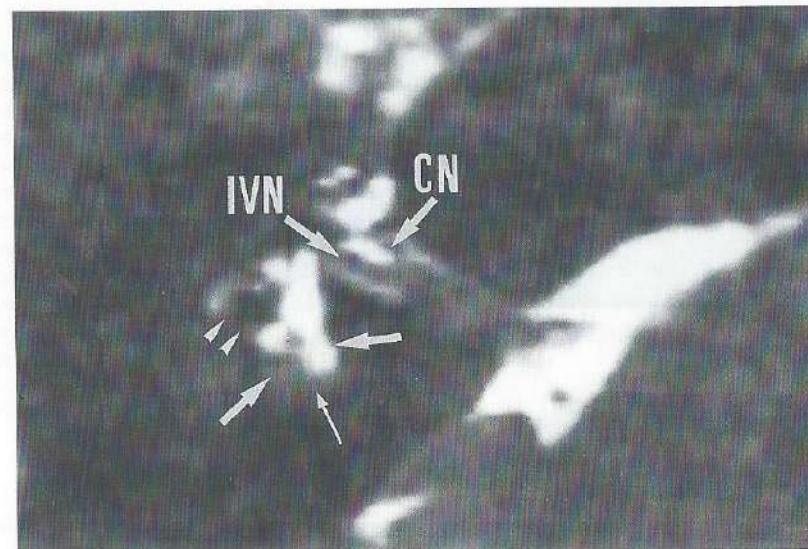


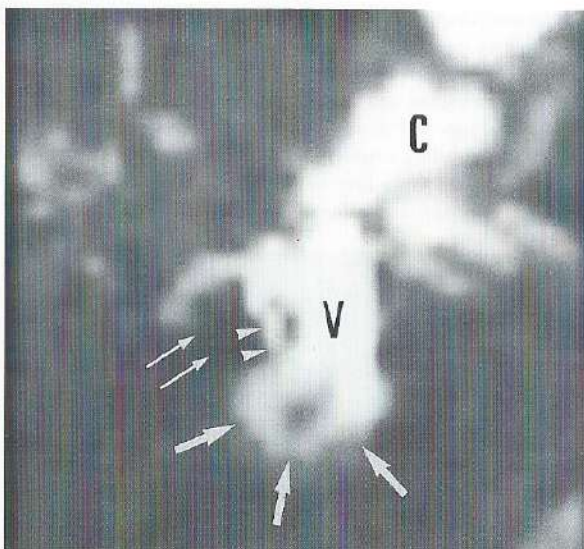
between soft-tissue lesions and surrounding bone can leave the lesions invisible on CISS images. This is certainly the case in parts of the inner ear where no or little CSF or intralabyrinthine fluid is present, as around the segments of the facial nerve located in the facial canal (cases 4 and 8).

In conclusion, the CISS sequence scheme allows reliable imaging of the labyrinth structures and the nerves inside the CPA and IAC. Localisation of the vascular loop in relation to the CPA, porus, or IAC is also promising. Additional information can be achieved when pathologic inner ears are studied with the CISS sequence scheme. Therefore, this short sequence was added to our routine inner ear protocol.

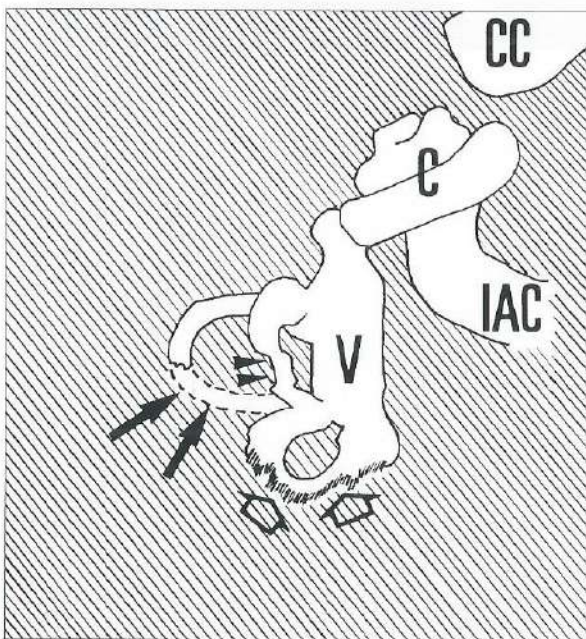
**Fig. 10.** Fifteen-year-old girl with fibrous dysplasia of the right temporal bone (case 9). Axial CISS image (A) and 3-D reconstruction of the right labyrinth (B) and drawing of B (C).

A. Involvement of the labyrinth in case of fibrous dysplasia is very rare. Unsharp delineation of the posterior part of the vestibulum and interruption of normal endolymph spaces in crus communis of posterior and superior semicircular canal (large white arrows), posterior limb of lateral semicircular canal (white arrowheads), and in ampulla and inferior part of the posterior semicircular canal (small white arrow) is seen. The labyrinth involvement was also confirmed on CT images. IVN, inferior vestibular nerve; CN, cochlear nerve.





**B.** On this craniocaudad oriented 3-D reconstruction of the right labyrinth, all three semicircular canals should be visible (see Fig. 4). This image shows definite interruption of the lateral semicircular canal (small white arrows). The posterior delineation of the endolymph in the posterior semicircular canal is irregular (large white arrows) and impression on the superior semicircular canal can be presumed (white arrowheads). Partial visualization of the lateral semicircular canal on Figure 1A could have been produced by an oblique cut through the canal but the 3-D reconstruction proves that this was not the reason and that a real interruption of the canal is present. C, cochlea; V, vestibule.



**C.** The lateral semicircular canal is interrupted (large black arrows), the posterior semicircular canal has an irregular posterior delineation (open black arrows), and an impression is seen on the superior semicircular canal (black arrowheads). The vestibule (V) and cochlea (C) are normal. CC, carotid artery in carotid canal; IAC, internal auditory canal.

## 1.6. ACKNOWLEDGEMENTS

We thank Siemens U B Med-Erlangen for putting to our disposal the work-in-progress version of CISS and we also thank Greta Vandemaele and Bavo Van Riet (MR-application, Siemens, Brussels) for adapting the CISS sequence to the needs of this study and for the information they provided concerning the CISS sequence scheme.

## 1.7. REFERENCES

1. Tanioka H, Shirakawa T, Machida T, Sasaki Y. Three dimensional reconstructed MR imaging of the inner ear. *Radiology* 1991; 178:141-144.
2. Brogan M, Chakeres DW, Schmalbrock P. High-resolution 3DFT MR imaging of the endolymphatic duct and soft tissues of the otic capsule. *AJNR* 1991; 12:1-11.
3. Tanioka H, Machida T, Zusho H. High resolution MRI of the temporal bone using a surface coil: normal anatomy. *Jpn J Med Imaging* 1989; 8:2-8.
4. Enzmann D, O'Donohue J. Optimizing MR imaging for detecting small tumors in the cerebellopontine angle and internal auditory canal. *AJNR* 1987; 8:99-106.
5. Deimling M, Laub GA. Constructive interference in steady state for motion sensitivity reduction (abstr). In: Book of abstracts: Society of Magnetic Resonance in Medicine 1989. Vol 1. Berkeley, CA: Society of Magnetic Resonance in Medicine, 1989:842.
6. Gyngel ML, Palmer ND, Eastwood LM. The application of steady state free precession (SSFP) in 2DFT MR imaging (abstr). In: Book of abstracts: Society of Magnetic Resonance in Medicine 1986. Vol 3. Berkeley, CA: Society of Magnetic Resonance in Medicine 1986:666.
7. Oppelt A, Graumann R, Barfuss H, Fischer H, Hartl W, Schajor W. FISP, a new fast MRI sequence. *Electromedica* 1986; 54:15-18.
8. Patz S. Some factors that influence the steady state in "steady state" free precession. *Magn Reson Imaging* 1988; 6:405-413.
9. Laub GA, Kaiser WA. MR angiography with gradient motion refocusing. *J Comput Assist Tomogr* 1988; 12:377-382.
10. Valvassori GE, Morales FG, Palacios E, Dobben GE. MR of the normal and abnormal internal auditory canal. *AJNR* 1988; 9:115-119.
11. Daniels DL, Haughton VM. The temporal bone. In: Daniels DL, Haughton VM, Naidich TP, eds. *Cranial and spinal magnetic resonance imaging: an atlas and guide*. New York: Raven, 1987:197-234.
12. Bergeron RT, Lo WW, Swartz JD, Hasso AN, Liu D, Broadwell RE. The temporal bone. In: Som PM, Bergeron RT, eds. *Head and neck imaging*. 2nd ed. St. Louis: Mosby, 1991:925-1115.
13. Mazzoni A. Internal auditory canal: arterial relations at the porus acusticus. *Ann Otol* 1969; 78:797-814.
14. Esfahani F, Dolan K. Air CT cisternography in the diagnosis of vascular loop causing vestibular nerve dysfunction. *AJNR* 1989; 10:1045-1049.
15. Seltzer S, Mark AS. Contrast enhancement of the labyrinth on MR scans in patients with sudden hearing loss and vertigo. *AJNR* 1991; 12:13-16.
16. Brogan M, Chakeres DW. Gd-DTPA-enhanced MR imaging of cochlear schwannoma. *AJNR* 1990; 11:407-408.

## 1.8. ADDENDUM I

The anatomic study of the normal inner ear, using the 3DFT-CISS sequence, was enlarged in order to confirm the findings described in the article on "Constructive interference in steady state - 3DFT MR imaging of the inner ear and cerebellopontine angle". Fifty normal inner ears, studied in the axial plane, were added to the 40 axial and 10 coronal inner ear studies of the article. The results are listed in Table I.

These results confirm the reliability of the CISS images to show the different parts of the cochlea, the vestibule, the internal carotid artery, the nerves in the internal auditory canal (IAC) and the different parts of the facial nerve inside the facial canal. However, the visualization of the vestibular aqueduct (56% in first study, now 45%) and canal of the subarcuate artery (58% in first study, now 43%) seems to be less reliable than was thought in the first study with only 50 patients.

The position of the vascular loop in relation to the cerebellopontine angle (CPA), IAC and internal acoustic porus was also studied in these additional 50 patients. The results from the first study (article) were confirmed. The only important change was that the loop was found inside the IAC in a larger number of patients than in the first study, (Table II).

As already mentioned in the article, one of the reasons why the nerves inside the IAC cannot always be separated is that in very narrow IACs the nerves are closer together and less cerebrospinal fluid is present. Therefore it is necessary to use thinner slices if one wants to separate the four nerves inside narrow IACs. An adapted CISS sequence was tested to separate these nerves in narrow IACs and the parameters of this sequence were: TR = 15 msec, TE = 21 msec, matrix size = 256 × 256, field of view = 170 mm, flip angle = 65°, total acquisition time = 2 times 4.03 minutes, and a slab of 22.4 mm (32 partitions) resulting in a slice thickness of 0.7 mm.

The first experience with this sequence is very promising. Very often, the additional thin slice (0.7 mm) 3DFT-CISS sequence is able to separate more nerves inside narrow IACs than the routine (1.0 mm) 3DFT-CISS sequence. However, the acquisition time is twice as long and therefore this sequence is only used when the routine 1.0 mm short 3DFT-CISS sequence is not able to separate the nerves inside narrow IACs.

Finally, the thickness of the four nerves inside the IAC was measured (when they were visualized) on the 3DFT-CISS images of the 50 added normal inner ear studies. The aim was to get a reference thickness of these nerves in order to recognize nerve atrophy or hypoplasia. The results are listed in Table III. Of the 200 nerves (50 inner ears), 186 nerves were visualized and measured.

*Table I: Reliability of CISS images to show inner ear structures.*

	100 Inner Ears 90 in the axial plane/10 in the coronal plane	
	Number visualized axial/coronal	Percentage visualized in 100 patients
<b>Cochlea (basal, second and apical turn)</b>	90/10	100%
<b>Vestibule</b>	90/10	100%
<b>LSC-PSC-SSC</b>	90/10	100%
<b>Internal carotid artery</b>	90/10	100%
<b>Cranial nerve VII</b>	85/9	94%
<b>Cochlear branch of nerve VIII</b>	82/9	91%
<b>Superior vestibular branch of nerve VIII</b>	80/7	87%
<b>Inferior vestibular branch of nerve VIII</b>	80/8	88%
<b>Anterior segment of facial nerve</b>	79/7	86%
<b>Geniculate ganglion</b>	82/5	87%
<b>Horizontal segment of facial nerve</b>	82/8	90%
<b>Posterior genu of facial nerve</b>	66/8	74%
<b>Vertical segment of facial nerve</b>	65/7	72%
<b>Canal of subarcuate artery</b>	43/2	45%
<b>Vestibular aqueduct</b>	43/0	43%

Note: LSC = lateral semicircular canal, PSC = posterior semicircular canal, SSC = superior semicircular canal.

*Table II: Position of arterial structures (vascular loop) in relation to the CPA, IPA and IAC.*

	100 Inner Ears 90 in the axial plane/10 in the coronal plane	
	Number visualized axial/coronal	Percentage visualized in 100 patients
<b>Vessel in CPA</b>	58/6	64%
<b>Vessel near or in IPA</b>	23/3	26%
<b>Vessel in IAC</b>	9/1	10%

Note: CPA = cerebellopontine angle, IPA = internal acoustic porus, IAC = internal auditory canal.

**Table III:** Thickness of the nerves inside the internal auditory canal.

	Minimum thickness (in mm)	Average thickness (in mm)	Maximum thickness (in mm)
Cranial nerve VII (49 nerves)	0.50	0.75	1.00
Cochlear branch of nerve VIII (44)	0.50	0.80	1.30
Inf. vestib. branch of nerve VIII (44)	0.40	0.68	1.00
Sup. vestib. branch of nerve VIII (47)	0.50	0.75	1.20

These results tell us that there is nearly no difference in thickness between the cochlear nerve and the other three nerves inside the IAC on 3DFT-CISS images. This is, of course, impossible; all surgeons and anatomy books state that the cochlear nerve is nearly twice as thick as the other nerves. The explanation is probably that we are looking at very thin structures (0.5 mm to 1.3 mm) using an MR technique with a slice thickness still of 1 mm and a spatial resolution still of  $0.69 \times 0.69$  mm. Thinner slices and higher spatial resolution are needed to achieve more accurate and reliable measurements.

However, only the cochlear nerve has a much smaller diameter on the 3DFT-CISS images than in reality, the other nerves have a more acceptable diameter on MR. Therefore the small diameter of the cochlear nerve on MR cannot be explained by the insufficient spatial resolution and too thick slices of the 3DFT-CISS technique alone. Another possible explanation is that the Schwann cell sheath is not visible on MR. Fat, for example near the stylomastoid foramen, has the same signal as fluid on the 3DFT-CISS images. As a result the fat containing Schwann cells can probably not be distinguished from the cerebrospinal fluid in the IAC and this could explain why nerves, and especially those with a thick layer of Schwann cells, appear thinner on the 3DFT-CISS images than they are in reality.

## 1.9. ADDENDUM II

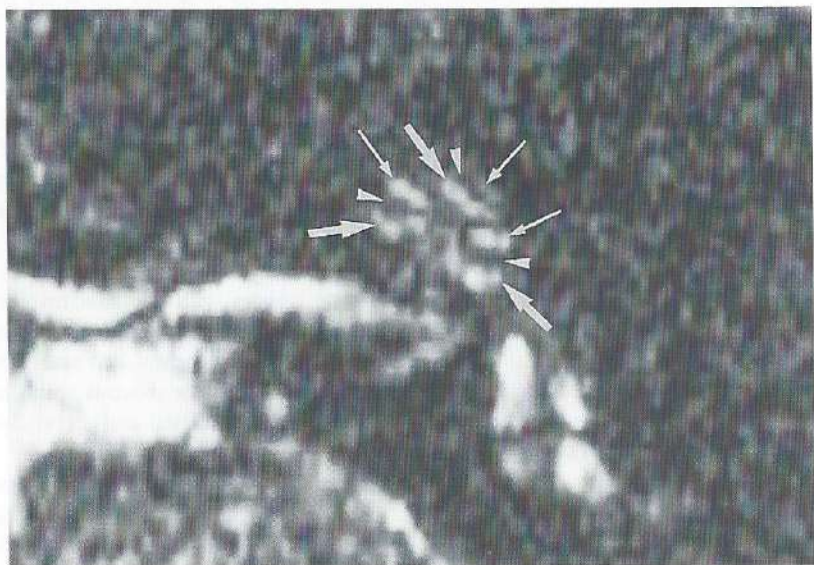
One of the limitations of the 3DFT-CISS sequence so far was that the scala tympani and scala vestibuli could not be distinguished from one another. Thinner slices and higher resolution were probably necessary to visualize these two compartments of the perilymphatic space separately.

In order to achieve thinner slices and higher spatial resolution, Dr. M. Deimling (Medical Engineering Group Siemens A.G., Erlangen, Germany) provided us with 3DFT-CISS sequences that allowed us to make 0.7 mm thick slices (see addendum 1) and images with a resolution down to  $0.34 \times 0.34$  mm. High spatial resolution can be obtained by using a routine  $256 \times 256$  matrix but with a very small field of view (FOV) or by using a larger  $512 \times 512$  matrix with a somewhat larger FOV. The best results were achieved with a  $410 \times 512$  matrix using a FOV of 160 mm and providing images with a spatial resolution of  $0.31 \times 0.39$  mm (Fig. 1). These images can be made in 2 times 3.15 minutes, using the standard circular polarized head coil. On these images the scala tympani and scala vestibuli can be distinguished, but the cochlear duct, Reisner's membrane, the osseous spiral lamina, the basilar membrane and the organ of Corti can not be distinguished and are visible as a low signal line between both compartments.

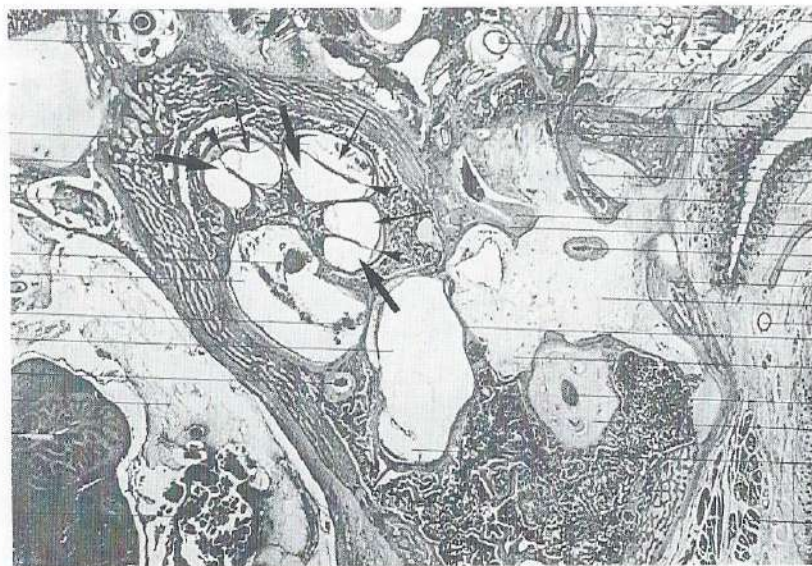
The clinical consequences of the radiological visualization of the scala tympani and scala vestibuli are not yet established. However, in patients requiring a cochlear implant, a patent scala tympani or vestibuli can suffice to allow implant installation. In these cases, obliteration inside the cochlea seen on a routine 3DFT-CISS sequence (making cochlear implantation difficult or impossible) can now be checked on high resolution 3DFT-CISS images which could show that the obliteration is, for instance, restricted to the scala vestibuli while the scala tympani is patent (fit for cochlear implant installation).

Finally it remains impossible to recognize Scarpa's ganglion deep in the IAC on these thin (0.7 mm) high resolution ( $410 \times 512$  matrix) images. But even during an operation it is impossible for the surgeons to recognize this ganglion situated in the trunk of the vestibular nerve. Therefore the very small size of this ganglion (hardly separable from the vestibular nerve) rather than an insufficient MR technique explains why this structure cannot be visualized on the MR images.

Fig. 1.



A



B

**Fig. 1.** Axial high resolution 3DFT-CISS image (A) and corresponding histological section (B) through the left cochlea showing high signal intensity perilymph (white) in the scala vestibuli (long arrows) and scala tympani (large arrows) separately. The black line between these two compartments of the perilymphatic space represents the cochlear duct, Reissner's membrane, the osseous spiral lamina, the basilar membrane and the organ of Corti (arrowheads). The parameters of the 3DFT-CISS sequence were: TR = 24 msec, TE = 11 msec, matrix size = 410 × 512, Field of view = 160, flip angle = 50°, acquisitions = 1, total acquisition time = 2 × 3.15 minutes and a slice thickness of 1 mm (slab = 32 mm). A standard head coil was used and both inner ears were imaged simultaneously.

## 2. Pathology of the Membranous Labyrinth: Comparison of T1- and T2-Weighted and Gadolinium-Enhanced Spin-Echo and 3DFT-CISS Imaging

Jan W. Casselman<sup>(1)</sup>, Rudolf Kuhweide<sup>(2)</sup>, Willy Ampe<sup>(2)</sup>,  
Ludo Meeus<sup>(1)</sup>, and Luc Steyaert<sup>(1)</sup>

From the departments of Radiology<sup>(1)</sup>, and Otorhinolaryngology<sup>(2)</sup>,  
A.Z. St.-Jan Brugge, Brugge, Belgium.

*Published in: Am J Neuroradiol 1993; 14:59-69.*

### 2.1. ABSTRACT

**Purpose:** To assess the value of unenhanced T1-weighted images, T2-weighted images, gadolinium-enhanced T1-weighted images, and three-dimensional Fourier transformation-constructive interference in steady state (3DFT-CISS) images in depicting lesions of the membranous labyrinth.

**Methods:** Six patients were studied using 1-T MR; both enhanced (gadolinium-tetraazacyclododecane tetraacetic acid) and unenhanced images were obtained and different sequences compared to determine which provided the most information.

**Results:** A combination of gadolinium-enhanced T1-weighted and 3DFT-CISS images could depict all membranous labyrinth pathology. Unenhanced T1-weighted images were necessary to exclude spontaneous hyperintensity in the membranous labyrinth. Gadolinium-enhanced T1-weighted images were needed to detect enhancing pathology such as labyrinthitis and tumours inside the membranous labyrinth. In these cases, 3DFT-CISS images allowed immediate differentiation between inflammation and tumour. In temporal bone tumours involving the bony and membranous labyrinth, unenhanced and enhanced T1-weighted images often sufficed to suggest the correct diagnosis. Only 3DFT-CISS images were able to demonstrate small structures (as fistulas) and to help us confirm or rule out obliteration of the labyrinthine fluid spaces. 3DFT-CISS images were necessary to detect small congenital malformations of the membranous labyrinth when only MR was performed. Uncalcified obliteration of the labyrinth fluid spaces could be reliably detected only on 3DFT-CISS images. Here also gadolinium-enhanced T1-weighted images had to be obtained because enhancement of the soft tissues inside the membranous labyrinth had been observed.

**Conclusion:** The CISS sequence and enhanced T1-weighted sequence formed the best sequence combination for diagnosis of membranous labyrinth lesions; additional, unen-

hanced T1-weighted images can help one differentiate labyrinthitis, proteinaceous fluid, subacute haemorrhage, or tumor inside the labyrinth.

Index terms: Temporal bone, magnetic resonance; Contrast media, paramagnetic; Magnetic resonance, technique.

## 2.2. INTRODUCTION

Initially, the radiologic study of the temporal bony labyrinth was restricted to conventional radiographic studies, later improved with polytomographic techniques. With the advent of computed tomography (CT), it became possible to detect soft-tissue lesions in the cerebellopontine angle and internal acoustic canal (IAC) and more detailed study of the bony labyrinth became possible. Recently magnetic resonance (MR) emerged as an excellent diagnostic method in the diagnosis of membranous labyrinth lesions. First only routine T1- and T2-weighted spin-echo sequences were used, showing normal anatomy, congenital lesions, and relatively large tumours of the membranous labyrinth (1). The application of gadolinium (Gd) was a major step forward and diagnosis of small intralabyrinthine tumours (schwannomas, extension of metastases along cranial nerves) and inflammatory lesions (labyrinthitis) became possible (2, 3). Finally, three-dimensional Fourier transform (3DFT) imaging made detailed anatomic studies (4, 5) of the membranous labyrinth possible and also had the potential to add new information to a routine spin-echo study of the pathologic membranous labyrinth (5, 6). The possibility of making multiplanar and 3-D reconstructions from a 3DFT data set certainly facilitated labyrinth examination (5, 6).

Six patients presenting with sensorineural hearing loss (SNHL) or vestibular dysfunction and who eventually had membranous labyrinth lesions were selected from a group of patients presenting with the same symptoms. All in the group were screened for acoustic schwannomas with unenhanced and enhanced T1-weighted images, T2-weighted images, and 3DFT-constructive interference in steady state (CISS) images. In the six patients selected, the different sequences were compared to find out which single sequence or pair of sequences provided optimal information.

## 2.3. SUBJECTS AND METHODS

Six patients (average age, 24 years; three women and three men) presenting with SNHL or vestibular dysfunction and who eventually had a membranous labyrinth lesion were studied. Clinical examination included audiometry and electronystagmographic vestibular examination (including both caloric and rotational chair tests). Patients with SNHL or vestibular dysfunction and a lesion only present in the IAC or patients with lesions along the facial nerve were excluded from the study. Pathology included labyrinthitis, intravestibular schwannoma, cholesterol granuloma with fistula towards the labyrinth, fibrous dysplasia with labyrinth involvement, large vestibular aqueduct syndrome, and Cogan syndrome.

All patients underwent MR on a 1.0-T superconductive active shielded magnet including 3-mm contiguous axial unenhanced and Gd-tetra-azacyclododecane tetraacetic acid-enhanced (Dotarem, Guerbet Laboratories, Aulnay-sous-Bois, France) T1-weighted 2-D spin-echo images, 500/15/4 (TR/TE/excitations), 4-mm axial T2-weighted 2-D spin-echo

images, 2500/15, 90/1 with a 0.8-mm gap, and 1-mm contiguous axial 3DFT-CISS images. The total acquisition time was 8 minutes 32 seconds for the T1- and 10 minutes 40 seconds for the T2-weighted images. All images were obtained using a circular polarized head coil. In each patient, the value of T1-, T2-, and Gd-enhanced T1-weighted images and CISS images were evaluated.

The following scoring system was applied: (-) = pathology not detected with this sequence or sequence pair alone, (+) = diagnosis possible, additional information provided by other sequences required, (++) = complete diagnosis can be made with this sequence or sequence pair alone. In each case the sequence or sequence pair providing the most adequate information was indicated by "\*".

The CISS sequence scheme, providing the CISS images, is a 3DFT sequence scheme using the steady-state free precession of spins (Deimling M et al, paper presented at the annual meeting of the Society for Magnetic Resonance in Medicine, Amsterdam, August 1989). In this sequence scheme a "true" fast imaging with steady precession (FISP) sequence is run once with alternating and once with non-alternating radiofrequency pulses. This sequence scheme was already described in more detail (see companion article) (5). In the CISS sequence scheme, flow compensation techniques are used to make sure that spins, independent of their actual velocity, are being refocused. The flow compensation is applied to each gradient over each repetition time (TR) cycle, unlike standard flow compensation sequences (eg, motion refocusing angiography sequences) in which the flow compensation is applied to the echo. All three gradients are balanced, indicating that the average value of each gradient is zero. In this case, spins moving at a constant velocity will have the same phase after the application of the gradient pulses that they had before (7), resulting in high signal of all cerebrospinal fluid and labyrinthine fluid (endolymph/perilymph) spaces.

Such a steady-state flow-compensated 3D-FISP sequence with symmetrical gradients will produce images that show bands of low signal intensity. These dark bands are caused by small magnetic field inhomogeneities and local field distortions due to susceptibility changes that are normally produced by the patient. The solution to this problem is to acquire two data sets successively with a true FISP sequence of alternating and nonalternating radiofrequency pulses (5). A mathematical postprocessing operation (maximum intensity projection (MIP)) takes the information of each pair of images of the two 3-D data sets created in this way to produce an image with a homogeneous intensity distribution over the whole image. Used parameters are 1 slab of 32-mm thickness, 32 partitions, TR = 20 msec, echo time (TE) = 8 msec, matrix = 256 × 256, field of view = 176 mm; the result is 1-mm sections with an in-plane resolution of 0.69 × 0.69 mm and a total acquisition time of 2 times 2 minutes 46 seconds. In four patients (cases 2, 4, 5, and 6) 3-D reconstructions of the membranous labyrinth were made by applying a targeted MIP on the 3DFT-CISS images.

## 2.4. RESULTS

All clinical and MR findings are presented in Table I. The diagnostic value of all single sequences and sequence pairs are evaluated in Table II. Clinical audiologic and vestibular signs correlated well with the anatomical localization and side where the pathology was found in all cases.

**Table I:** Clinical and MR data on patients with membranous labyrinth pathology

Case	Age/ Sex	Diagnosis/ Affected Side	Clinical Presentation (Audiologic/Vestibular)	MR Findings		
				T1/T2	T1-Gd	CISS
1	46/M	Labyrinthitis/R	Sudden deafness/vestibular areflexia	Normal	Enhancement of C, V, ampullae of LSC, PSC and SSC	Normal
2	17/F	Schwannoma in vestibulum/L	SNHL/spontaneous nystagmus to the right, pathologic rotational and caloric tests	2-mm isointensity <sup>a</sup> lesion in V/signal loss in V	Enhancement in V and ampulla of PSC	Filling defect in V
3	46/F	Cholesterol granuloma fistula to PSC/L	SNHL in the low-frequency range/vestibular areflexia	High-intensity <sup>a</sup> lesion posterior of porus and in V	Same findings, no enhancement	Visualization of fistula
4	15/F	Fibrous dysplasia with labyrinth involvement/R	Slight SNHL in the low frequency range/vestibular areflexia	Hypointense <sup>a</sup> abnormal bone and LSC, PSC, SSC destruction + EAC narrowing/hypointense <sup>a</sup> bone	Weak enhancement of bone, destruction LSC, PSC, SSC	Obliteration of semicircular canals
5	14/M	Large vestibular aqueduct syndrome/R	Progressive SNHL, mainly in the high-frequency range	Enlarged VA	Enlarged VA	Enlarged VA
6	22/M	Cogan syndrome	Bilateral subtotal SNHL/bilateral vestibular areflexia interstitial keratitis	Normal	Normal	Narrowing of PSC and SSC

Note: Abbreviations: C = cochlea, EAC = external auditory canal, LSC = lateral semicircular canal, PSC = posterior semicircular canal, SSC = superior semicircular canal, V = vestibulum, VA = vestibular aqueduct, SNHL = sensorineural hearing loss.

<sup>a</sup> Hyper-, iso- or hypointense compared to brain tissue.

On T1- and T2-weighted images, a complete diagnosis was possible in three and two cases, respectively. Gd-enhanced T1-weighted images detected pathology in five cases, but additional information provided by other sequences was necessary to make the exact diagnosis in three cases. When a combination of unenhanced and Gd-enhanced T1-weighted images was used, then pathology was detected in five cases and an exact diagnosis was possible in four of the six cases. In one case (case 3), the final diagnosis was made when both unenhanced T1- and T2-weighted images were used. The CISS sequence provided important additional information in four cases, also resulting in the best single

**Table II:** Value of different sequences in patients with membranous labyrinth pathology

Case	Diagnosis	T1	T2	T1-Gd	CISS	T1 + T2	T1 + T1-Gd	T1 + CISS	T2 + T1-Gd	T2 + CISS	T1-Gd + CISS
1	Labyrinthitis	-	-	+	-	-	++*	-	+	-	+
2	Utriculosaccular schwannoma	++	-	+	+	++	++*	++	+	+	++
3	Cholesterol granuloma with fistula to PSC	+	+	+	+	++*	+	+	+	+	+
4	Fibrous dysplasia with labyrinth destruction	++	++	++	+	++	++	++	++	++	++*
5	Large vestibular aqueduct syndrome	++	++	++	++*	++	++	++	++	++	++
6	Cogan syndrome	-	-	-	+	-	-	+	-	+	+

Note: (-) = diagnosis not possible with this single sequence or pair of sequences; (+) = pathology was recognized, additional information provided by other sequences required to make exact diagnosis; (++) = diagnosis can be made with this single sequence or pair of sequences alone; (\*) = optimal single sequence or pair of sequences in this case; PSC = posterior semicircular canal.

sequence in cases 5 and 6 and best sequence pair in case 4. A combination of CISS images and Gd-enhanced T1-weighted images was necessary to detect the pathology in all cases and also made an exact diagnosis possible in three of the six cases.

## 2.5. DISCUSSION

More lesions of the labyrinth are being diagnosed since the introduction of MR, especially with Gd-enhanced and 3DFT imaging techniques (2-6). A good choice of sequences is necessary to detect the lesion and make the correct diagnosis. These sequences should also be used when one is screening for acoustic schwannomas. An acoustic schwannoma is often difficult to differentiate from a labyrinthine lesion on a clinical basis (3); therefore, screening sequences must be selected so that a maximum of labyrinthine lesions can be detected in case no IAC or cerebellopontine angle schwannomas are found. Our study shows that the Gd-enhanced T1-weighted sequence is very sensitive; however, uncalcified obliteration of the intralabyrinthine fluid spaces is recognized only on CISS images. The value of the different sequences depends on the pathology one is dealing with. In our study, the combination of a Gd-enhanced T1-weighted sequence and a CISS sequence scheme resulted in the highest sensitivity (Table II).

### 2.5.1. Pathology Causing Contrast Enhancement Inside the Membranous Labyrinth

Localised enhancement in the labyrinth in cases of inflammation (case 1) (Fig. 1) and of tumours (case 2) (Fig. 2) has been described (2, 3, 8). It is caused by breakdown of the blood-brain/labyrinth barrier (9, 10) and explains the high sensitivity of the Gd-enhanced T1-weighted sequence. In case of inflammation (viral and luetic labyrinthitis), Gd accumulation in the affected membranous labyrinth and its endolymphatic content probably causes the enhancement. In these cases, often more than one part (cochlea-vestibule-semicircular canals) of the labyrinth enhances and the edges of the enhancement are not sharp (Fig. 1). These signs can be used in the differential diagnosis between inflammatory and tumoural enhancement of the membranous labyrinth. When a tumour is present inside the membranous labyrinth, the contrast enhancement is more likely restricted to one part of the membranous labyrinth and the edges of the enhancing lesion are sharp (Fig. 2B), although it can still be difficult to differentiate between inflammation and tumour even when both clinical information and the Gd-enhancement pattern are known. In these cases, follow-up studies have been used to make differentiation possible. In case of labyrinthitis, the enhancement disappears after some months, while in case of tumour the enhancement persists. Immediate differentiation is now possible when 3DFT-CISS images are available. In case of labyrinthitis, Gd accumulation inside the membranous labyrinth will not be recognized on the CISS images and normal labyrinthine fluid spaces will be seen. But

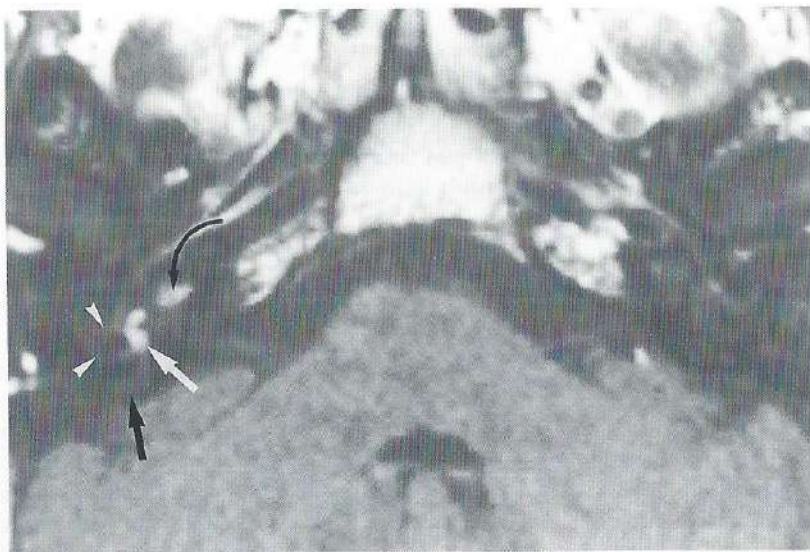
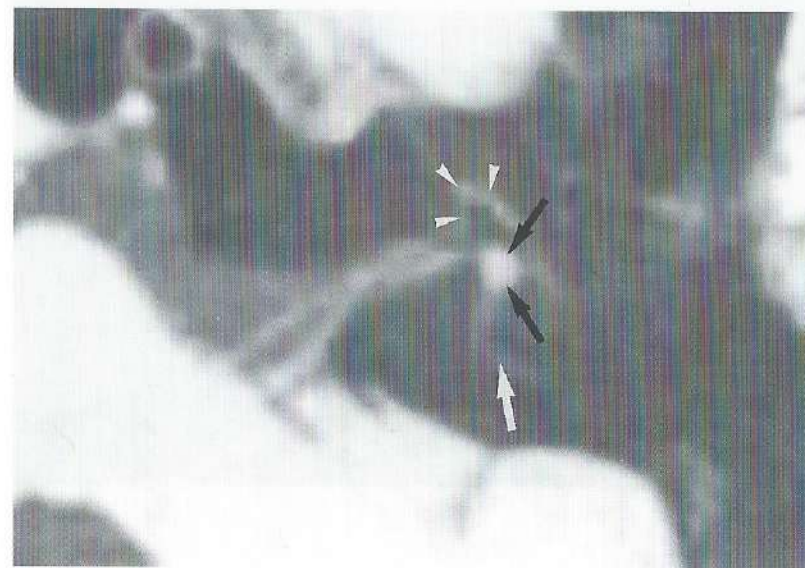


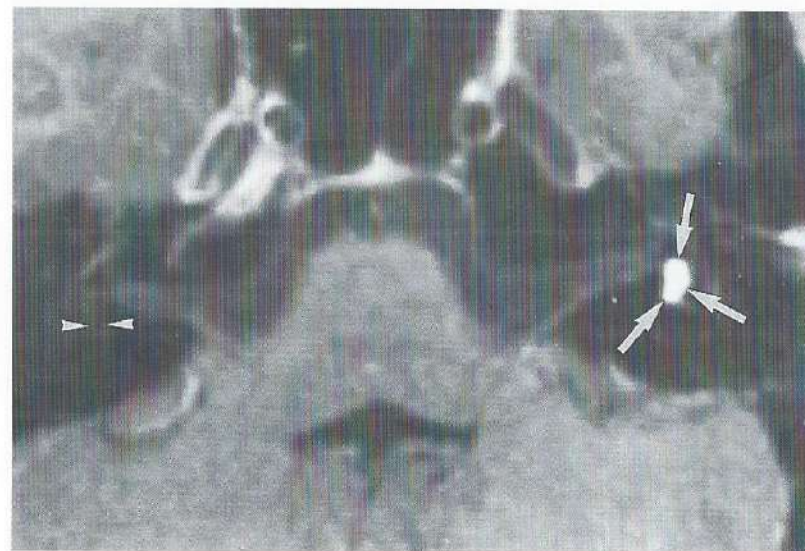
**Fig. 1.** Presumed viral labyrinthitis (case 1). Axial Gd-enhanced T1-weighted image (500/15/4) through both inner ears.

Marked enhancement is seen in the right cochlea (curved black arrow), utriculosaccular structures (large white arrow), posterior (large black arrow), and lateral semicircular canal (white arrowheads). Normal intensities are seen in the left cochlea and labyrinth.

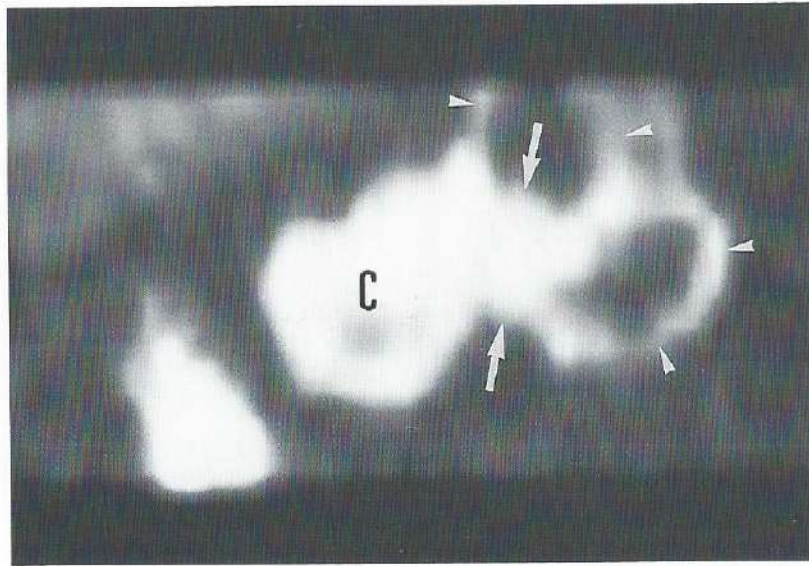
**Fig. 2.** Utriculosaccular schwannoma.



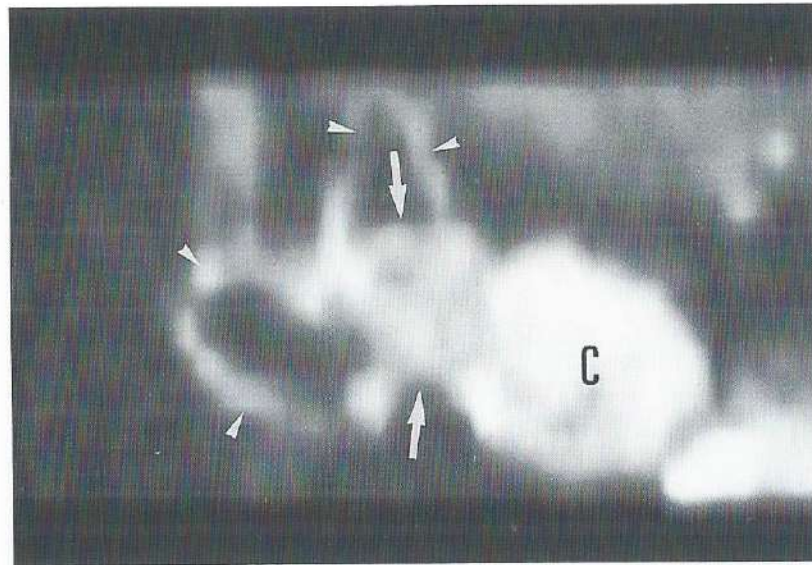
A



B



C



D

**A.** Axial unenhanced T1-weighted image (500/15/4) through the left membranous labyrinth. Appropriate windowing makes a small lesion in the utriculosaccular structures visible as a 1.5-mm hyperintense lesion (large black arrows). Posterior semicircular canal (large white arrow), anterior segment, geniculate ganglion, and horizontal segment of the facial nerve (white arrowheads).

**B.** Gd-enhanced axial T1-weighted image (500/15/4) through both inner ears. Marked enhancement is seen throughout the left utriculosaccular structures in a larger area than could be expected on the unenhanced images (large white arrows). Compare with the normal low signal in these structures on the right (white arrowheads).

**C-D.** 3-D MIP reconstructions (from CISS images) of the right (C) and left (D) cochlea and labyrinth. Normal high signal intensity in cochlea (C), utriculosaccular structures (large white arrows), and semicircular canals (white arrowheads) on the right (C). On the left side (D) the endolymph is replaced by a tumour mass inside the utriculosaccular structures, resulting in lower signal (large white arrows). Semicircular canals (white arrowheads), cochlea (C).

when a tumour is present, the tumour mass will replace the endolymph and loss of high signal can be seen (Fig. 2). It can, however, be difficult to decide whether one is dealing with a lesion or a volume-averaging artifact when such a signal loss is seen on a 1-mm axial section. In these cases, the 3-D labyrinth reconstructions play an important role. Volume-averaging artifacts can be excluded when 3-D membranous labyrinth reconstructions are made (Figs. 2C-2D) and pathology is more easily recognized when the 3-D reconstructions of both sides are compared.

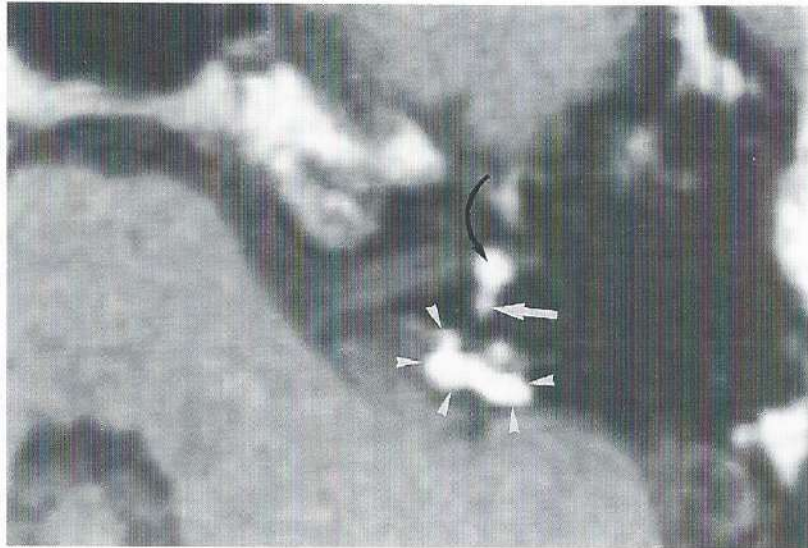
Spontaneous high signal inside the labyrinth on T1-weighted images is theoretically possible in case of subacute haemorrhage in the labyrinth and when a high protein level is present inside the fluid spaces (elevated protein in perilymphatic fluid has been reported in patients with acoustic schwannomas). Therefore, it is necessary to start the study with an unenhanced T1-weighted sequence in order to differentiate enhancement from spontaneous hyperintensity. The value of CT in case of labyrinthitis and intralabyrinthine tumours is limited; in cases 1 and 2, the pathology was not recognized on CT. CT can detect only the end stage of labyrinthitis: "labyrinthine ossification".

In conclusion, unenhanced and enhanced T1-weighted images in combination with CISS images are able to show the above-mentioned pathology and lead to the correct diagnosis. T2 and CISS images alone cannot be used as screening sequences because they do not show labyrinth inflammation.

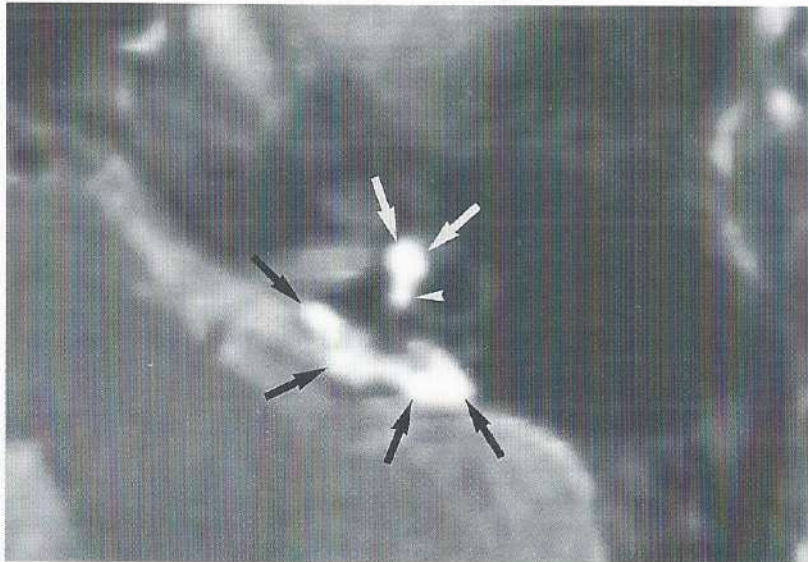
### 2.5.2. Temporal Bone Tumours Involving the Bony and Membranous Labyrinth

Benign and malignant tumoural lesions can cause destruction of the bony labyrinth and can also obliterate the labyrinthine fluid spaces (cases 3 and 4). Unenhanced and Gd-enhanced T1-weighted images and T2-weighted images all contribute to the tissue characterization of the lesions. T2-weighted images, however, are not always necessary. In case 3 (surgically confirmed cholesterol granuloma), the T2-weighted images allowed further differentiation between a cholesterol granuloma and a congenital cholesteatoma. Both can present as a spontaneous high-signal lesion on T1-weighted images (Fig. 3A). In the first

**Fig. 3.** Temporal bone cholesterol granuloma posterior to the IAC. Axial images at the level of the left IAC and lateral semicircular canal (case 3).



A



B



C

**A.** Unenhanced T1-weighted image (500/15/4). A spontaneous high signal intensity lesion (white arrowheads) is seen in the bone posterior to the IAC but also in the utriculosaccular structures (curved black arrow) and ampulla of the posterior semicircular canal (large white arrow).

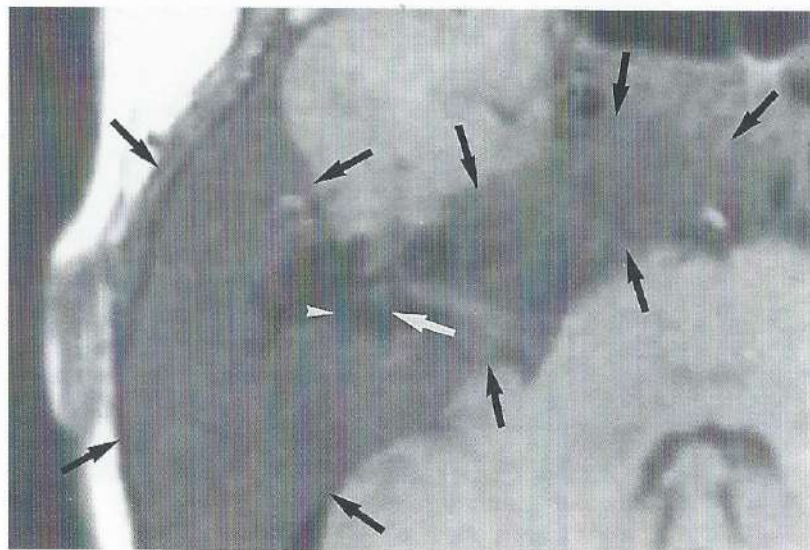
**B.** T2-weighted image (2500/90/1). High signal intensity is still seen in the bone posterior to the IAC (large black arrows) and in the utriculosaccular structures (large white arrows) and ampulla of the posterior semicircular canal (white arrowhead).

**C.** 3DFT-CISS image (20/8/1). The 1-mm CISS image is able to show the fistula (large white arrow) between the lesion in the bone posterior to the IAC (large black arrows) and the posterior semicircular canal (white arrowheads). However, the intensity of the lesion cannot be distinguished from cerebrospinal fluid in the cerebellopontine angle and from the labyrinthine fluid on this CISS image. Ampulla of posterior semicircular canal (curved black arrow).

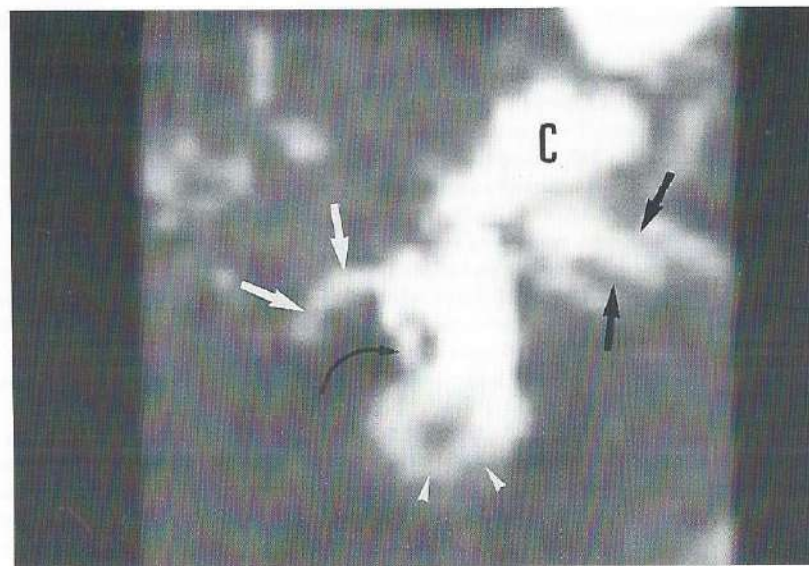
case, the signal remains very high (Fig. 3B), in the latter, slight fading is seen on T2-weighted images (1). But high signal on T1-weighted images in case of congenital cholesteatoma is rare; most often, signal intensities intermediate to the intensities of liquor and brain tissue are described (11). This reduces the value of T2-weighted images in this particular case. In many other lesions, as in the case of fibrous dysplasia (case 4), T1-weighted images without and with Gd administration suffice to make the exact diagnosis and T2-weighted sequences are of limited value.

In contrast, additional important information is often added by 3DFT-CISS images (cases 3 and 4). Thin adjacent sections with high spatial and contrast resolution are needed to detect small lesions, such as fistulas, between tumours and the membranous labyrinth (Fig. 3C). These small lesions or structures can be missed on 3- to 4-mm T1- and

Fig. 4. Fibrous dysplasia with labyrinth involvement (case 4).



A



C



B



D

A. Axial unenhanced T1-weighted image (500/15/4) through the right inner ear. Thickening of the temporal bone and sphenoid bone (large black arrows) is seen. The diffuse bone alteration is hypointense compared to brain tissue and the lateral (white arrowhead) and posterior semicircular canal (large white arrow) seem to be interrupted; however, volume-averaging artifacts (3-mm sections) can make a definite diagnosis impossible.

B. Axial 1-mm 3DFT-CISS image (20/8/1) through the right inner ear. The posterior part of the fluid in the lateral semicircular canal was seen neither on this image nor on the adjacent sections (curved black arrow). The fluid inside the posterior semicircular canal (white arrowheads) was also absent, confirming obliteration of this canal. The borders of the posterior semicircular canal ampulla and of the common crus were irregular and represent partial obliteration of these structures (large white arrows). Cochlear nerve (CN), inferior vestibular nerve (IVN). Normally there is no involvement of the otic capsule and labyrinth structures in case of temporal bone fibrous dysplasia (12, 13). Here, involvement of the labyrinth was proven by CT and MR and the diagnosis of fibrous dysplasia was confirmed by biopsy.

C. 3-D reconstructions of the right labyrinth made by applying a targeted MIP on the 3DFT-CISS images. Only part of the fluid in the lateral (large white arrows) and posterior (white arrowheads) semicircular canal was seen, proving that there is obliteration of these structures. An impression on the superior semicircular canal is also demonstrated (curved black arrow). Normally these 3-D reconstructions can always be turned in space so that all three semicircular canals are visible (see also Fig. 4 in chapter V.1.). Cochlea (C), nerves inside the IAC (large black arrows).

Note: For corresponding drawing of this 3-D reconstructions see Figure 10C in chapter V.1. (Casselman et al (5)).

D. Axial CT image through the right labyrinth. Diffuse bone alteration (large black arrows) is present in the temporal bone. Involvement of the posterior part of the lateral semicircular canal (curved black arrow) and bone alterations in the region where the posterior semicircular canal is expected (white arrowheads). CT proves that bone destruction is present but allows no evaluation of the exact amount of labyrinthine fluid that is still present inside the altered bony labyrinth.

T2-weighted images. 3DFT-CISS images are also required to detect obliteration of the labyrinthine fluid spaces. Obliteration is confirmed when the high signal of the labyrinthine fluid is lost. Here again oblique sections through the labyrinth structures and volume-averaging artifacts could give a false impression of obliteration on the axial thin CISS images. On 3-D reconstructions, the three semicircular canals, the cochlea, and the vestibule are always completely visible. Any interruption of these structures on the 3-D reconstructions represents obliteration of the labyrinthine fluid spaces (Figs. 4B and 4C). Consequently the Gd-enhanced T1 and CISS sequence pair turned out to be the best sequence combination in case 4 and allowed detection of the pathology in case 3.

CT was able to make the correct diagnosis in case 4 but obliteration of the fluid spaces inside the posterior and lateral semicircular canal could only be suspected. In case 3, CT allowed detection of the lesion in the bone posterior to the IAC but the exact diagnosis of cholesterol granuloma was not possible without MR. The fistula and extension of the granuloma inside the membranous labyrinth were not recognized on CT. These cases show that in case of temporal bone tumours with involvement of the bony and membranous

labyrinth T1- and T2-weighted MR often surpasses CT in the characterization of the lesion, and that obliteration of the labyrinthine fluid spaces is best demonstrated on 3DFT-CISS images.

### 2.5.3. Congenital Malformations of the Membranous Labyrinth

Patients with congenital malformations of the membranous and bony labyrinth frequently present with SNHL (14). Clinicians cannot always make the distinction between SNHL due to congenital labyrinth malformation and SNHL due to acoustic schwannoma, therefore, many of these patients are initially studied with MR in order to exclude or detect an acoustic schwannoma. However, when the MR technique is not adapted to this problem, small labyrinth malformations (malformations of the lateral semicircular canal, large endolymphatic duct and sac, etc) are more difficult to see (Fig. 5A) and may even remain undetected. With a 3DFT-CISS technique these malformations are easier to detect because a better contrast is achieved between the labyrinthine fluid and the surrounding bony labyrinth, and because more detailed evaluation of the membranous labyrinth is possible with the 1-mm adjacent sections (Fig. 5B). Moreover 3-D reconstructions of the membranous labyrinth can be made when 3DFT-CISS images are used, thus enabling one to evaluate the exact dimensions of the malformed structures in all planes. In case 5, the largest diameter of the enlarged endolymphatic duct and sac (large vestibular aqueduct syndrome) (14-16) are not obvious on the axial CISS image (Fig. 5B) but are visible on the 3-D reconstruction when the rather sagittally orientated endolymphatic sac is turned 30° towards the axial plane (Figs. 5C and 5D). Even in case of enlargement of the endolymphatic duct and sac, additional Gd-enhanced T1-weighted images are mandatory because Gd enhancement has been noticed inside an enlarged endolymphatic sac in patients with Meniere disease (idiopathic hydrops) (Mark AS et al, paper presented at the annual meeting of the American Society of Neuroradiology, Washington, June 1991). These malformations of the inner ear can of course be detected on CT, but, as already mentioned, these patients are often first screened with MR to exclude acoustic schwannomas. Therefore, the routine MR technique should include a 3DFT-CISS sequence to detect small congenital malformations of the labyrinth.

### 2.5.4. Pathology Causing Obliteration of the Labyrinthine Fluid Spaces

CT is able to demonstrate calcified obliteration of the labyrinthine fluid spaces (labyrinthitis ossificans). However, it is probable that calcified obliteration is the end stage of earlier and more frequent uncalcified soft tissue obliteration. This soft-tissue obliteration is not visible on CT, but can be seen on 3DFT-CISS. On these images, the normal high signal of the labyrinthine fluid is replaced by low-signal soft tissues (Fig. 6), which can also be seen when a tumour is present inside the membranous labyrinth (Fig. 2). Again, 1-mm sections are necessary to exclude obliteration of small structures, and 3-D reconstructions are very helpful to exclude volume-averaging artifacts. Moreover, images displaying high contrast between the labyrinthine fluid and surrounding bone are needed. The 3DFT-CISS images offer all these advantages and possibilities and, therefore, often detect obliteration when 3- to 4-mm T2- and unenhanced and Gd-enhanced T1-weighted images and CT are

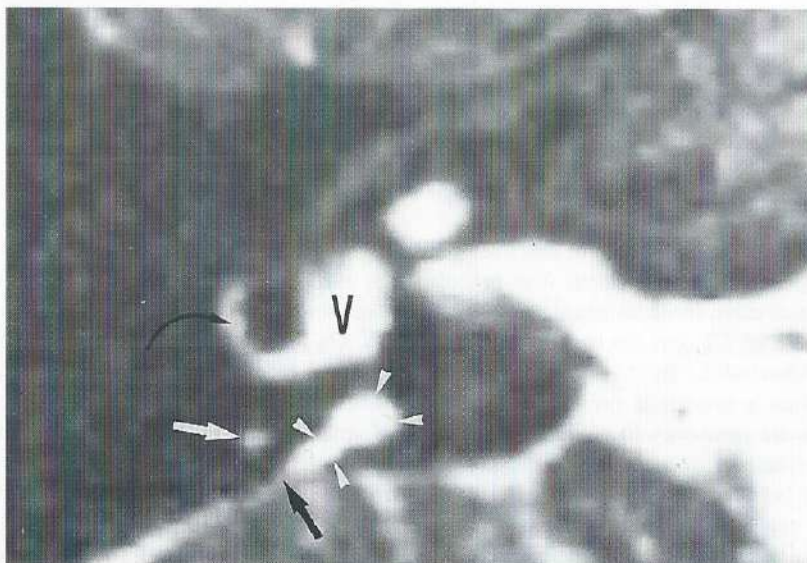
**Fig. 5. Large vestibular aqueduct syndrome (case 5).**

**A.** Axial unenhanced T1-weighted image (500/14/4) at the level of the right lateral semicircular canal. The enlarged endolymphatic sac (large white arrows) can be seen medial of the ascending limb of the posterior semicircular canal (white arrowhead).

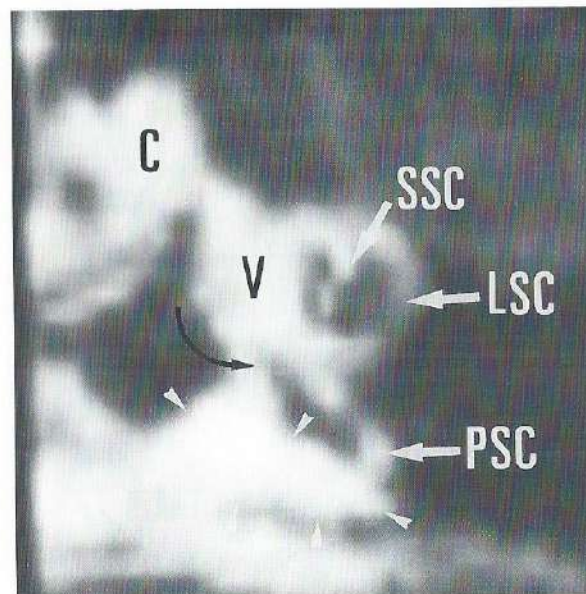
**B.** Axial 1-mm CISS image (20/8/1) at the level of the right lateral semicircular canal. The enlarged vestibular aqueduct (white arrowheads) and its relation to the posterior semicircular canal (large white arrow) is better seen. The endolymphatic sac can also be seen close to the cerebrospinal fluid in the posterior fossa (large black arrow) but no fistula is present. Lateral semicircular canal (curved black arrow), vestibule (V).



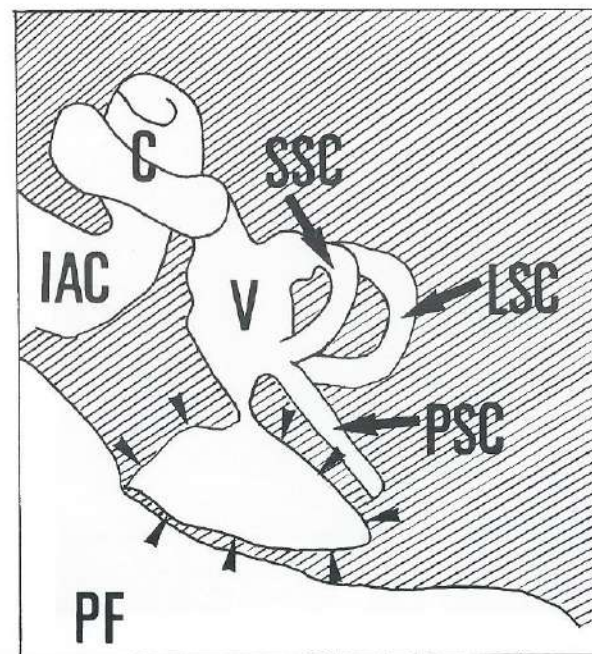
A



B



**C.** 3-D reconstruction of the labyrinth made by applying a targeted MIP on the 3DFT-CISS images. This 3-D reconstruction was rotated so that the normal parasagittal-orientated vestibular aqueduct was turned 30° towards the axial plane. In this projection, the real dimension of the endolymphatic sac can be appreciated and is now seen as a plane (triangle) rather than as the linear structure that was seen on the axial image. The connection (curved black arrow) between the enlarged endolymphatic sac (white arrowheads) and the vestibulum (V) was recognized. Lateral semicircular canal (LSC), posterior semicircular canal (PSC), superior semicircular canal (SSC), and cochlea (C).



**D.** Drawing of the 3-D reconstruction of the labyrinth (C). Only 3-D membranous labyrinth reconstructions allow evaluation of the largest dimensions of the endolymphatic sac (black arrowheads) because these images can be rotated freely in space. Cochlea (C), internal auditory canal (IAC), lateral (LSC), posterior (PSC), and superior semicircular canal (SSC), vestibule (V), posterior fossa (PF).

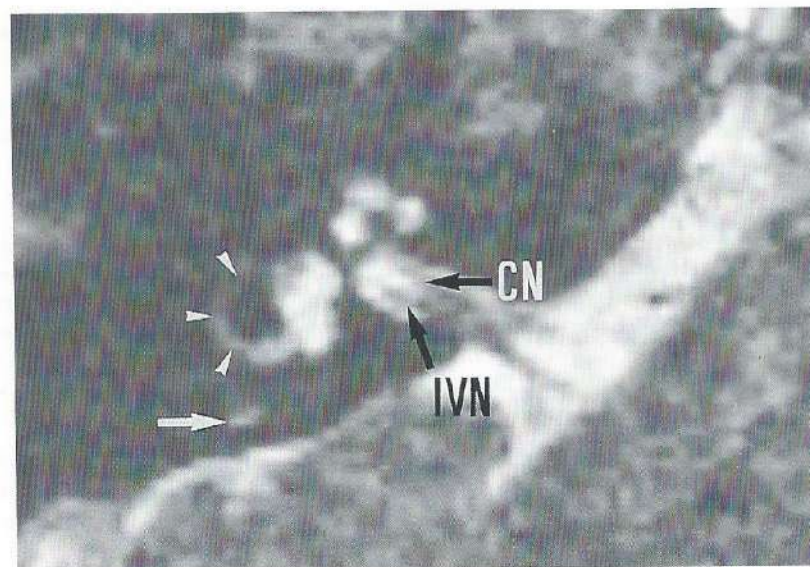
Fig. 6. Patient with Cogan syndrome (case 6). CT was normal; no pathology was seen on T1-, T2-, and Gd-enhanced T1-weighted images.



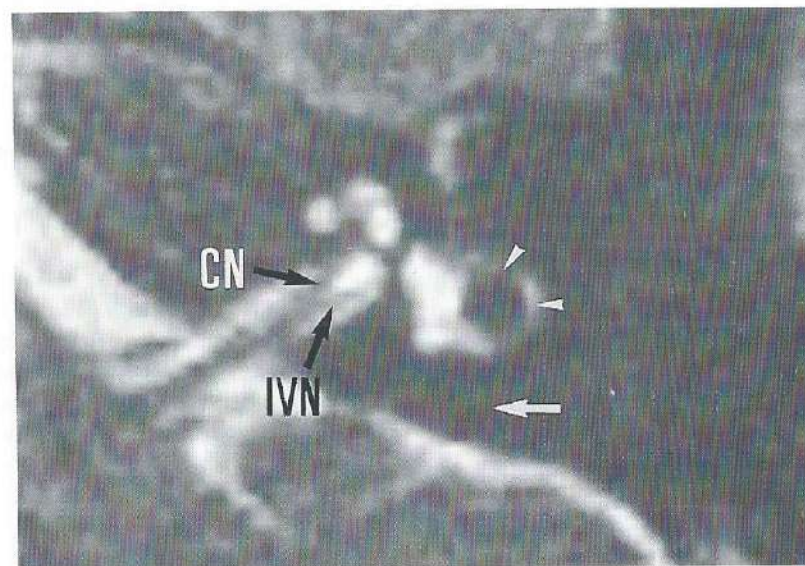
A



B



C



D

*A. Axial CISS image at the level of the right superior semicircular canal. Normal signal intensity and diameter of the anterolateral (large white arrow) and posteromedial (white arrowhead) limb of the superior semicircular canal.*

*B. Axial CISS image at the level of the left superior semicircular canal. Endolymph is seen inside the posteromedial limb (white arrowhead) of the superior semicircular canal, but only very little endolymph can be detected in the anterior limb due to narrowing of the canal (large white arrow).*

*C. Axial CISS image through the right vestibule and cochlea. The endolymph inside the posterior semicircular canal can be seen (large white arrow). Lateral semicircular canal (white arrowheads), cochlear nerve (CN), and inferior vestibular nerve (IVN) (large black arrows).*

*D. Axial CISS image through the left vestibulum and cochlea. The fluid inside the posterior semicircular canal cannot be visualized (large white arrow) representing total or subtotal obliteration of the canal. Lateral semicircular canal (white arrowheads), cochlear nerve (CN), and inferior vestibular nerve (IVN) (large black arrows).*

normal. We have found uncalcified soft-tissue obliteration of the labyrinthine fluid spaces (recognized only on 3DFT-CISS images) in patients with Cogan syndrome, (case 6) and otosclerosis, as well as in cochlear implant candidates who were suffering from postmeningitic deafness.

Gd-enhanced T1-weighted images remain necessary to differentiate between a rare intralabyrinthine tumour (case 2) and inflammatory soft-tissue obliteration. But differentiation can even then remain difficult, as when we recently found Gd enhancement in the obliterating soft tissues in a patient with Cogan syndrome. Cogan syndrome is a rare syndrome, occurring in young adults presenting with nonsyphilitic interstitial keratitis, vestibuloauditory dysfunction, and vasculitis. Thickening of the membranous lining of the labyrinth walls and the presence of connective tissue with a mesenchymatous appearance or acidophilic coagulae inside the labyrinth have been reported (17, 18). Gd enhancement of the membranous labyrinth in these patients probably reflects active disease with inflammation of the blood vessels of the stria vascularis.

### 2.5.5. Conclusion

The CISS sequence and the enhanced T1-weighted MR sequence (3-mm sections) formed the most sensitive sequence pair in the diagnosis of membranous labyrinth lesions. Moreover, they allow excellent screening for acoustic schwannomas and labyrinth lesions, which are difficult to differentiate clinically. An additional unenhanced T1-weighted sequence should be considered in order to differentiate labyrinthitis, proteinaceous fluid, subacute haemorrhage, or tumour inside the labyrinth.

### 2.6. ACKNOWLEDGMENTS

We thank Siemens U B Med.-Erlangen for putting to our disposal the work-in-progress version of the CISS sequence scheme and we also thank Greta Vandemaele and Bavo Van Riet (MR-application, Siemens, Brussels) for adapting the CISS sequence scheme to the needs of this study and for the information they provided concerning this sequence. We also thank Dr J. Clarysse and Dr R. Loncke (Department of Otorhinolaryngology, H. Hart

Hospital Roeselare, Belgium) and Dr M. Majoor (Department of Otorhinolaryngology, Academisch Ziekenhuis, Utrecht, The Netherlands) for referring the patient described in cases 2 and 6, respectively.

### 2.7. REFERENCES

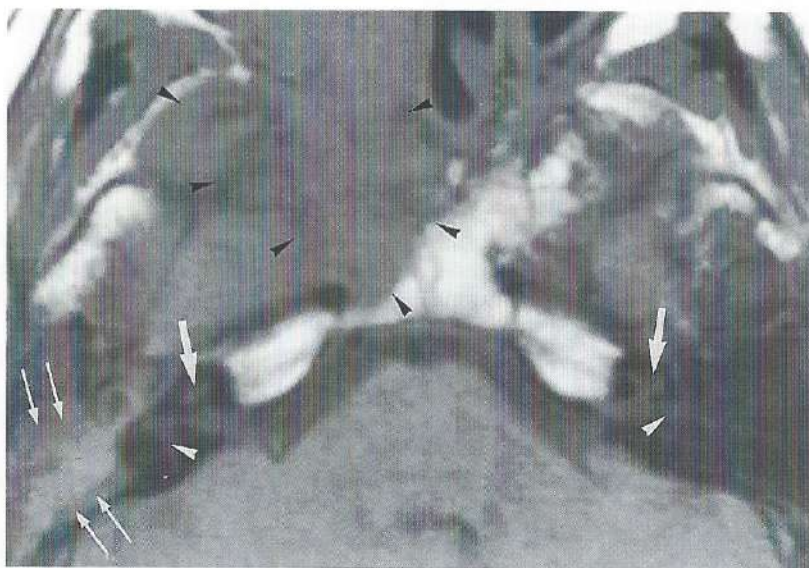
- Holliday RA, Reede DL. MRI of mastoid and middle ear disease. *Rad Clin North Am* 1989; 27:283-299.
- Brogan M, Chakeres DW. Gd-DTPA-enhanced MR imaging of cochlear schwannoma. *AJNR* 1990; 11:407-408.
- Seltzer S, Mark AS. Contrast enhancement of the labyrinth on MR scans in patients with sudden hearing loss and vertigo: evidence of labyrinthine disease. *AJNR*; 12:13-16.
- Brogan M, Chakeres DW, Schmalbrock P. High-resolution 3DFT-MR imaging of the endolymphatic duct and soft tissues of the otic capsule. *AJNR* 1991; 12:1-11.
- Casselmann JW, Kuhweide R, Deimling M, Ampe W, Dehaene I, Meeus L. Constructive interference in steady state (CISS)-3DFT MR imaging of the inner ear and cerebellopontine angle. *AJNR* 1993; 14:47-57.
- Tanioka H, Shirakawa T, Machida T, Sasaki Y. Three dimensional reconstructed MR imaging of the inner ear. *Radiology* 1991; 178:141-144.
- Patz S. Some factors that influence the steady state in "steady state" free precession. *Magn Reson Imaging* 1988; 6:405-413.
- Babin RW, Harker LA. Intralabyrinthine acoustic neurinomas. *Otolaryngol Head Neck Surg* 1980; 88:455-461.
- Matthews VP, Kuharik MA, Edwards MK, D'Amour PG, Azzarelli B, Dreesen RG. Gd-DTPA-enhanced MR imaging of experimental bacterial meningitis: evaluation and comparison with CT. *AJNR* 1988; 9:1045-1050.
- Brant-Zawadzki M, Berry I, Osaki L, et al. Gd-DTPA in clinical MR of the brain. I. Intraaxial lesions. *AJR* 1986; 147:1223-1230.
- Lo WM. Tumors of the temporal bone and the cerebellopontine angle. In: Som PM, Bergeron RT, eds. *Head and neck imaging*. 2nd ed. St. Louis: Mosby, 1991:925-1115.
- Swartz JD. The otodystrophies. In: Swartz JD, ed. *Imaging of the temporal bone*. New York: Thieme, 1986:161-177.
- Swartz JD. Trauma and miscellaneous disorders. In: Som PM, Bergeron RT, eds. *Head and neck imaging*. 2nd ed. St. Louis: Mosby, 1991:1030-1046.
- Mafee MF, Charletta D, Kumar A, Belmont H. Large vestibular aqueduct and congenital sensorineural hearing loss. *AJNR* 1992; 13:805-819.
- Jackler RK, De La Cruz A. The large vestibular aqueduct syndrome. *Laryngoscope* 1989; 99:1238-1242.
- Levenson MJ, Parisier SC, Jacobs M, Edelstein DR. The large vestibular aqueduct syndrome in children. *Arch Otolaryngol Head Neck Surg* 1989; 115:54-58.
- Fisher ER, Hellstrom HR. Cogan's syndrome and systemic vascular disease. *Arch Pathol* 1961; 72:572-592.
- Wolff D, Bernhard WG, Tsutsumi S, Ross IS, Nussbaum HE. The pathology of Cogan's syndrome causing profound deafness. *Ann Otol Rhinol Laryngol* 1965; 74:507-520.

## 2.8. ADDENDUM: POSSIBLE CAUSES OF LABYRINTH ENHANCEMENT - UPDATED OVERVIEW

### 2.8.1. Enhancement in the membranous labyrinth

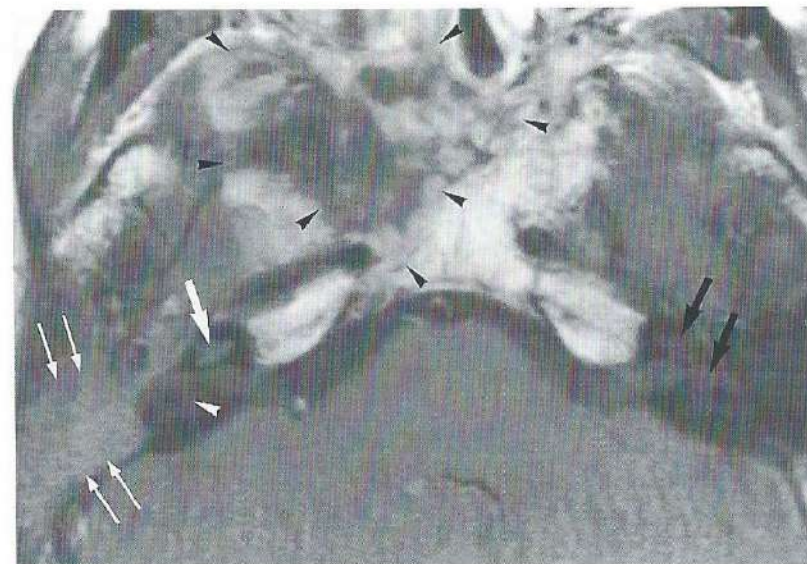
The vascular supply of the labyrinth is derived from the anterior inferior cerebellar artery, and less frequent from the accessory anterior cerebellar artery or the posterior inferior cerebellar artery (1). A loop of this artery gives rise to the internal auditory artery or labyrinthine artery, which further divides into a common cochlear artery and other membranous labyrinth ramifications (1, 2). These terminal branches are the only arteries supplying the membranous labyrinth and its stria vascularis and explain its precarious vascularization (3) (see III.1.4.5.). Breakdown of the blood-brain barrier due to inflammation (Fig. 1) or neoplastic (Figs. 2, 3) pathology causing leakage of Gd into brain lesions has been reported and the mechanism of this blood-brain barrier breakdown is now better

**Fig. 1.** 25-year-old man who was irradiated (nasopharynx tumour) and developed a skullbase sarcoma due to the therapy. This tumour occluded the Eustachian tube and led to a middle ear infection, resulting in a bacterial labyrinthitis and sudden deafness on the right side. Axial nonenhanced (A) and Gd-enhanced (B) T1-weighted images (500/15/4) through both inner ears.



A

**A:** The skull base tumour (black arrowheads) and middle ear infection (long white arrows) can be recognized. Normal intermediate signal intensity intralabyrinthine fluid is seen in the right and left cochlear (large white arrows) and vestibular (white arrowheads) structures.



B

**B:** After Gd administration selective enhancement is seen in the cochlea (large white arrow) on the right; no enhancement can be observed in the vestibule and semicircular canals (white arrowhead). Normal intermediate intensity intralabyrinthine fluid is present in the left vestibule and cochlea (large black arrows). Tumour (black arrowheads), middle ear infection (long white arrows).

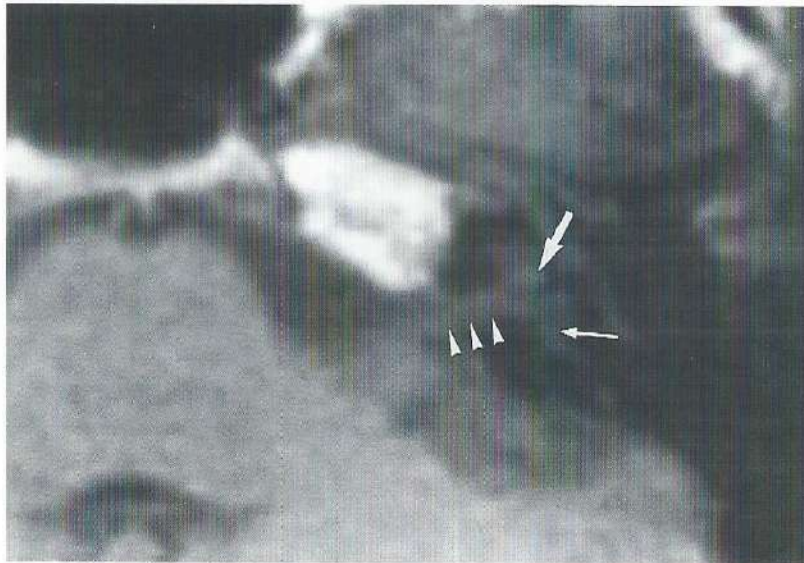
understood (4). A similar barrier probably exists at the junction of the terminal vascular branches and the membranous labyrinth soft tissues and endolymphatic spaces. This junction represents the "labyrinth membrane" which probably functions as a blood-labyrinth barrier. Leakage of Gd through this labyrinthine membrane in cases of pathology, with accumulation of the contrast in the membranous labyrinth soft tissues (especially in the stria vascularis) and subsequent diffusion in the endolymph, is believed to cause the intralabyrinthine contrast enhancement.

Unfortunately there is a threshold effect. In case of viral or bacterial labyrinthitis the intralabyrinthine enhancement will only be seen in patients with severe cochlear and/or vestibular function loss (Fig. 1), while in patients with milder inner ear disorders no enhancement will be present. However a good correlation between labyrinthine enhancement and loss of cochlear and/or vestibular function is found once enhancement occurs. Enhancement limited to certain segments of the cochlea correlating with hearing loss in the expected frequency range has been reported (5, 6).

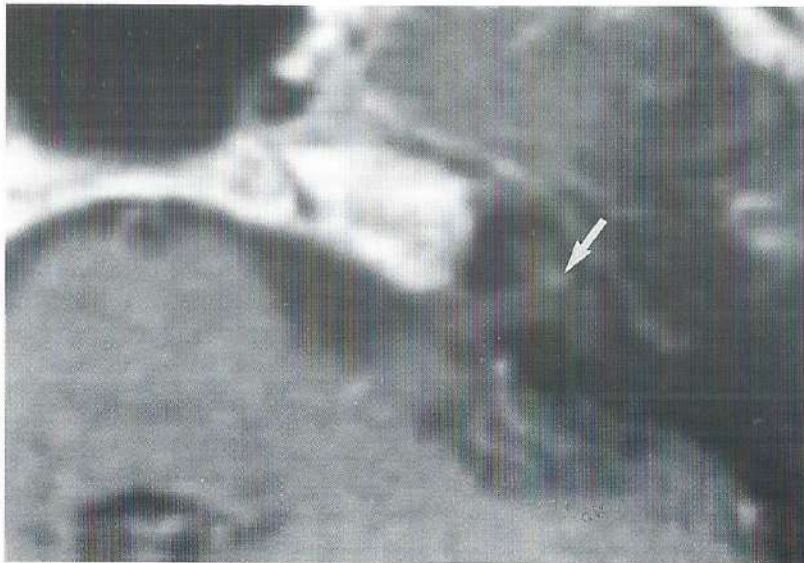
The enhancement of intralabyrinthine schwannomas has been described above (see V.2.5.1.). Enhancement has also been seen in other tumours, see Table I.

**Ischaemic injury** to the labyrinth, due to the precarious vascularization, has been hypothesized as a cause of sudden hearing loss and experimental studies on guinea pigs

**Fig. 2.** 43-year-old man with a 6 month progressive high-frequency hearing loss on the left side. Axial nonenhanced (A) and Gd-enhanced (B) T1-weighted image (500/15/4) through the left labyrinth.



A



B

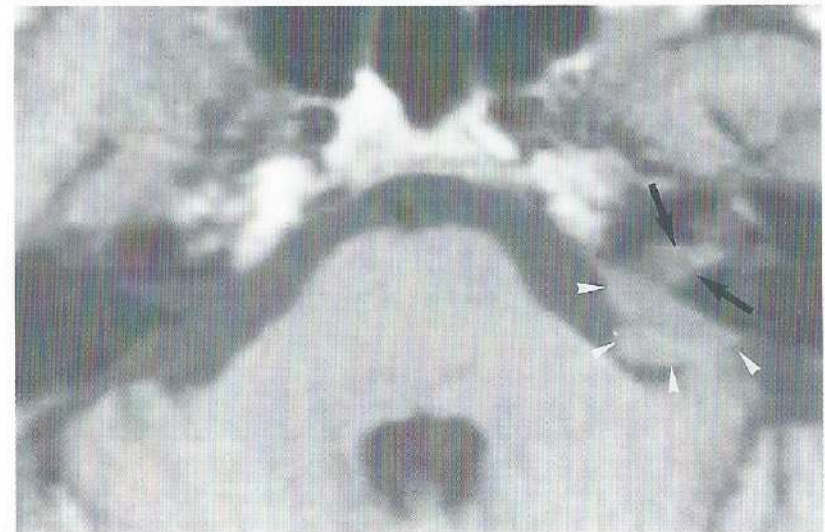
**A:** A small lesion with a signal intensity slightly higher than the intralabyrinthine fluid can be seen in the posterior part of the basal turn of the cochlea (large white arrow). Vestibule (long white arrow), IAC (white arrowheads).

**B:** Clear enhancement of the lesion can be recognized after Gd administration (large white arrow). High-frequency hearing loss corresponds with the localization of the lesion in the basal turn of the cochlea. Diagnosis: Schwannoma inside the cochlea.

have shown that ischaemia of 30 minutes or longer results in permanent severe loss of inner ear function (7, 8). Clinical cases of ischaemic injury with permanent hearing loss and enhancement inside the membranous labyrinth on T1-weighted images or obliteration of the intralabyrinthine fluid spaces have only been reported in patients with Cogan's syndrome (see chapter V.3.).

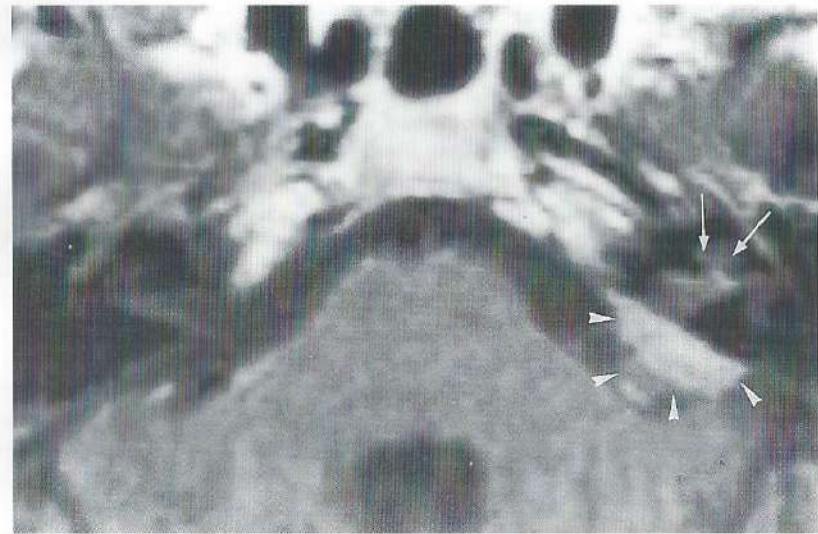
Enhancement inside the cochlea and vestibulum can be found in patients who have had a head trauma (6). Intralabyrinthine haemorrhage, causing spontaneous hyperintensity of the intralabyrinthine fluid, should of course be excluded on the precontrast T1-weighted

**Fig. 3.** 60-year-old woman with breast carcinoma and a metastasis in the CPA, IAC and with tumour growth along the cochlear nerve into the cochlea. She first presented with a facial nerve palsy and then developed progressive high and low-frequency hearing loss on the left side. Axial nonenhanced (A) and Gd-enhanced (B) T1-weighted images (500/15/4) through the left inner ear and axial gradient echo 3DFT-CISS images through the right (C) and left (D) inner ear.



A

**A:** A tumour mass with signal intensity slightly higher than cerebrospinal fluid can be seen in the left CPA (white arrowheads) and IAC (large black arrows).



B



C

**B:** Enhancement of the tumour in the CPA is visible (white arrowheads) and tumour extension and enhancement are also noticed in the cochlea (long white arrows). The high and low frequency hearing loss does not correlate with the involvement of the basal turn of the cochlea (high frequencies) but is probably caused by the diffuse tumoural involvement of the cochlear nerve in the IAC and CPA.

**C:** A normal amount of high signal CSF is present in the right CPA angle (large black arrows) and normal fluid is seen in the basal turn of the cochlea (long white arrows).



D

**D:** Low signal intensity tumour is replacing the fluid in the left CPA (black arrowheads), IAC (white arrowheads) and in the basal turn of the cochlea (long white arrow).

images. Head or direct ear trauma and barotrauma can also lead to perilymphatic fistulas. These fistulas result from a tear in the round window membrane or a tear in the ligamentous attachment of the stapedial footplate. The haemorrhages resulting from these tears are too small to be detected on the nonenhanced images. The subsequent inflammatory changes developing during the days following the occurrence of the tear can however result in intralabyrinthine enhancement. Therefore enhancement inside the cochlea and/or vestibule could be a possible sign of perilymphatic fistulas (6). Until now enhancement inside the semicircular canals has not been reported in patients with perilymphatic fistulas and has only been seen in patients with labyrinthitis.

Blood-brain barrier breakdown can be the result of **ionizing radiation**, but the permeability of the blood-brain barrier can be increased or decreased (9, 10). Irradiation of the temporal bone therefore has the potential to alter the labyrinth membrane resulting in leakage of Gd in the membranous labyrinth. Hearing loss or vestibular function loss due to temporal bone irradiation is however very rare (11) and therefore the chance of seeing membranous labyrinth enhancement seems to be small and has not been reported so far.

### 2.8.2. Enhancement in the bony labyrinth

With the advent of Gd-enhanced MRI it became possible to recognize contrast enhancement in bone structures. This led also to the detection of enhancement in the "bony"

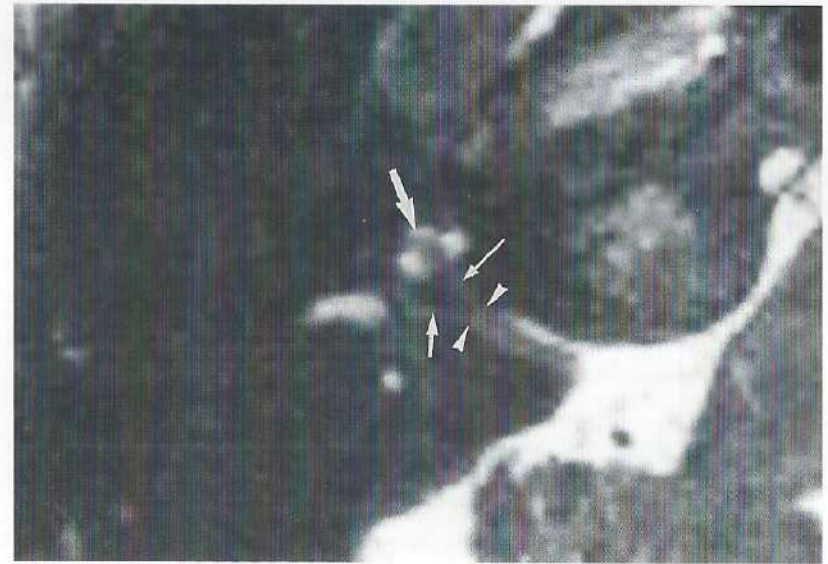
**Fig. 4.** 51-year-old man presenting with retrocochlear sensorineural hearing loss on both sides. Axial nonenhanced T1-weighted image (500/15/4) through the right inner ear (A), axial Gd-enhanced T1-weighted image through both inner ears (B), axial 3DFT-CISS image (C) and CT image (D) through the right inner ear.



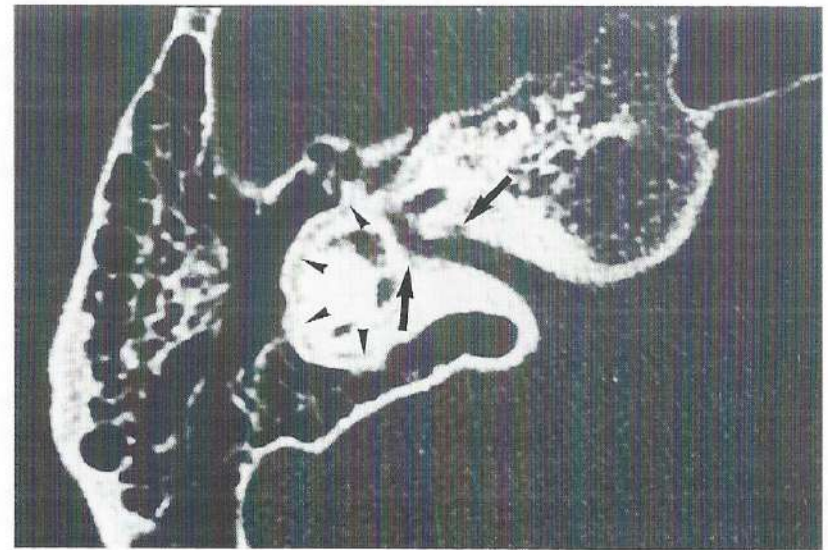
A



B



C



D

**A:** The cochlear (long white arrow) and inferior vestibular nerve (small white arrow) can be distinguished deep in the IAC and are surrounded by low intensity tissue. Cochlea (white arrowhead).

**B:** After Gd administration, enhancing lesions are seen on both sides, deep "in" the IAC, mimicking acoustic neurinomas (large black arrows). Cochlea (long white arrows).

**C:** The CISS image shows that the CSF stops halfway in the IAC (white arrowheads) and that the cochlear (long white arrow) and inferior vestibular nerve (small white arrow) in the distal part of the IAC are surrounded by low signal intensity bone. This means that the enhancing regions seen on image B are not localized "in" but around the IAC and represent abnormal spongy vascular new bone in the pericochlear and perivestibular bone. Cochlea (large white arrow).

**D:** The CT image confirms the diagnosis of otospongiosis and shows the lytic and sclerotic areas in the perilymphatic bone around the fundus of the IAC (large black arrows) but also shows typical lesions around the semicircular canals (black arrowheads).

labyrinth. The vascular supply of the bony labyrinth and temporal bone is more abundant and is not dependent on changes in the labyrinth membrane. Diffuse metastatic destruction of the temporal bone with involvement of the bony and often also the membranous labyrinth is one example. Involvement of the bony labyrinth can also be seen for instance in cases of fibrous dysplasia (12, 13). More selective enhancement of the bony labyrinth with an intact membranous labyrinth has been noticed in cases of otosclerosis. The regions of enhancement probably correspond with the regions of resorption of the enchondral layer of bone, between the inner endosteum and outer periosteum of the otic capsule, with deposition of spongy vascular new bone (otospongiosis). This enhancement can even mimic an acoustic schwannoma, and gradient-echo images (3DFT-CISS images) or high resolution MR images are required to differentiate the pericochlear or perivestibular enhancement from intralabyrinthine enhancement on MR (Fig. 4).

### 2.8.3. Conclusion

Very often the sensorineural hearing loss and/or vertigo of patients can be explained by membranous labyrinth pathology, and this pathology will not be detected unless Gd-enhanced MR is used.

Nonenhanced T1-weighted images are also necessary to exclude intralabyrinthine haemorrhage. Gradient-echo (3DFT-CISS) images can help in the differential diagnosis or are sometimes the only images that can show the pathology.

The list of pathologies causing intralabyrinthine enhancement is getting longer and includes different types of labyrinthitis, tumours, vasculitis, autoimmune disease, trauma, irradiation etc. (see Table I).

Membranous labyrinth enhancement must be differentiated from pericochlear or perivestibular enhancement.

**Table I: Possible causes of membranous labyrinth enhancement**

<b>Inflammation - infection:</b>	– Presumed viral labyrinthitis (clinical signs of upper respiratory tract infection, no virus identified)
	– Bacterial labyrinthitis
	– Luetic labyrinthitis
	– Mumps labyrinthitis
	– Rubella labyrinthitis
	– Endolymphatic hydrops
<b>Tumours:</b>	– Intracochlear schwannoma
	– Utriculosaccular schwannoma
	– Metastasis
	– Lymphoma
<b>Vasculitis - autoimmune:</b>	– Cogan's syndrome
	– Autoimmune labyrinthitis
<b>Trauma:</b>	– Posttraumatic perilymphatic fistula

### Irradiation?

### 2.8.4. References

- Bergeron RT. Introduction to the temporal bone. In: Head and neck imaging, second edition, ed. Som PM, Bergeron RT, Mosby, St. Louis, 1991:927-944.
- Roland J, Bracard S, Picard L. Vascularisation de l'os temporal normal. In: Imagerie de l'oreille. ed Veillon F, Flammarion Médecine-Sciences, Paris, 1991:69-74.
- Schuknecht HF. Pathology of the ear. Harvard University Press, Cambridge Mass., 1974.
- Greenwood J. Mechanisms of blood-brain barrier breakdown. *Neuroradiology* 1991; 33: 95-100.
- Mark AS, Seltzer S, Nelson-Drake J, Chapman JC, Fitzgerald DC, Gulya AJ. Labyrinthine enhancement on Gd-MRI in patients with sudden deafness and vertigo: correlation with audiologic and electronystagmographic studies. *Ann Otol Rhinol Laryngol* 1992; 101: 459-464.
- Mark AS, Fitzgerald D. Segmental enhancement of the cochlea on contrast-enhanced MR: correlation with the frequency of hearing loss and possible sign of perilymphatic fistula and autoimmune labyrinthitis. *AJNR* 1993; 14:991-996.
- Perlman H, Kimura R. Experimental obstruction of venous drainage and arterial supply of the inner ear. *Ann Otol Rhinol Laryngol* 1957; 66:537-546.
- Perlman H, Kimura R, Fernandez C. Experiments on temporary obstruction of the internal auditory artery. *Laryngoscope* 1959; 69:591-613.

9. Qin DX, Zheng R, Tang J, Li JX, Hu YH. Influence of radiation on the blood-brain barrier and optimum time of chemotherapy. *Int J Radiat Oncol Biol Phys* 1990; 19: 1507-1510.
10. Trnovec T, Kallay Z, Bezek S. Effects of ionizing radiation on the blood brain barrier permeability to pharmacologically active substances. *Int J Radiat Oncol Biol Phys* 1990; 19: 1581-1587.
11. Paparella MM, Shumrick DA, Gluckman JL, Meyerhoff WL. *Otolaryngology*, volume IV, Saunders, Philadelphia, 1991:3221.
12. Casselman JW, Kuhweide R, Ampe W, Meeus L, Steyaert L. Pathology of the membranous labyrinth: comparison of T1- and T2-weighted and gadolinium-enhanced spin-echo and 3DFT-CISS imaging. *AJNR* 1993; 14:59-69.
13. Casselman JW, De Jonge I, Neyt L, De Clercq C, D'Hont G. MRI in craniofacial fibrous dysplasia. *Neuroradiology* 1993; 35:234-237.

### 3. MR of the Inner Ear in Patients with Cogan Syndrome

Jan W. Casselman<sup>(1)</sup>, M.H.J.M. Majoor<sup>(2)</sup>, and Frans W. Albers<sup>(3)</sup>

From the department of Radiology<sup>(1)</sup>,  
A.Z. St.-Jan Brugge, Brugge, Belgium,  
the departments of Otorhinolaryngology,  
University Hospital, Utrecht, the Netherlands<sup>(2)</sup>,  
and University Hospital, Gent, Belgium<sup>(3)</sup>.

*Published in: Am J Neuroradiol 1994; 15:131-138.*

#### 3.1. ABSTRACT

**Purpose:** To determine whether the bony and soft-tissue obliterations of the intralabyrinthine fluid spaces reported in pathologic studies of patients with Cogan syndrome can be detected with MR or CT.

**Methods:** The inner ears of six patients with Cogan syndrome were studied. High-resolution CT was performed in five patients; all six patients were studied with MR, including T1-weighted spin-echo images with and without gadolinium administration, T2-weighted spin-echo images, and three-dimensional Fourier transform constructive interference in steady state images.

**Results:** In two patients, small calcified obliterations were detected on CT but the three-dimensional Fourier transform constructive interference in steady state images revealed more extensive soft-tissue obliteration in five of the six patients. High signal inside the membranous labyrinth on precontrast T1-weighted images and contrast enhancement inside the membranous labyrinth on the postcontrast T1-weighted images were seen in one patient.

**Conclusions:** The study showed that calcific obliteration and soft-tissue obliteration of the intralabyrinthine fluid spaces in patients with Cogan syndrome can be demonstrated radiologically and that soft-tissue obliteration is more frequent than calcified obliteration. MR detected the intralabyrinthine disease far more frequently than did CT. The three-dimensional Fourier transform constructive interference in steady state sequence proved to be the most sensitive MR sequence. Hyperintensity inside the membranous labyrinth on the precontrast T1-weighted images and enhancement on the contrast-enhanced T1 images were less frequent and probably represent leakage through the abnormal labyrinthine membrane from active disease.

**Index terms:** Ear, abnormalities and anomalies; Ear, magnetic resonance; Temporal bone, abnormalities and anomalies; Temporal bone, magnetic resonance; Nervous system, diseases; Magnetic resonance, technique.

### 3.2. INTRODUCTION

Cogan syndrome is a rare syndrome affecting young adults. The patients present with nonsyphilitic interstitial keratitis and audiovestibular dysfunction (1-3). Associated cardiac and diffuse vascular lesions are often detected. The prognosis for vision is good, although permanent deafness occurs in most instances. Pathologic studies have mentioned obliteration of the endo- and perilymphatic fluid spaces in these patients caused by acidophilic coagulum, cellular debris, connective tissue, hypertrophy of the stria vascularis, and even pathologic bone formation.

We studied six patients with Cogan syndrome to determine whether these bony and/or soft tissue obliterations of the intralabyrinthine fluid spaces (IFS) reported in pathologic studies could be detected with computed tomography (CT) or magnetic resonance (MR). CT was used to detect calcifications in the IFS and a three-dimensional Fourier transform (3DFT) constructive interference in steady state (CISS) MR sequence was used to look for soft-tissue obliteration of the IFS.

This 3DFT MR technique has already been proved to be very sensitive for the detection of intralabyrinthine soft-tissue obliterations (4, 5). With the use of both CT and MR, differentiation between bony and soft-tissue obliteration is possible and the frequency of both types of obliteration can be evaluated.

Finally, T1-weighted images with and without intravenous gadolinium administration were used to detect abnormal contrast enhancement in the membranous labyrinth (ML).

### 3.3. SUBJECTS AND METHODS

Six patients with Cogan syndrome (5 men, 1 woman; average age, 25 years) underwent radiologic examination of the temporal bones. The diagnosis of Cogan syndrome was made when the clinical symptoms were in agreement with the diagnostic criteria formulated by Cogan (6). Therefore, only patients with a typical nonulcerative stromal keratitis in conjunction with audiovestibular symptoms in the absence of congenital syphilis were selected for the study.

Five patients underwent a coronal and axial high-resolution CT scan (9800 Hilight, General Electric, Milwaukee, Wis). Section thickness was 1.5 mm and sections were made every 1 mm. We looked for calcific obliteration of the IFS on these CT images.

All patients were also studied with MR on a 1.0 tesla superconductive active shielded magnet (Magnetom SP 42, Siemens, Erlangen). They were studied with 3-mm contiguous two-dimensional spin-echo T1-weighted images without and with intravenous gadolinium administration 500/15/4 (repetition time/echo time/excitations) and 4-mm-thick axial two-dimensional spin-echo T2-weighted images 2500/15, 90/1 with a 0.8-mm gap.

Finally, 1-mm thick contiguous axial 3DFT CISS images were acquired in all patients. The basic principles and description of the 3DFT CISS sequence scheme have been reported (4, 5, 7, 8). Fast imaging with steady precession (FISP) and contrast-enhanced fast acquisition steady-state sequences basically rely on the steady state of both longitudinal and transversal magnetization (9, 10). This steady state is established by excitation of the spin system with radio frequency pulses at a short repetition time  $\ll T_2$ . The development of this state is achieved using a short equilibration time of about 1 second before starting

the data acquisition itself. As is well known from flow imaging, moving spins will accumulate additional phase shifts when moving along field gradients. If the motion is not constant in time, transverse magnetization may cancel completely, thus completely avoiding a steady state of the transverse magnetization. Therefore, moving cerebrospinal fluid does not produce any signal when standard FISP or contrast-enhanced fast-acquisition steady-state sequences are used. Even for very slow flow, the cerebrospinal fluid signal may disappear because these flow-induced phase shifts will accumulate over many repetition time intervals, thus creating a large amount of phase shifts in the magnetization.

Flow-compensation techniques have to be used to ensure that spins, independent of their actual velocity, are being refocused. The flow compensation must be applied to each gradient over each repetition time cycle, unlike standard flow-compensation sequences (eg, motion-refocusing angiography sequences), in which the flow compensation is applied to the echo. A steady-state flow-compensated three-dimensional FISP sequence is shown in Figure 1. All three gradients are balanced, indicating that the average value of each gradient is zero. In this case, spins moving at a constant velocity will have the same phase after the application of the gradient pulses as they had before (7). Running a sequence as shown in Figure 1 will produce an image that shows bands of low signal intensity. The occurrence of these bands is not a result of any system imperfection but is related to basic physical effects. These dark bands are caused by very small magnetic-field inhomogeneities and local field distortions attributable to susceptibility changes that are normally produced by the patient. These inhomogeneities cause corresponding frequency offsets. If the frequency at a given location is such that the phase angle accumulation over one repetition time period corresponds to  $\pi$ , or odd integers thereof, the magnetization cancels, and a dark point appears in the image. At another location, the frequency offset might be larger (eg,  $2\pi$  or a multiple thereof), and the magnetization will interfere constructively, resulting in a high signal intensity at this particular point.

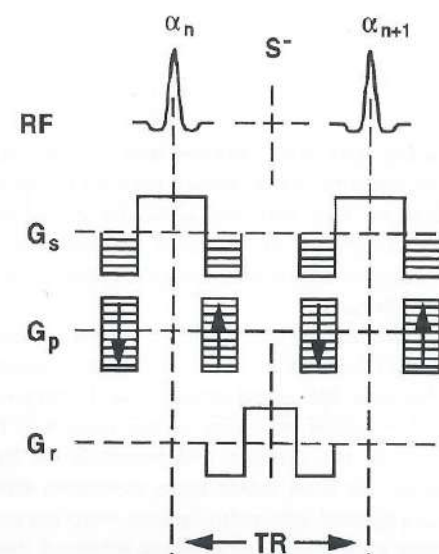


Fig. 1. True three-dimensional FISP sequence.

The three gradients are balanced indicating that the average value of each gradient in the section selection ( $G_s$ ), phase encoding ( $G_p$ ) and frequency encoding ( $G_r$ ) direction is zero. This true FISP sequence is repeated twice when the CISS sequence scheme is used, once with nonalternating radio frequency ( $\alpha_n = \alpha_{n+1} = \alpha^{++}$ ) and once with alternating radio frequency ( $\alpha_n = \alpha_{n+1} = \alpha^{+-}$ ).

The solution to this inherent problem is to acquire two data sets successively with a "true FISP" (9) sequence of alternating (+-) and non-alternating (++) radio frequency pulses. The position of the dark bands is shifted in the second data set to the position of high intensity of the first data set. A simple mathematical postprocessing operation (maximum intensity projection (11)) takes the information of each pair of images of the two three-dimensional data sets and produces an image with a homogeneous intensity distribution over the whole image and very good contrast between the high-signal intralabyrinthine fluid and the low signal of the surrounding bony labyrinth. Moreover, the 1-mm-thin contiguous sections allow detailed evaluation of the ML and IFS and can minimize partial volume artifacts (4, 5).

Each data set covers a volume of 32 mm for application in the inner ear. This slab is divided into 32 partitions, resulting in an effective section thickness of 1mm. The measurement parameters are: 20/8, matrix size 256 × 256, field of view 176 mm, and flip angle 50°. The result is a total acquisition time of 2 times 2.46 minutes and an inplane resolution of each of the three-dimensional partitions of 0.69 × 0.69 mm.

A targeted maximum intensity projection on the CISS data set also allows three-dimensional reconstructed imaging of the inner ear (14). The use of a field of view of 176 mm also allows examination of both inner ears when the head coil is used.

On all MR images we looked for obliteration of the IFS inside the three semicircular canals, the common crus, the vestibule, and the basal and apical turn of the cochlea. The use of both CT and MR made differentiation between "bony" and "fibrous" obliteration possible. Bony or calcified obliteration can be seen as calcifications or regions of high density inside the IFS on CT images, and on MR images at the same site obliteration (signal loss) of the IFS is seen. Fibrous obliteration is present when no calcific obliteration is seen on CT and loss of high signal of the intralabyrinthine fluid is found on MR images. Finally, we also checked whether gadolinium enhancement inside the ML occurred, indicating leakage of gadolinium through the abnormal labyrinthine membrane.

### 3.4. RESULTS

All patients had bilateral sensorineural hearing loss with tinnitus and vertigo. An interstitial keratitis was seen in each patient. All six patients experienced a period of general illness with fatigue. Two patients also had arthralgia. Two men had testicular pain. One patient complained of myalgia. One had multiple aneurysms of the major abdominal and thoracic arteries. An increased erythrocyte sedimentation rate and leucocytosis were found in all patients. All serologic tests for syphilis were negative.

Obliteration of the IFS was seen in 5 of the 6 patients on the 3DFT CISS images, and calcification inside the IFS was detected in 2 patients (Table I). In these 2 patients calcifications were found in the basal turn of the cochlea near the round window in 3 temporal bones and bony narrowing of the lateral semicircular canal was seen in one inner ear. In one patient high signal intensity was present inside the cochlea and vestibule on the unenhanced T1-weighted images and enhancement was seen inside these structures after gadolinium administration. In all patients the T2-weighted spin-echo images were normal and failed to demonstrate disease. The semicircular canals were more often involved than

**Table I:** Sensitivity of CT and different MR sequences in the detection of obliteration of the intralabyrinthine fluid spaces in 6 patients with Cogan syndrome

Case	Sex	CT	T1	T2	CISS	T1-Gadolinium
1	Male	-	-	-	-	-
2	Female	-	+	-	+	*
3	Male	NA <sup>a</sup>	-	-	+	-
4	Male	+	-	-	+	-
5	Male	-	-	-	+	-
6	Male	+	-	-	+	-

Note: -, no disease; +, obliteration of the intralabyrinthine fluid spaces; \*, enhancement inside the membranous labyrinth.

<sup>a</sup>NA, not applicable.

**Table II:** Frequency of obliteration of the different parts of the intralabyrinthine fluid spaces in six patients with Cogan syndrome (12 membranous labyrinths)

Part of the ML Involved	Number of MLs in Which Part Is Involved
Superior semicircular canal	8
Common crus	8
Lateral semicircular canal	7
Posterior semicircular canal	6
Basal turn of cochlea	5
Vestibule	4
Second turn of cochlea	2

the vestibule and cochlea. The frequencies of obliteration of the lumen of these ML structures are listed in Table II.

### 3.5. DISCUSSION

Cogan described in 1945 for the first time a unique syndrome characterized by non-syphilitic interstitial keratitis and vestibuloauditory dysfunction (1). Later, Cody and Williams (12) emphasized the systemic manifestations of this syndrome (12). The cause and

pathogenesis are still unknown, but viral infection, autoimmune disease, and systemic (vascular) disease are mentioned in the etiology. Most often young adults are affected and symptoms usually develop during the second through fifth decades of life (1). Treatment consists of high-dose glucocorticoid therapy. Serious clinical outcomes, especially deafness, and less often vasculitis, aortic insufficiency, blindness, and even death have been reported.

The temporal-bone disease of Cogan syndrome has been described (2, 3, 13). Thickening of the membranous lining of the ML, hypertrophy of the stria vascularis, obliteration of the endolymphatic ducts of the cochlea and semicircular canals by an acidophilic coagulum, cellular debris inside the scala media and connective tissue in the scala tympani and scala vestibuli (3), and even new bone formation or osteogenesis (2, 13) have been reported. New bone formation should be visible on CT.

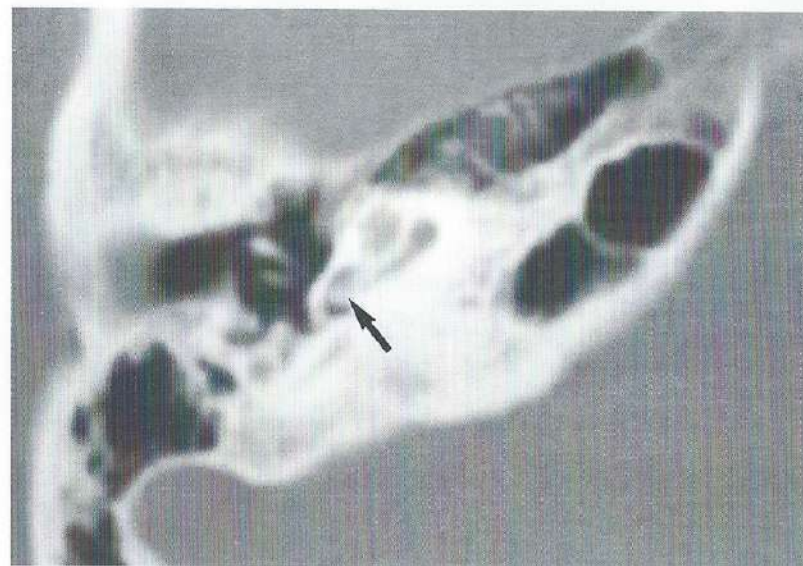
In the autopsy reports (2, 13), bone was found in the cochlea in the apical turns and near the round window niche and was also discovered in the semicircular canals. In our study new bone formation or calcification was present near the round window in cases 4 and 6 (Fig. 2A) and bony narrowing of the lateral semicircular canal was seen in case 6. It was mentioned by Wolff et al (2) that connective tissue disease precedes formation of new bone. CT is unable to detect soft-tissue obliteration of the IFS, but MR has the potential to show soft-tissue obliteration because it better shows the fluid inside the lumen of the ML. Routine T1- and T2-weighted spin-echo images are 3 to 4 mm thick and therefore some parts of the ML and IFS are missed because of partial volume artifacts. In our study, soft-tissue obliteration of the IFS could not be detected on the T1- and T2-weighted spin-echo images. Partial voluming artifacts and the low signal intensity of the intralabyrinthine fluid, only slightly hyperintense compared with the surrounding bony labyrinth, can explain the poor performance of T1 images. It is harder to explain the lack of sensitivity of the T2-weighted images. Again, partial volume artifacts may be responsible but another possible explanation is that the thickening of the membranous lining and the hypertrophy of the stria vascularis of the ML have a signal intensity close to the signal intensity of the intralabyrinthine fluid and are consequently difficult to recognize.

3DFT gradient-echo techniques are better suited for the study of small structures like the labyrinth because they provide thin, 1-mm contiguous sections (4, 5, 14-16). Moreover, they display the intralabyrinthine fluid as high signal in contrast to the surrounding low signal of the bony labyrinth. In a study of 50 normal inner ears, high signal intensity inside the cochlea, vestibule, and semicircular canals was always seen on 3DFT CISS images (4). Recently, good results were also reported with 1-mm contiguous fast spin-echo images (17).

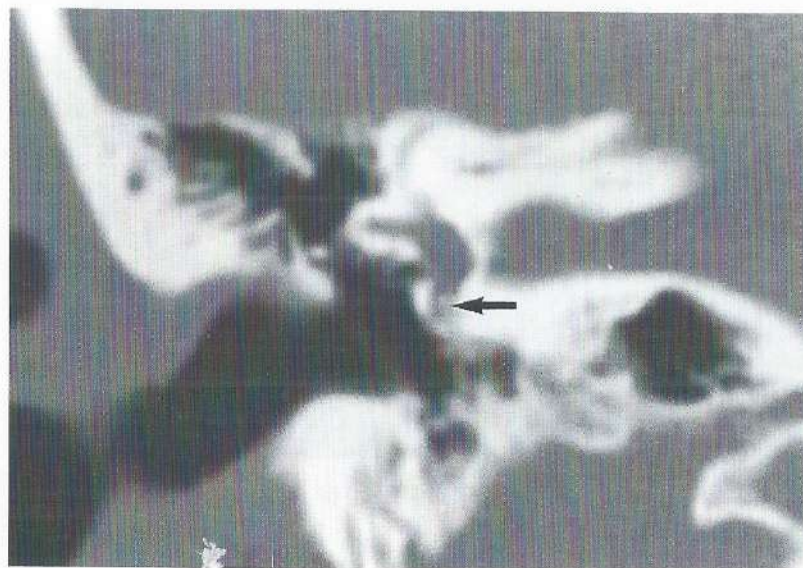
We found soft-tissue obliterations that were not seen on CT images in 5 of the 6 patients. In the two patients with calcifications inside the IFS on CT, more extensive soft-tissue obliterations were found in other parts of the IFS on the 3DFT CISS images (Fig. 2B-C). This proves that soft-tissue obliteration is more frequent than bony obliteration and supports the hypothesis of Wolff et al (2) that abnormal connective tissue in the IFS probably precedes formation of new bone. These results also reveal better contrast between fluid and soft tissues inside the IFS on 3DFT CISS images than on T2-weighted spin-echo images.

In one patient no obliterations were found on CT nor on the most sensitive (3DFT CISS) MR images. This was also the only patient with a complete recovery of the senso-

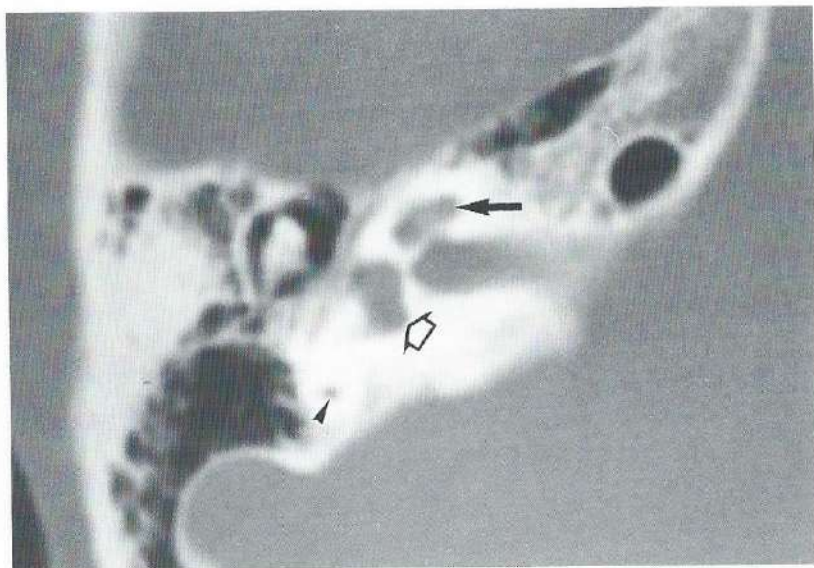
*Fig. 2. Axial and coronal CT scan of the right temporal bone at the level of the basal turn of the cochlea (A, B) and axial CT (C) and 1-mm-thick three-dimensional CISS MR image (20/8/1) (D) at the level of the right vestibule and three-dimensional CISS MR image through the left vestibule (E) for comparison (case 6).*



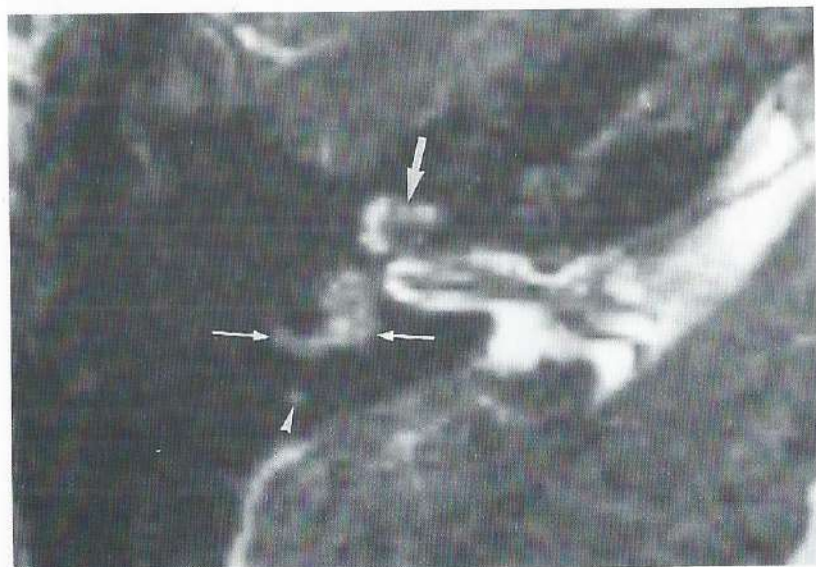
A



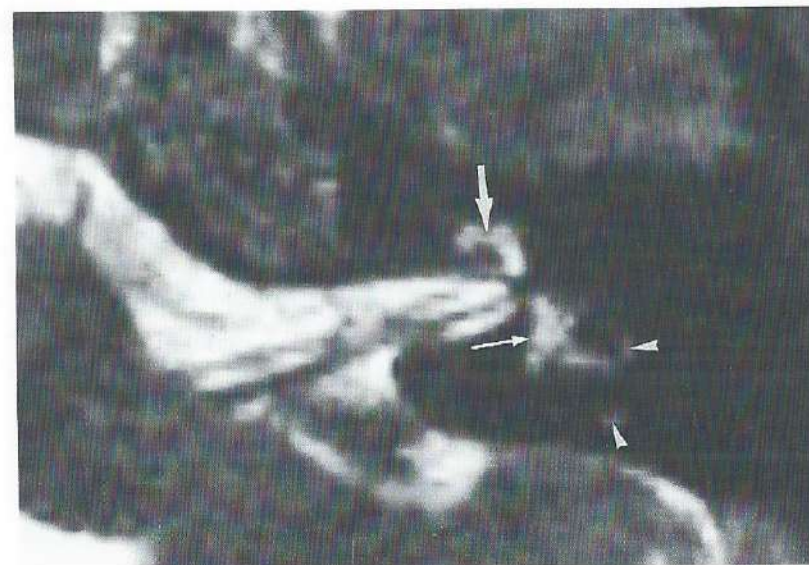
B



C



D



E

A. Calcification is present inside the basal turn of the cochlea near the round window niche (arrow).

B. On this coronal CT image the calcification can again be seen in the basal turn of the cochlea (arrow).

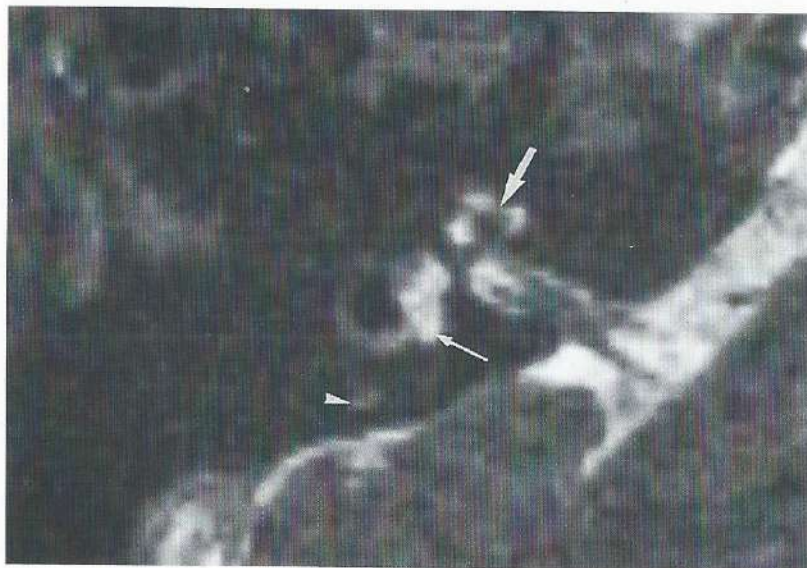
C. Normal low-density fluid is seen in the right cochlea (large black arrow), vestibule (open black arrow), and posterior semicircular canal (black arrowhead) on the CT image.

D. The corresponding CISS MR image demonstrates intermediate signal intensity in the posterior semicircular canal (white arrowhead), vestibule and lateral semicircular canal (long white arrows), and in the anterior part of the cochlea (large white arrow). Normally the signal intensity of the fluid inside these structures is isointense with the cerebrospinal fluid inside the internal auditory canal but in this patient the high signal of the intralabyrinthine fluid is replaced by soft tissue. Fluid can be recognized only in parts of the cochlea and around the cochlear and inferior vestibular nerve inside the internal auditory canal.

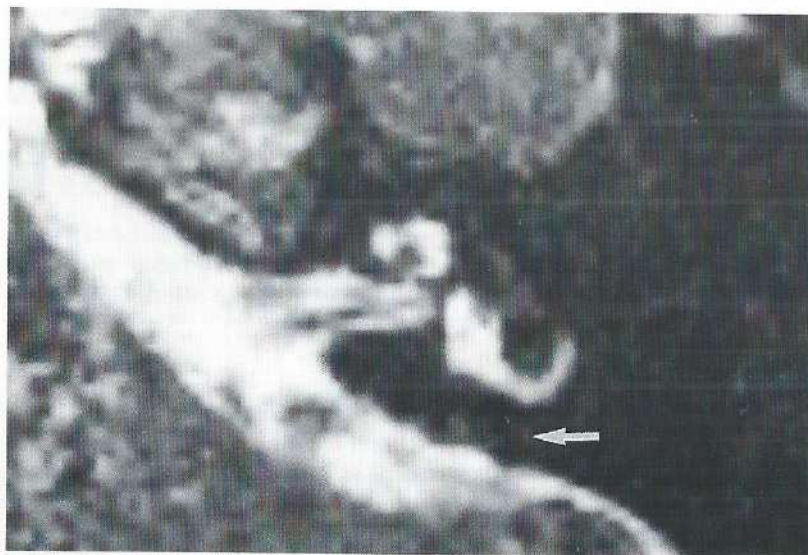
E. This CISS image through the left labyrinth shows that normal high-signal fluid is visible in the anterior part of the cochlea (large white arrow), vestibule (thin white arrow), and in the visible parts of the lateral and posterior semicircular canals (white arrowheads). The signal in these structures is isointense with the signal of cerebrospinal fluid in the internal auditory canal.

rineural hearing loss, suggesting that patients with a less severe clinical presentation have less chance of obliteration of the IFS. In the other five patients, narrowing or obliteration of parts of the semicircular canals (Figs. 2, 3) was seen on the 3DFT images; in three of these patients abnormal soft tissues were also found in the vestibule (Figs. 2, 4). This correlated well with the clinical findings. All five patients suffered from vertigo. In three patients (cases 2, 4, and 6), parts of the cochlea were obliterated (Figs. 2, 4) and again these findings were consistent with the audiometry. In two patients, however (cases 3 and 5), deaf-

**Fig. 3.** Axial three-dimensional CISS MR image (20/8/1) through the right (A) and left (B) labyrinth at the level of the lateral semicircular canal (case 5).



A



B

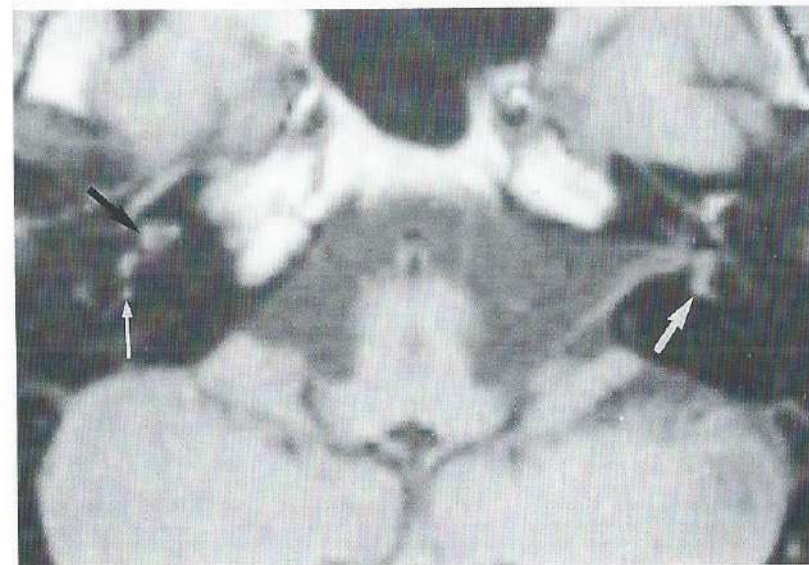
**A.** Normal high-signal-intensity fluid, isointense with the fluid in the internal auditory canal and cerebellopontine angle, can be seen inside the cochlea (large white arrow), vestibule (thin white arrow) and posterior semicircular canal (white arrowhead). The 3DFT CISS images of 50 normal inner ears proved that high signal intensity inside the cochlea, vestibule, and the three semicircular canals is always visible (4).

**B.** On the left side the high signal intensity of the fluid inside the posterior semicircular canal is absent (arrow), representing "bony" or "soft tissue" obliteration. However the corresponding CT image showed a normal patent posterior semicircular canal, proving that the obliteration seen on the MR image was caused by soft tissues.

ness or subtotal deafness was found clinically but normal cochlear structures were seen on MR and CT. This shows that the radiologic-clinical correlation is good but not perfect.

In only one patient was high signal intensity seen inside the cochlea, vestibule, and semicircular canals on the unenhanced T1-weighted images, and enhancement was seen in these structures on the right side after gadolinium administration (Fig. 4). The patient was

**Fig. 4.** Axial 3-mm-thick unenhanced (A) and gadolinium-enhanced (B) T1-weighted images (500/15/4) through both labyrinths; axial three-dimensional CISS MR image (20/8/1) through the right labyrinth (C); three-dimensional reconstructions of the right labyrinth (D) (case 2); and normal three-dimensional labyrinth reconstruction (E) for comparison.

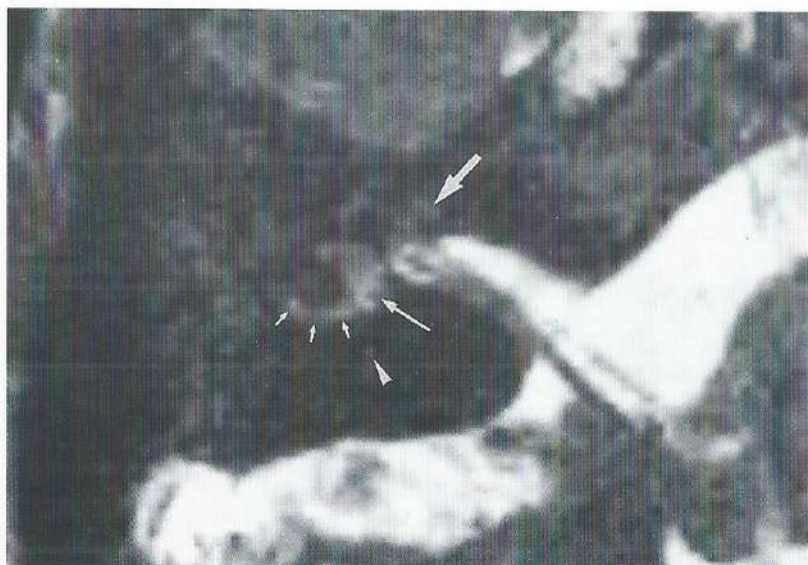


A

**A.** High signal intensity is seen in the right cochlea (black arrow), right posterior semicircular canal (thin white arrow), and left vestibule (large white arrow). Normally on T1-weighted images intralabyrinthine fluid is isointense with the cerebrospinal fluid in the internal auditory canal and cerebellopontine angle.



B



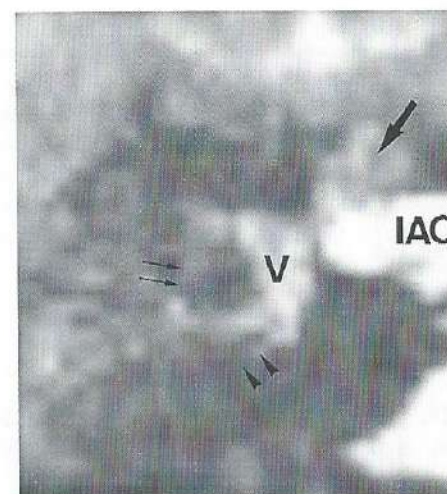
C

**B.** Enhancement is seen inside the cochlea (open black arrow), and vestibule and posterior semicircular canal (white arrows) after intravenous gadolinium administration.

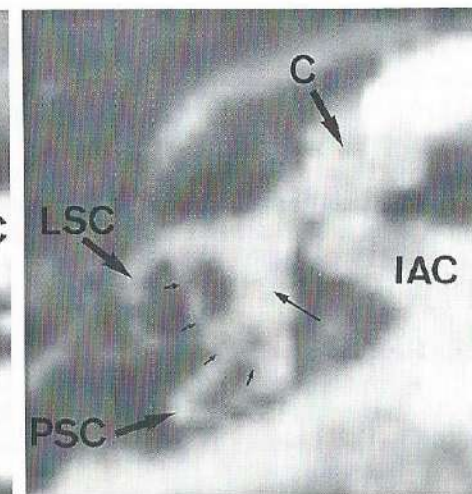
**C.** The high signal intensity of fluid is lost completely in the cochlea (large white arrow), vestibule (thin white arrow), and lateral semicircular canal (small white arrows) and is replaced by "soft tissue" intermediate signal intensity. The posterior semicircular canal is completely obliterated and all signal inside the canal is lost (white arrowhead).

**D.** The three-dimensional reconstruction of the right labyrinth confirms loss of high-signal-intensity intralabyrinthine fluid in the total cochlea (large black arrow), posterior semicircular canal (black arrowheads), and in the lateral semicircular canal (thin black arrows). Even in the vestibule (V) signal loss is recognized (compare with the high signal intensity in the internal auditory canal). The superior semicircular canal is completely obliterated and can not be seen. On the axial 1-mm-thick CISS image (C) the anterior part of the lateral semicircular canal is missing, but this could have been because of an oblique cut through the canal. However on the three-dimensional reconstructions the anterior part of the canal is still absent proving that the signal loss is caused by obliteration of the canal and not by an oblique cut through the canal.

**E.** The fluid-filled lateral semicircular canal (LSC), posterior semicircular canal (PSC), superior semicircular canal (small black arrows), the cochlea (C), and the vestibule (thin black arrow) can all be seen as high signal intensity structures on a three-dimensional reconstruction of a normal labyrinth. IAC designates the internal auditory canal.



D



E

completely deaf on both sides and showed no response to caloric stimuli at the time of CT and MR examination. High signal inside the ML on unenhanced T1-weighted images has been described in two patients with sudden hearing loss and vertigo (18). Fast or slow flow are unlikely causes for the hyperintensity on the unenhanced images but high protein content inside the intralabyrinthine fluid cannot be excluded as possible explanation (18). However, the association of Cogan syndrome and systemic vascular disease is known and lesions resembling those seen in polyarteritis nodosa and thromboangiitis obliterans were found in patients with Cogan syndrome (3). Moreover, haemorrhage into the IFS was seen in animals after experimental venous occlusion (19). Therefore, haemorrhage seems to be the most likely explanation for the high signal intensity inside the perilymphatic and endolymphatic spaces on unenhanced T1-weighted images.

Gadolinium enhancement in the ML has also been studied (5, 20, 21) and represents gadolinium leakage through the abnormal labyrinth membrane. This has been reported in cases of viral, luetic, and bacterial labyrinthitis (20, 21) and in cases of intralabyrinthine schwannoma (5, 22).

Ischemia or vasculitis are also mentioned as a possible cause. The ML has precarious vascularisation and no collateral circulation (23). As already mentioned, vasculitis is frequently found in patients with Cogan syndrome (1, 3). Moreover, Perlman et al (13) observed osteogenesis and diseased soft tissues in the inner ear after experimental obstruction of the arterial supply of the inner ear in guinea pigs (24). These findings suggest that the enhancement seen in our patient is most likely caused by vasculitis and probably represents active disease.

### 3.6. CONCLUSIONS

1) In the majority of patients with Cogan syndrome, obliterations of the intralabyrinthine fluid spaces are found on CT or MR.

2) CT is the most sensitive technique to detect bony obliteration. 3DFT CISS MR imaging is the most sensitive technique to detect the far more frequent soft-tissue obliteration.

3) Hyperintensity inside the ML on precontrast T1-weighted images (seen in one patient) probably represents haemorrhage. Gadolinium enhancement of the ML in patients with Cogan syndrome represents gadolinium leakage through an abnormal labyrinthine membrane and probably represents active disease.

### 3.7. REFERENCES

- Vollertsen RS, McDonald TJ, Younge BR, Banks PM, Stanson AW, Ilstrup DM. Cogan's syndrome: 18 cases and a review of the literature. *Mayo Clin Proc* 1986; 61:344-361.
- Wolff D, Bernhard WG, Tsutsumi S, Ross IS, Nussbaum HE. The pathology of Cogan's syndrome causing profound deafness. *Ann Otol Rhinol Laryngol* 1965; 74:507-520.
- Fisher ER, Hellstrom HR. Cogan's syndrome and systemic vascular disease: analysis of pathologic features with reference to its relationship to thromboangiitis obliterans (Buerger). *Arch Pathol* 1961; 72:575-592.
- Casselmann JW, Kuhweide R, Deimling M, Ampe W, Dehaene I, Meeus L. Constructive interference in steady state (CISS)-3DFT MR imaging of the inner ear and cerebellopontine angle. *AJNR Am J Neuroradiol* 1993; 14:47-57.
- Casselmann JW, Kuhweide R, Ampe W, Meeus L, Steyaert L. Pathology of the membranous labyrinth: Comparison of T1-, and T2-weighted and gadolinium-enhanced spin-echo and 3DFT-CISS imaging. *AJNR Am J Neuroradiol* 1993; 14:59-69.
- Cogan DG. Syndrome of nonsyphilitic interstitial keratitis and vestibuloauditory symptoms. *Arch Ophthalmol* 1945; 33:144-149.
- Patz S. Some factors that influence the steady state in "steady state" free precession. *Magn Reson Imaging* 1988; 6:405-413.
- Deimling M, Laub GA. Constructive interference in steady state for motion sensitivity reduction (abstr). In: *Book of abstracts: Society of Magnetic Resonance in Medicine* 1989, Vol. 1. Berkeley, CA: Society of Magnetic Resonance in Medicine, 1989:842.
- Gyngell ML, Palmer ND, Eastwood LM. The application of steady state free precession (SSFP) in 2DFT MR imaging (abstr). In: *Book of abstracts, Vol. 3. Berkeley, CA: Society of Magnetic Resonance in Medicine*, 1986:666.
- Oppelt A, Graumann R, Barfuss H, Fischer H, Hartl W, Schajor W. FISP, a new fast MRI sequence. *Electromedica* 1986; 54:15-18.
- Laub GA, Kaiser WA. MR angiography with gradient motion refocusing. *J Comput Tomogr* 1988; 12:377-382.
- Cody DTR, Williams HL. Cogan's syndrome. *Laryngoscope* 1960; 70:447-478.
- Rarey KE, Bicknell JM, Davis LE. Intralabyrinthine osteogenesis in Cogan's syndrome. *Am J Otolaryngol* 1986; 4:387-390.
- Tanioka H, Shirakawa T, Machida T, Sasaki Y. Three dimensional reconstructed MR imaging of the inner ear. *Radiology* 1991; 178:141-144.
- Brogan M, Chakeres DW, Schmalbrock P. High-resolution 3DFT MR imaging of the endolymphatic duct and soft tissues of the otic capsule. *AJNR Am J Neuroradiol* 1991; 12:1-11.
- Tanioka H, Machida T, Zusho H. High resolution MRI of the temporal bone using a surface coil: normal anatomy. *Jpn J Med Imaging* 1989; 8:2-8.
- Tien RD, Felsberg GJ, Macfall J. Fast spin-echo high-resolution MR imaging of the inner ear. *AJR Am J Roentgenol* 1992; 159:395-398.
- Weissman JL, Curtin HD, Hirsch WL. High signal from the otic labyrinth on unenhanced magnetic resonance imaging. *AJNR Am J Neuroradiol* 1992; 13:1183-1187.
- Perlman H, Kimura R. Experimental obstruction of venous drainage and arterial supply of the inner ear. *Ann Otol Rhinol Laryngol* 1957; 66:537-546.
- Seltzer S, Mark AS. Contrast enhancement of the labyrinth on MR scans in patients with sudden hearing loss and vertigo: evidence of labyrinthine disease. *AJNR Am J Neuroradiol* 1991; 12:13-16.
- Mark AS, Seltzer S, Nelson-Drake J, Chapman JC, Fitzgerald DC, Gulya AJ. Labyrinthine enhancement on gadolinium-enhanced magnetic resonance imaging in sudden deafness and vertigo: correlation with audiologic and electronystagmographic studies. *Ann Otol Rhinol Laryngol* 1992; 101:459-464.
- Brogan M, Chakeres DW. Gd-DTPA-enhanced MR imaging of cochlear schwannoma. *AJNR Am J Neuroradiol* 1990; 11:407-408.
- Schuknecht HF. *Pathology of the ear*. Cambridge, MA: Harvard University, 1974; 61:258-262.
- Perlman H, Kimura R, Fernandez C. Experiments on temporary obstruction of the internal auditory artery. *Laryngoscope* 1959; 69:591-613.

## 4. Magnetic Resonance Examination of the Inner Ear and Cerebellopontine Angle in Patients with Vertigo and/or Abnormal Findings at Vestibular Testing

Jan W. Casselman<sup>(1)</sup>, Rudolf Kuhweide<sup>(2)</sup>, Ides Dehaene<sup>(3)</sup>,  
Willy Ampe<sup>(2)</sup> and Francis Devlies<sup>(1)</sup>

From the departments of Radiology<sup>(1)</sup>,  
Otorhinolaryngology<sup>(2)</sup>, and Neurology<sup>(3)</sup>,  
A.Z. St.-Jan Brugge, Brugge, Belgium.

*Published in: Acta Otolaryngol (Stockh) 1994; Suppl 513:15-27.*

### 4.1. ABSTRACT

The inner ears of 167 patients with vertigo and/or abnormal findings at vestibular testing were studied using magnetic resonance (MR). Pathology, potentially explaining vertigo was found in 54 patients, and was detected in the posterior fossa (28%), the internal auditory canal (28%) and the membranous labyrinth (44%). The overall percentage of pathology and the percentage of pathology found in the membranous labyrinth was high and was probably influenced by the referral pattern in our hospital where high resolution MR of the inner ear (three dimensional Fourier transformation-constructive interference in steady state sequence; 3DFT-CISS sequence) is available. Unenhanced and especially gadolinium (Gd)-enhanced T1-weighted spin-echo images, are needed to detect most of the pathology inside the internal auditory canal, and some of the lesions inside the membranous labyrinth. 3DFT-CISS images are the only images that can show fibrous obliteration of the intralabyrinthine fluid spaces, and are therefore necessary to recognize most of the intralabyrinthine pathology. Finally, T2-weighted spin-echo images are best suited to demonstrate cerebellar or brain stem infarction. An additional MR-angiography sequence (three dimensional Fourier transformation-fast imaging with steady precession; 3DFT-FISP) is used when vascular compression of the cochleovestibular nerve is suspected. MR is the method of choice to look for pathology in patients with vertigo, and allows detection of pathology that remains invisible with other imaging techniques. However, well adapted sequences are needed to detect these lesions. Key words: ear, abnormalities, ear, MR studies, Meniere's disease, temporal bone abnormalities, Temporal bone MR studies.

## 4.2. INTRODUCTION

In the past, the radiological study of patients with vertigo was difficult, and conventional radiographic studies and polytomography techniques rarely demonstrated the underlying pathology. Computed tomography (CT) represented a major advance in the study of the bony labyrinth (1) and the cerebellopontine angle (CPA), but its contribution to the clinical diagnosis of vertigo was limited. The advent of T1- and T2-weighted spin-echo magnetic resonance (MR) imaging allowed the detection of lesions in the CPA and internal auditory canal (IAC) in a more accurate way. However, the main step forward was achieved with the introduction of gadolinium (Gd)-enhanced MR imaging. With this technique very small intracanalicular lesions and intralabyrinthine lesions were visualized for the first time, and helped to explain the vertigo in considerably more patients (2-5). Finally, new three-dimensional Fourier transformation (3DFT) gradient-echo MR techniques provided very thin slices through the membranous labyrinth, IAC and CPA (6, 7). The 3DFT-constructive interference in steady state (CISS) MR technique visualizes the intralabyrinthine fluid and the cerebrospinal fluid (CSF) in the CPA and IAC in detail (6). Hence the combination of high contrast and high spatial resolution allows visualization of the facial nerve, the cochlear branch, the inferior vestibular branch and the superior vestibular branch of the cochleovestibular nerve separately (Fig. 1A-E) (6). Detection of intralabyrinthine fluid space obliterated by fibrous tissue has also become possible (8-11). This has enabled us to recognize minute pathology of the membranous labyrinth (8), as well as small nerve pathology or vascular pathology in the CPA and IAC.

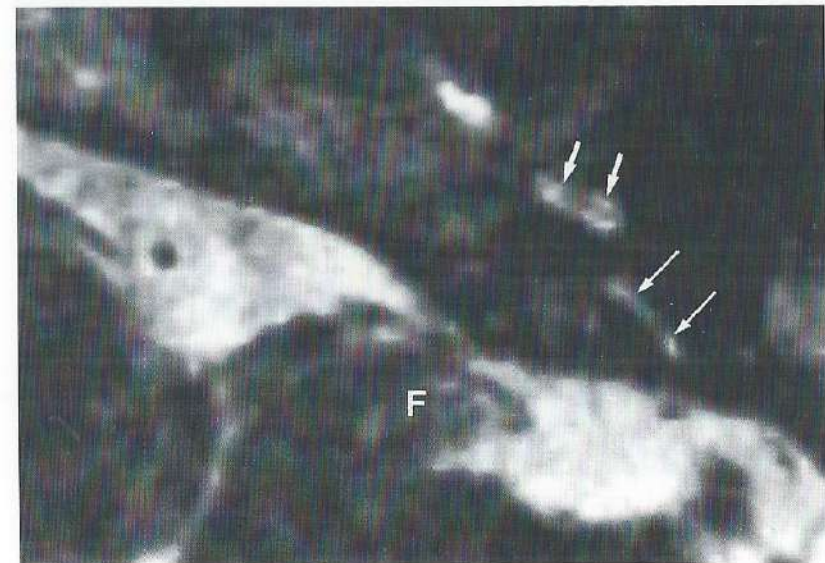
In this study we reviewed the MR examinations of the inner ear and posterior fossa of the 167 patients who were referred with vertigo and/or abnormal findings at vestibular testing, often in association with sensorineural hearing loss (SNHL). In these patients, the percentage of positive selective MR studies was rated; the distribution of the lesions in the posterior fossa, IAC and labyrinth was evaluated; and those lesions that could explain the vertigo and/or abnormal findings at vestibular testing were listed (Table I). Furthermore, we tried to identify which MR techniques were best adapted to detect specific pathologies.

## 4.3. SUBJECTS AND METHODS

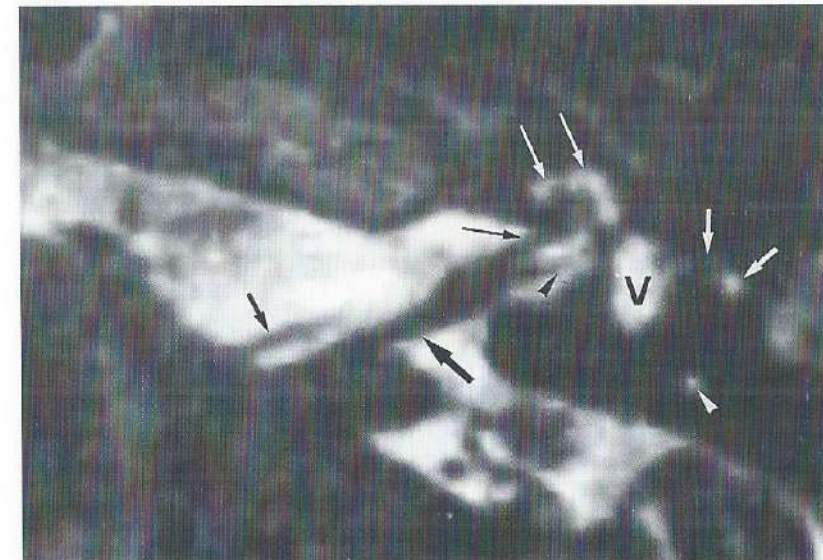
### 4.3.1. Patients

Over a period of 30 months (April 1991 to October 1993), 650 patients with SNHL and/or vertigo were referred for a selective MR study of the inner ear. Patients clinically suspected of having posterior fossa tumours or major cerebrovascular, especially vertebrobasilar, ischaemic disease underwent a routine brain examination and were excluded from the selective inner ear MR study. Of 650 patients, 167 had vertigo and/or abnormal findings at vestibular testing, and pathology findings were evident in 54 patients. The selective MR studies of these 54 patients (28 females, 26 men; average age 48 years) were reviewed.

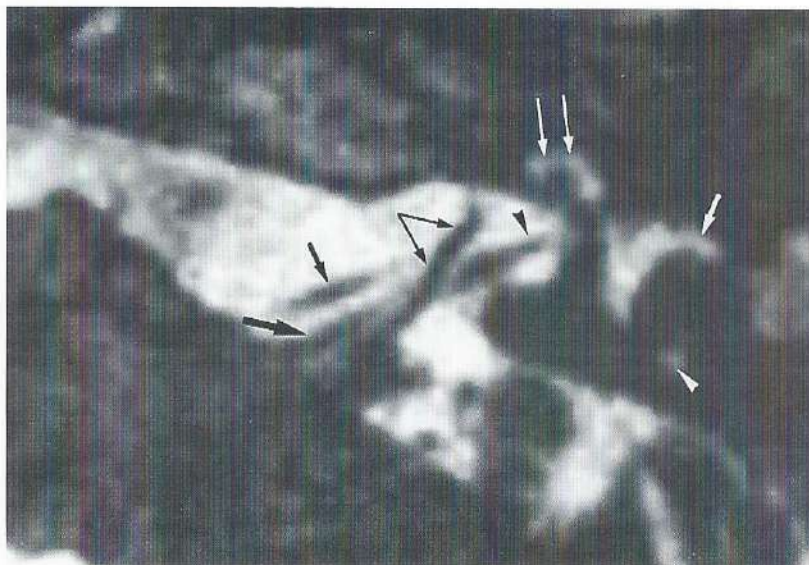
Fig. 1. Axial 0.7 mm thin CISS images through a normal left inner ear.



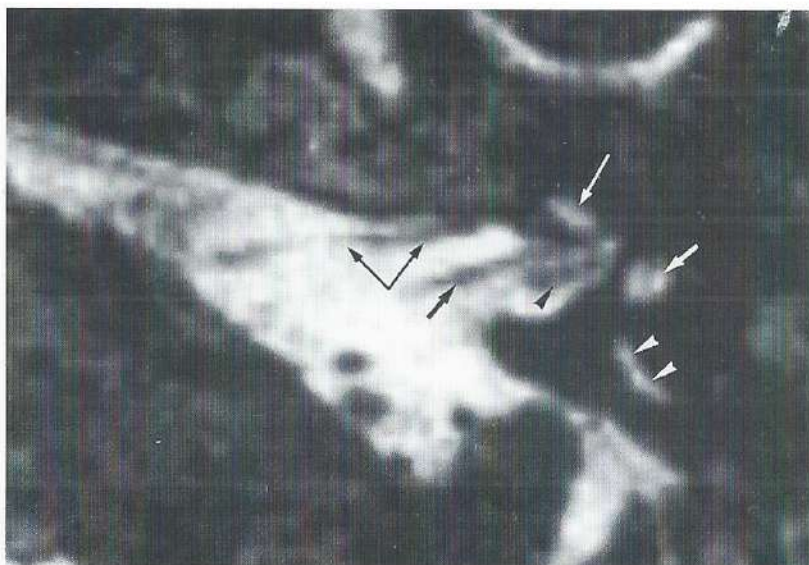
A



B



C



D



E

*A. At the level of the basal turn of the cochlea. The high signal of the fluid inside the basal turn of the cochlea (small white arrows) and posterior semicircular canal (long white arrows) can be recognized. At this level the floccule (F) can be seen in the cerebellopontine angle and is surrounded by high signal CSF.*

*B. At the level of the inferior part of the IAC. The facial nerve (small black arrow) is seen in the CPA and is just leaving the brain stem. The cochleovestibular nerve (large black arrow) can be followed throughout the CPA and is lying against the anterior wall of the floccule. The cochlear (long black arrow) and inferior vestibular (black arrowhead) branch of the cochleovestibular nerve are visible deep in the IAC. The typical bifurcation of the cochleovestibular nerve at this level makes identification of these branches possible. Normal high signal intralabyrinthine fluid is present inside the basal and second turn of the cochlea (long white arrows), vestibule (V), lateral semicircular canal (small white arrows) and posterior semicircular canal (white arrowhead).*

*C. At the level of the middle part of the IAC. The facial nerve (small black arrow) crosses the middle of the CPA and the cochleovestibular nerve can be followed from its root entry zone (large black arrow) to its inferior vestibular branch (black arrowhead) deep in the IAC. A large vascular loop is crossing the cochleovestibular nerve and can be followed deep in the IAC (long black arrows). A normal amount of fluid is again seen in the cochlea (long white arrows), lateral (small white arrow) and posterior (white arrowhead) semicircular canal.*

*D. At the level of the superior part of the IAC. At this level the typical parallel course of the facial nerve (small black arrow) and the superior vestibular branch of the cochleovestibular nerve (black arrowhead) in the IAC can be seen. The vascular loop (see Fig. 1C) is turning anteriorly and can be followed into the CPA (long back arrows). Intralabyrinthine fluid is recognized in the superior part of the cochlea (long white arrow), superior part of the vestibule (small white arrow) and in the crus commune of the superior and posterior semicircular canal (white arrowheads).*

*E. At the level of the superior semicircular canal. CSF is still seen in the superior part of the IAC (large black arrow) and normal fluid is recognized in the anterior (long white arrow) and posterior (small white arrow) limb of the superior semicircular canal.*

**Table 1:** Pathology found in the three different regions with listing of the number of patients in whom pathology was found. The best sequence or sequence pair to detect the pathology is indicated.

<b>PATHOLOGY-DIAGNOSIS</b>	<b>NUMBER OF PATIENTS</b>	<b>BEST SEQUENCE OR SEQUENCE PAIR</b>
<b>POSTERIOR FOSSA</b>		
Vertebrobasilar ischaemic disease	12	T2 SE
Vessel in contact with the cochleovestibular nerve	3	3DFT-FISP & CISS
<b>INTERNAL AUDITORY CANAL</b>		
Schwannomas	9	Gd-T1 SE
Neuritis	2	Gd-T1 SE
Metastasis (breast carcinoma)	1	Gd-T1 SE
Meningioma	1	Gd-T1 SE
Chondrosarcoma (presumed)	1	Gd-T1 SE
Postoperative changes (nerve resection)	1	CISS
<b>MEMBRANOUS LABYRINTH</b>		
Labyrinthitis Chronic Acute	5	CISS
Acute labyrinthitis	2	Gd-T1 SE
Congenit. Malf. saccular lateral semicircular canal	2	CISS
Large vestibular aqueduct syndrome	2	CISS
Short lateral semicircular canal	1	CISS
Aplasia of the semicircular canals	1	CISS
Cogan's syndrome	5	(& Gd-T1 in 1 patient)
Postoperative intralabyrinthine obliterations	2	CISS
Fibrous dysplasia	1	T2 SE & CISS
Cholesterol granuloma	1	T1 SE & CISS
Cholesteatoma	1	CISS
Vestibular schwannoma	1	Gd-T1 SE & CISS
<b>TOTAL = 54 PATIENTS WITH PATHOLOGY</b>		

CISS = Constructive interference in steady state sequence, gradient-echo sequence

FISP = Fast imaging with steady precession, gradient-echo time of flight sequence

Gd = Gadolinium

T1-SE = T1-weighted spin-echo sequence

T2-SE = T2-weighted spin-echo sequence

#### 4.3.2. Techniques

All studies were performed on a one tesla active shielded superconductive system (Magnetom SP 42, Siemens, Erlangen, Germany). A standard circular polarized head coil was used allowing simultaneous imaging of both inner ears. All patients were studied with axial 3 mm thick contiguous T1-weighted spin-echo images, 500/15/4 (repetition time/ echo time/ excitations) with and without intravenous gadolinium administration. They were also examined with a coronal contrast-enhanced T1-weighted sequence. In all patients, 0.1 mmol/kg of Gd-tetra-azacyclododecane tetraacetic acid (Dotarem, Guerbet Laboratories, Aulnay-sous-Bois, France) or Gd-diethylenetriamine pentaacetic acid (Magnevist, Schering AG, Berlin, Germany) was used. Moreover, a 3DFT- CISS gradient-echo sequence was used in all patients. The most important parameters of this sequence are: one slab 32 mm thick, 32 partitions, repetition time (TR) = 20 ms, echo time = 8 ms, matrix = 256 × 256, field of view = 176 mm. This results in 1 mm sections with in-plane resolution of 0.69 × 0.69 mm and a total acquisition time of 5 min 32 s (flip angle = 50°). Further details of this sequence have been published (3, 8, 9).

An additional T2-weighted sequence, 2000/15, 90/1, was used to study the posterior fossa in most of the patients older than 45 years, in order to exclude discrete vertebrobasilar ischaemic disease as the causative pathology (central vestibular disease). Four mm thick T2-weighted images were only used in younger patients in whom demyelinating disease was suspected, or if there was an increased risk of vascular disease. This 10 min 42 s sequence was avoided in other patients.

A vascular 3DFT-fast imaging with steady precession (FISP) sequence was used whenever a vascular anomaly or malformation was suspected on the routine T1- and T2-weighted spin-echo images. This sequence was also used to differentiate between solid lesions and vascular structures in the CPA and IAC. The parameters of this 3DFT-FISP vascular sequence were: TR = 35 ms, echo time = 10 ms, matrix = 196 × 256, field of view = 200 mm, one slab of 32 mm thickness with 32 partitions resulting in 1 mm thick slices and a flip angle of 30°. This sequence is a "time of flight" sequence and only the flowing blood has a high signal (white) on these images, while all other tissues have a lower signal intensity (grey or black). Therefore, definite differentiation between vessels and other structures is possible on these images. The value of MR angiography in patients with pulsatile tinnitus has been reported (12).

#### 4.3.3. Treatment of the data

The number of patients who had vertigo and/or abnormal findings at vestibular testing (often in association with SNHL), and who were referred for selective MR-study of the inner ear was determined. The aim of this study was to find out which of the different sequences (T1, T1-Gd, T2, 3DFT-CISS and 3DFT-FISP) were best suited to detect the different pathologies occurring in the posterior fossa, IAC and membranous labyrinth in this patient group. Furthermore, we wanted to illustrate the different kinds of lesions in the inner ear and CPA responsible for vertigo and/or abnormal findings at vestibular testing that can be demonstrated using MR today.

Retrospectively, the number of patients in whom lesions, explaining the clinical symptoms were found were identified. Moreover, the investigators tried to ascertain in how

many cases the causative pathology was detected in the posterior fossa, the IAC and the membranous labyrinth. These data are considerably influenced by the specific referral pattern in our hospital where high resolution MR of the inner ear (3DFT-CISS sequence) is available, and thus are only of relative value.

#### 4.4. RESULTS

Six hundred and fifty patients underwent a selective MR-study of the inner ear. Of these, 167 (26%) had vertigo and/or abnormal findings at vestibular testing (often in association with SNHL). Pathology was found in 54 (32%) of these 167 patients. In 15 (28%) of these patients the pathology was situated in the posterior fossa, and in another 15 (28%) it occurred in the IAC. Most of the pathology was located in the membranous labyrinth (24 patients; 44%). The different pathologies found in the posterior fossa, IAC and membranous labyrinth are listed in Table I.

##### 4.4.1. Posterior Fossa

Cerebellar and brain stem infarction and/or atrophy were the most frequent lesions found in the posterior fossa (80%). The T2-weighted spin-echo sequence was the most sensitive sequence in the detection of these lesions. The vascular anomalies with cross-compression of the cochleovestibular nerve were best evaluated using the 3DFT-CISS and 3DFT-FISP images.

##### 4.4.2. IAC

Acoustic schwannoma was the most frequent pathology seen in the IAC. The Gd-enhanced T1-weighted sequence was the most sensitive sequence in 14 of the 15 patients with pathology in the IAC, but the 3DFT-CISS images often added important information. In one patient the pathology could only be recognized on the CISS images (Table I).

##### 4.4.3. Membranous labyrinth

The largest variety of symptoms was discovered in the membranous labyrinth. The diagnosis of acute or old labyrinthitis, congenital malformation and fibrous obliteration of the intralabyrinthine fluid spaces in patients with Cogan's syndrome was frequently made. In 18 of the 24 patients the pathology was only detectable on the CISS images. In the other 6 patients the CISS images provided important additional information.

#### 4.5. DISCUSSION AND COMMENTS

In recent years, MR of the inner ear has become the method of choice to study patients with SNHL (13). Often these patients also have vertigo or vestibular disease (14). Vestibular symptoms consist of rotational dizziness (vertigo) and unsteadiness (disequilibrium), and vestibular signs include spontaneous, position or positional nystagmus and abnormal

postural stability. Electronystagmographic examination may reveal hypo- or non-responsiveness to caloric testing (horizontal semicircular canal paresis), or a directional nystagmus preponderance on the caloric or rotational test. A caloric hypo-responsiveness may be present without any dizziness due to central nuclear compensation. In a considerable number of patients vestibular symptoms occur without hearing disturbance. The possible mechanisms underlying vertigo and vestibular disease are well known but many of them remain undetected (15). In this study more than a quarter of the patients examined, using selective MR of the inner ear, had vertigo or vestibular disease; the pathology explaining the symptoms was found in nearly one-third of them. In 28% of these patients the pathology was found in the posterior fossa, in 28% it was located in the IAC, and in 44% the lesion was detected in the labyrinth. The surprisingly high percentage of positive studies is accentuated by the exclusion of posterior fossa or brain stem tumours, and clinically apparent vertebrobasilar ischaemic disease from this study.

However, all these percentages are influenced by the referral pattern. A lot of patients from other hospitals were only referred following a negative CT study. Clinicians also referred selected patients in whom they suspected inner ear pathology, or even intralabyrinthine pathology, because they knew that high resolution imaging of the inner ear was available in our hospital.

In some cases one can almost be sure that the pathological findings explain the vestibular symptoms (for example, schwannoma on a vestibular nerve). In other cases, however, it is difficult to prove a direct relationship between the lesion and the vestibular symptoms and the causative relationship can only be presumed. The results of this study show that the high number of positive studies is related to the use of the Gd-enhanced T1-weighted sequence and the newer 3DFT-CISS and 3DFT-FISP MR techniques.

##### 4.5.1. Posterior fossa pathology

The classic T2-weighted images were most sensitive for the detection of vascular ischaemic disease (infarctions) in the brain stem and/or cerebellum (9 patients). Pathology of the vertebral artery (16, 17), or infarction in the region of the anterior inferior cerebellar artery (18, 19), or posterior inferior cerebellar artery (20) is known to be a cause of vertigo.

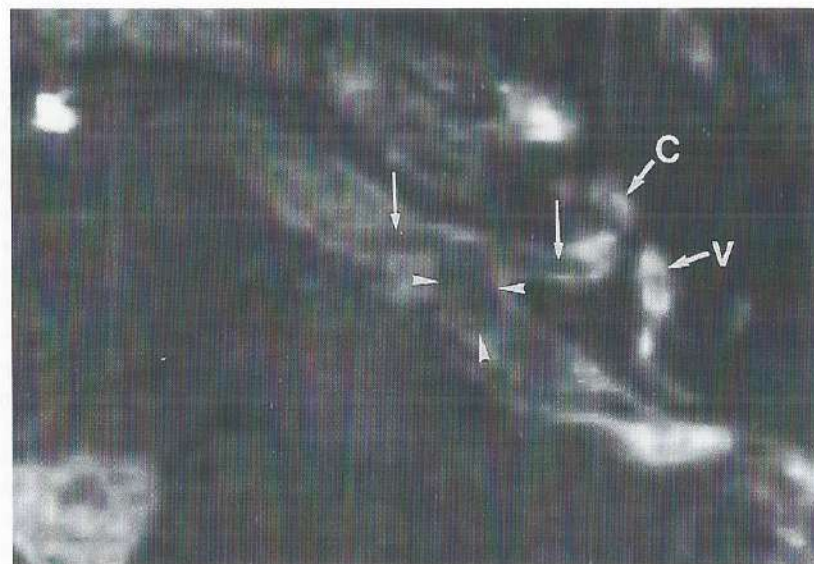
The detection of the remaining pathology in the posterior fossa has become feasible with the newer MR techniques. In 3 patients, a contact between the cochleovestibular nerve and a vessel in the CPA was demonstrated using 1 mm thick vascular time of flight images and/or CISS images. In the first patient a tortuous basilar artery was in contact with the nerve at its root-entry zone, and in a second patient an anomaly of the posterior inferior cerebellar artery (PICA) was touching the nerve at the same site. In a third patient, an ectatic loop of the superior petrous sinus was lying on top of the nerves near the porus of the internal auditory canal (Fig. 2A-E).

The relationships between vessels and nerves are only detectable on the one mm thin 3DFT-CISS and 3DFT-FISP images. The 3DFT-FISP vascular images can also prove that the structure in contact with the nerve is really a vessel, as only vessels are seen as white structures on these images. Compression of the cochleovestibular nerve can cause vertigo, continuous disequilibrium and acquired motion intolerance (cochleovestibular nerve compression syndrome) (21, 22). Air CT cisternography was the first method that could clearly

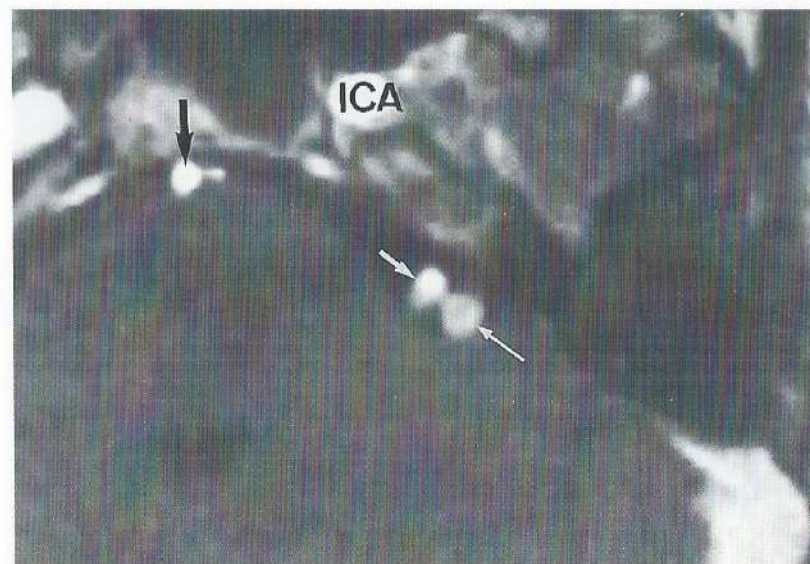
Fig. 2. Venous ectasia in contact with the left cochleovestibular nerve in a patient with SNHL (left) and vertigo (clinical picture of Meniere's disease) thought to be an acoustic schwannoma on contrast-enhanced CT.



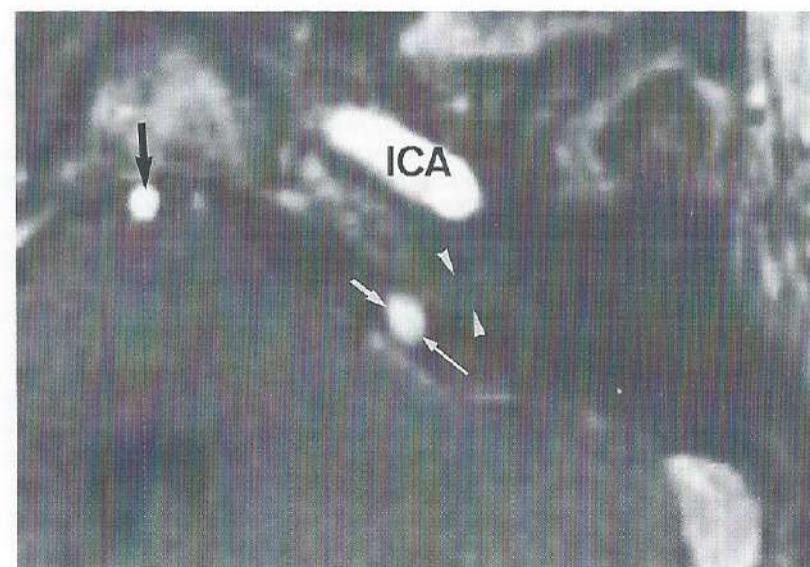
A



B



C



D



E

**A.** Axial Gd-enhanced T1-weighted spin-echo image at the superior border of the porus of the IAC. An enhancing nodule (long white arrows) is present in the CPA but is centred a little above the porus of the IAC. Superior part of IAC (large black arrows).

**B.** Axial 1 mm thick 3DFT-CISS image through the superior part of the IAC. A nerve in the CPA and IAC (long white arrows) can be depicted and the eccentric lesion (white arrowheads) seems to be fixed on the nerve. Normal fluid is seen in the cochlea (C) and vestibule (V).

**C-D.** Axial 3DFT-FISP (vascular time of flight) image above the level of the porus (C) and at the level of the porus (D). On these images only flowing blood is seen as high signal intensity (white). High signal is therefore seen inside the internal carotid artery (ICA) and the basilar artery (large black arrow). At the level just above the porus a vessel is seen posteriorly (long white arrow) and anteriorly (small white arrow) in the upper part of the CPA (C). These vessels have a common loop with inferior convexity (long and small white arrow), and this loop is in contact with the superior border of the nerves at the level of the porus (D). The nerves can be seen in the IAC on this image (white arrowheads).

**E.** 3-dimensional reconstruction of the vessels in and around the left CPA. The superior petrous vein can be followed along the superior border of the petrous bone (long white arrows). The superior petrous vein continues as an ectatic loop, hanging with its inferior convexity at the level of the CPA (small white arrows). The vein then continues superiorly and anteriorly (white arrowhead). The angle between the vertical and horizontal intratemporal portion of the internal carotid artery (large black arrow), the vertebral arteries (long black arrows) and basilar artery (short black arrow) can also be recognized.

show the vessel-nerve contact (23). However, today MR has become the method of choice, thanks to better contrast-resolution, the ability to image the nerves and vessels at all planes, and the non-invasive character of the technique (12, 24).

The impact of the T1 and CISS sequences on the pathology discovered in the posterior fossa is limited.

#### 4.5.2. Internal Auditory Canal pathology

The detection of pathology in the IAC was possible using the Gd-enhanced T1-weighted images in 14 of the 15 cases. In all these cases, the CISS-images helped to further differentiate the lesion or demonstrate the extension of the lesion in more detail.

Schwannomas on the superior and inferior vestibular branch of the cochleovestibular nerve or a schwannoma on the cochlear branch of the cochleovestibular nerve, with compression on one of the vestibular branches, can cause vertigo. On Gd-enhanced T1-weighted images both small acoustic schwannomas and neuritis of the vestibular branches are seen as a region of contrast enhancement along the nerves inside the IAC. CISS images make differentiation possible. A hypointense nodule will be seen inside the IAC replacing the CSF in the case of an acoustic schwannoma. One can even tell on which nerve branch the schwannoma is situated if the schwannoma is small enough (Fig. 3A, B).

On the contrary, in the case of neuritis, normal nerves will be seen in the IAC on the CISS images. (Fig. 4A-C).

An interesting finding is that six of the nine schwannomas found in our study were small and were strictly intracanalicular. Clinical studies showed that purely intracanalicular acoustic schwannomas result in earlier onset of vestibular symptoms (25, 26), and this explains the high percentage of small and intracanalicular schwannomas in our study. These

**Fig. 3.** Small schwannoma near the fundus of the IAC in a 65-year-old man presenting with vertigo and SNHL (clinical picture of Meniere's disease) on the right side.



A



B

*A. Axial T1-weighted spin-echo image through the IAC. An enhancing lesion is seen in the distal part of the IAC (long white arrow). Cochlea (white arrowhead), vestibule (small white arrow) and fat containing marrow inside the petrous apex (large black arrow).*

*B. Axial 3DFT-CISS image through the IAC. A hypointense nodule (long black arrow) is replacing the CSF deep in the IAC. This lesion is situated anteriorly in the fundus and is therefore probably originating on the cochlear branch of the cochleovestibular nerve. The vertigo in this patient can be explained by the compression of the mass on the inferior vestibular branch of the cochleovestibular nerve (long white arrows). Normal endolymph and/or perilymph is visible in the cochlea (large black arrow), lateral semicircular canal (white arrowheads), posterior semicircular canal (small white arrow) and vestibule (V).*

schwannomas often remain undetected on CT and unenhanced MR and therefore Gd-enhanced T1 and/or 3DFT-CISS images are needed.

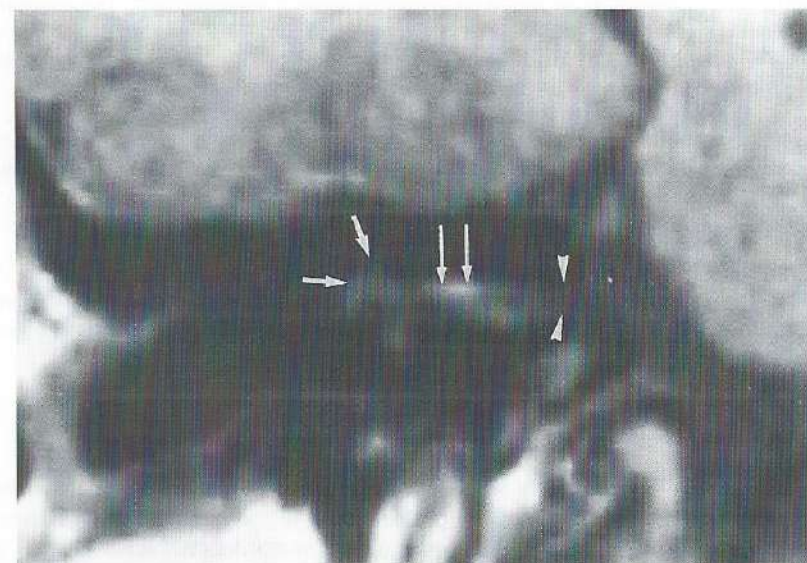
3DFT-CISS images can also play a role in the differential diagnosis of acoustic schwannoma and other tumours like a meningioma. When the facial and cochleovestibular nerves can be seen coming out of a tumour in a perpendicular way, then an acoustic schwannoma is unlikely (6). The CISS sequence also allowed a better visualization of the relationship between tumor and nerves in a previously reported patient, with a breast carcinoma metastasis (13), and in the patient with the presumed chondrosarcoma (Table I), both growing into the IAC. Although these lesions were already detected on the Gd-enhanced T1-weighted images.

Finally, in one patient the pathology could only be depicted on the CISS images. In this patient the absence of the superior and inferior vestibular branch of the cochleovestibular nerve, caused by previous surgery, was only visible on the thin high contrast CISS images (Fig. 5A-D).

*Fig. 4. 22-year-old woman with acute vertigo due to vestibular neuritis.*



A



B



C

A. Axial Gd-enhanced T1-weighted spin-echo image through the IAC. A fusiform enhancement is seen posteriorly in the deep part of the IAC (long white arrows), corresponding with the normal course of the superior vestibular branch of the cochleovestibular nerve. Porus of the IAC (white arrowheads), anterior wall of the IAC (small white arrows).

B. Coronal Gd-enhanced T1-weighted spin-echo image through the IAC. This coronal image is made through the posterior part of the IAC, and through the posterior and lateral semicircular canals (small white arrows). A more linear enhancement can be seen just under the roof of the IAC (long white arrows). Porus of the IAC (white arrowheads).

C. Axial 3DFT-CISS image through the superior part of the IAC. A normal superior vestibular branch of the cochleovestibular nerve can be seen in the superior and posterior part of the IAC (long white arrow), excluding the possibility of a schwannoma. Intralabyrinthine fluid in the cochlea (small white arrow), the vestibule and anterior part of the lateral semicircular canal (white arrowheads).

The resection of these nerves was performed several years before and therefore we cannot state that the vestibular symptoms are explained by the MR findings, as central nuclear compensation could have occurred in this patient.

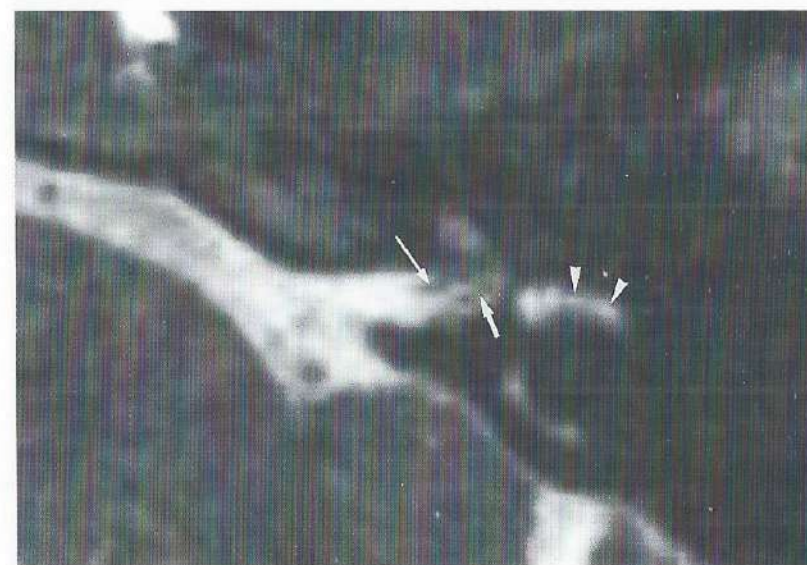
#### 4.5.3. Membranous labyrinth pathology

The largest amount of pathology was found within the labyrinth. This is a new finding although theoretically not surprising. It is probably due to the fact that only patients with unexplained vertigo were referred to our hospital for a more detailed inner ear MR study, while the more easily detectable posterior fossa and IAC pathology was already recognized on the CT examination.

Fig. 5.



A



B



C



D

**Fig. 5.** Axial 3DFT-CISS images of the inner ear in a patient presenting with vertigo, who was operated upon 10 years previously for an acoustic schwannoma, with resection of the vestibular branches of the cochleovestibular nerve, using a posterior fossa approach. Images through the abnormal inner ear on the right at the superior (A) and inferior (C) part of the IAC and corresponding images through the normal left inner ear (B, D).

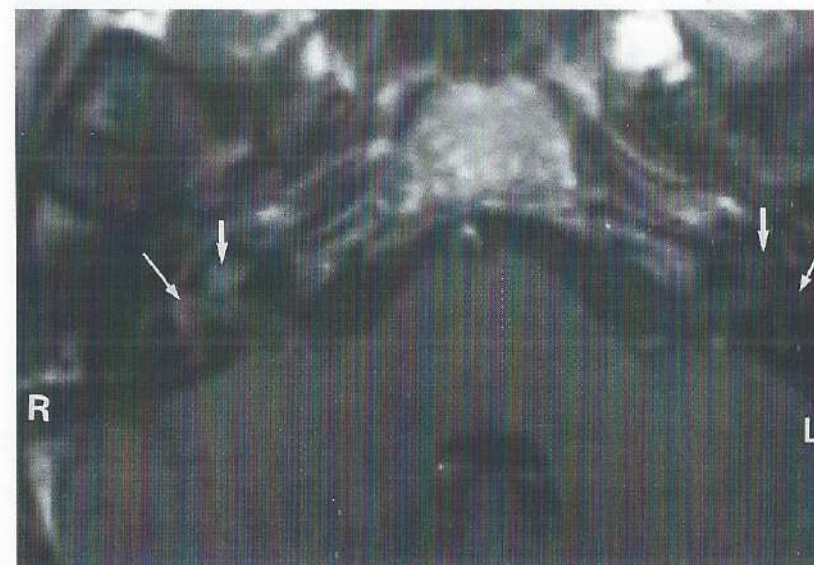
**A-B.** Only the facial nerve (long white arrow) can be recognized high in the right IAC. On the left side both the facial nerve (long white arrow) and superior vestibular branch of the cochleovestibular nerve (small white arrow) can be seen parallel to one another. Fluid in the anterior part of the lateral semicircular canal (white arrowheads).

**C-D.** The cochlear branch of the cochleovestibular nerve (long white arrow) can be seen in the right IAC, the inferior vestibular branch could not be found. Both the cochlear (long white arrow) and the inferior vestibular branch (small white arrow) of the cochleovestibular nerve are recognized in the inferior part of the IAC. Fluid in the vestibule and posterior part of the lateral semicircular canal (white arrowheads).

The use of Gd-enhanced T1-weighted images allowed radiological detection of intralabyrinthine pathology such as labyrinthitis (Fig. 6) and intralabyrinthine schwannomas for the first time (5, 8, 14).

**Fig. 6.** Axial Gd-enhanced T1-weighted spin-echo image in a 46-year-old man with acute vertigo and SNHL on the right side due to viral labyrinthitis.

Normal low signal fluid is seen in the left cochlea (small white arrow) and left vestibule (long white arrow). Abnormal contrast enhancement is seen in the right cochlea (small white arrow) and vestibule (long white arrow). The axial 3DFT-CISS image of this patient made at the same level was normal, proving that the enhancement was caused by leakage of Gd through an abnormal labyrinthine membrane into the intralabyrinthine fluid (and Gd is not visible on 3DFT-CISS images).

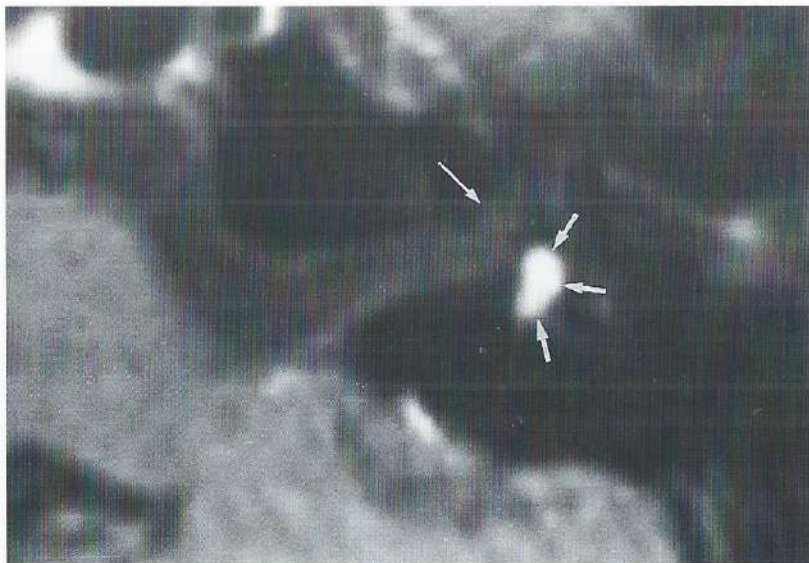


However, it remains difficult to differentiate between both entities when an enhancing lesion is seen inside the vestibule. Before the 3DFT-CISS sequence was used, follow-up studies were necessary to distinguish between these pathologies. In the case of labyrinthitis the enhancement disappeared after some months, while it persisted in case of schwannoma. With the use of the 3DFT-CISS sequence immediate differentiation is possible. The CISS images only show the intralabyrinthine fluid inside the membranous labyrinth, and the presence of Gd is not seen on these images. Therefore, the normal high signal intensity of intralabyrinthine fluid is seen in the case of labyrinthitis, and a low signal is seen in the case of schwannoma where the intralabyrinthine fluid is replaced by the soft tissue mass (Fig. 7A, B) (8).

The ability to recognize fibrous or tumoural obliteration of the intralabyrinthine fluid spaces makes the CISS-sequence the most sensitive sequence, in the detection of pathology in the vestibular part of the membranous labyrinth. The Gd-enhanced T1-weighted sequence was the most sensitive sequence in 4 patients, whereas the CISS sequence was the only sequence able to detect the pathology in 18 of the 24 patients.

Gd enhancement inside the membranous labyrinth is seen in the acute phase of labyrinthitis, but in the chronic phase fibrous obliteration occurs. This is only visible on the CISS images, as was seen in 5 patients. In the very late stage, calcified obliteration will be seen, which is visible on CT. The fibrous obliteration seems to be far more frequent than the

**Fig. 7.** Vestibular schwannoma in a young female presenting with SNHL and spontaneous nystagmus to the right with pathologic rotational and caloric tests. Axial Gd-enhanced T1-weighted spin-echo image (A) and 3DFT-CISS image (B) at the level of the left vestibule.



A



B

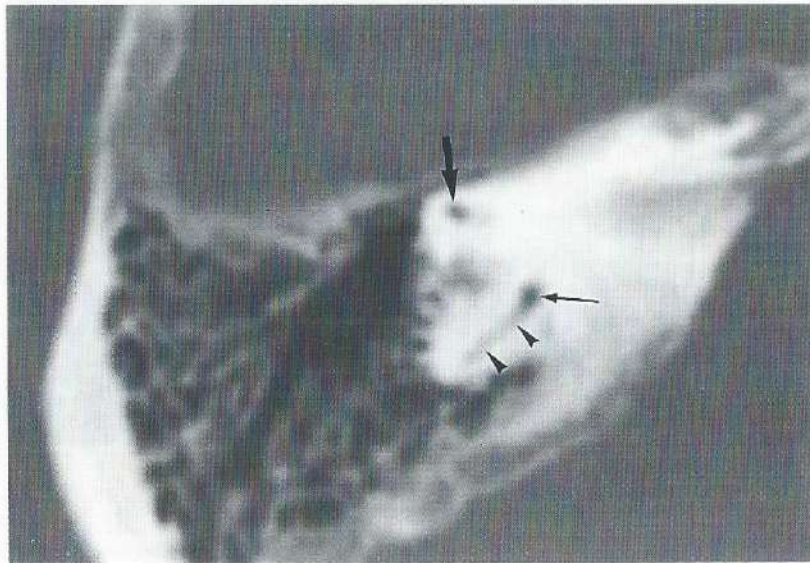
**A.** Clear and well delineated enhancement is seen in the left vestibule (small white arrows). No enhancement is visible in the cochlea (long white arrow).

**B.** Normal high signal fluid is seen in the IAC, cochlea (long white arrow) and posterior semicircular canal (white arrowhead). The high signal fluid in the vestibulum is nearly totally replaced by a low signal mass (small white arrows) proving that we were not dealing with Gd accumulation in the intralabyrinthine fluid but with Gd accumulation inside a soft tissue tumor (schwannoma). Cochlear (long black arrow) and inferior vestibular (large black arrow) branch of the cochleovestibular nerve.

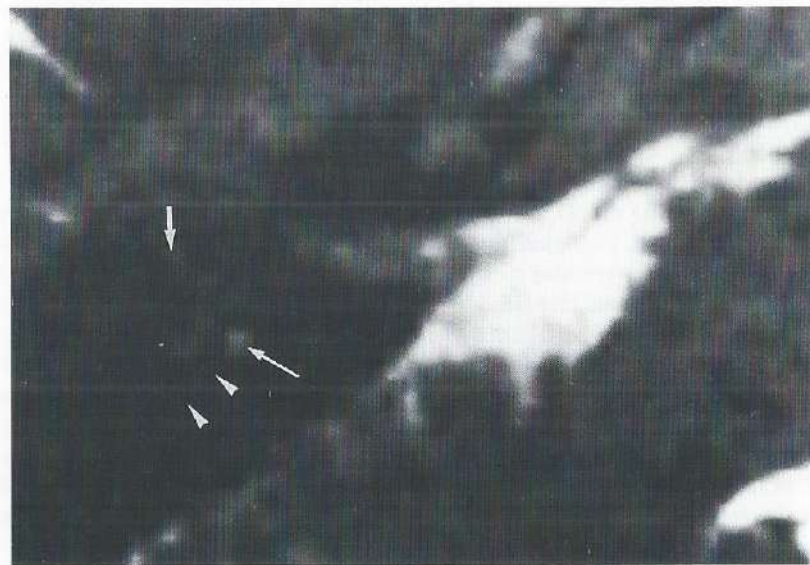
calcified "end-stage" obliteration. However, the diagnosis of fibrous obliteration of the vestibule or semicircular canals, can only be made when obliteration of the fluid spaces is seen on the CISS image, in conjunction with a negative CT examination (Fig. 8A-D).

Fibrous obliterations were also seen in patients with Cogan's syndrome (9, 10). Cogan's syndrome is a rare syndrome consisting of non-syphilitic interstitial keratitis and audiovestibular dysfunction and primarily affects young adults. The cause is most probably a systemic vasculitis, possibly of autoimmune origin. In 5 patients with Cogan's syndrome, soft tissue obliterations were seen in the membranous labyrinth, especially in the vestibule and semicircular canals, which explained the vertigo in these patients. Obliteration of the intralabyrinthine fluid spaces, due to connective tissue ingrowth and cellular debris, has been reported in histological studies and correlates well with the findings on the CISS images (Fig. 9A-C). Intralabyrinthine Gd-enhancement was seen in only one of the patients with Cogan's syndrome. This leakage of Gd through the blood-labyrinth barrier is probably only seen in the acute phase of the disease, and therefore the Gd-enhanced T1-weighted sequence is less sensitive than the 3DFT-CISS sequence in patients with Cogan's syndrome (9).

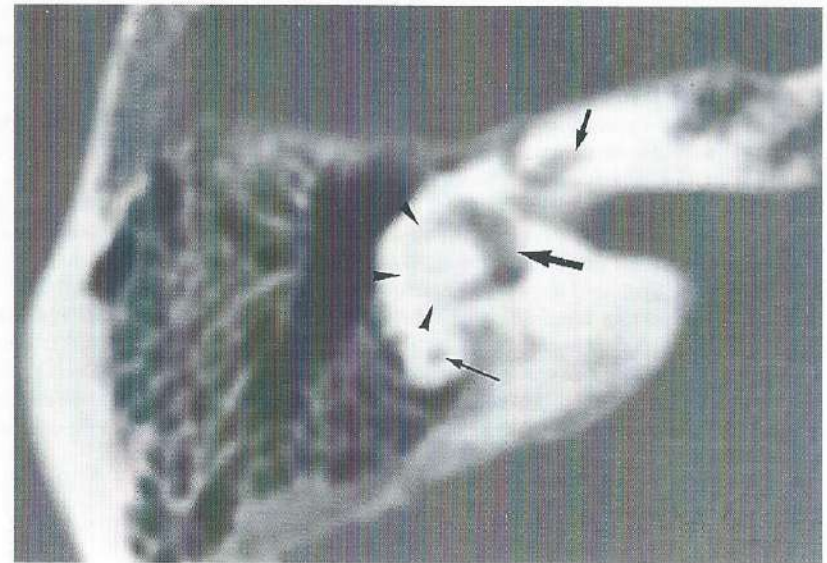
*Fig. 8. 64-year-old woman presenting with vertigo and with an abnormal electronystagmographic study, axial corresponding computed tomography (CT) images and 3DFT-CISS MR images through the right inner ear at the level of the superior semicircular canal (A-B) and the vestibule (C-D).*



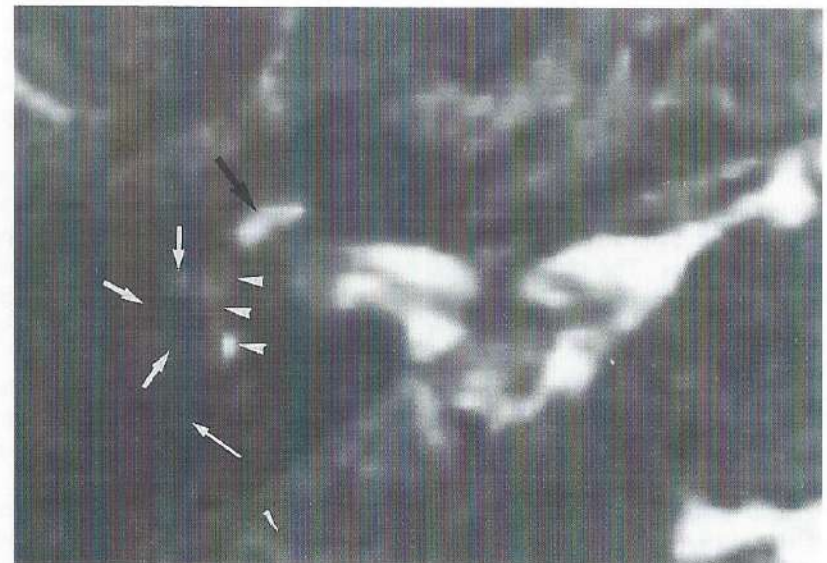
A



B



C



D

*A. A normal patent anterior (large black arrow) and posterior limb (long black arrow) of the superior semicircular canal and crus commune of the superior and posterior semicircular canal (black arrowheads) are seen on CT.*

*B. Normal intralabyrinthine fluid is only seen in the posterior limb of the superior semicircular canal (long white arrow) and no fluid is found in the anterior limb of this canal (small white arrow) and in the crus commune (white arrowheads). The obliteration must be caused by soft tissues as no calcifications were seen on CT.*

*C. A normal patent vestibule (large black arrow), posterior semicircular canal (long black arrow) and superior part of the cochlea (small black arrow) are visualized. But there is a calcific obliteration of the lateral semicircular canal (black arrowheads), better known as "labyrinthitis ossificans", and these findings are seen in cases of chronic labyrinthitis.*

*D. A normal amount of intralabyrinthine fluid is only visible in the cochlea (large black arrow). The absence of fluid in the lateral semicircular canal (small white arrows) is explained by the calcifications inside this canal that were seen on CT but the absence of fluid in the posterior semicircular canal (long white arrow) and in the main part of the vestibule (white arrowheads) is not caused by calcifications (normal on CT) and must therefore be caused by soft tissue obliteration.*

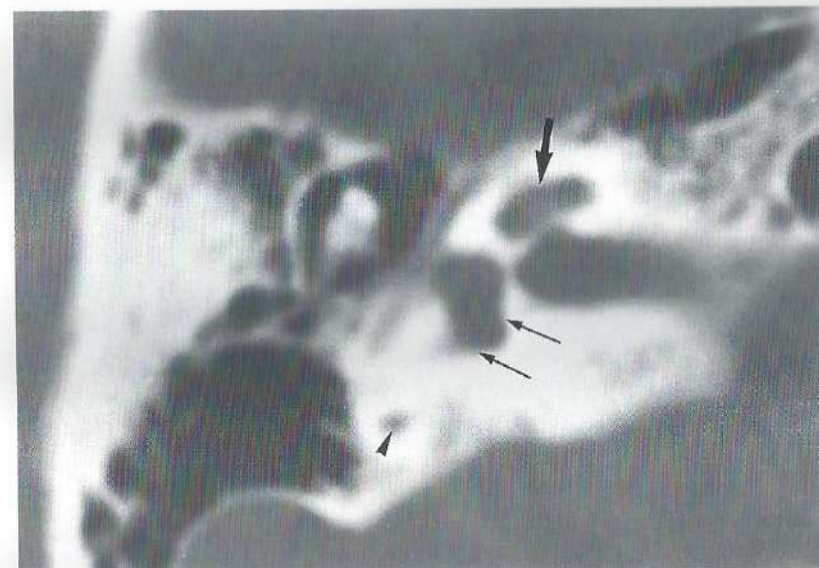
After surgical or traumatic opening of the labyrinth, fibrous obliteration is often found in the cochlea. This is probably caused by the loss of the intralabyrinthine fluid, and bleeding due to the removal of the posterior labyrinth (vestibule and semicircular canals). This was seen in 2 patients in whom translabyrinthine removal of an acoustic neuroma was performed. Obliterations are even seen after resection of deep intracanalicular schwannomas via a suboccipital approach. Another patient was operated upon because of a cholesteatoma, with fistulization of the lateral semicircular canal. The MR, which was taken several months after surgery, showed complete obliteration of all semicircular canals and part of the vestibule (Fig. 10A-C).

Tumours can also grow into the membranous labyrinth causing similar replacement of the intralabyrinthine fluid. They will result in vertigo when the vestibule or semicircular canals are involved. Such an extension was seen in a case of very aggressive biopsy-proven cholesterol granuloma. The obliteration of the vestibule and the posterior semicircular canal, caused by the cholesterol granuloma, was best seen on the T1-weighted images but the fistula between the lesion and the posterior semicircular canal was only visible on the CISS images (8).

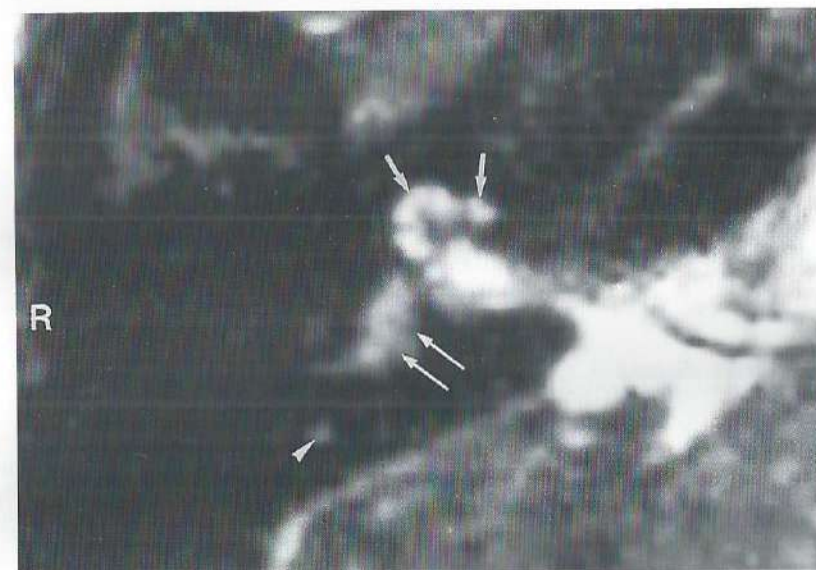
Finally bone disease such as fibrous dysplasia can alter the bony labyrinth and can compress or destroy the vestibular part of the membranous labyrinth. The CISS images again offer the possibility of evaluation, if the intralabyrinthine fluid spaces are patent (6, 8).

Congenital malformations of the labyrinth were the most frequent lesions found in patients with vertigo. The lesions are difficult to recognize on routine T1, T2 and Gd-enhanced T1-weighted spin-echo images, because these images are too thick, and volume averaging artifacts can render the lesions invisible. The 1 mm thin 3DFT-CISS images, however, are far more sensitive and show the malformations in detail. In 2 patients a saccular lateral semicircular canal was found, one patient had an abnormally short lateral semicircular canal, 2 had an enlarged endolymphatic sac (large vestibular aqueduct syn-

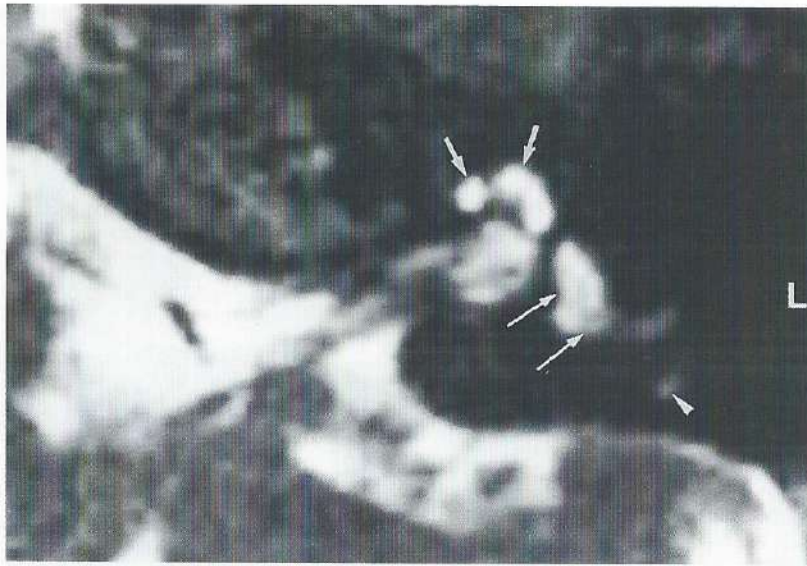
**Fig. 9.** 20-year-old man with Cogan's syndrome presenting with SNHL and vertigo. Axial CT (A) through the right labyrinth and axial 3DFT-CISS image through the abnormal right (B) and normal left (C) vestibule.



A



B



C

**A.** Normal low density is seen inside the cochlea (large black arrow), the vestibule (long black arrows) and the posterior semicircular canal (black arrowhead).

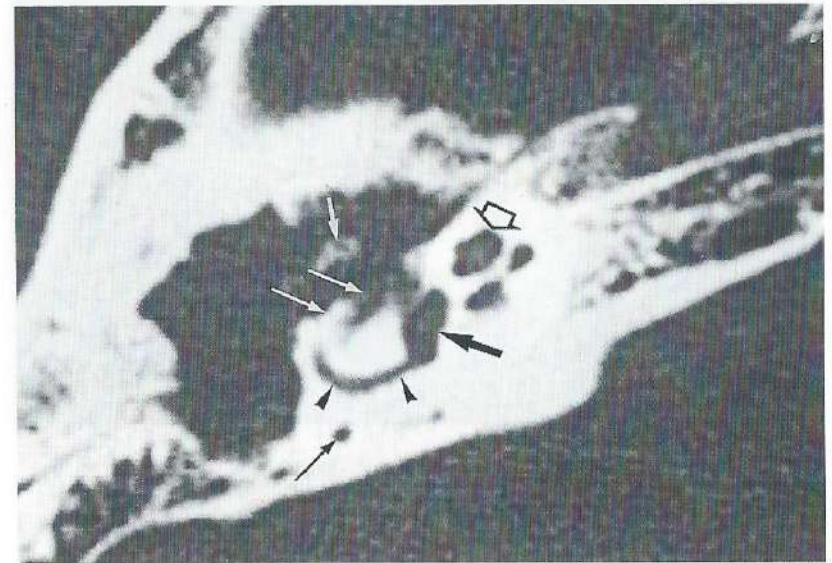
**B-C.** High signal intralabyrinthine fluid is seen in the cochlea (small white arrows) and the posterior semicircular canal (white arrowheads) on both sides. Normal fluid can also be seen in the vestibule on the left side but there is a reduced signal intensity inside the vestibule on the right side (long white arrows). Compare also the signal intensity of the right vestibule with the signal intensity seen in the right cochlea, in normal circumstances all compartments of the membranous labyrinth have the same signal intensity (see also Fig. 1). The loss of signal inside the right vestibule must be due to soft tissue obliteration (known in Cogan's syndrome) as no calcifications inside the vestibule are seen on CT.

drome) (Fig. 11A-D) and one had an aplasia of all semicircular canals. This last patient also had a cleft palate, bilateral caloric unresponsiveness, and was completely deaf on the left side.

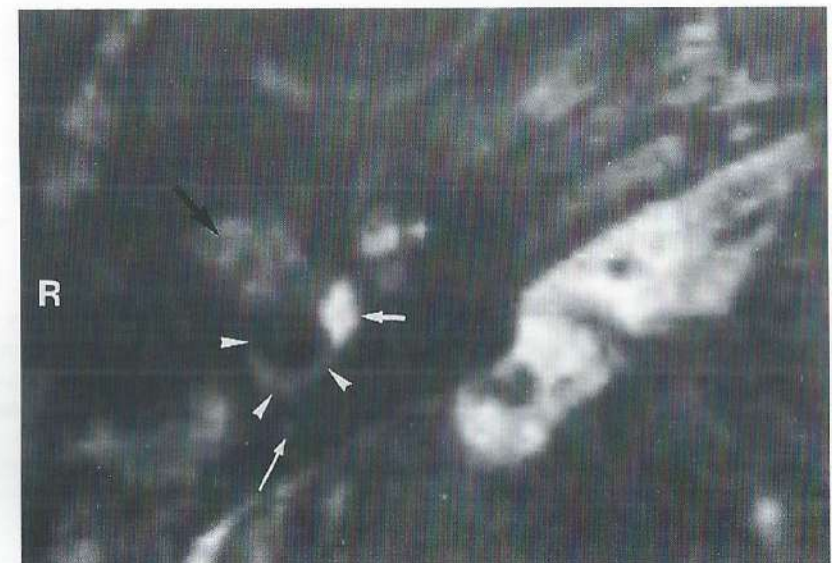
#### 4.5.4. Meniere's disease

A clinical diagnosis of "Meniere's disease" was made in 52 of the 167 patients with vertigo. However, in 9 (17%) of these patients other pathology was found including: intracanalicular acoustic schwannoma (3 patients, also the patient illustrated in Fig. 3), postoperative fibrous obliteration of the vestibular system (2 patients), cerebellar and brainstem infarction (2 patients), venous ectatic loop compressing the cochleovestibular nerve (one patient [see Fig. 2]) and a congenitally malformed saccular lateral semicircular canal (one patient).

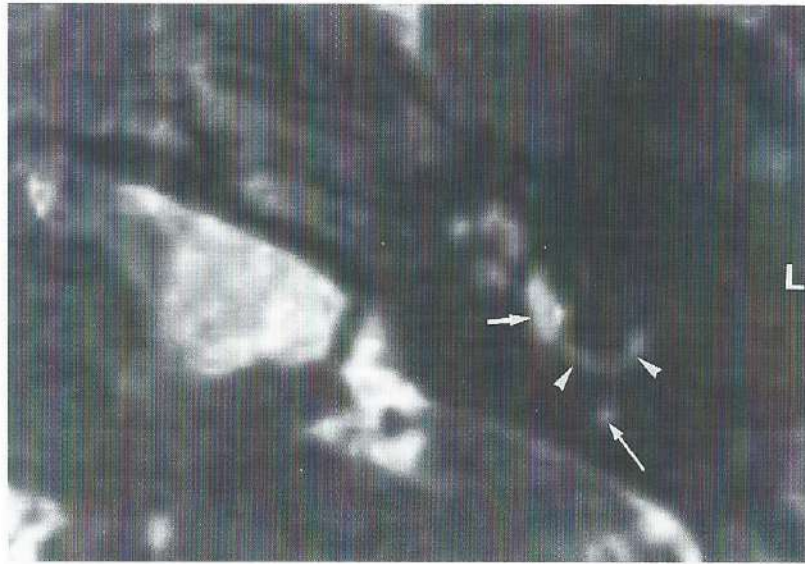
**Fig. 10.** 21-year-old man with a history of cholesteatoma with involvement of the lateral semicircular canal on the right side, he complained of vertigo in the first days following surgery. Preoperative CT of the right inner ear (A) and postoperative 3DFT-CISS MR (several months after surgery) through the right (B) and left (C) labyrinth.



A



B



C

*A.* A middle ear cholesteatoma nearly completely destroyed the ossicles (small white arrow) and fistulization to the lateral semicircular canal (long white arrows) was also seen on the CT images. A normal patent cochlea (open black arrow), vestibule (large black arrow), posterior part of the lateral semicircular canal (black arrowheads) and posterior semicircular canal (long black arrow) was seen.

*B-C.* Postoperative and/or inflammatory changes are present in the middle ear (large black arrow). The fluid in the posterior part of the lateral semicircular canal (white arrowheads) and in the posterior semicircular canal (long white arrow) is lost. Compare with the normal amount of fluid in the left lateral (white arrowheads) and posterior (long white arrow) semicircular canals and with the normal fluid inside the vestibule on both sides (short white arrows). The fibrous obliteration must have occurred during the period when the cholesteatoma invaded the lateral semicircular canal as no fluid leaked out of the canal during operation. Therefore obliteration of the lateral and posterior semicircular canal was probably present when the preoperative CT images were made but could not be detected.

The radiological findings were non-specific for Meniere's disease and apparently these lesions are able to mimic the disease. The low percentage of pathological findings in patients with clinical "Meniere's disease" is an important finding. If the patients with clinical "Meniere's disease" had been excluded from the study, we would have found pathology in 39% (45/115) of the patients.

#### 4.6. CONCLUSIONS

1. Pathology was found following selective inner ear MR studies in 32% of the patients presenting with vertigo and/or abnormal vestibular findings.

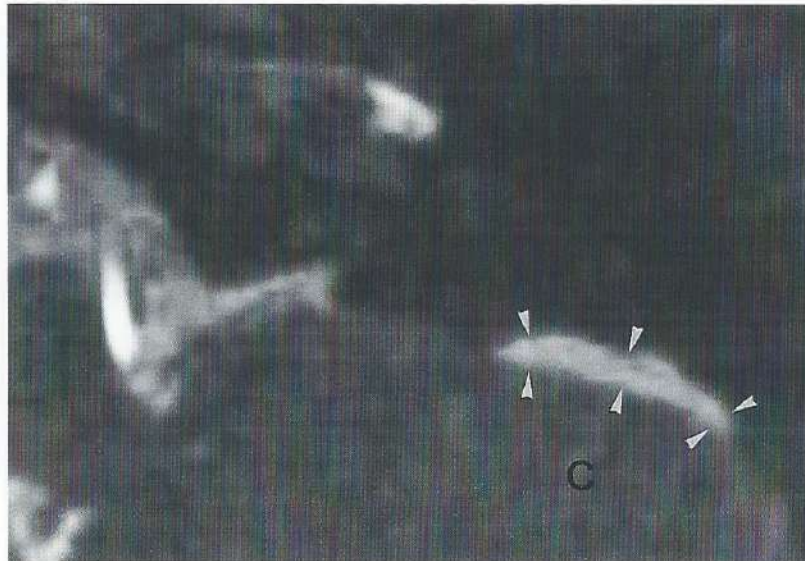
**Fig. 11.** 19-year-old man presenting with vertigo. Axial T1-weighted spin-echo image through the left labyrinth (A) and axial 3DFT-CISS image through the membranous labyrinth (B) and low posterior fossa (C) and 3DFT-CISS sagittal reconstruction (D).



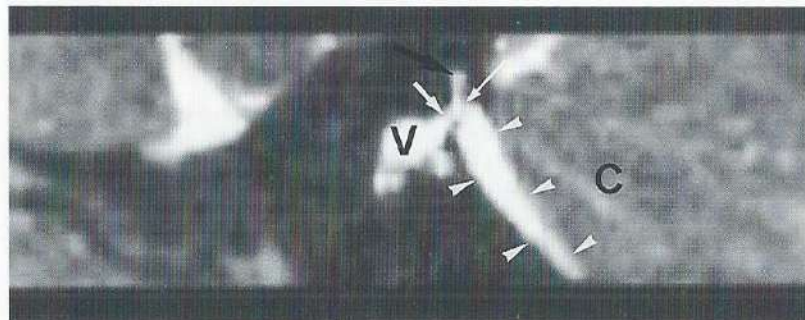
A



B



C



D

*A. The enlarged endolymphatic sac (white arrowheads) was only seen in retrospect after appropriate windowing. Cochlea (small white arrows).*

*B. The fluid filled enlarged endolymphatic sac (white arrowheads) is far better seen than on the T1-weighted image and is in contact with the anterior wall of the left cerebellum. The connection (long white arrow) with the vestibule (V) can also be recognized. The diameter of the posterior semicircular canal (small white arrow) is much smaller than the diameter of the endolymphatic sac. Cochlear branch (large black arrow) and inferior vestibular branch (black arrowhead) of the cochleovestibular nerve.*

*C. The largest volume of the endolymphatic sac can be found between the temporal bone and the cerebellum (white arrowheads). This part of the sac outside the vestibular aqueduct cannot be evaluated on routine CT and T1-weighted images and can even be missed on T2-weighted images. Cerebellum (C).*

*D. The thin slices and detailed visualization (high contrast) of the endolymphatic sac on the CISS images enable us to make clear reconstructions at all planes. On this sagittal reconstruction, the cranio-caudal extension of the endolymphatic sac (white arrowheads) can be evaluated and the relation with the cerebellum (C) is seen. The connection with the labyrinth (long white arrow) is visible. The superior semicircular canal (large black arrow), the crus commune (small white arrow) and the vestibule (V) can all be recognized in detail.*

- In these patients the pathology was most frequently (44%) found in the membranous labyrinth. The 3DFT-CISS sequence was the most sensitive sequence to identify intralabyrinthine pathology, showing the soft tissue obliterations of the intralabyrinthine fluid spaces. Additional unenhanced and Gd-enhanced T1-weighted images remained necessary to detect the pathology in some patients.
- In 28% of the patients pathology was found in the IAC and was best detected on Gd-enhanced T1-weighted images. (In one postoperative case the pathology was only visible on the CISS images.)
- Pathology was found in the posterior fossa in 28% of the patients and here the T2-weighted images were most sensitive for the detection of vertebrobasilar ischaemic disease. CISS images and especially the FISP-vascular images were necessary to show the relationship of the vessels to the nerves, when a vascular compression of the cochleovestibular nerve was suspected.
- Selective MR of the inner ear is the imaging method of choice in patients with vertigo. Unenhanced and Gd-enhanced T1-weighted spin-echo images, and additional good quality gradient-echo images (3DFT-CISS) are necessary to recognize all pathology. Vascular sequences are only needed when vascular compression of the cochleovestibular nerve is suspected on the routine sequences.

#### 4.7. REFERENCES

- Jackler RK, Dillon WP. Computed tomography and magnetic resonance of the inner ear. *Otolaryngol Head Neck Surg* 1988; 99:494-504.
- Valvassori GE. Diagnosis of retrocochlear and central vestibular disease by magnetic resonance imaging. *Ann Otol Rhinol Laryngol* 1988; 97:19-22.
- Casselmann JW, Kuhweide R. Prise de contraste dans le labyrinthe en IRM. *Radiologie J CEPUR* 1993; 13:26-31.

4. Mark AS, Seltzer S, Fitzgerald D. Enhancement of the endolymphatic sac on gadolinium-enhanced MRI in patients with hearing loss and vertigo: a possible sign of endolymphatic hydrops. *Ann Neurol* 1992; 32:296.
5. Mark AS, Seltzer S, Nelson-Drake J, Chapman JC, Fitzgerald DC, Gulya AJ. Labyrinthine enhancement on Gd-MRI in patients with sudden deafness and vertigo: correlation with audiologic and electronystagmographic studies. *Ann Otol Rhinol Laryngol* 1992; 101:459-464.
6. Casselman JW, Kuhweide R, Deimling M, Ampe W, Dehaene I, Meeus L. Constructive Interference in steady state-3DFT MR imaging of the inner ear and cerebellopontine angle. *AJNR Am J Neuroradiol* 1993; 14:47-57.
7. Brogan M, Chakeres DW, Schmalbrock P. High-resolution 3DFT MR imaging of the endolymphatic duct and soft tissues of the otic capsule. *AJNR Am J Neuroradiol* 1991; 12: 1-11.
8. Casselman JW, Kuhweide R, Ampe W, Meeus L, Steyaert L. Pathology of the membranous labyrinth: Comparison of T1- and T2-weighted and gadolinium-enhanced spin-echo and 3DFT- CISS imaging. *AJNR Am J Neuroradiol* 1993; 14:59-69.
9. Casselman JW, Majoor MHJM, Albers FW. Magnetic resonance imaging of the inner ear in patients with Cogan syndrome. *AJNR Am J Neuroradiol* 1994; 15:131-138.
10. Majoor MHJM, Albers FWJ, Casselman JW. Clinical relevance of magnetic resonance imaging and computed tomography in Cogan's syndrome. *Acta Otolaryngol (Stockh)* 1993; 113:625-631.
11. Harnsberger HR, Dart DJ, Parkin JL, Smoker WRK, Osborn AG. Cochlear implant candidates assessment with CT and MR imaging. *Radiology* 1987; 164:53-57.
12. Stenglein C, Cidlinsky K. MR-angiographie: diagnostik des pulsatilen tinnitus. *HNO* 1993; 41:274-277.
13. Mark AS, Seltzer S, Harnsberger HR. Sensorineural hearing loss: more than meets the eye? *AJNR Am J Neuroradiol* 1993; 14:37-45.
14. Seltzer S, Mark AS. Contrast enhancement of the labyrinth on MR scans in patients with sudden hearing loss and vertigo: evidence of labyrinthine disease. *AJNR Am J Neuroradiol* 1991; 12:13-16.
15. Moret J, Boulin A. Acouphènes, vertiges: bilan radiologique. In: Veillon F, ed. *Imagerie de l'oreille*. Paris: Medecine-Sciences Flammarion, 1991:471-473.
16. Vibert D, Rohr-Le-Floch J, Gauthier G. Vertigo as manifestation of vertebral artery dissection after chiropractic neck manipulations. *ORL J Otorhinolaryngol Relat spec* 1993; 55:140-142.
17. Kikuchi S, Kaga K, Yamasoba T, Higo R, O'Uchi T, Tokumaru A. Slow blood flow of the vertebrobasilar system in patients with dizziness and vertigo. *Acta Otolaryngol (Stockh)* 1993; 113:257-260.
18. Oas JC, Baloh RW. Vertigo and the anterior inferior cerebellar artery syndrome. *Neurology* 1992; 42:2274-2279.
19. Amarenco P, Roullet E, Chemouilli P, Marteau R. Lateral inferior pontine infarction: 2 clinical aspects. *Rev Neurol (Paris)* 1990; 146:433-437.
20. Masson C, Sterkers O, Chaigne P, Colombani JM, Masson M. Isolated vertigo disclosing infarction in the area of the posterior and inferior cerebellar arteries. *Ann Otolaryngol Chir Cervicofac* 1992; 109:80-86.
21. Schwaber MK, Hall JW. Cochleovestibular nerve compression syndrome. I. Clinical features and audiovestibular findings. *Laryngoscope* 1992; 102:1020-1029.
22. Sakaki T. Neurovascular cross-compression as a cause of severe vertigo and surgical treatment. *No Shinkei Geka* 1991; 19:501-510.
23. Esfahani F, Dolan KD. Air CT cisternography in the diagnosis of vascular loop causing vestibular nerve dysfunction. *AJNR Am J Neuroradiol* 1989; 10:1045-1049.
24. D'Andrea F, Maiuri F, Gangemi M, Iaconetta G. Megadolichobasilar anomaly. Clinical and diagnostic considerations on 30 cases. *Acta Neurol (Napoli)* 1992; 14:611-619.
25. Samii M, Matthies C, Tatagiba M. Intracanalicular acoustic neurinomas. *Neurosurgery* 1991; 29:189-198.
26. Selesnick SH, Jackler RK, Pitts LW. The changing clinical presentation of acoustic tumors in the MRI era. *Laryngoscope* 1993; 103:431-436.

## 5. The Value of Gradient-Echo (3DFT-CISS) MR Imaging in the detection of congenital inner ear malformations

Jan W. Casselman<sup>(1)</sup>, Rudolf Kuhweide<sup>(2)</sup>, Willy Ampe<sup>(2)</sup>,  
Guido D'Hont<sup>(2)</sup>, Erwin F. Offeciers<sup>(3)</sup>, Wim Faes<sup>(1)</sup>  
and Gerard Pattyn<sup>(1)</sup>

From the department of Radiology<sup>(1)</sup>,  
the department of Otorhinolaryngology<sup>(2)</sup>,  
A.Z. St.-Jan Brugge, Brugge, and the department of E.N.T.,  
Sint-Augustinus Medical Institute,  
University of Antwerp<sup>(3)</sup>, Antwerp, Belgium.

*Unpublished work*

### 5.1. INTRODUCTION

MR imaging is accepted as the method of choice to look for pathology in patients with sensorineural hearing loss (SNHL) and/or vertigo. Acoustic schwannomas still remain the primary reason for MR imaging in case of SNHL and/or vertigo, and are best detected on Gadolinium (Gd)-enhanced T1-weighted spin-echo images. Therefore the MR-study of the inner ear is limited in a lot of institutions to an unenhanced and Gd-enhanced T1-weighted sequence in order to save time. However, a lot of other pathologies in the posterior fossa, cerebellopontine angle (CPA), internal auditory canal (IAC) and inner ear can also result in SNHL and/or vertigo, and their clinical presentation is often similar to that of acoustic schwannomas. These pathologies, and especially congenital inner ear malformations, can frequently only be recognized on additional gradient-echo images. In this study we reviewed the MR studies of the CPAs, IACs and inner ears of 650 patients presenting with SNHL and/or vertigo. All patients were examined with unenhanced and Gd-enhanced T1-weighted images and gradient-echo three-dimensional Fourier transformation-constructive interference in steady state (3DFT-CISS) images. The number of congenital inner ear malformations and the different kinds of malformations that could be found in these patients were evaluated. Finally, the value of the unenhanced and Gd-enhanced T1-sequence and 3DFT-CISS sequence in the detection of congenital inner ear malformations was compared.

## 5.2. MATERIALS AND METHODS

During a period of 34 months (from February 1991 to December 1993) 650 patients with SNHL and/or vertigo underwent an MR study of the CPA, IAC and inner ear. Retrospectively the number of congenital inner ear malformations that were detected on MR in these patients was counted and the different kinds of congenital malformations were listed (Table I). Patients clinically suspected to have a congenital middle or inner ear malformation were examined using computed tomography (CT), hence only congenital inner ear malformations mimicking other inner ear or CPA pathology were examined on MR. In one patient MR was performed after the diagnosis had already been made using CT (case 16) because only MR could answer the very specific questions of the surgeon. This case is not included in the study on the MR detection rate of congenital inner ear malformations, but is used in this article to illustrate the high potential of the gradient-echo (3DFT-CISS) sequence in the detailed evaluation of the congenital inner ear malformations, the patency of the cochlea and the presence and thickness of the cochlear nerve. All studies were performed on a 1 tesla active shielded superconductive system (Magnetom SP 42, Siemens, Erlangen, Germany). A standard circular polarized head coil was used to allow simultaneous imaging of both inner ears. All patients were studied with axial 3 mm thick contiguous T1-weighted spin-echo images, 500/15/4 (repetition time/echo time/excitations) with and without intravenous Gd administration. They were also examined with a coronal Gd-enhanced T1-weighted sequence. In all patients a dosage of 0.1 mmol/kg gadolinium-tetraazacyclododecanetetraacetic acid (Dotarem, Guerbet Laboratories, Aulnay-sous-Bois, France) or gadolinium-diethylenetriamine pentaacetic acid (Magnevist, Schering AG, Berlin, Germany) was used. The patients were also examined with a 3DFT-CISS gradient-echo sequence. The details of this gradient-echo sequence have been published previously (1, 2). The most important parameters of this sequence are: 1 slab of 32 mm thickness, 32 partitions, 20 msec repetition time, 8 msec echo time, 256 × 256 matrix, a field of view of 176 mm and a flip angle of 50°. This results in 1 mm sections with an in-plane resolution of 0.69 × 0.69 mm and a total acquisition time of 5 min 32 sec. In 2 patients (cases 10 and 16) a new 3DFT-CISS sequence providing even thinner slices was used. The parameters of this new CISS sequence are: 1 slab of 22.4 mm thickness, 32 partitions, 15 msec repetition time, 21 msec echo time, a field of view of 170 mm, a 256 × 256 matrix, 2 acquisitions and a flip angle of 65°. This results in 0.7 mm sections with an in-plane resolution of 0.66 × 0.66 mm and a total acquisition time of 8 min 6 sec. The thin contiguous 3DFT-CISS images allow one to make high quality multiplanar reconstructions, and 3-dimensional reconstructions can also be made using "maximum intensity projection" software. Seven millimeter thick T2-weighted spin-echo images (2000/15,90/1) were made in 4 patients; acquisition time of this sequence was 4 min 51 sec. The sensitivity of the T1 spin-echo sequences, the 3DFT-CISS sequence and, when available, the T2 spin-echo sequence and CT, were rated on a "-", "0", "+" scale. "-" means that the lesion was not recognized, "0" corresponds with a lesion that was only partially visible or that was only recognized retrospectively and "+" stands for a lesion that was immediately and completely recognized.

Finally the vestibular aqueduct (CT) or the endolymphatic duct (MR) were considered enlarged when their diameter exceeded the diameter of the posterior semicircular canal or they were more than 1.5 mm in diameter, measured halfway between the common crus and the external aperture of the vestibular aqueduct (3-5).

*Table I: Data for 16 patients with congenital inner ear malformation visualized on MR*

No	Age/ Sex	CT	T1 & T1-Gd	CISS	T2	Clinical presentation SNHL / VERTIGO / TINNITUS	MR results R inner ear	MR results L inner ear
1	14/M	NP	+	+	NP	SNHL in high frequencies of the right ear, vertigo	LED	-
2	17/M	NP	+	+	NP	SNHL bilateral	LED	-
3	32/M	NP	+	+	NP	SNHL bilateral since childhood	LED	-
4	34/M	+	0	+	NP	SNHL, anacusis of the right ear	LED	-
5	7/F	+	0	+	NP	SNHL bilateral (triggered by a trauma)	LED	LED
6	9/M	NP	-	+	NP	SNHL bilateral	LED	LED
7	19/M	NP	0	+	NP	SNHL bilateral (triggered by traumata), vertigo and tinnitus	LED	LED
8	24/F	-	-	+	+	SNHL bilateral, tinnitus in the right ear	LED	LED
9	26/F	NP	+	+	NP	SNHL bilateral, anacusis of the right ear (history of meningitis)	LED	LED
10	55/M	NP	-	+	NP	SNHL predominantly of the left ear	LED	LED
11	45/M	NP	-	+	-	SNHL of the left ear, vertigo and vestibular hyporeflexia on the right side	CLSSC	-
12	46/M	NP	0	+	NP	SNHL, tinnitus and vestibular hyporeflexia on the right side	CLSSC	-
13	50/F	NP	-	+	NP	SNHL bilateral	CLSSC	CLSSC
14	16/M	NP	0	+	-	SNHL bilateral, abnormal vestibular findings (history of meningitis)	ASSCs	LED
15	34/M	+	-	+	0	SNHL, anacusis of the left ear, bilateral vestibular areflexia, cleft palate and mental retardation	ASSCs	ASSCs
16	11/F	+	0	+	NP	SNHL bilateral, nearly completely deaf on both sides	Mondini	Mondini

ASSCs = Aplasia all semicircular canals

CISS = Constructive interference in steady state

F = Female

Gd = Gadolinium

LED = Large endolymphatic duct and sac = Large Vestibular Aqueduct Syndrome when no other inner ear anomalies are present.

M = Male

NP = Not performed

CLSSC = Cystic lateral semicircular canal = Lateral Semicircular Canal - Vestibule Dysplasia when no other inner ear anomalies are present.

SNHL = Sensorineural hearing loss

- = Lesion not recognized

0 = Lesion only visualized retrospectively or only part of the lesion was visualized

+ = Lesion immediately and completely visualized

### 5.3. RESULTS

Out of 650 patients with SNHL and/or vertigo who were examined with MR, 15 (11 men, 4 women, with ages ranging from 7 to 55 years with an average of 28.5 years) or 2.3% finally had a congenital inner ear malformation. The most frequent pathology found was an enlarged endolymphatic duct and sac (Large Vestibular Aqueduct Syndrome) (11 patients, bilateral in 6 patients) and a cystic lateral semicircular canal which was confluent with the vestibule (Lateral Semicircular Canal - Vestibule Dysplasia) (3 patients, bilateral in 1 patient) (Table I). All the patients with an enlarged endolymphatic duct and sac had SNHL. Only 3 of them also had vertigo and/or abnormal findings at vestibular testing and 2 patients, with a bilateral enlarged endolymphatic sac, also had tinnitus. Four of the 5 patients with malformations of one or more semicircular canals presented with vertigo, all of them had SNHL and one also complained of tinnitus.

In all patients the CISS sequence provided the best images, leading to the exact diagnosis (Figs. 1-4). In four of the 15 patients the diagnosis was also possible on the T1-weighted images, although the visualization of the lesions was less detailed and clear than on the CISS images. In 5 patients the T1-images showed only part of the lesion or the lesion was only recognized retrospectively (after the diagnosis was made on the CISS images). In 6 patients the malformation was not visible on the T1-images. In the 4 patients that were examined with the T2-sequence, a straightforward diagnosis was possible only once.

In one patient, not included in the statistics, CT had already given the diagnosis but additional information that could only be provided by gradient-echo (3DFT-CISS) MR was required prior to cochlear implant surgery (Fig. 3) (case 16). In another patient (case 8) a bilateral enlarged endolymphatic duct and sac was found on MR after a negative CT scan had been performed in another hospital. Review of these CT documents revealed that the pathology was visible on CT but was not recognized at that time. In 3 other cases (cases 4, 5 and 15) a control CT scan confirmed the malformations detected on MR.

### 5.4. DISCUSSION

CT remains the method of choice to evaluate congenital malformations of the inner ear. It has the advantage of providing simultaneous visualization of the middle ear. However, the middle and external ear develop distinctly from the inner ear and therefore anomalies of the middle ear are not necessarily linked to anomalies of the inner ear and vice versa. In fact, the majority of inner ear malformations occur without any middle or external ear involvement. Patients with pure inner ear malformations present with SNHL and/or vertigo. Most frequently there are no other malformations and especially after childhood and when asymmetric SNHL is found, patients are referred for an MR examination to rule out an acoustic schwannoma. Indeed, MR is currently accepted as the most sensitive imaging technique in the detection of pathology in patients with SNHL and/or vertigo (6). Therefore the MR technique must be adapted in order not to overlook congenital inner ear malformations. In many institutions MR examination time is scarce due to waiting lists and high costs, and hence inner ear imaging is limited to unenhanced and Gd-enhanced T1-weighted sequences. These sequences are excellent when looking for lesions in the CPA and IAC, but previous reports have already shown that some intralabyrinthine pathology and inner

ear malformations can remain undetected (2, 6-7). As a result we added a short gradient-echo 3DFT-CISS sequence to the T1 sequences used for the MR study of the inner ear. In 15 (2.3%) of the 650 patients examined with these sequences, a previously unknown congenital malformation was found. In 11 cases there was an enlarged endolymphatic duct and sac (Fig. 1), which is the MR counterpart of the Large Vestibular Aqueduct Syndrome. In 3 cases there was a cystic lateral semicircular canal, also known as Lateral Semicircular Canal - Vestibule Dysplasia (Fig. 2).

In 1987 Jackler et al. proposed a new classification scheme for the congenital malformations of the inner ear (8). They noted a striking resemblance between the various morphological patterns of inner ear anomalies and the different stages of inner ear embryogenesis. It looks as if development halted at a certain point during embryogenesis. This forms the basis of the theory that the deformities result from an arrest of development at a particular stage of inner ear embryogenesis. Jackler et al. also pointed out that an enlarged vestibular aqueduct and a cystic lateral semicircular canal are the most frequent findings in malformed inner ears. This is probably due to the fact that both structures acquire their definite form in the latest stages of inner ear embryogenesis. The vestibular aqueduct undergoes a progressive narrowing by the end of the labyrinth formation and the lateral is the last of the semicircular canals to be formed by central resorption of the half-disc-shaped folds from the vestibular bud. Hence both structures are particularly vulnerable to early derangement.

#### 5.4.1. Large Vestibular Aqueduct Syndrome (LVAS)

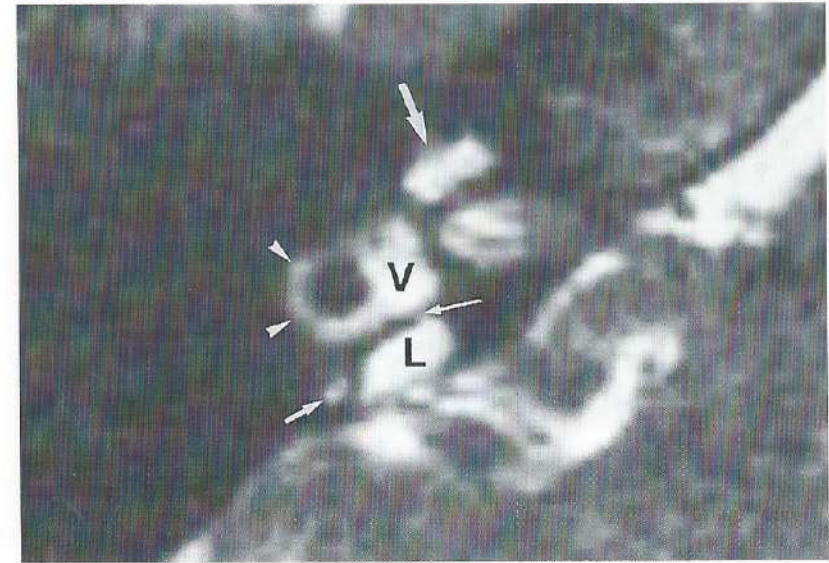
In a review of 3700 consecutive polytomographic temporal bone examinations, Valvassori and Clemis found in 1978 an enlarged (> 1.5mm) vestibular aqueduct in 1.3%. They introduced the term LVAS (3). Emmett found 1% of enlarged (> 1.5mm) vestibular aqueducts in 2683 consecutive polytomographic examinations (9). However, in the majority of cases in both studies the enlarged vestibular aqueduct was accompanied by other inner ear anomalies. In view of the arrested development theory of the origin of inner ear malformations, this is not surprising. Accordingly Jackler and others have suggested consideration of the diagnosis of LVAS only when an enlarged vestibular aqueduct is the sole radiographically detectable inner ear anomaly (8, 10-11).

We found an enlarged endolymphatic duct and sac (enlarged vestibular aqueduct) as the sole anomaly (LVAS) in 11 or 1.7% of 650 MR temporal bone examinations. This figure is higher than the 1.3% of Valvassori (3) and the 1% of Emmett (9) considering the fact that the majority of their cases did not fulfil the present definition of LVAS. This also confirms that LVAS is the most frequent morphogenetic cause of hearing loss (4). The high figure is moreover stressed by the fact that in our hospital a CT is usually performed on suspicion of a congenital temporal bone malformation, since we don't believe MR or even gradient-echo 3DFT-CISS MR or comparable but still thicker (2mm) fast spin-echo MR (12), are better than CT in the diagnosis of LVAS. On the other hand the referral pattern in our hospital might be responsible for a higher percentage of pathology.

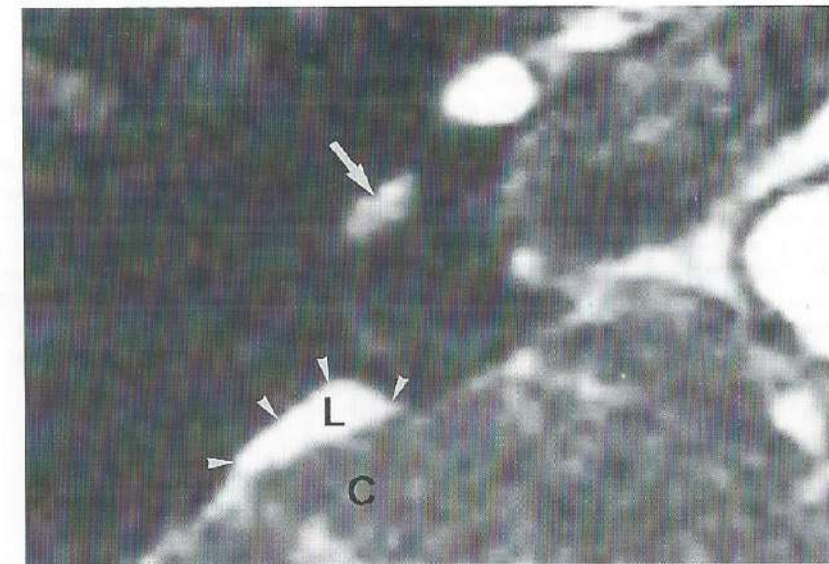
The enlarged endolymphatic duct and sac was bilateral in 6 (55%) and unilateral in 5 (45%) patients whereas other authors have mentioned bilateral lesions in up to 94% (10). A nearly 3 to 1 ratio of men to women (8 men, 3 women) was found. All patients had SNHL (bilateral in 9 patients). Only three or 27% of them also had vertigo, and this cor-

responds well with the 29% found in the series of Jackler and De la Cruz (10). In several patients there had been one or more sudden hearing losses triggered by a relatively minor head trauma. In previous studies on a total of 55 ears in 29 patients (10-11) the SNHL was reported to be variable but as a rule progressive with sudden drops. The hearing loss was predominantly situated in the high frequency range and sometimes considerable fluctuation was noted (as was observed in our case 7). As seen in other inner ear malformations, these sudden losses in LVAS often occur after relatively minor head trauma, or after a barotrauma. Hence early detection may have important clinical implications. The enlarged endolymphatic sacs/ducts (11 patients, 17 ears) were best evaluated on the gradient-echo images (Figs. 1B-C).

This is explained by the high contrast between the fluid filled duct and sac and the surrounding hypointense bone, by the 0.7 - 1.0 mm very thin contiguous slices and the high spatial resolution of 0.662 - 0.692 mm. These images have already proved able to demonstrate normal endolymphatic sacs/ducts in 72.5% of a control group (1). Moreover multiplanar and 3D-reconstructions allow further detailed study of the normal (1, 7) and enlarged endolymphatic duct and sac (Figs. 1D-F). The T1 images led to an immediate correct diagnosis in merely 3 of the 11 patients. The enlarged endolymphatic duct and sac was recognized retrospectively or only partially in 4 (Fig. 1A) of them, while in 3 patients it was not visible at all. The 3 mm thick slices, the lack of contrast between intralabyrinthine fluid and bone, and especially cerebrospinal fluid (CSF), together with the lower

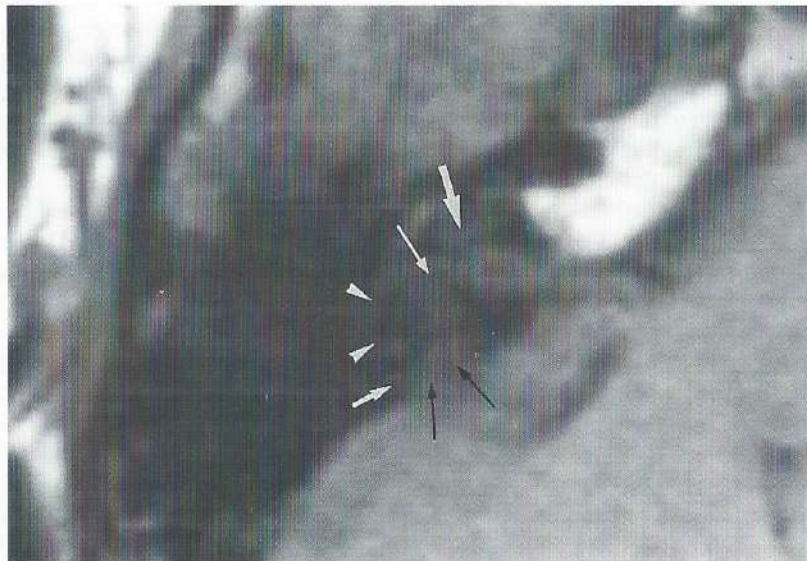


B

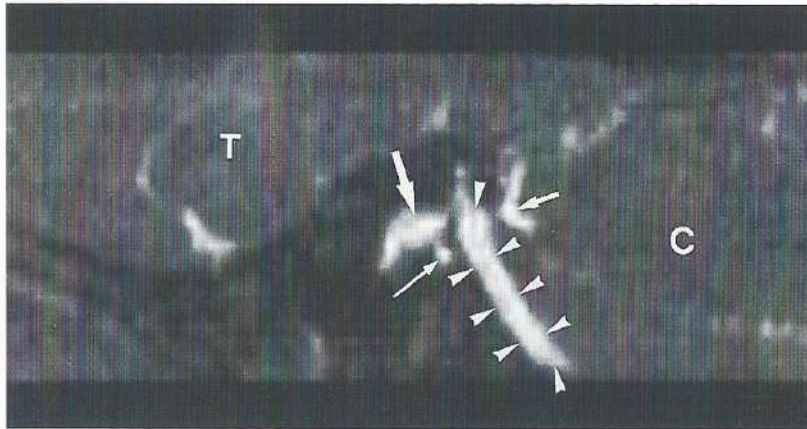


C

*Fig. 1. Images of the right inner ear of a 19-year old man with bilateral SNHL, vertigo and tinnitus (case 7).*



A



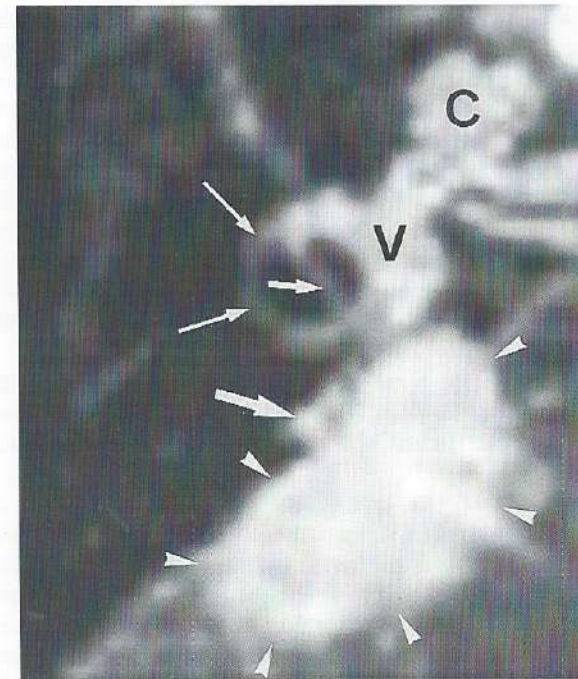
D

A. Axial T1-weighted spin-echo image (500/15). Intermediate to low signal intensity can be seen in the cochlea (large white arrow), vestibule (long white arrow), lateral (white arrowheads) and posterior semicircular canal (small white arrow). The 3mm thick slices didn't allow detailed visualization of the "posterior semicircular canal - endolymphatic sac" region and lacked contrast resolution. It was only realized retrospectively that the blurred hypointense region (long black arrows) adjacent to the posterior fossa represented a large endolymphatic sac.

B-C. Axial 3DFT-CISS images (20/8; flip angle, 50°). (B) High signal fluid can be recognized in the cochlea (large white arrow), lateral (white arrowheads) and posterior semicircular canal (small white arrow), the vestibule (V) and inside a now clearly visible enlarged endolymphatic sac (L). The fluid filled connection between the vestibule and endolymphatic sac is also visualized (long white arrow). (C) Axial image through the basal turn of the cochlea (large white arrow). This image reveals the extension of the endolymphatic sac in the posterior fossa (white arrowheads - L), a structure often difficult to delineate on CT images. C = cerebellum.

D. 3DFT-CISS image, sagittal reconstruction. The fluid filled vestibule (large white arrow) and posterior semicircular canal (long white arrow) can be seen anteriorly to the fluid filled enlarged endolymphatic sac (white arrowheads). This endolymphatic sac is lying against the anterior surface of the cerebellum. Cerebrospinal fluid in the posterior fossa (small white arrow), C = cerebellum, T = temporal lobe.

E



F



E-F. Three dimensional 3DFT-CISS reconstruction (E) and corresponding drawing (F). The intralabyrinthine fluid in the cochlea (C), vestibule (V), lateral (long arrows), superior (small arrow) and posterior semicircular canal (large arrow) can be seen. The 3D-reconstruction clearly shows the real dimensions of the enlarged endolymphatic sac (arrowheads) and confirms that the major part of the sac is situated inside the posterior fossa. It also demonstrates the connection between the vestibule and the endolymphatic sac.

spatial resolution explain why T1-weighted images were less accurate. The use of Gadolinium can facilitate the detection as it causes dura enhancement resulting in a better posteromedial delineation of the extension of the endolymphatic sac in the posterior fossa (13). However in our study this phenomenon did not ameliorate the sensitivity of the T1 images. Once again the 3DFT-CISS images were superior in showing the posterior fossa extension of the sac, which very often turned out to be the major part of the enlarged endolymphatic structure (Fig 1C). The explanation is that both the endolymph inside the sac and the CSF in the posterior fossa have a high signal on the CISS images but the endolymphatic sac has a slightly higher signal intensity because unlike CSF the endolymph flow is low. Moreover the thin 3DFT-CISS images can show the dural lining between the sac and the CSF. Finally the thin contiguous slices enable us to follow the endolymphatic duct and sac from the vestibule to the posterior fossa.

The T2-weighted images have the same high contrast resolution as the gradient-echo images but they are much thicker than the CISS slices. This explains why in one of the two patients with an enlarged endolymphatic sac studied with a T2 sequence the diagnosis was missed due to partial volume averaging.

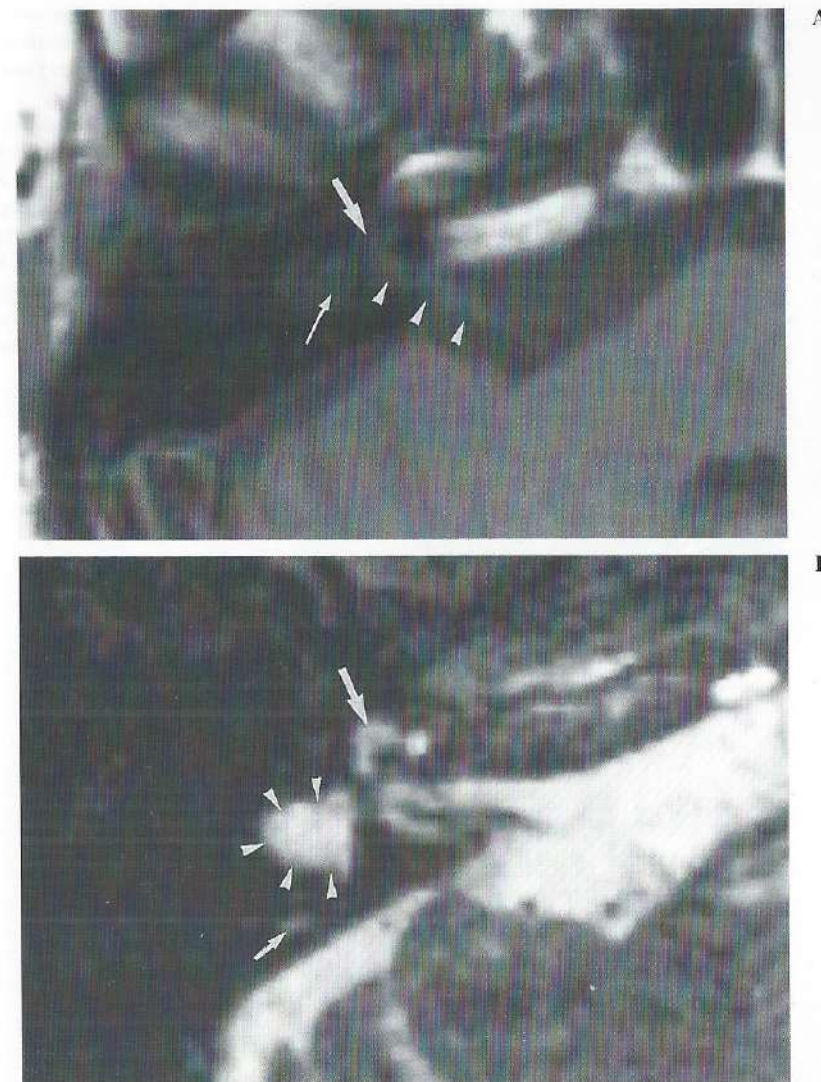
Finally, in one patient presenting with SNHL and vestibular problems (case 14) an enlarged endolymphatic sac was found on the left side and no intralabyrinthine fluid was seen in the semicircular canals on both sides, in the left cochlea and in part of the left vestibule. The patient had a history of meningitis and therefore the fluid loss was probably caused by fibrous or calcified obliteration (labyrinthitis ossificans) of the intralabyrinthine fluid spaces. Differentiation between congenital aplasia and labyrinthitis ossificans and between fibrous and calcified obliteration is possible with a combined gradient-echo 3DFT-CISS MR and CT study of the inner ear (2, 6, 14), but unfortunately no CT was performed in this patient.

#### 5.4.2. Lateral Semicircular Canal - Vestibule Dysplasia (LCVD)

It has been reported that a cystic lateral semicircular canal is the overall most frequent finding in a malformed inner ear (8, 15-16). This is in accordance with the arrested development theory on congenital malformations since the lateral semicircular canal is the last single structure to be formed during embryogenesis. Several authors have reported on isolated lateral semicircular canal abnormalities in combination with a normal cochlea (8, 17-19). In their study on inner ear malformations, Jackler et al. stated that the morphology of a short and broad cystic lateral semicircular canal confluent with an enlarged vestibule as an isolated deformity was probably common enough to be considered as a separate syndrome (8). They introduced the term LCVD when this occurs as a sole radiographically detectable anomaly. Usually the SNHL is mild.

In our study 3 patients had a cystic lateral semicircular canal as an isolated finding (2 unilateral, 1 bilateral). They can be diagnosed as having LCVD. The ratio of 11 cases of LVAS to 3 cases of LCVD as a single ear deformity confirms the observation by Mafee that the enlarged vestibular duct and sac, and not the cystic lateral semicircular canal, is the anomaly that is most frequently found radiographically in patients with congenital inner ear malformations (4). Vertigo and/or vestibular hyporeflexia was present in 2 of the 3 patients,

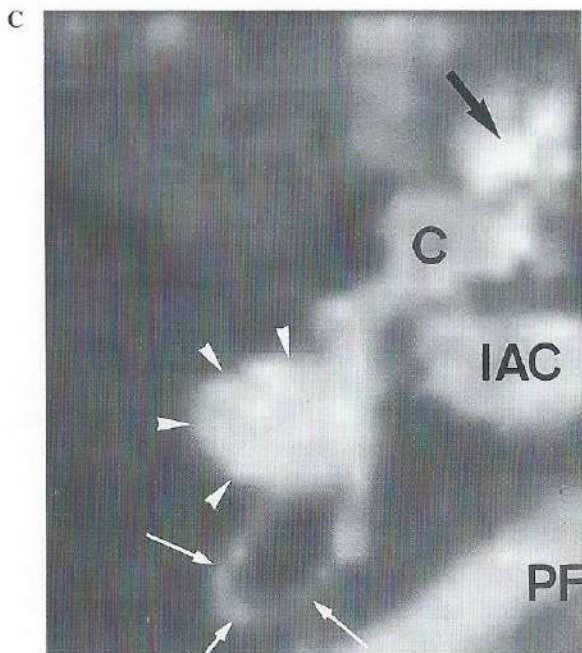
*Fig. 2. MR-images of the right inner ear of a 45-year old man with vertigo and vestibular hyporeflexia on the right (case 11).*



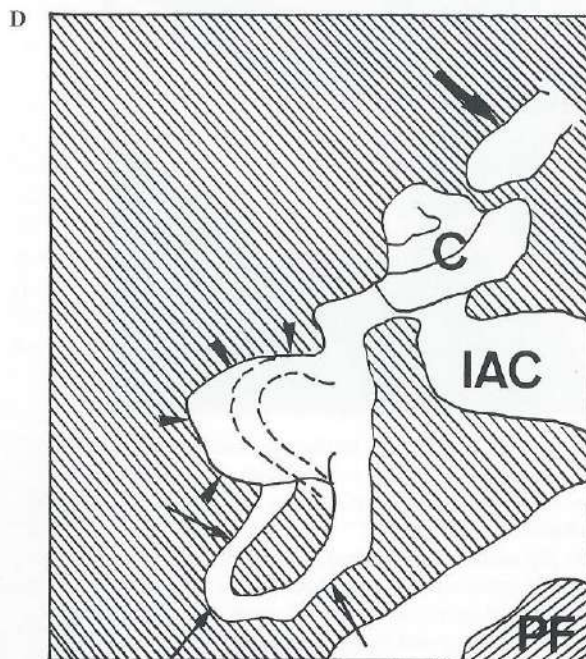
*A. Axial T1-weighted spin-echo image (500/15). Fluid, displaying intermediate signal intensity, is present inside the cochlea (large white arrow) and vestibule (long white arrow). No malformation was detected on the 3mm thick T1-weighted images. Nerve bundle inside the internal auditory canal (white arrowheads).*

*B. Axial 3DFT-CISS image (20/8; flip angle, 50°). Normal fluid is recognized in the cochlea (large white arrow) and posterior semicircular canal (small white arrow). However the vestibule can no longer be separated from the lateral semicircular canal and both structures form a fluid filled cystic or saccular semicircular canal (white arrowheads).*

C. Three dimensional 3DFT-CISS reconstruction (C) with corresponding drawing (D).



The fluid filled cochlea (C), the complete posterior semicircular canal (long arrows) and cystic semicircular canal (arrowheads) can be seen. The superior semicircular canal is not visible in this view because it projects on the dilated vestibule - lateral semicircular canal structure (dotted lines). IAC = internal auditory canal, PF = posterior fossa, internal carotid artery (large arrow).



whereas in the LVAS group only 3 of the 11 patients complained of vertigo. This probably reflects the site of the pathology.

The detection of semicircular canal anomalies requires thin slices and high contrast resolution between intralabyrinthine fluid and surrounding bone. The lesions were easy to detect in all patients using 3DFT-CISS images (Figs. 2B-D) but on the T1 images they were invisible in 2 patients (Fig. 2A) and were only seen in retrospect in the other patient. This was due to poor contrast resolution and volume-averaging artefacts. Volume-averaging artefacts were also responsible for the non-visualization of the lesion in the one patient who was also studied with T2-weighted images.

#### 5.4.3. Other Pathologies

Not all observed inner ear malformations fit into the arrested development theory. Some may result from an aberrant rather than an arrested development (8). Recently Parnes and Chernoff presented the first report of two patients with bilateral complete semicircular canal aplasia and normal or near-normal cochleas (20). If this was due to an arrested development, the cochlea should have been malformed as well. Apparently a specific aberration must have taken place, halting further development at a confined place.

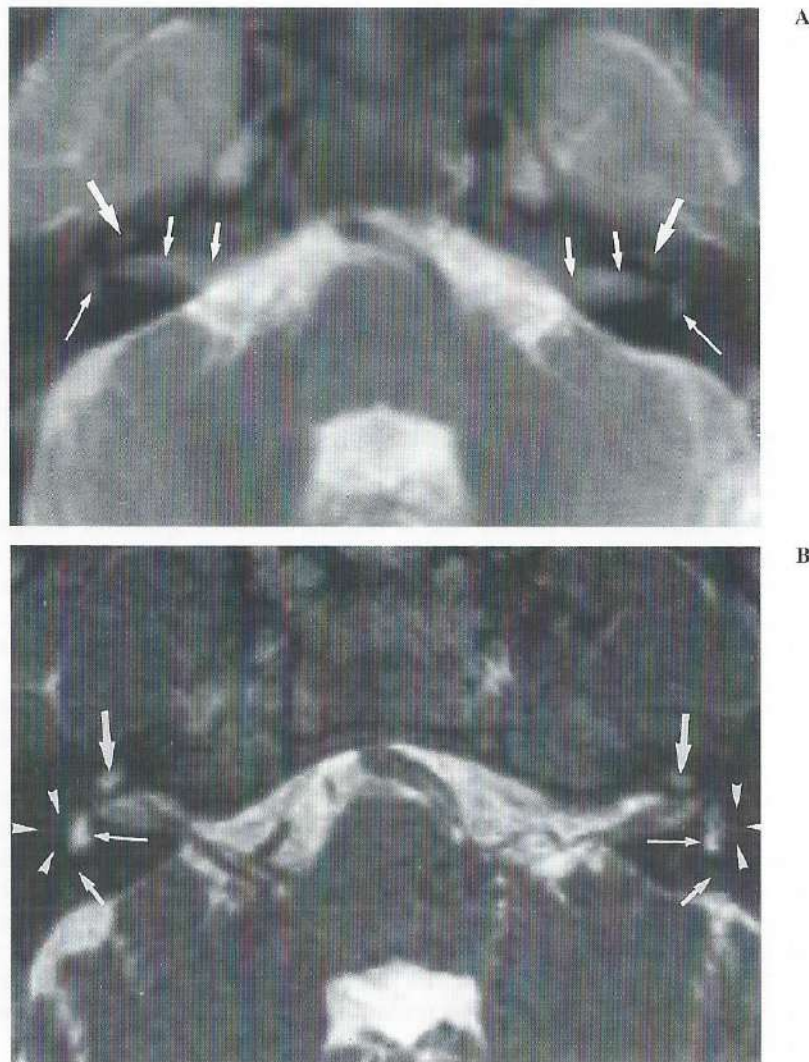
From our series we add another case of bilateral complete aplasia of all semicircular canals with normal cochlea (case 15). As expected the patient showed bilateral areflexia at vestibular testing, but was also completely deaf in his left ear. The aplasia was suspected on the T2-weighted images (Fig. 3A) but thinner gradient-echo slices were necessary to confirm that all semicircular canals were involved (Figs. 3B-D). The anomaly was overlooked on T1-weighted images.

In one patient with classical Mondini's dysplasia (Fig. 4) (case 16) an MR study was performed prior to cochlear implant surgery. The abnormal membranous labyrinth was recognized on the T1-weighted images but evaluation of the different parts of the membranous labyrinth was impossible (Fig. 4B). Gradient-echo MR confirmed the lesion seen on CT (Fig. 4A) with accuracy. The abnormal cochlea, dilated vestibule and short lateral and posterior semicircular canal and a dilated anterior limb of the superior semicircular canal on both sides were all recognized on the gradient-echo images. Moreover, 3DFT-CISS images provided the surgeon with important additional information. First the images showed that the abnormal cochlea was filled with fluid and was not obliterated with soft tissues (2, 7, 14) so that a cochlear implant could be introduced (21-22). Secondly the 0.7 mm thin CISS images showed that the cochlear branch of the cochleovestibular nerve had a normal calibre (Figs. 4C-D).

#### 5.5. CONCLUSION

- This study shows that congenital malformations of the inner ear are frequently found (2.3%) in patients with SNHL and/or vertigo and in whom no congenital malformation was suspected prior to the MR study.
- The study also confirms that a large endolymphatic duct and sac is the most frequent congenital malformation of the inner ear demonstrated on MR imaging of the inner ear.

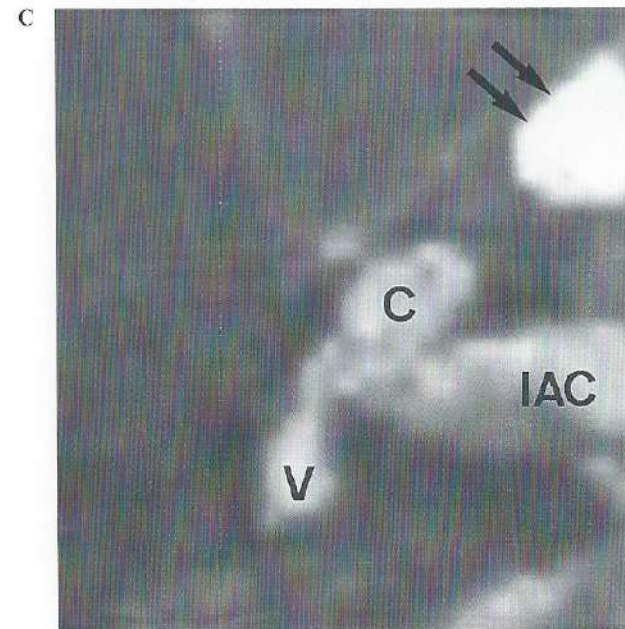
**Fig. 3.** Membranous labyrinth images of the inner ears in a 34-year old man presenting with SNHL and bilateral vestibular areflexia.



**A.** Axial T2-weighted spin-echo image (2000/90) through both inner ears. High signal fluid is present in the cochlea (large white arrow), vestibule (long white arrow) and internal auditory canal (small white arrows) on both sides. But even on 4 mm thick images at least a part of the lateral and/or posterior semicircular canal should be visible at this "mid" membranous labyrinth level.

**B.** Axial 3DFT-CISS image (20/8; flip angle, 50°). Normal fluid is seen in the cochlea (large white arrows) and vestibule (long white arrows). No fluid is seen at the sites where the lateral semicircular canals (white arrowheads) and posterior limbs of the posterior semicircular canals (small white arrows) are normally situated.

**C-D.** Three dimensional 3DFT-CISS image (**C**) and corresponding drawing (**D**) of the right membranous labyrinth.



High signal cerebrospinal fluid and intralabyrinthine fluid is seen in the internal auditory canal (IAC) and in the cochlea (C) - vestibule (V) respectively. The semicircular canals are absent (dotted lines on drawing) and no intralabyrinthine fluid is seen lateral and posterior to the vestibule. Internal carotid artery (large black arrows).

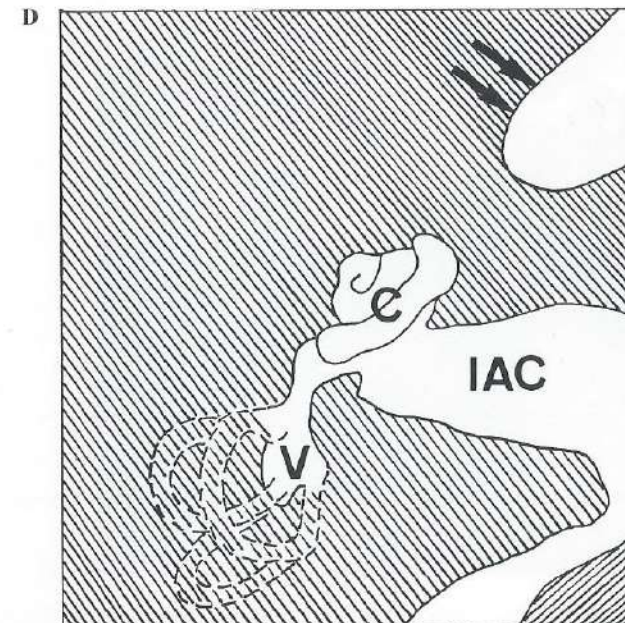
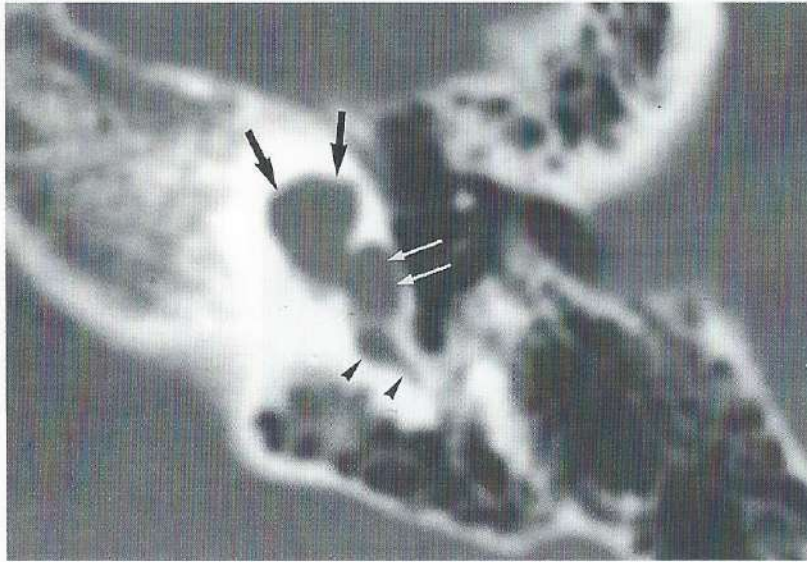
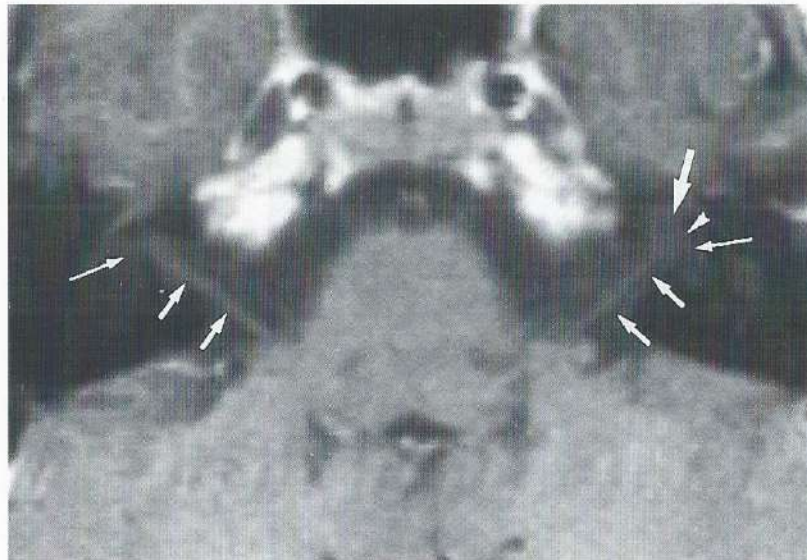


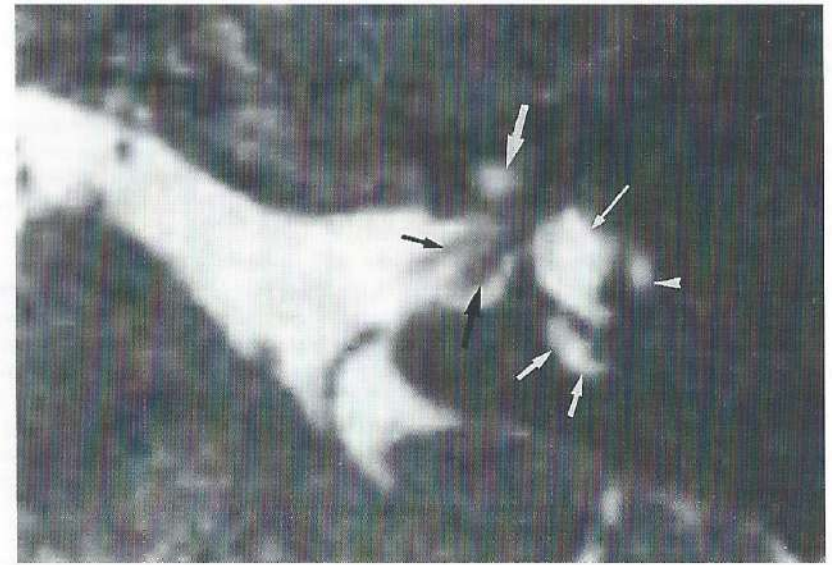
**Fig. 4.** Study of the inner ears of a 11-year old girl prior to possible cochlear implant installation. Mondini malformation.



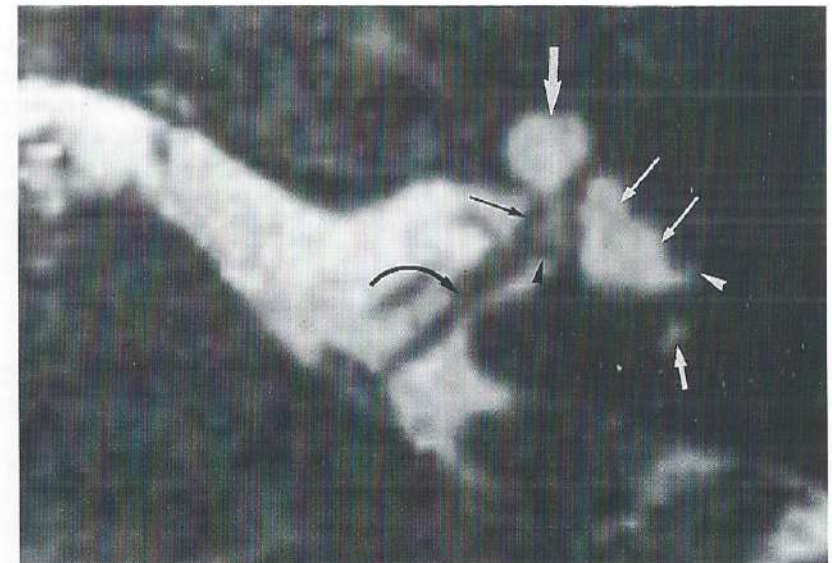
A



B



C



D

**A.** Axial CT-images through the left labyrinth. A dysplastic cochlea without turns or modiolus is seen (large black arrows) and there is a broad connection with a large vestibule (long white arrows). The posterior semicircular canal is too short and small (black arrowheads).

**B.** Axial T1-weighted spin-echo image (500/15) through both inner ears. Normal fluid is seen in the vestibule (long white arrows) on both sides and normal nerve bundles are seen in both internal auditory canals (small white arrows). However on the left side a rather round and large cochlea (large white arrow) with a broad opening towards the internal auditory canal and/or vestibule is detected (white arrowhead).

**C-D.** Axial 3DFT-CISS images (20/8; flip angle, 50°) through the left membranous labyrinth. Image at the level of the superior (C) and inferior part (D) of the internal auditory canal. These 1.0 mm thin images confirm the presence of a dysplastic cochlea without turns and modiolus (large white arrows), an enlarged vestibule (long white arrows) and a short abnormal lateral (white arrowheads) and posterior (small white arrows) semicircular canal. Moreover the cochlea is contiguous with the deep internal auditory canal. These images tell the surgeon that the malformed cochlea is however completely filled with fluid and that a normal cochlear nerve (long black arrow) is present. The opening between the cochlea and deep internal auditory canal makes a connection between the CSF and intralabyrinthine fluid possible, therefore a potential "gusher" ear cannot be excluded (This "gusher ear" was confirmed during operation, nevertheless the cochlear implant could be installed and functioned very well). Facial nerve (small black arrow), superior (large black arrow) and inferior (black arrowhead) vestibular branch of the vestibulocochlear nerve (curved black arrow).

- Gradient-echo (3DFT-CISS) images are required to detect all inner ear malformations on MR and therefore a gradient-echo sequence should be included in all routine MR studies of the inner ear. A negative MR-study should be complemented by a CT of the inner ear to look for inner ear malformations if the MR-study does not include a gradient-echo sequence (or comparable but thicker fast spin-echo images).
- Gradient-echo images also allow evaluation of the patency of the membranous labyrinth and the normal calibre of the cochlear nerve prior to cochlear implant installation.

## 5.6. REFERENCES

1. Casselman JW, Kuhweide R, Deimling M, Ampe W, Dehaene I, Meeus L. Constructive interference in steady state-3DFT MR imaging of the inner ear and cerebellopontine angle. *Am J Neuroradiol* 1993; 14:47-57.
2. Casselman JW, Majoor MHJM, Albers FW. MR of the inner ear in patients with Cogan syndrome. *Am J Neuroradiol* 1994; 15:131-138.
3. Valvassori GE, Clemis JD. The large vestibular aqueduct syndrome. *Laryngoscope* 1978; 88:723-728.
4. Mafee MF, Charletta D, Kumar A, Belmont H. Large vestibular aqueduct and congenital sensorineural hearing loss. *Am J Neuroradiol* 1992; 13:805-819.
5. Veillon F, Phillippe H, Bourjat P, Binter H. Malformations de l'os temporal. In: Veillon F, ed. *Imagerie de l'oreille*. 1st ed. Paris: Médecine-Sciences Flammarion, 1991; 203-242.
6. Casselman JW, Kuhweide R, Dehaene I, Ampe W, Devlies F. Magnetic resonance examination of the inner ear and cerebellopontine angle in patients with vertigo and/or abnormal findings at vestibular testing. *Acta Otolaryngol (Stockh)* 1994; Suppl 513:15-27.
7. Casselman JW, Kuhweide R, Ampe W, Meeus L, Steyaert L. Pathology of the membranous labyrinth: comparison of T1- and T2-weighted and gadolinium-enhanced spin-echo and 3DFT-CISS imaging. *Am J Neuroradiol* 1993; 14:59-69.
8. Jackler RK, Luxford WM, House WF. Congenital malformations of the inner ear: a classification based on embryogenesis. *Laryngoscope* 1987; 97:2-14.
9. Emmett JR. The large vestibular aqueduct syndrome. *Am J Otol* 1985; 6:387-415.
10. Jackler RK, De La Cruz A. The large vestibular aqueduct syndrome. *Laryngoscope* 1989; 99:1238-1243.
11. Levenson MJ, Parisier SC, Jacobs M, Edelstein DR. The large vestibular aqueduct syndrome in children. *Arch Otolaryngol Head Neck Surg* 1989; 115:54-58.
12. Tien RD, Felsberg GJ, Macfall J. Fast spin-echo high-resolution MR imaging of the inner ear. *AJR* 1992; 159:395-398.
13. Hirsch BE, Weissman JL, Curtin HD, Kamerer DB. Magnetic resonance imaging of the large vestibular aqueduct. *Arch Otolaryngol Head Neck Surg* 1992; 118:1124-1127.
14. Majoor MHJM, Albers FWJ, Casselman JW. Clinical relevance of magnetic resonance imaging and computed tomography in Cogan's syndrome. *Acta Otolaryngol (Stockh)* 1993; 113:625-631.
15. Sando I, Takahara T, Ogawa A. Congenital anomalies of the inner ear. *Ann Otol Rhinol Laryngol* 1984; 93(Suppl 112):110-117.
16. Petasnick JP. Congenital malformations of the ear. *Otolaryngol Clin North Am* 1973; 6:413-428.
17. Lagundoye SB, Martinson FD, Fajemisin AA. The syndrome of enlarged vestibule and dysplasia of the lateral semicircular canal in congenital deafness. *Radiology* 1975; 115:377-37.
18. Mafee MF, Selis JE, Yannias DA et al. Congenital sensorineural hearing loss. *Radiology* 1984; 150:427-434.
19. Phelps PD. Congenital lesions of the inner ear, demonstrated by tomography. *Arch Otolaryngol* 1974; 100:11-18.
20. Parnes LS, Chernoff WG. Bilateral semicircular canal aplasia with near-normal cochlear development. *Ann Rhinol Laryngol* 1990; 99:957-959.
21. Harnsberger HR, Dart DJ, Parkin JL, Smoker WRK, Osborn AG. Cochlear implant candidates: assessment with CT and MR imaging. *Radiology* 1987; 164:53-57.
22. Klein HM, Bohndorf K, Hermes H, et al. Computed tomography and magnetic resonance imaging in the preoperative work-up for cochlear implantation. *Eur J Radiol* 1992; 15:89-92.

## 6. Three-Dimensional Magnetic Resonance Imaging of the Inner Ear in Idiopathic Sudden Sensorineural Hearing Loss

F.W.J. Albers<sup>(1)</sup>, K.M.N.P. Demuyne<sup>(2)</sup>, and J.W. Casselman<sup>(3)</sup>

From the departments of Otorhinolaryngology, University Hospital Groningen, the Netherlands<sup>(1)</sup>, and the University Hospital Ghent, Belgium<sup>(2)</sup>, and the department of Radiology<sup>(3)</sup>, A.Z. St.-Jan Brugge, Brugge, Belgium.

*Published in: ORL 1994; 56:1-4.*

### 6.1. ABSTRACT

Five patients with idiopathic sudden sensorineural hearing loss (ISSHL) were examined by a combination of high-resolution computed tomography and special magnetic resonance imaging techniques. By three-dimensional constructive interference in steady state magnetic resonance imaging excellent visualization of the membranous labyrinth was obtained. No fibrous or osseous obliteration of the intralabyrinthine fluid spaces was observed in all investigated temporal bones. The results provide further evidence for a viral pathogenesis of ISSHL.

Key words: Inner ear, Sudden hearing loss, Magnetic resonance imaging.

### 6.2. INTRODUCTION

Many etiological factors associated with sudden sensorineural hearing loss have been reported in the literature (1-5). The pathophysiology of the idiopathic manifestation of sudden sensorineural hearing loss (ISSHL) is still unknown. Different theories have been proposed to explain the etiology of ISSHL. The most commonly suggested causes are viral infections, vascular disorders and membrane ruptures.

Magnetic resonance imaging with gadolinium-diethylenetriamine pentaacetic acid enhancement (Gd-DTPA-enhanced MRI) has already proven to be a very sensitive imaging method to detect lesions in the cerebellopontine angle and internal auditory canal. Excellent visualization of pathological changes in the membranous labyrinth can be achieved by the application of special three-dimensional reconstructed MRI techniques (6-10).

In this study the temporal bones of 5 patients with ISSHL are investigated 6 months after the onset of the hearing loss by high-resolution computed tomography and three-dimensional Fourier transformation constructive interference in steady-state (3DFT-CISS) MRI in order to investigate possible irreversible sequelae in the membranous labyrinth. The results of this study are discussed in correlation with postmortem temporal bone studies in order to further elucidate the pathogenesis of ISSHL.

### 6.3. SUBJECTS AND METHODS

In this study 5 patients (3 men and 2 women, average age: 52.4 years) with ISSHL were examined. ISSHL was defined according to the following criteria: (1) nonfluctuating sensorineural hearing impairment in one or both ears of at least 30 dB in three subsequent frequencies, that occurred abruptly within a period of 24 h; (2) sensorineural hearing impairment of unknown etiology after exclusion of specific causes of sudden sensorineural hearing loss. All patients were therefore submitted to the following investigations: audiometry including pure-tone and speech audiometry and brainstem electric response audiometry, electronystagmography and caloric tests, chest X-ray, electrocardiogram, urine analysis, haematology including serological and immunological investigations, CT scan of the temporal bones, and Doppler ultrasonography of the carotid and vertebral arteries. In all patients a severe unilateral sensorineural hearing loss with tinnitus was manifest with fulfillment of all above-mentioned criteria of ISSHL. The patients did not complain of vertigo, and vestibular investigations including caloric testing did not reveal any abnormalities. None of the patients showed any improvement of the hearing loss after therapy with corticosteroids and vasodilators. Six months after the initial onset of ISSHL high-resolution computed tomography with 1.5-mm axial images and MRI of the temporal bone was performed.

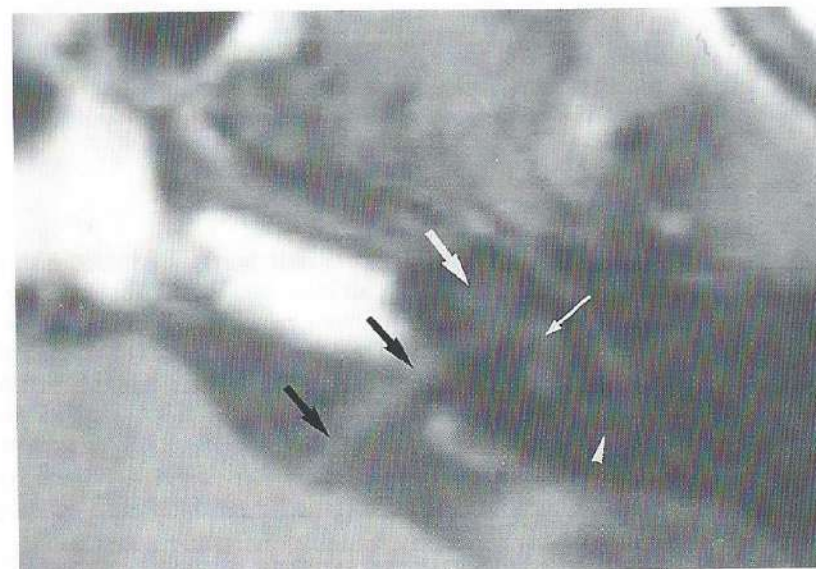
All patients were studied by MRI on a 1.0 Tesla superconductive active shielded magnet (Magnetom SP 42, Siemens, Erlangen, FRG), including 3-mm axial and coronal unenhanced and gadolinium-DTPA-enhanced (Magnevist, Schering AG, Berlin, FRG) T1-weighted 2D spin echo images, followed by 1-mm contiguous axial 3DFT-CISS images. Further details of the MRI technique used have been described in earlier reports (9, 10).

### 6.4. RESULTS

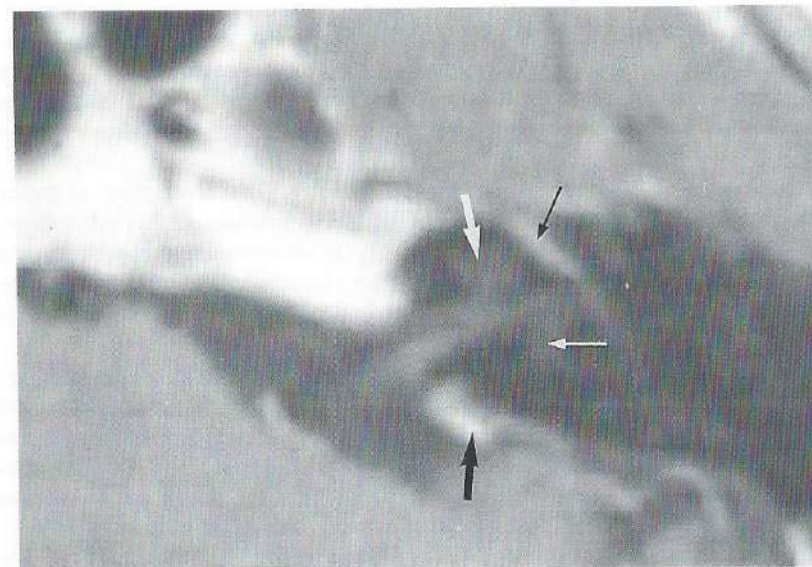
All 5 patients investigated suffered from ISSHL according to the criteria defined above. High-resolution computed tomography with 1.5-mm axial images demonstrated no intralabyrinthine calcification in all temporal bones investigated.

Axial unenhanced T1-weighted magnetic resonance images did not show spontaneous high signal intensity in the membranous labyrinth (Fig. 1A). Axial and coronal gadolinium-DTPA-enhanced T1-weighted spin echo images revealed no abnormal gadolinium-enhancement (Fig. 1B). 3DFT-CISS MRI provided a consistent high signal of the labyrinthine fluids in all temporal bones. On the three-dimensional reconstructions of the membranous labyrinth, the cochlea, vestibule and semicircular canals were always completely visible (Fig. 2). Membranous obliteration of the intralabyrinthine fluid spaces was excluded in all inner ears investigated.

Fig. 1. Axial T1-weighted magnetic resonance image through the left labyrinth without (A) and with gadolinium-DTPA enhancement (B).



A



B

*A. Intermediate signal intensity fluid can be seen inside the cochlea (large white arrow), the vestibule (long white arrow), and in the posterior semicircular canal (white arrowhead). The nerve bundle inside the internal auditory canal and the cerebellopontine angle can also be recognized (large black arrows). No masses or hyperintensities can be detected in the labyrinth.*

*B. Blood vessels posterior to the internal acoustic pore (large black arrow) and near the geniculate ganglion (long black arrow) are enhancing after gadolinium injection. No enhancement is seen in the cochlea (large white arrow) or vestibule (long white arrow).*

## 6.5. DISCUSSION

All patients were studied by high-resolution computed tomography of the temporal bones with 1.5 mm slice thickness. Subsequently, all inner ears were investigated by MRI including a combination of unenhanced and gadolinium-enhanced T1-weighted spin echo images followed by 3DFT-CISS images (9, 10). The 3DFT-CISS sequence scheme allows a detailed visualization of the membranous labyrinth by the high intensity of the labyrinthine fluids, the 1-mm-thin slices and the possibility to obtain three-dimensional reconstructions (9, 10). Narrowing or obliteration of the membranous labyrinth can be detected by 3DFT-CISS MRI (9, 10). The combination of high-resolution computed tomography and MRI enables the differentiation between a fibrous or osseous proliferation in the membranous labyrinth (11, 12).

Three theoretical concepts have been mentioned to explain the pathogenesis of ISSHL: membrane ruptures, vascular disorders and virus infections. Simmons (13) suggested the double-membrane breaks syndrome as the causative mechanism involved in ISSHL. He postulated that the sensorineural hearing loss is caused by the mixing of endolymph and perilymph following the disruption of the cochlear membranes. Gussen (14) demonstrated a rupture of Reissner's membrane in temporal bone studies of 3 patients with sudden hearing loss. Schuknecht and Donovan (15) found no histological evidence of cochlear membrane rupture or healed breaks in the temporal bones of 12 cases of ISSHL and emphasized that fistulae of the cochlear duct are not associated with a generalized decrease in cochlear function (15).

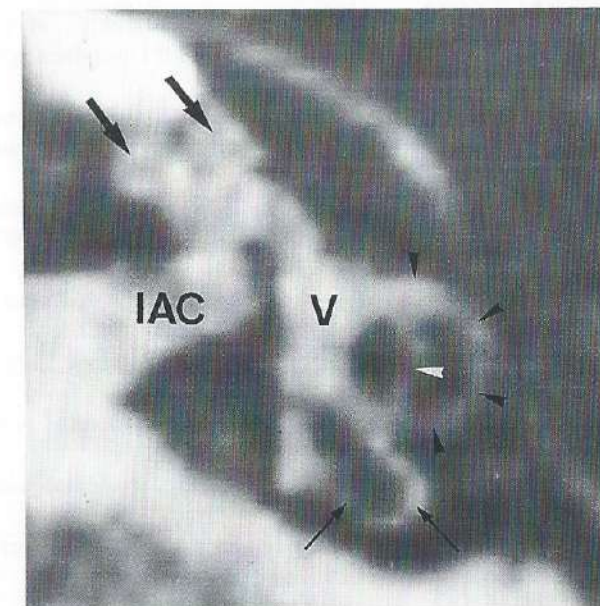
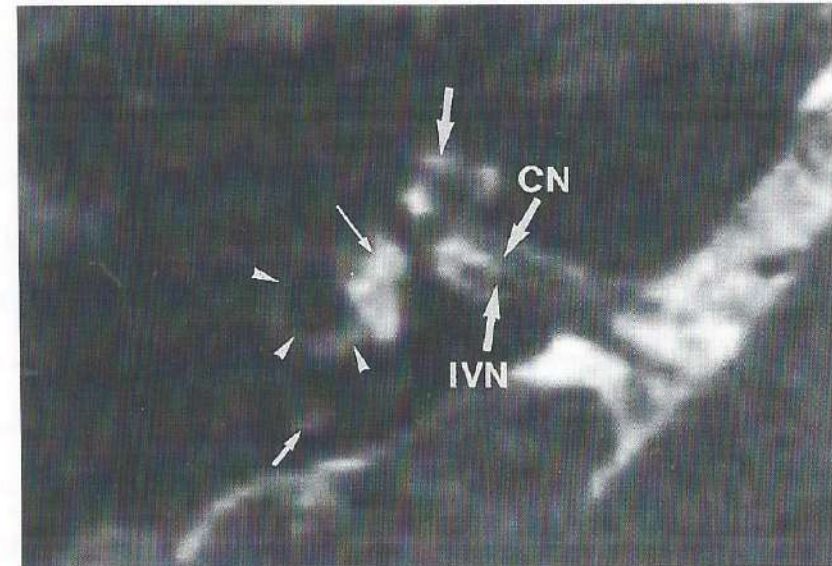
The sudden onset of ISSHL favors a vascular etiology. Total obstruction of the arterial blood supply to the cochlea causes destruction of the membranous labyrinth followed by fibrous tissue proliferation and ossification (16, 17). In several animal experiments micro-embolisation of cochlear arteries was followed by fibrosis and ossification of cochlear structures (18, 19). However, no fibrous or osseous proliferation was demonstrated in the temporal bones of 12 ISSHL cases (15).

A preceding respiratory infection has been reported in 30-40% of the patients with ISSHL (20). In the human temporal bone study on 12 ISSHL patients Schuknecht and Donovan (15) observed severe atrophy of the organ of Corti and the tectorial membrane with less involvement of the vestibular labyrinth and the stria vascularis. Similar pathological changes without fibrous and osseous proliferation in the inner ear were found in temporal bone studies of established cases of viral labyrinthitis (15).

Labyrinthine enhancement on gadolinium-enhanced MRI is described in the acute phase of sudden deafness and vertigo (21, 22). The accumulation of gadolinium in the labyrinth may represent the leakage of gadolinium through the abnormal labyrinthine membrane fol-

*Fig. 2. 3DFT-CISS magnetic resonance image in the axial plane through the right labyrinth (A) and three-dimensional reconstruction of the intralabyrinthine fluid spaces (B).*

*A. On the axial CISS images high signal fluid is seen inside the cochlea (large white arrow), vestibule (long white arrow), lateral (white arrowheads) and posterior semicircular canal (small white arrow). This high signal of fluid is lost when calcifications or soft tissue proliferations are present inside the labyrinth. The low signal cochlear nerve (CN) and the inferior vestibular nerve (IVN) can be seen inside the internal auditory canal and are surrounded by high-intensity cerebrospinal fluid.*



*B. On the three-dimensional reconstruction high signal fluid is seen inside the basal and second turn of the cochlea (large black arrows), the vestibule (V), the lateral semicircular canal (black arrowheads), the superior semicircular canal (white arrowhead) and the posterior semicircular canal (long black arrows). The three-dimensional reconstructions exclude partial volume artefacts ensuring all intralabyrinthine fluid is present. IAC = Internal auditory canal.*

lowing the breakdown of the blood-brain barrier. The gadolinium enhancement of the labyrinth appears to be highly indicative of labyrinthine disease (21, 22).

In this study high-resolution computed tomography and 3DFT-CISS MRI were performed after an average interval of 6 months following the onset of the ISSHL in order to detect irreversible sequelae in the inner ear. None of the investigated patients showed fibrous and osseous proliferation in the membranous labyrinth. The absence of fibrosis or ossification in the inner ear provides further evidence for a viral pathogenesis of ISSHL.

## 6.6. REFERENCES

1. Byl MF. Seventy-six cases of presumed sudden hearing loss occurring in 1973: prognosis and incidence. *Laryngoscope* 1977; 87:817-825.
2. Byl MF. Sudden hearing loss: eight years' experience and suggested prognostic table. *Laryngoscope* 1984; 94:647-661.
3. Cole RR, Jahrsdoerfer RA. Sudden hearing loss: an update. *Am J Otol* 1988; 9:211-215.
4. Jaffe BF. Hypercoagulation and other causes of sudden hearing loss. *Otolaryngol Clin North Am* 1975; 8:395-403.
5. Kumar A, Maudelonde C, Mafee M. Unilateral sensorineural hearing loss: analysis of 200 consecutive cases. *Laryngoscope* 1986; 96:14-18.
6. Brogan M, Chakeres DW. Gd-DTPA-enhanced MR imaging of cochlear schwannoma. *AJNR* 1990; 11:407-408.
7. Brogan M, Chakeres DW, Schmalbrock P. High-resolution 3DFT MR imaging of the endolymphatic duct and soft tissues of the otic capsule. *AJNR* 1991; 12:1-11.
8. Tanioka H, Shirakawa T, Machida T, Sasaki Y. Three dimensional reconstructed MR imaging of the inner ear. *Radiology* 1991; 178:141-144.
9. Casselman JW, Kuhweide R, Ampe W, Meeus L, Steyaert L. Pathology of the membranous labyrinth: comparison of T1-, T2- and Gd-enhanced T1-weighted spin echo imaging and 3DFT-CISS imaging. *AJNR* 1993; 14:47-57.
10. Casselman JW, Kuhweide R, Deimling M, Ampe W, Dehaene I, Meeus L. Constructive interference in steady state (CISS)-3DFT MR imaging of the inner ear and cerebellopontine angle. *AJNR* 1993; 14:59-69.
11. Majoor MHJM, Albers FWJ, Casselman JW. The clinical relevance of computed tomography and MR imaging in Cogan's syndrome. *Acta Otolaryngol (Stockh)* 1993; 113:625-631.
12. Casselman JW, Albers FWJ, Majoor MHJM. MR imaging in patients with Cogan's syndrome. *AJNR* 1994; 15:131-138.
13. Simmons FB. The double-membrane breaks syndrome in sudden hearing loss. *Laryngoscope* 1979; 89:59-66.
14. Gussen R. Sudden hearing loss associated with cochlear membrane rupture. *Arch Otolaryngol* 1981; 107:598-600.
15. Schuknecht HF, Donovan ED. The pathology of idiopathic sudden sensorineural hearing loss. *Arch Otorhinolaryngol* 1986; 243:1-15.
16. Perlman HB, Kimura R. Experimental obstruction of the venous drainage and arterial supply of the inner ear. *Ann Otol Rhinol Laryngol* 1957; 66:537-546.
17. Belal A. The effects of vascular occlusion on the human inner ear. *J Laryngol Otol* 1979; 93:955-968.
18. Igarashi M, Alford BR, Konishi S, Shaver EF, Guilford FR. Functional and histopathological correlations after microembolism of the peripheral labyrinthine artery in the dog. *Laryngoscope* 1969; 79:603-623.
19. Suga F, Preston J, Snow JB Jr. Experimental microembolization of cochlear vessels. *Arch Otolaryngol* 1970; 92:603-623.
20. Van Dishoeck HAE, Bierman TA. Sudden perspective deafness and viral infection. *Ann Otol Rhinol Laryngol* 1957; 66:959-969.
21. Seltzer S, Mark AS. Contrast enhancement of the labyrinth on MR scans in patients with sudden hearing loss and vertigo: evidence of labyrinthine disease. *AJNR* 1991; 12:13-16.
22. Mark AS, Seltzer S, Nelson-Drake J, Chapman JC, Fitzgerald CD, Gulya AJ. Labyrinthine enhancement on gadolinium-enhanced magnetic resonance imaging in sudden deafness and vertigo: correlation with audiologic and electronystagmographic studies. *Ann Otol Rhinol Laryngol* 1992; 101:459-464.

## 7. 3DFT-Magnetic Resonance Imaging of the Inner Ear in Meniere's Disease

F.W.J. Albers<sup>(1)</sup>, R. Van Weissenbruch<sup>(1, 2)</sup> and J.W. Casselman<sup>(3)</sup>

From the department of Otorhinolaryngology, University Hospital, Groningen, The Netherlands<sup>(1)</sup>, department of Otorhinolaryngology, University Hospital, Ghent, Belgium<sup>(2)</sup> and the department of Radiology, A.Z. St.-Jan Hospital, Brugge, Belgium<sup>(3)</sup>

*In Press: Acta Otolaryngol (Stockh) 1994*

### 7.1. ABSTRACT

Three dimensional Fourier transformation constructive interference in steady state (3DFT-CISS) magnetic resonance imaging (MRI) allows a detailed visualization of the membranous labyrinth of the inner ear. In this study the endolymphatic duct and sac is investigated in patients with Meniere's disease using 3DFT-CISS MRI. In addition, the distance between the vertical part of the posterior semicircular canal and the fossa posterior is quantified. Key words: magnetic resonance imaging, Meniere's disease, endolymphatic sac.

### 7.2. INTRODUCTION

With the advent of magnetic resonance imaging (MRI) it has become possible to detect soft-tissue lesions in the inner ear. MRI with Gadolinium enhancement has already proved a very sensitive imaging method to detect lesions in the cerebellopontine angle and internal auditory canal. The introduction of a special three-dimensional MRI technique by Casselman is a major step forward in the imaging of the inner ear (1-4). This imaging technique is called three-dimensional Fourier transformation constructive interference in steady state (3DFT-CISS) MRI. The 3DFT-CISS sequence scheme allows a detailed visualization of the membranous labyrinth by the high intensity of the labyrinthine fluids, 1 mm thin slices and the possibility of obtaining 3-dimensional reconstructions. Narrowing or obliteration of the membranous labyrinth can be detected by 3DFT-CISS MRI (1-3).

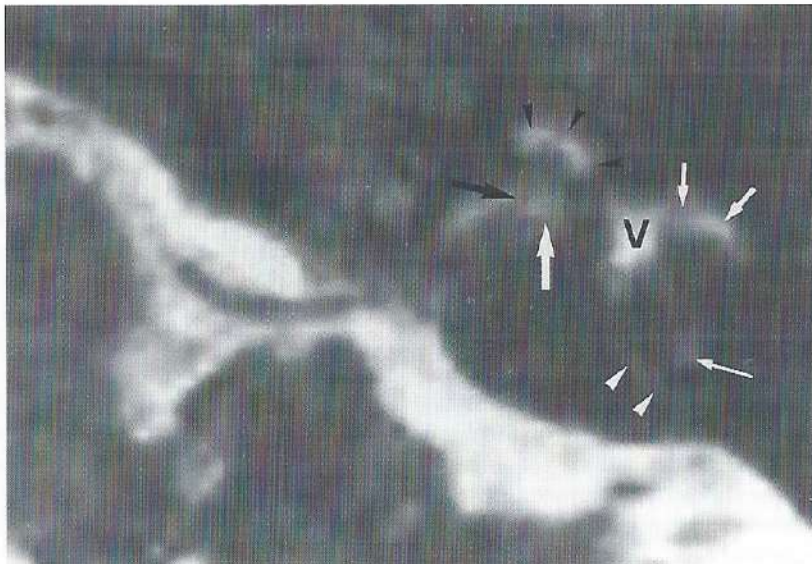
Radiological visualization of the vestibular aqueduct in patients with Meniere's disease is investigated by conventional polytomography or computed tomography (5-15). However, the endolymphatic duct and sac running through the vestibular aqueduct cannot be visualized by conventional tomography and high resolution computed tomography. 3DFT-CISS MRI enables the identification of the membranous endolymphatic duct and sac in the human temporal bone.

In this study the endolymphatic duct and sac is investigated in patients with Meniere's disease using 3DFT-CISS MRI. In addition, the distance between the vertical part of the posterior semicircular canal and the fossa posterior is quantified.

### 7.3. SUBJECTS AND METHODS

Twenty patients suffering from Meniere's disease were included in this study. The diagnosis of Meniere's disease was defined by the following criteria: cochlear hearing loss, tinnitus, periodic attacks of vertigo and periodic fullness of the ears. In order to assess the diagnosis of Meniere's disease the patients were examined according to a diagnostic protocol including routine ORL-examination, auditory and vestibular tests, X-chest and CT-scan of the temporal bones, routine laboratory investigation and consultation of internal medicine, neurology and ophthalmology. Of these 20 patients 17 suffered from unilateral and 3 from bilateral Meniere's disease. The number of affected ears was 23 and the number of non-affected ears was 17. Fifty ears with normal cochlear and vestibular function were used as control.

*Fig. 1. Axial 1 mm thin 3DFT-CISS image at the level of the left vestibule: visualization of a normal endolymphatic sac. Normal intralabyrinthine fluid is recognized in the cochlea (black arrowheads), the vestibule (V), the lateral (small white arrows) and posterior (long white arrow) semicircular canal. High signal intensity (white) fluid is also seen inside the endolymphatic sac (white arrowheads). Normally the diameter of the endolymphatic sac is always smaller than the diameter of the posterior semicircular canal. The cochlear branch (large black arrow) and inferior vestibular branch (large white arrow) of the vestibulocochlear nerve can be separated inside the internal auditory canal (IAC).*



All patients were studied by MRI on a 1.0 Tesla superconductive active shielded magnet (Magnetom SP 42, Siemens, Erlangen FRG), including 3 mm axial and coronal unenhanced and gadolinium-DOTA-enhanced (Dotarem, Guerbet Laboratories, France) T1-weighted 2D spin-echo images, followed by 1 mm contiguous axial 3DFT-CISS images. Further details of the 3DFT-CISS MRI technique used have been described in earlier reports (1, 2). All MRI images were randomized and examined blindly by one investigator. In this study the definition of a normal endolymphatic duct and sac included visualization on more than one MRI section.

### 7.4. RESULTS

3DFT-CISS MRI provided a consistent high signal of the labyrinthine fluids in all temporal bones. On the three-dimensional reconstructions of the membranous labyrinth, the cochlea, vestibule and semicircular canals were always completely visible (Fig. 1).

The visualization of the membranous endolymphatic duct and sac (Fig. 1) in the control group was classified as normal in 72.5% of the cases (Table I).

*Table I: Visualization of vestibular aqueduct or endolymphatic duct and sac in control group*

Authors	Year	Method	Control
Visualization of vestibular aqueduct in control group			
Brünnner & Pedersen (5)	1974	Tomography	88 %
Stahle & Wilbrand (6)	1974	Tomography	100%
Oigaard et al. (7)	1976	Tomography	95 %
Arenberg et al. (8)	1977	Tomography	100%
Valvassori & Clemis (9)	1978	Tomography	92 %
Kraus & Dubois (10)	1979	Tomography	70 %
Austin (11)	1980	Tomography	95 %
Dauphin et al. (12)	1981	Tomography	90 %
Hall et al. (13)	1983	Tomography	53 %
Valvassori & Dobben (14)	1984	CT-scan	92 %
De Groot (15)	1987	CT-scan	74 %
Visualization of the endolymphatic duct and sac in control group (n=50)			
Albers et al.	1993	3DFT-MRI	72.5 %

In the affected ears of patients with Meniere's disease the endolymphatic duct and sac were normally visible in only 26% of the cases. A narrowed or non-visualized endolymphatic duct and sac (Figs. 2A-B) was observed in 74% (Table II).

**Table II:** Narrowed or non-visualized vestibular aqueduct or duct and sac in the affected ears of patients with Meniere.

Authors	Year	Method	Meniere
Narrowed or non-visualized vestibular aqueduct in the affected ears of patients with Meniere			
Brüner & Pedersen (5)	1974	Tomography	84%
Stable & Wilbrand (6)	1974	Tomography	41%
Oigaard et al. (7)	1976	Tomography	57%
Arenberg et al. (8)	1977	Tomography	41%
Valvassori & Clemis (9)	1978	Tomography	56%
Kraus & Dubois (10)	1979	Tomography	43%
Austin (11)	1980	Tomography	88%
Dauphin et al. (12)	1981	Tomography	53%
Hall et al. (13)	1983	Tomography	53%
Valvassori & Dobben (14)	1984	CT-scan	56%
De Groot (15)	1987	CT-scan	73%
Narrowed or non-visualized endolymphatic duct and sac in the affected ears (n=23) of patients with Meniere			
Albers et al.	1993	3DFT-MRI	74%

In the non-affected ears of patients with unilateral Meniere's disease a narrowed or non-visualized endolymphatic duct and sac was observed in 79% (Table III).

Furthermore, the distance between the vertical part of the posterior semicircular canal and the fossa posterior was measured in the same group of Meniere's patients, whereas 20 ears with normal cochlear and vestibular function were used as control.

The distance between the posterior semicircular canal and the posterior fossa (Figs. 2-3) was significantly shorter in the Meniere group (Table IV). No significant difference was observed between the affected versus the non-affected ears (Table V).

**Table III:** Narrowed or non-visualized vestibular aqueduct or endolymphatic duct and sac in affected versus non-affected ears in Meniere.

Authors	Year	affected	non-affected
Narrowed or non-visualized vestibular aqueduct in affected versus non-affected ears in Meniere			
Stable & Wilbrand (6)	1974	41%	35%
Oigaard et al. (7)	1976	57%	53%
Hall et al. (13)	1983	53%	43%
De Groot (15)	1987	73%	60%
Narrowed or non-visualized endolymphatic duct and sac in the affected (n=23) versus non-affected (n=17) ears in Meniere			
Albers et al.	1993	74%	79%

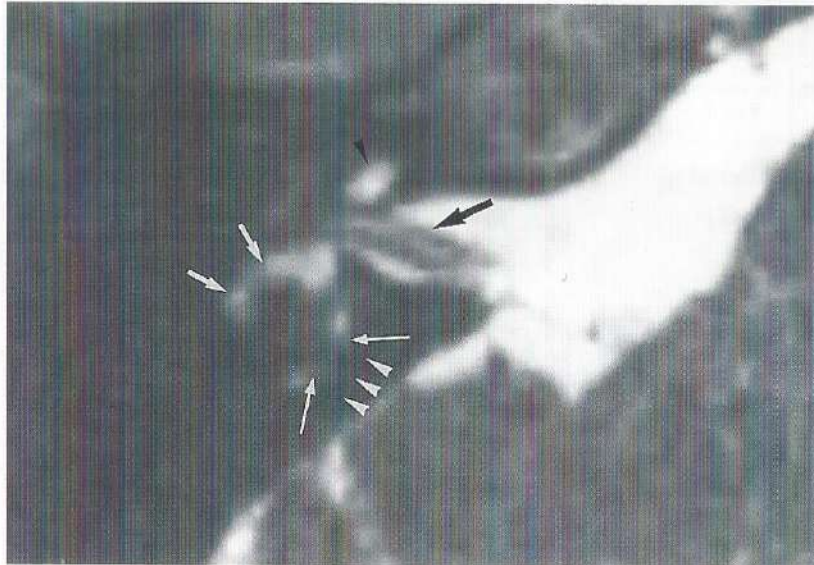
**Table IV:** Distance between posterior semicircular canal and fossa posterior.

Authors	Year	control (n=20)	Meniere (n=23)
Albers et al.	1993	3.12 mm	1.88 mm
Significant difference (Student's test $p < 0.01$ )			

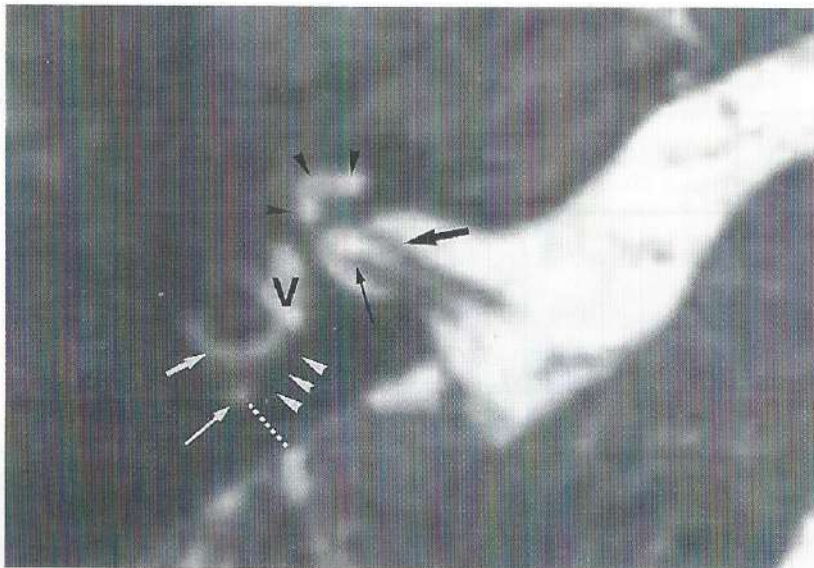
**Table V:** Distance between posterior semicircular canal and fossa posterior in the affected versus non-affected ears.

Authors	Year	affected (n=23)	non-affected (n=17)
Albers et al.	1993	1.88 mm	2.26 mm
No significant difference (Student's test $p > 0.2$ )			

**Fig. 2.** Axial 1 mm 3DFT-CISS image at the level of the right common crus (A) and superior part of the right superior semicircular canal (B). Normal distance between the posterior semicircular canal and posterior fossa and non-visualization of the endolymphatic sac.



A

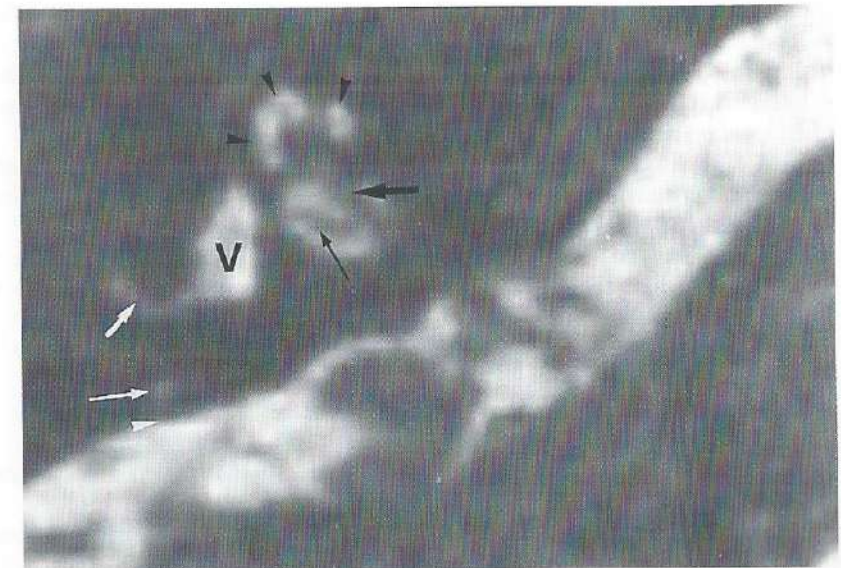


B

**A.** The first part of the endolymphatic duct and sac can normally be seen at the level of the common crus (long white arrows); it has an orientation parallel to the common crus and is situated between the common crus and the posterior fossa. However, often the endolymphatic sac is very small and can no longer be recognized (white arrowheads), as is illustrated in this patient. Normal intralabyrinthine fluid is present in the lateral semicircular canal (small white arrows) and in the cochlea (black arrowhead). The facial nerve (large black arrow) can be separated high in the IAC.

**B.** The endolymphatic sac is still not detectable on this image made 1 mm inferior to image 2A (white arrowheads). At this level the fluid filled posterior semicircular canal can be seen as a separate structure for the first time (long white arrow) and the distance between this canal and the posterior fossa was always measured at this level. A normal distance of more than 3 mm (white dotted line) is seen in this patient. Normal fluid is again recognized in the lateral semicircular canal (small white arrow), vestibule (V) and in the cochlea (black arrowheads). Cochlear branch (large black arrow) and inferior vestibular branch (long black arrow) of the cochleovestibular nerve.

**Fig. 3.** Axial 1 mm thin 3DFT-CISS image at the level of the right vestibule: diminished distance between the posterior semicircular canal and the posterior fossa. The distance between the fluid in the posterior semicircular canal (long white arrow) and the cerebrospinal fluid in the posterior fossa is less than 1mm (white arrowhead). Compare this with the thicknesses of the cochlear branch (large black arrow) and inferior vestibular branch (long black arrow) of the cochleovestibular nerve, which are approximately 1 mm thick. Normal intralabyrinthine fluid is again seen in the cochlea (black arrowheads), vestibule (V) and in the lateral semicircular canal (small white arrow).



## 7.5. DISCUSSION

The results of radiological examination of the vestibular aqueduct in patients with Meniere's disease using conventional tomography or computed tomography show great variations (5-15) (Tables 1-3). In this study direct visualization of the membranous endolymphatic duct and sac is obtained using 3DFT-CISS MRI. The correlation between the radiological and anatomical characteristics of the vestibular aqueduct was first described by Wilbrand et al. (16). The results of this study are in agreement with the recent results of the histological investigations of the vestibular aqueduct in Meniere's disease by Sando & Ikeda (17) and by Hebbar et al. (18):

- The vestibular aqueduct and endolymphatic sac are significantly smaller in Menière than in the control group.
- No significant differences between affected and non-affected ears are observed.

Imaging of the membranous labyrinth by 3DFT-CISS MRI shows a significant difference in the size of the endolymphatic duct and sac in the affected and non-affected ears of patients with Meniere's disease as compared to the control group. Therefore, hypoplasia of the endolymphatic duct and sac can be regarded as a predisposing factor in the pathogenesis of Meniere's disease. However, other factors may also be operational in Meniere's disease, such as periodic overproduction of endolymph by the stria vascularis. The two-phase concept of Meniere's disease (diminished absorption of endolymph by hypoplasia of the endolymphatic duct and sac and the periodic overproduction of endolymph by the stria vascularis) needs further attention in inner ear research.

## 7.6. REFERENCES

1. Casselman JW, Kuhweide R, Ampe W, Meeus L, Steyaert L. Pathology of the membranous labyrinth: comparison of T1- and T2-weighted and gadolinium-enhanced spin-echo and 3DFT-CISS imaging. *Am J Neuroradiol* 1993; 14:47-57.
2. Casselman JW, Kuhweide R, Deimling M, Ampe W, Dehaene I, Meeus L. Constructive interference in steady state (CISS)-3DFT MR imaging of the inner ear and cerebellopontine angle. *Am J Neuroradiol* 1993; 14:59-69.
3. Majoor MHJM, Albers FWJ, Casselman JW. Clinical relevance of magnetic resonance imaging and computed tomography in Cogan's syndrome. *Acta Otolaryngol (Stockh)* 1993; 113:625-631.
4. Albers FWJ, Demuyneck KMNP, Casselman JW. Three dimensional magnetic resonance imaging of the inner ear in idiopathic sudden sensorineural hearing loss. *ORL* 1993; 56:1-4.
5. Brünner S, Brahe Pedersen C. Radiological evaluation of Meniere's disease. *Adv Otorhinolaryngol* 1974; 21:1-8.
6. Stahle J, Wilbrand H. The vestibular aqueduct in patients with Meniere's disease. *Acta Otolaryngol (Stockh)* 1974; 78:36-48.
7. Oigaard A, Thomsen J, Jensen J, Dorph S. The vestibular aqueduct in Meniere's disease. *Acta Otolaryngol (Stockh)* 1976; 82:279-281.
8. Arenberg IK, Gado MH, Spector GJ. Polytomographic delineation and variations of the vestibular aqueduct in adult humans. *Rev Laryngol* 1976; 97:675-687.
9. Valvassori GE, Clemis JD. Abnormal vestibular aqueduct in cochleovestibular disorders. *Adv Otorhinolaryngol* 1978; 24:100-105.
10. Kraus EM, Dubois PJ. Tomography of the vestibular aqueduct in ear disease. *Arch Otolaryngol* 1979; 105:91-98.
11. Austin DF. Use of polytomography in Meniere's disease. *Arch Otolaryngol* 1980; 106:377-382.
12. Dauphin D, Laffont J, Garand G, Reynaud J. Menière's disease, petrous bone tomography, a new radiographic sign? *Neuroradiology* 1981; 22:15-18.
13. Hall SF, O'Conner AF, Thakkar CH, Wylie IG, Morrison AW. The value of lateral tomography of the petrous bone in Meniere's disease. *Rev Laryngol* 1983; 104:403-404.
14. Valvassori GE, Dobben GD. Multidirectional and computerized tomography of the vestibular aqueduct in Meniere's disease. *Ann Otol Rhinol Laryngol* 1984; 93:547-550.
15. De Groot JAM, Huizing EH. Computed tomography of the petrous bone in otosclerosis and Meniere's disease. *Acta Otolaryngol (Stockh)* 1987; Suppl 434:95-135.
16. Wilbrand HF, Rask-Andersen H, Gilström D. The vestibular aqueduct and the paravestibular canal. An anatomic and roentgenologic investigation. *Acta Radiol Diag* 1974; 15:337-355.
17. Sando I, Ikeda M. The vestibular aqueduct in patients with Meniere's disease. *Acta Otolaryngol (Stockh)* 1984; 97:558-570.
18. Hebbar GK, Rask-Andersen H, Linthicum FH. Three-dimensional analysis of 61 human endolymphatic ducts and sacs in ears with and without Meniere's disease. *Ann Otol Rhinol Laryngol* 1991; 100:219-225.

## VI. CONCLUSION AND SUMMARY

In this thesis I assessed the value of a gradient-echo MR sequence, three-dimensional Fourier transformation - constructive interference in steady state (3DFT-CISS), in the visualization of small anatomic structures of the inner ear and cerebellopontine angle (CPA). I changed some of the parameters of this abandoned 3DFT-CISS sequence in order to make this sequence more adapted for the study of the inner ear. The results became very promising and I started to use this sequence in all patients. Later, in co-operation with Dr. M. Deimling (Medical Engineering Group Siemens A.G., Erlangen, Germany), the sequence was changed more fundamentally, resulting in 0.7 mm high resolution images of the inner ear. Furthermore the value of different MR sequences, including the 3DFT-CISS sequence, in the detection of inner ear pathology was compared.

### 1. Anatomy

The 3DFT-CISS sequence proved to be 100% reliable in the visualization of the membranous labyrinth and even the four nerves inside the internal auditory canal (IAC) could nearly always be visualized separately with this technique in 100 normal temporal bones. The vascular loop can also be recognized in the CPA, near the internal acoustic pore or in the IAC, and its relationship with the facial and vestibulocochlear nerve can be appreciated. The 3DFT-CISS sequence allows a detailed anatomic study of the inner ear because it provides 1 mm thin high-resolution images with good contrast between fluid (cerebrospinal fluid and intralabyrinthine fluid) and nerves or bone. New versions of this 3DFT-CISS sequence even produce images with a thickness of 0.7 mm and with a spatial resolution of  $0.31 \times 0.39$ . On these images one is able to distinguish the scala tympani from the scala vestibuli. The results prove that the 3DFT-CISS technique is a very reliable technique to study the anatomy of the inner ear and CPA in detail. Only the visualization of the endolymphatic duct and sac is less convincing.

### 2. MR Sequences Used to Study the Inner Ear

Nonenhanced T1-weighted images remain necessary when the inner ear is studied, otherwise it is impossible to differentiate enhancement from spontaneous hyperintensity. Spontaneous high signal inside the membranous labyrinth can be found in case of subacute haemorrhage (trauma, vasculitis), when a high protein level is present inside the fluid spaces (has been found in case of schwannoma) or when a tumour (schwannoma, cholesterol granuloma, lipoma...) is present inside the cochlea or vestibule.

The **gadolinium-enhanced T1-weighted images** are the most sensitive images able to detect pathology in the CPA and IAC and are also able to detect some of the intralabyrinthine pathology. Neuritis and acute labyrinthitis can only be detected on Gd-enhanced images. The list of possible causes of enhancement of the membranous labyrinth is getting longer and longer as more experience is gained. The most frequent known causes are viral, bacterial and autoimmune labyrinthitis, vasculitis, trauma (posttraumatic perilymphatic fistula) and inner ear surgery. MR can also detect enhancement in abnormal bone. Therefore membranous labyrinth enhancement must be differentiated from pericochlear or perivestibular enhancement in the bony labyrinth, as can be seen in case of fibrous dysplasia, otospongiosis, etc.

The **3DFT-CISS sequence** provides us with very thin images with high contrast (high signal intralabyrinthine fluid). The thin images result in the detection of small lesions along the nerves inside the IAC and lead to the detection of membranous labyrinth malformations. Moreover this sequence is very sensitive in the detection of soft tissue or calcified obliteration of the intralabyrinthine fluid spaces. In these cases the high signal fluid is replaced by low signal tissue. However only an additional CT can prove if calcifications or soft tissues cause the obliteration; a normal CT indicates that the intralabyrinthine low signal region seen on the 3DFT-CISS images is caused by soft tissues. Three-dimensional reconstructions of the membranous labyrinth can be made when the 3DFT-CISS sequence is used and enable us to search for intralabyrinthine lesions or obliterations from all possible angles.

**T2-weighted sequences** are less important but can sometimes help in the characterization of tumoural lesions although T1, Gd-enhanced T1 and 3DFT-CISS images most often suffice to make the correct diagnosis. The main reason why T2-weighted images are used is because they are the most sensitive technique in the detection of brain stem and cerebellum lesions, potentially explaining the sensorineural hearing loss (SNHL) or vertigo of the patients.

In very select cases a vascular sequence, **3DFT-FISP time of flight sequence**, can be used to differentiate soft tissue lesions from vascular structures in the CPA and IAC. The same sequence can also be used to evaluate the relationship of the vascular structures to the cranial nerves but this is also possible on the CISS images.

### 3. The Value of the different MR Sequences in the Study of Inner Ear Pathologies

The most frequent pathology found by MR in patients with SNHL and/or vertigo are **acoustic schwannomas** in the CPA and IAC. The most sensitive technique to detect acoustic schwannomas and even small intracanalicular schwannomas is the Gd-enhanced T1-weighted sequence. But 3DFT-CISS images can provide important additional information. The tumour size can more exactly be measured and followed on these thin images, and erosions of the bony porus and IAC walls can be recognized, making an additional CT superfluous. Moreover in the case of very small intracanalicular schwannomas the CISS images can even tell on which nerve the tumour is located. One of the major advantages is that the CISS images show with a lot of precision if there is still CSF left between the

schwannoma and the fundus of the IAC (fluid can sometimes be recognized on the CISS images when no fluid is detected on the T2-weighted images). The fluid inside the cochlea and hearing can only be preserved when fluid is present between the schwannoma and the fundus of the IAC. This can influence the surgical approach; fossa posterior approach (attempt to preserve hearing) versus approach through the inner ear (when hearing cannot be preserved).

As already mentioned, neuritis, most often facial nerve **neuritis**, can only be detected on Gd-enhanced T1-weighted images. But 3DFT-CISS images are often required to differentiate between neuritis of one of the nerves deep inside the IAC and a very small schwannoma. The CISS images show a normal nerve in case of neuritis but a small nodule will be seen in the course of the nerve in case of schwannoma.

Schwannomas and neuritis of the geniculate ganglion, horizontal segment, posterior genu and vertical segment of the facial nerve are all best depicted on Gd-enhanced T1-weighted images. 3DFT-CISS images can only add information in case of large schwannomas, when involvement of the membranous labyrinth is suspected.

Acute **labyrinthitis** can also only be recognized on Gd-enhanced T1-weighted images. However differentiation with an enhancing intralabyrinthine schwannoma or tumour is not possible on these images, although involvement of more than one intralabyrinthine compartment (cochlea and vestibule) and unsharp borders of the enhancement rather suggest labyrinthitis. A spontaneous slightly hyperintense region on the nonenhanced T1-weighted images, on the other hand, rather supports the diagnosis of schwannoma or tumour. Immediate differentiation between both entities is only possible on 3DFT-CISS images. In case of labyrinthitis normal high signal intensity fluid is present inside the membranous labyrinth; in case of schwannoma or tumour the intralabyrinthine fluid is replaced by the schwannoma and a low signal intensity region is seen.

**Soft tissue obliteration of the intralabyrinthine fluid spaces**, the second most frequent MR finding in patients with SNHL and/or vertigo, can be found after trauma in patients with Cogan's syndrome and in case of an intralabyrinthine tumour (see above), but the most frequent causes are surgery in and around the labyrinth and labyrinthitis or meningitis. These soft tissue obliterations are far more frequent than the end stage calcified obliterations (visible on CT) and can only be detected on the 3DFT-CISS images. So far the combination of soft tissue obliteration on the CISS images and enhancement of these soft tissues on the Gd-enhanced T1-weighted images has been seen in case of intralabyrinthine tumours, in patients who have been recently operated upon and in one patient with Cogan's syndrome (presumed vasculitis). Differentiation with less frequent calcified obliteration (chronic labyrinthitis or labyrinthitis ossificans) or congenital narrowing of the labyrinth is only possible when an additional CT examination of the inner ear is performed.

**Bony and soft tissue tumours can also grow into the membranous labyrinth or can cause compression on it.** The characterization of these tumours is possible with nonenhanced and Gd-enhanced T1-weighted images; T2-weighted images only rarely add information. Narrowing of the intralabyrinthine fluid spaces due to tumour compression or obliteration due to tumour invasion can only be detected in a reliable way on thin 3DFT-CISS images. Moreover only 1 mm thin high resolution images are able to demonstrate small fistules between tumours and the membranous labyrinth.

The third most frequent lesions found on MR in patients with SNHL and/or vertigo are **congenital malformations**. Very often the clinical presentation of congenital inner ear

malformations is similar to that of acoustic schwannomas. This explains why the clinicians often ask for an MR examination in these patients instead of a CT (CT is performed when a congenital inner ear malformation is suspected clinically). The enlarged vestibular duct and sac and the cystic lateral semicircular canal were the two most frequent malformations detected on MR. These unexpected lesions are difficult to recognize on T1 and T2-weighted images and can only be depicted in a trustworthy way on 3DFT-CISS images. Therefore the CISS sequence or a comparable sequence is mandatory when MR is used as the only technique to study patients with SNHL and/or vertigo. Multiplanar and three-dimensional 3DFT-CISS reconstructions are very helpful in the study of these lesions. The 3DFT-CISS images are also the only images that allow evaluation of the patency of the membranous labyrinth and the normal calibre of the cochlear nerve prior to cochlear implant installation.

Finally the 1 mm thick 3DFT-CISS (white fluid, grey nerves, black vessels) or 3DFT-FISP images (white blood, grey nerves, black fluid) prove to be the best imaging techniques to detect vascular compression on the cochleovestibular nerve or facial nerve, causing SNHL, vertigo or facial paralysis. All other radiological techniques, including angiography, CT and routine MR sequences, are unable to demonstrate cross-compression of these nerves by tortuous or anomalous vessels.

#### 4. Value of MR and Especially the 3DFT-CISS Technique in the Study of Patients Presenting with Specific Signs and Symptoms

MR is able to detect much more pathology in patients with **vertigo and/or abnormal findings at vestibular testing** than any other radiological technique. In our series, pathology, potentially explaining vertigo, was found in 32% of the patients. Most of the pathology was found inside the membranous labyrinth (44%), and many of the lesions (soft tissue obliterations of the intralabyrinthine fluid spaces) were only visible on the CISS images. In 28% of the patients pathology was found in the IAC and was best detected on Gd-enhanced T1-weighted images. Pathology was found in the posterior fossa in 28% of the patients and here the T2-weighted images were most sensitive for the detection of vertebrobasilar ischaemic disease. CISS images and especially the FISP-vascular images were necessary to show the relationship of the vessels to the nerves, when a vascular compression of the vestibulocochlear nerve was suspected.

The bony and soft tissue obliterations of the intralabyrinthine fluid spaces reported in pathologic studies of patients with **Cogan's syndrome** can be detected on CT and MR. However the soft tissue obliterations are far more frequent and could only be detected on the CISS images. A good correlation existed between the clinical findings and the obliterations in the vestibule and semicircular canals. But in two of the six patients the status of the cochlea seen on MR didn't correspond with the clinical findings. Gadolinium enhancement of the membranous labyrinth was seen in one patient and this probably represents active disease (vasculitis).

Labyrinthine enhancement has been described on Gd-enhanced T1-weighted images in the acute phase of sudden deafness and vertigo. Yet the 3DFT-CISS images could not demonstrate irreversible sequelae in the membranous labyrinth (obliterations) in patients

with **idiopathic sudden sensorineural hearing loss (ISSHL)** and this supports the viral pathogenesis of ISSHL.

The 3DFT-CISS images (visualizing the endolymphatic duct and sac) can only confirm the CT (visualizing the vestibular aqueduct) findings in patients with **Meniere's disease**. The endolymphatic sac and duct are significantly smaller in patients with Meniere's disease than in the control group and there is no difference in size of the duct and sac between the affected and non-affected (opposite side) ears. Therefore we can conclude that so far MR has not provided additional information in patients with Meniere's disease in comparison with CT.

MR imaging and especially Gd-enhanced T1-weighted and 3DFT-CISS images of the inner ear and CPA led to the detection of pathology that could not be visualized before. This provides the clinician with an explanation for the symptoms (often SNHL and/or vertigo) in far more patients than ever before and can in some cases influence the therapy (extension of schwannomas, tumoural invasion in the membranous labyrinth, neuritis or labyrinthitis versus schwannoma, evaluation of cochlea and cochlear nerve prior to cochlear implant surgery etc.). However in a lot of other cases the MR technique is able to detect pathology and helps to explain the patient's symptoms, but nothing can be done, like in the cases where fibrous obliteration of the intralabyrinthine fluid spaces was found. This gives the impression that some of the MR findings have no clinical consequences. Nevertheless a patient can be reassured when an explanation for his symptoms is found and he will no longer consult one specialist after another and will no longer be exposed to different and sometimes invasive diagnostic procedures (e.g. selective angiography). Moreover some of the new findings may even stimulate clinicians and surgeons to find new therapeutic solutions.

#### 5. Conclusion

MR imaging became the method of choice to study the normal and pathologic inner ear. No other radiological technique can detect so much pathology in patients with sensorineural hearing loss and/or vertigo. But the success of the MR technique depends on the sequences that are chosen. Unenhanced T1-weighted spin-echo images and especially Gd-enhanced T1-weighted spin-echo images and good quality gradient-echo images (3DFT-CISS) are necessary to recognize all inner ear pathology. Therefore these three MR sequences should always be included in the routine inner ear protocol.

Additional T2-weighted images are not necessary in the study of the inner ear or internal auditory canal, but they can detect lesions in the brainstem or cerebellum, potentially explaining sensorineural hearing loss and/or vertigo.

Finally we hope that new sequences, providing again thinner images with again higher resolution, will further reveal the anatomy and pathology of the inner ear. This could enable us to understand more of the pathogenesis of inner ear diseases and could further refine the diagnostic and therapeutic possibilities in patients with sensorineural hearing loss and/or vertigo.

## VI. SAMENVATTING EN CONCLUSIE

In deze studie bestudeerde ik de waarde van een echo-gradient MR sekwentie, namelijk een drie-dimensionele Fourier transformatie - Constructive Interference in steady state (3DFT-CISS) sekwentie, bij het in beeld brengen van kleine anatomische structuren van het binnenoor en de brughoek. Ik veranderde enkele van de parameters van deze "verlaten - niet meer gebruikte" sekwentie zodat deze sekwentie meer geschikt zou worden voor het onderzoek van het binnenoor. De resultaten werden veel belovend en ik begon deze sekwentie routinematig te gebruiken. Later werd in samenwerking met Dr. M. Deimling (Medical Engineering Group Siemens A.G., Erlangen, Germany) meer fundamenteel aan de sekwentie gesleuteld en dit resulteerde in 0.7 mm dunne hoge resolutie beelden van het binnenoor. Ook werd de waarde van verschillende MR sekwenties, met inbegrip van de 3DFT-CISS sekwentie, vergeleken bij het opsporen van brughoek en binnenoor pathologie.

### 1. Anatomie

In een studie van 100 normale rotsbeenderen was de 3DFT-CISS sekwentie 100% betrouwbaar bij het visualiseren van het membraneuze labyrint en zelfs de vier zenuwen in de inwendige gehoorgang konden bijna steeds van elkaar worden onderscheiden met deze techniek. De vasculaire loop kan op de CISS beelden steeds worden herkend in de brughoek, tegenaan de porus acusticus of binnen de inwendige gehoorgang en de verhouding met de nervus facialis en vestibulocochlearis kan eveneens worden beoordeeld. De 3DFT-CISS sekwentie laat een gedetailleerde studie van het binnenoor toe dankzij de 1 mm dunne hoge resolutie beelden die met deze sekwentie worden bekomen en die bovendien nog een goed contrastonderscheid toelaten tussen vocht (cerebrospinaal vocht en intralabyrinthair vocht), zenuwen en bot. De nieuwste versie van de 3DFT-CISS sekwentie laat zelfs toe beelden te bekomen met een dikte van 0.7 mm en met een resolutie van  $0.39 \times 0.39$  mm. De scala vestibuli en scala tympani kunnen op deze beelden van elkaar worden onderscheiden. De resultaten bewijzen dat de 3DFT-CISS techniek zeer betrouwbaar is voor het in beeld brengen van de fijne anatomie van het binnenoor en de brughoek. Enkel de visualisatie van de ductus endolymphaticus is minder betrouwbaar.

### 2. MR Sekwenties Gebruikt bij de Studie van het Binnenoor

Spontane hyperintensiteiten in het binnenoor kunnen enkel van contrastaankeuringen worden onderscheiden indien men ook over T1-gewogen beelden zonder contrast-

**toediening** beschikt. Spontane hyperintensiteiten kunnen binnen het membraanuze labyrint worden gevonden wanneer een subacute bloeding (trauma, vasculitis), een verhoogd proteïnegehalte in het intralabyrinthaire vocht (wordt beschreven in aanwezigheid van schwannoma's) of een tumor (schwannoma, cholesterol granuloma, lipoma) aanwezig is binnen de cochlea of het vestibulum.

**T1-gewogen beelden na toediening van gadolinium** zijn de meest gevoelige beelden voor het opsporen van letsels in de brughoek en inwendige gehoorgang en zijn ook in staat om intralabyrinthaire pathologie te detecteren. Neuritis en labyrinthitis kunnen bijvoorbeeld enkel na toediening van contraststof worden herkend. De lijst van mogelijke oorzaken van kontrastaankleuring binnen het membraanuze labyrint wordt langer naarmate grotere groepen patiënten werden onderzocht. De meest frekwent gevonden oorzaken voor deze aankleuringen zijn tot nog toe virale, bacteriële of autoimmune labyrinthitis, vasculitis, trauma (posttraumatische perilymfatische fistels) en binnenoorchirurgie. Maar ook aankleuringen in het benign labyrint kunnen worden herkend. Het is dan ook van belang om membraanuze labyrinthaankeuringen te onderscheiden van pericochleaire en perivestibulaire aankleuringen (kan worden gezien in geval van otospongiose, fibreuse dysplasie etc.) binnen het benign labyrint.

De **3DFT-CISS sekwentie** maakt het mogelijk om zeer dunne kontrastrijke beelden te maken, waarop het intralabyrinthaire vocht een hoog signaal heeft. Op deze dunne beelden kunnen kleine letsels langs de zenuwen in de inwendige gehoorgang en malformaties van het membraanuze labyrint worden gedetecteerd. Bovendien is deze sekwentie zeer sensitief voor het opsporen van verkalkte of niet verkalkte (weke delen) obliteraties van de intralabyrinthaire met vocht gevulde ruimten. In deze gevallen wordt het hoge signaal van het vocht vervangen door laag signaal weefsel. Maar enkel een bijkomend CT-onderzoek kan bewijzen of het om een gecalcificeerde of om een weke delen obliteratie gaat. Normale bevindingen op CT wijzen erop dat de laag signaal zone binnen het membraanuze labyrint, zichtbaar op de 3DFT-CISS beelden, te wijten is aan een weke delen obliteratie. De 3DFT-CISS beelden laten ook toe om drie-dimensionele reconstructies van het membraanuze labyrint te maken waarop intralabyrinthaire letsels en obliteraties vanuit alle mogelijke hoeken kunnen worden opgespoord.

De **T2-gewogen beelden** zijn minder belangrijk maar helpen soms bij de weefseltypering van de letsels alhoewel T1 beelden zonder en met contrasttoediening en 3DFT-CISS beelden vaak reeds volstaan om de juiste diagnose te stellen. De reden waarom men toch nog T2-gewogen beelden gebruikt is dat ze de meest sensitieve beelden zijn voor het opsporen van letsels in de hersenstam en de kleine hersenen, en deze letsels zijn vaak een potentiële verklaring voor de perceptiedoofheid of vertigo van de patiënten.

In uitzonderlijke gevallen wordt een **3DFT-FISP "time of flight" sekwentie** aangewend ter differentiatie van bloedvaten en weke delen letsels in de brughoek en inwendige gehoorgang. Dezelfde sekwentie kan ook gebruikt worden om de verhouding van bloedvaten en craniale zenuwen te beoordelen doch dit kan ook beoordeeld worden op de CISS beelden.

### 3. De Waarde van de Verschillende MR Sekwenties bij de Studie van Binnenoorletsels

De meest frekwente letsels die men vindt op MR bij patiënten met perceptiedoofheid en/of vertigo zijn **acousticus schwannoma's** van de brughoek of inwendige gehoorgang. De T1-gewogen beelden na toediening van contraststof zijn de meest sensitieve beelden voor het opsporen van acousticus schwannoma's en zelfs kleine intracanaliculaire schwannoma's kunnen op deze beelden worden herkend. Maar de 3DFT-CISS beelden kunnen belangrijke bijkomende informatie verschaffen. Op deze dunne beelden kunnen de afmetingen van de tumor exacter worden gemeten en gevolgd. Erosies van de porus en wanden van de inwendige gehoorgang kunnen ook worden beoordeeld waardoor een bijkomend CT onderzoek vermeden wordt. In geval van kleine intracanaliculaire schwannoma's kan men op de CISS beelden zelfs zien op welke zenuw de tumor zich bevindt. Een van de grootste voordelen van de CISS beelden is dat men kan zien of er zich nog cerebrospinaal vocht bevindt tussen de tumor en de fundus van de inwendige gehoorgang (dit vocht kan op de CISS beelden worden herkend terwijl de T2-gewogen beelden geen vocht aantonen). Het gehoor en de endo- en perilymfe binnen de cochlea kunnen slechts worden bewaard wanneer nog vocht aanwezig is tussen de tumor en de fundus van de inwendige gehoorgang. Dit kan de chirurgische toegangsweg beïnvloeden, een fossa posterior toegang wordt gekozen als men poogt het gehoor te bewaren, een toegang doorheen het binnenoor wordt gekozen als men geen kans meer heeft om het gehoor te bewaren.

Zoals reeds vermeld werd kan **neuritis**, in de meeste gevallen neuritis van de nervus facialis, enkel op T1-gewogen beelden na toediening van contraststof worden herkend. Maar bijkomende 3DFT-CISS beelden zijn vaak nodig om met zekerheid neuritis van een van de vier zenuwen diep in de inwendige gehoorgang te onderscheiden van een klein schwannoma. In geval van neuritis tonen de CISS beelden een normale zenuw doch indien het om een schwannoma gaat kan een kleine nodule op het verloop van de zenuw worden gezien.

Schwannomas en neuritis van het ganglion geniculi, het horizontaal segment en verticaal segment van de nervus facialis kunnen best worden herkend op T1-gewogen beelden na toediening van contraststof. De 3DFT-CISS beelden kunnen enkel bijkomende informatie verschaffen wanneer het om grote schwannomas gaat waarbij aantasting van het membraanuze labyrint wordt vermoed.

Acute **labyrinthitis** kan ook alleen op T1-gewogen beelden na contraststof toediening worden opgespoord. Op deze beelden kan evenwel geen onderscheid worden gemaakt met aankleurende schwannomas of tumoren, alhoewel aantasting van meer dan één intralabyrinthair kompartiment (cochlea en vestibulum) en onscherpe randen van de aankleurende zone reeds suggestief zijn voor labyrinthitis. Een discrete spontane intralabyrinthaire hyperintensiteit op de T1-gewogen beelden zonder contraststof toediening ondersteunt eerder de diagnose van een schwannoma of tumor. Onmiddellijke differentiatie van beide letsels is enkel mogelijk op de 3DFT-CISS beelden. In geval van labyrinthitis kan normaal hoog signaal vocht binnen het membraanuze labyrint worden gezien, doch in geval van schwannoma of tumor wordt het hoog signaal vocht vervangen door de tumor en ziet men op deze plaats een laag signaal zone.

**Weke delen obliteratie van de intralabyrinthaire met vocht gevulde ruimten** is de tweede frekwentste pathologie die met MR wordt gevonden bij patiënten met perceptiedoofheid en/of vertigo. Dergelijke obliteraties worden gezien na trauma, in patiënten met Cogan's syndroom en in geval van intralabyrinthaire tumoren (zie boven) doch de meest frekwente oorzaken zijn heelkundig ingrijpen in en rond het membraneuze labyrint en labyrinthitis of meningitis. Deze weke delen obliteraties zijn veel frekwenter dan de "eindstadium" verkalkte obliteraties (zichtbaar op CT) en kunnen enkel op de 3DFT-CISS beelden worden gedetecteerd. Tot nog toe werd de combinatie van weke delen obliteratie, zichtbaar op de CISS beelden, en aankleuring van deze weke delen op de T1-gewogen beelden na toediening van gadolinium gezien bij intralabyrinthaire tumoren, bij recent geopereerde patiënten en in één patiënt met Cogan's syndroom (veronderstelde vasculitis). Differentiatie met minder frekwente gecalcificeerde obliteraties (chronische labyrinthitis of labyrinthitis ossificans) of congenitale vernauwingen van het membraneuze labyrint is enkel mogelijk wanneer een bijkomend CT onderzoek van het binnenoor wordt uitgevoerd.

**Bot en weke delen tumoren kunnen in het membraneuze labyrint groeien of er compressie op uitoefenen.** Weefseltypering van deze tumoren is meestal mogelijk op de T1-gewogen beelden voor en na contrasttoediening, T2-gewogen beelden kunnen slechts zelden bijkomende informatie bieden. De vernauwing van de intralabyrinthaire met vocht gevulde ruimten door tumorale compressie of de obliteratie van deze ruimten door tumorale invasie kan enkel op een betrouwbare wijze worden herkend op de 3DFT-CISS beelden. Kleine fistels tussen tumoren en het membraneuze labyrint kunnen eveneens slechts op 1 mm dunne hoge resolutie beelden worden aangetoond.

**Congenitale malformaties** zijn de derde meest frekwent gevonden letsels op MR bij patiënten met perceptiedoofheid en/of vertigo. Het klinisch beeld van een congenitale binnenoormalformatie lijkt vaak op het klinisch beeld dat wordt gevonden bij een schwannoma. Daarom vragen de clinici vaak een MR als eerste onderzoek aan in plaats van een CT (een CT wordt in eerste instantie aangevraagd wanneer klinisch een congenitale binnenoormalformatie wordt vermoed). Een verbrede endolymfatische ductus en saccus en een kystisch lateraal semicirculair kanaal waren de twee frekwentste malformaties die op MR werden gevonden. Deze toevallig gevonden letsels zijn moeilijk herkenbaar op routine T1- en T2-gewogen beelden en kunnen enkel op een betrouwbare wijze worden aangetoond op 3DFT-CISS beelden. Daarom is het gebruik van de CISS sekwentie of een vergelijkbare sekwentie noodzakelijk wanneer MR de enige techniek is die gebruikt wordt bij de studie van patiënten met perceptiedoofheid en/of vertigo. Bovendien bieden multiplanaire en driedimensionale reconstructies bijkomende informatie bij de studie van deze letsels. Wanneer men tenslotte overweegt om een cochleair implantaat te plaatsen kunnen enkel de CISS beelden aantonen of de cochlea vrij is (vocht bevat) en of er een nervus cochlearis met een normale diameter aanwezig is.

De 1 mm dunne 3DFT-CISS (wit vocht, grijze zenuwen, zwarte bloedvaten) en 3DFT-FISP beelden (wit stromend bloed, grijze zenuwen, zwart vocht) bleken de beste beeldvormende technieken te zijn bij het opsporen van **vasculaire compressies** op de nervus vestibulocochlearis en facialis, bij patiënten met perceptiedoofheid, vertigo of facialis paralysie. Alle andere beeldvormende technieken, angiographie, CT en routine MR sekwenties inbegrepen, zijn niet in staat om compressie op deze zenuwen door tortueuze of abnormale bloedvaten aan te tonen.

#### 4. De Waarde van MR en in het bijzonder de 3DFT-CISS Techniek bij het Onderzoek van Patiënten met Welbepaalde Klinische Tekens en Symptomen

MR kan meer letsels aantonen bij patiënten met **vertigo en/of afwijkende vestibulaire testen** dan alle andere radiologische technieken. In onze studie werd pathologie, mogelijks de vertigo verklarend, gevonden in 32% van de patiënten. Meest frekwent werden letsels in het membraneuze labyrint gevonden (44%) en de meeste van deze letsels (weke delen obliteraties van de endo/perilymfatische ruimten) konden enkel op de CISS beelden worden gezien. Bij 28% van de patiënten werden de letsels binnen de inwendige gehoorgang gevonden en waren best zichtbaar op de T1-gewogen beelden na contraststof injectie. Eveneens bij 28% van de patiënten werden de letsels in de fossa posterior gevonden en hier waren de T2-gewogen beelden de meest sensitieve beelden bij het detecteren van vertebrobasilaire ischemische letsels. Wanneer een vasculaire compressie van de nervus vestibulocochlearis werd vermoed waren CISS beelden en/of FISP-vasculaire beelden noodzakelijk voor het aantonen van de relatie tussen zenuwen en bloedvaten.

De histologisch beschreven weke delen en osseuse obliteraties in de intralabyrinthaire met vocht gevulde ruimten bij patiënten met **Cogan's syndroom** kunnen worden herkend op CT en MR. De weke delen obliteraties blijken evenwel veel meer voor te komen en kunnen enkel herkend worden op de CISS beelden. Bovendien bestaat een goede correlatie tussen de klinische bevindingen en de obliteraties van het vestibulum en de semicirculaire kanalen. Maar bij twee van de zes patiënten kwam het MR beeld van de cochlea niet overeen met het klinisch beeld. Tenslotte werd bij één patiënt een aankleuring van het membraneuze labyrint gezien, hetgeen vermoedelijk wijst op een opstoot van de ziekte (vasculitis).

Aankleuring van het membraneuze labyrint op de T1-gewogen beelden na contraststof toediening werd reeds beschreven tijdens de acute fase van plotse doofheid en vertigo. De 3DFT-CISS beelden konden evenwel geen irreversiebele sekwellen binnen het membraneuze labyrint (obliteraties) aantonen bij patiënten met **idiopatische plotse perceptiedoofheid** en deze bevinding ondersteunt de virale pathogenese van idiopatische plotse perceptiedoofheid.

De 3DFT-CISS beelden kunnen rechtstreeks de endolymfatische ductus en saccus aantonen en bevestigen de CT bevindingen (visualisatie van de vestibulaire aqueductus) bij patiënten met de **ziekte van Ménière**. De endolymfatische ductus en saccus zijn beduidend nauwer bij patiënten met de ziekte van Ménière dan bij de normale populatie. Bovendien is er ook geen significant verschil in de afmetingen van de ductus en saccus van het pathologische en het normale (andere kant) binnenoor. Hieruit kunnen we besluiten dat MR tot op heden geen bijkomende informatie biedt bij patiënten met de ziekte van Ménière in vergelijking met CT.

MR en in het bijzonder T1-gewogen beelden na contraststof toediening en 3DFT-CISS beelden van het binnenoor en de brughoek maakten het mogelijk om letsels aan te tonen die tot nog toe met andere technieken niet konden worden gevisualiseerd. Hierdoor bekomt de clinicus bij veel meer patiënten dan voorheen een verklaring voor hun symptomen (vaak

perceptiedoofheid en/of vertigo). Bovendien kunnen de MR bevindingen de therapie beïnvloeden: extensie van schwannomas tot aan de fundus of niet, visualisatie van tumorale invasie in het membraneuze labyrint, differentiatie tussen neuritis of labyrinthitis enerzijds en schwannoma anderzijds, preoperatieve beoordeling van de cochlea en nervus cochlearis bij cochleaire implant kandidaten etc. In andere gevallen kan MR de pathologie aantonen en helpt de symptomen van de patiënt verklaren, maar de patiënt kan niet worden geholpen, zoals in de gevallen waarbij obliteraties worden gevonden in de endo/perilymphatische ruimten. Dit kan de indruk wekken dat deze MR bevindingen geen klinische consequenties hebben. Men mag evenwel niet vergeten dat men een patiënt kan geruststellen wanneer men een verklaring vindt voor zijn symptomen en dat hij dan niet langer de ene specialist na de andere gaat opzoeken en ook niet langer zal blootgesteld worden aan verschillende en soms invasieve diagnostische procedures (zoals selectieve angiografie). Bovendien kunnen sommige van deze nieuwe bevindingen op MR misschien klinici en chirurgen aanzetten tot het ontwikkelen van nieuwe behandelingen.

## 5. Conclusie

MR werd de meest geschikte techniek voor het onderzoek van het normale en pathologische binnenoor. Geen enkele andere radiologische techniek is in staat om zoveel pathologie te detecteren bij patiënten met perceptiedoofheid en/of vertigo. Maar het succes van de MR-techniek hangt af van de sekwenties die worden gekozen. T1-gewogen beelden à blanc en in het bijzonder T1-gewogen beelden na contrastinjectie en goede gradiënt-echo beelden (3DFT-CISS) zijn noodzakelijk om alle pathologie te herkennen. Daarom moeten deze drie MR sekwenties behoren tot het routine onderzoek van het binnenoor.

Aanvullende T2-gewogen beelden zijn niet echt nodig bij het onderzoek van het binnenoor en de brughoek, maar ze kunnen wel letsels in de hersenstam of de kleine hersenen aantonen die eventueel de perceptiedoofheid en/of vertigo van de patient kunnen verklaren.

Tenslotte hopen we dat nieuwe sekwenties ons in staat zullen stellen nog dunnere beelden met nog hogere resolutie te bekomen en dat deze beelden ons nog beter de anatomie en de pathologie van het binnenoor zullen tonen. Dit zou kunnen leiden tot een beter inzicht in de pathogenese van binnenoor pathologie en een verfijnen van de diagnostische en therapeutische mogelijkheden bij patiënten met perceptiedoofheid en/of vertigo.

---

## BIJKOMENDE STELLINGEN

---

1. Magnetische Resonantie van de borst biedt een juiste diagnose in 80% van de borsttumoren waarbij geen eensluitende diagnose kon worden bekomen met behulp van klinisch onderzoek, mammografie en echografie.
2. De locale staging van larynxtumoren is exacter met Magnetische Resonantie dan met Computertomografie.
3. Magnetische Resonantie - en Computertomografische beelden zijn bijzonder geschikt voor het aanleren van normale anatomie, doch helaas wordt hier onvoldoende gebruik van gemaakt.
4. Nodeloze arthroscopische knieonderzoeken kunnen worden vermeden door systematisch MR onderzoek van de knie bij deze patiënten, hetgeen tevens een besparing zou opleveren.
5. De beeldvorming van de craniale zenuwen maakt momenteel een enorme vooruitgang door en biedt de clinicus veel bijkomende informatie waardoor het aantal aanvragen voor onderzoek van de craniale zenuwen sterk zal stijgen.
6. Echografische staging van halsklieren is minder betrouwbaar dan CT-staging.